Aix*Marseille université
Socialement engagée

NNT/NL : 2020AIXM0001/001ED000

THÈSE DE DOCTORAT

Soutenue à Aix-Marseille Université
le 16 décembre 2022 par

Longji Bing

Mapping the dusty star formation at high redshift with the NIKA2 cosmological surveys

Discipline
Physique et Sciences de la Matière

Spécialité
Astrophysique et Cosmologie

École doctorale
ED 352

Laboratoire/Partenaires de recherche
Laboratoire d'Astrophysique de Marseille (LAM)
Institut de Radioastronmie Millimétrique (IRAM)

Composition du jury

James Geach University of Hertfordshire	Rapporteur
Carlotta Gruppioni INAF-OAS Bologna	Rapportrice
Benjamin Magnelli CEA Saclay, DAp	Examinateur
Jonathan Freundlich Université de Strasbourg	Examinateur
Roberto Neri IRAM	Examinateur
Roser Pello Aix-Marseille Université	Présidente du jury
Guilaine Lagache Aix-Marseille Université	Directrice de thèse
Alexandre Beelen Aix-Marseille Université	Invité

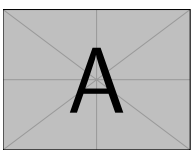

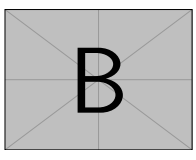

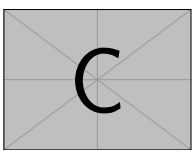

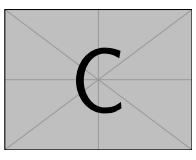

Affidavit

I, undersigned, Longji Bing, hereby declare that the work presented in this manuscript is my own work, carried out under the scientific direction of Guilaine Lagache, in accordance with the principles of honesty, integrity and responsibility inherent to the research mission. The research work and the writing of this manuscript have been carried out in compliance with both the french national charter for Research Integrity and the Aix-Marseille University charter on the fight against plagiarism.

This work has not been submitted previously either in this country or in another country in the same or in a similar version to any other examination body.

Marseille 10/10/2022

Liste de publications et participation aux conférences

Liste des publications réalisées dans le cadre du projet de thèse :

1. Searching for high-z DSFGs with NIKA2 and NOEMA, L. Bing et al. mm Universe @ NIKA2 - Observing the mm Universe with the NIKA2 Camera, Rome (Virtual), Italy, Edited by De Petris, M. ; Ferragamo, A. ; Mayet, F. ; EPJ Web of Conferences, Volume 257, id.00006.
2. Faint millimeter NIKA2 dusty star-forming galaxies : finding the high-redshift population. L.-J. Bing, G. Lagache, A. Beelen et. al. submitted to A&A.

Participation aux conférences et écoles d'été au cours de la période de thèse :

1. Observing the millimeter Universe with the NIKA2 camera, Jun. 28-Jul. 2, 2021, Sapienza University in Rome (on line)
2. The growth of galaxies in the Early Universe - VII, Mar. 11 - Mar. 15, 2022, Sesto, Italy
3. Journées scientifiques "Galaxies" du PNCG 2022, Jun.20 - Jun.22, 2022 Strasbourg, France

Résumé

Cette thèse se concentre sur l'étude des galaxies poussiéreuses à grand décalage vers le rouge et de la formation d'étoiles dans l'Univers. Elle a été réalisée dans le cadre des relevés profonds cosmologiques avec NIKA2 (N2CLS), un instrument récent installé sur le télescope de 30m de l'IRAM. Un nouveau cadre d'analyse est développé pour les données N2CLS pour estimer précisément les biais dans la détection des sources et les mesures de flux. Grâce à ce cadre, nous mesurons les comptages de source à 1,2 et 2 mm dans le relevé N2CLS avec une profondeur et une couverture en flux sans précédent. Pour la première fois, nous tenons compte de l'impact du regroupement des sources et de leur superposition sur les comptages. Nous comparons nos résultats avec les observations provenant des interféromètres et les modèles d'évolution de galaxies. Cette comparaison révèle un excès de sources brillantes par rapport à la plupart des modèles.

La thèse porte également sur la stratégie de mesure des décalage vers le rouge (z) pour notre échantillon de galaxies poussiéreuses. Nous introduisons une nouvelle méthode pour contraindre le z des sources en utilisant conjointement la photométrie multi-longueur d'ondes et la spectroscopie NOEMA. La méthode prouve son efficacité et sa robustesse sur cinq sources issues des données de vérification scientifique de NIKA2. Cette méthode automatique pourra être appliquée à de grands échantillons de données millimétriques. L'étude sur ces 5 sources permet de concevoir la stratégie de suivi de notre échantillon complet de N2CLS et les premiers résultats sur le champ GOODS-N sont également présentés.

Mots clés : galaxie à grand décalage vers le rouge, galaxie sub-millimétrique, formation d'étoiles, formation et évolution des galaxies

Abstract

This thesis focus on the studies on high-redshift dusty galaxies and obscured star formation using the NIKA2 Cosmological Legacy Survey (N2CLS). This survey is using 300h of NIKA2, a recent continuum camera installed on the IRAM 30m telescope. A new analysis framework for N2CLS is developed to more completely estimate biases in high-z source detection and flux measurements. With this framework, we measure the number counts at 1.2 and 2 mm with unprecedented depth and flux coverage. For the first time, we account for the impact of sources blending and clustering on single-dish number counts and make fair comparison of our results with interferometric observations and models. An excess of bright sources relative to most models is noticed from the comparison.

The thesis also works on the strategy of efficient redshift measurements on large sample of obscured galaxies for studying the cosmic history of obscured star formation. We introduce a new method to jointly constrain the source redshift with the information from the multi-wavelegth photometry and NOEMA spectroscopy. The method proves its effectiveness and robustness on five sources from NIKA2 Science Verification data. We highlight the application of this highly automatic method to large millimeter datasets, including N2CLS, and design the follow-up strategy on the N2CLS GOODS-N sample, where the first results are also presented.

Keywords: high-redshift galaxy, sub-millimeter galaxy, star formation, galaxy formation and evolution

Acknowledgments

All along my PhD, I have benefited from discussions, suggestions and supports from many people. In the first place, I would like to thank my advisor, Guilaine Lagache for the opportunity she gave me and also for her support, her patience and her priceless advice for my research and professional development. I am also extremely grateful to Alexandre Beelen for his continuous support from the valuable scientific and technical discussions and advice over the last three years, to Matthieu Bethermin for sharing his experience in the research and proposal preparation and kindly offering suggestions and help on the data analysis and simulation in my research. I would also like to express my gratitude to Stefano Berta, Roberto Neri and Nicolas Ponthieu for their discussions, suggestions and help on the data analysis and IRAM proposal preparation throughout my doctoral research, especially at the time in Grenoble during the most difficult period of the pandemic.

I would also like to thank committee members James Geach and Carlotta Gruppioni, together with reviewers Benjamin Magnelli, Jonathan Freundlich, and Rose Pello who helped me improve the content of my thesis. I also benefited from the interactions with David Elbaz, Olivier Ilbert, Veronique Buat, and Denis Burgarella on the envision and applications of my research. I am thankful to the GECO group and LAM, my officemates Guillaume and Junais, as well as the other students including but not limited to Olivier, Siju, Gayathri, Athanasia, and Mathilde, for creating a warm and friendly environment. I would also like to express my gratitude to the operation team of the IRAM 30m telescope, for their kind and continuous support in the observation runs during these special years.

I would like to thank my parents who supported my choices and gave me motivation and support throughout my academic life. I would also like to thank Mengyuan for her constant support, for listening to my complaints and joys about my research, as well as for the generous suggestions and help when I was in difficulties. I am also grateful to Fransçoise for her help in all kinds of administrative processes during my stay at LAM.

Long Résumé

De nos jours, les observatoires au sol et spatiaux prennent des images de tout ou partie du ciel sur l'ensemble du spectre électromagnétique. Ces relevés permettent d'obtenir des échantillons représentatifs de millions de galaxies depuis les premières centaines de millions d'années après le Big-Bang. Chaque longueur d'onde fournit des informations différentes sur les propriétés physiques des galaxies. L'émission stellaire domine la lumière que nous observons dans l'UV, l'optique et le proche infrarouge, où l'émission de la jeune population stellaire domine dans les plus courtes longueurs d'onde et les étoiles âgées dominent dans les plus grandes longueurs d'onde. À plus grande longueur d'onde, dans l'infrarouge moyen et lointain, l'émission des galaxies est principalement produite par la poussière qui absorbe la lumière des étoiles. Les trous noirs accrétant de la matière, ou noyaux actifs de galaxie, produisent également des émissions caractéristiques, notamment dans les rayons X et en radio.

En particulier, les observations profondes aux longueurs d'onde (au repos) UV et optiques ont considérablement amélioré notre compréhension de la formation et de l'évolution des galaxies au cours des trois dernières décennies. Les observations en optique et en infrarouge permettent d'identifier un grand nombre de galaxies dans l'Univers primitif. Les observations les plus récentes indiquent déjà leur existenceà $z > 10$, où l'Univers n'a que quelques centaines de millions d'années. L'émission de ces galaxies est dominée par les jeunes étoiles en UV et ces observations fournissent l'un des moyens importants de mesurer la densité du taux de formation d'étoiles cosmique (SFRD). Cependant, l'existence de poussières pourrait atténuer les émissions des galaxies massives précoces et fausser les études statistiques sur l'évolution des galaxies et le SFRD. Les observations dans l'infrarouge lointain jusqu'au millimétrique permettent de sonder l'émission du milieu interstellaire froid responsable de l'atténuation de la lumière des étoiles et de retracer le lieu de naissance des étoiles. Ces observations fournissent donc des informations très complémentaires aux observations optiques en sondant directement l'émission de la poussière, ainsi que certaines molécules clés comme le CO.

Les relevés millimétriques profonds systématiques sur de grands volumes cosmologiques ont longtemps été limités par le manque de capacité d'observations sensibles et sur de grande régions du ciel (i.e. quelque degrés carré). L'émergence récente de nouvelles installations et de nouveaux instruments ouvre de nouvelles possibilités. L'interférométrie (sub)millimétrique sensible et à haute résolution spatiale a été largement appliquée à l'observation de galaxies poussiéreuses faibles mais représentatives de l'Univers lointain, avec des détails sans précédent. Les grands téle-

scopes (monolytiques), bien qu'ayant une résolution spatiale beaucoup plus faible, offrent une capacité d'observation sur de grands champs de vue. Ils sont donc très utiles pour recenser les galaxies poussiéreuses sur une grande surface et dans un volume cosmique, ce qui est hors de portée des interféromètres dont le champ de vue est beaucoup plus étroit. Ce n'est qu'en combinant ces deux types d'observations que nous pourrons obtenir une image complète de la population de galaxies poussiéreuses dans l'Univers sur une large gamme de luminosité, de masse, d'environnement et de décalage vers le rouge.

Cette thèse se concentre sur l'étude des galaxies poussiéreuses à haut z et de la formation d'étoiles obscurcies à l'aide de l'instrument NIKA2 (New IRAM KIDs Array2), une caméra continuum récente, installée sur le télescope de 30m de l'IRAM, observant à 1.2 et 2 mm. NIKA2 offre un grand champ de vue instantané, une haute sensibilité et une résolution spatiale relativement élevée parmi les instruments qui observent le continuum et qui fonctionnent sur des télescopes millimétriques. Grâce à ses avantages en termes de vitesse de relevé et d'observations simultanées aux deux bandes, NIKA2 offre une capacité sans précédent pour des grands relevés profonds dans le millimétrique afin de sonder l'émission de la poussière des galaxies à grand décalage vers le rouge. Ces avantages nous permettent également de concevoir et d'effectuer des relevés de champs cosmologiques, comme le fait le NIKA2 Cosmological Legacy Survey (N2CLS). Le relevé N2CLS observe deux champs profonds extragalactiques emblématiques, GOODS-N et COSMOS. Les observations des deux champs sont conçues pour obtenir une combinaison sans précédent de couverture et de profondeur à 1.2 et 2 mm. Cela permet un échantillonnage plus complet des sources millimétriques de différents flux, et fournit une vue d'ensemble sur les propriétés statistiques des sources accessibles à NIKA2. Les détails des aspects de NIKA2, du relevé N2CLS et des observations d'autres champs cosmologiques avec NIKA2 peuvent être trouvés dans le chapitre 2 de la thèse.

En tant que nouvel instrument à base de KIDs, NIKA2 présente également des défis pour la réduction et l'interprétation des données. Dans le chapitre 2, nous décrivons les procédures et les configurations permettant de produire les cartes NIKA2/N2CLS à partir des données brutes, en utilisant le cadre de réduction des données fourni par le pipeline PIIC. Plus précisément, nous présentons également la nouvelle fonction de simulation de PIIC. Ce module de simulation permet de faire passer des modèles de ciel réalistes au travers des processus complets de réduction des données, après étalonnage. Au cours de ce processus, les effets systématiques et les biais dans la réduction des données, la détection des sources et la mesure des flux seront imprimés dans les cartes de sortie. Ces impacts sur la détection des sources et les mesures de flux peuvent ensuite être récupérés en comparant les propriétés des sources dans le modèle d'entrée et dans la carte de sortie. Les termes spécifiques et l'origine des biais et des effets systématiques à prendre en compte dans l'analyse de la simulation sont également résumés dans le chapitre 2. Une illustration du modèle d'entrée et du résultat de sortie de la simulation est donnée dans la Fig. 1.

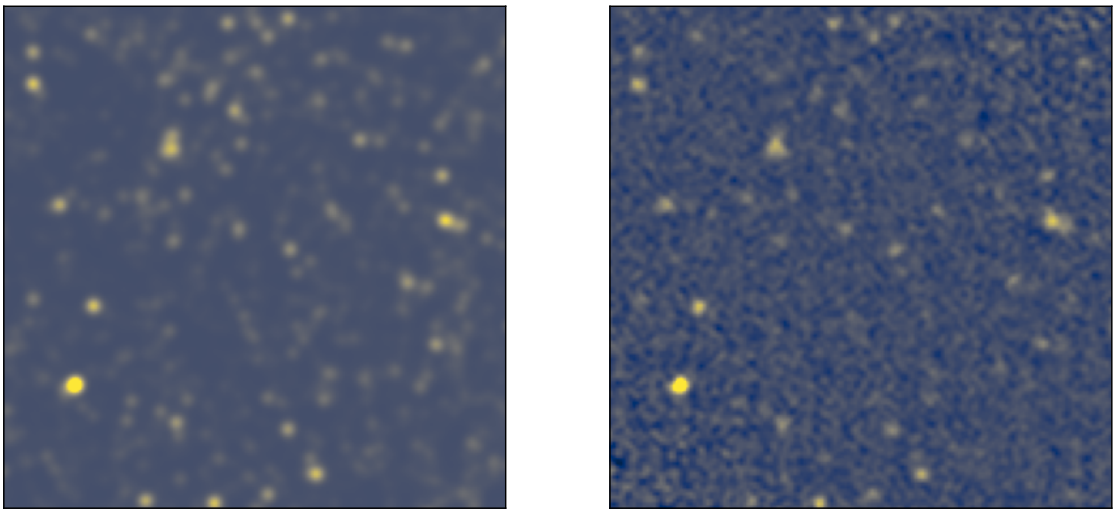

Figure 1 – Exemple du modèle de ciel basé sur la simulation SIDES/Uchuu (à gauche) injecté dans les données réelles de bruit en temps pour la simulation PIIC, et carte PIIC en sortie de simulation, après 5 itérations (à droite). Ces exemples sont des découpages du modèle et de la simulation réalisés pour les corrections de biais des observations N2CLS du champ GOODS-N à 1,2 mm.

Avec ce nouveau cadre, je présente au chapitre 3 les détails de l'analyse des données et les principaux résultats actuels du relevé N2CLS. Les données du relevé sont réduites en suivant les configurations et les procédures décrites dans le chapitre 2, et les cartes résultantes sont présentées. Après la production des cartes du relevé, je décris les procédures de détection des sources, ainsi que la photométrie des sources, basée sur l'ajustement d'une Gaussienne.

En plus donc de la réduction des données et de la détection des sources dans les cartes N2CLS, j'effectue également la simulation PIIC basée sur des modèles de ciel provenant des simulations SIDES/Uchuu, et je calcule la pureté de l'échantillon, les biais sur les flux mesurés (flux boosting), et la complétude. La pureté décrit la probabilité qu'une source détectée soit réelle à un S/N de détection donné. Le "flux boosting" décrit le rapport entre les flux des sources mesurés sur les cartes de sortie de la simulation et les cartes du modèle sans bruit, en fonction du S/N de détection. La complétude décrit la probabilité de récupérer des sources à des flux intrinsèques/vrais et des niveaux de bruit donnés dans les cartes obtenues à partir des observations (simulées). Pour tenir compte de la non-uniformité de la profondeur des observations N2CLS, nous donnons en outre l'accessibilité des sources dans la carte par la surface effective, qui est équivalente à la somme des surfaces des pixels pondérée par la complétude attendue de la détection dans toute la région du relevé. La forme numérique ou analytique, ainsi que le calcul de ces facteurs de correction, peuvent être trouvés dans la section 3.2.3. Les estimations de ces biais et systématiques sont basées sur la

même détection de sources et la même mesure de flux que dans la section 3.2, ce qui préserve la cohérence de l'ensemble des procédures d'analyse.

Grâce à l'analyse de la pureté, de la complétude, et du "flux boosting" par la simulation, nous déduisons les corrections à appliquer à chaque source détectée dans N2CLS et produisons le catalogue de sources en conséquence. À partir des relevés à 1.2 mm de N2CLS, nous détectons 120 et 195 sources dans les champs GOODS-N et COSMOS, avec un rapport signal/bruit (S/N) correspondant à une pureté supérieure à 80%. À partir des relevés à 2.0 mm, nous détectons 67 et 76 sources dans les champs GOODS-N et COSMOS, avec un rapport signal/bruit (S/N) correspondant à une pureté supérieure à 80%. Le catalogue des sources avec les coordonnées, les flux corrigés, la pureté et la surface effective est donné dans la section 3.2.4. À partir des informations énumérées ci-dessus, je décris plus en détail la méthode d'estimation des comptages de sources à 1.2 et 2 mm dans la section 3.3.1. Cependant, avant de calculer les comptages de sources N2CLS, je teste tout d'abord la récupération correcte des comptages par la simulation et mon cadre de correction des biais. En utilisant le même calcul des facteurs de correction que celui appliqué aux sources N2CLS, j'obtiens des comptages de sources cohérents par rapport au modèle d'entrée à partir des catalogues de détection dans la carte de sortie des simulations. De plus, en comparant les comptages de sources soumises à la convolution par le lobe de l'instrument à ceux obtenus sans ce "lissage", nous remarquons également un biais systématique entre les deux. Bien que notre simulation ait pu récupérer correctement les comptages de sources dans le modèle, les biais entre les comptages de sources et de galaxies subsistent et sont estimés quantitativement. L'impact du lobe de l'instrument sur les comptages de sources a été suggéré pendant des années ; notre travail le révèle pour la première fois à partir de simulations réalistes prenant plus complètement en compte à la fois le bruit instrumental et le regroupement des galaxies poussiéreuses.

En gardant à l'esprit les biais sur les comptages de sources provenant du lobe de l'instrument, nous calculons les comptages en nombre à 1.2 et 2 mm dans chaque champ à partir des flux corrigés, de la pureté et de la surface effective de chaque source (donnée dans les catalogues de sources). Les rapports entre les comptages de sources (mesurés) et les comptages de galaxies(intrinsèques) sont ensuite utilisés pour corriger les comptages de sources observées et ainsi obtenir les comptages de galaxies. Ces résultats sont présentés dans la section 3.3.3, et comparés aux observations précédentes et aux prédictions de modèles. La figure 2 donne un exemple de nos mesures des comptages, en plus des résultats des observations précédentes. Nous constatons que les comptages sont généralement cohérents entre nos mesures et les mesures précédentes utilisant un grant télescope unique. Nos comptages sont légèrement supérieurs à ceux obtenus grâce aux observations de l'interféromètre ALMA à haute résolution angulaire. Mais notre correction permettant de passer des comptages de sources aux comptages de galaxies rend ces résultats cohérents. Cela suggère que la correction de l'impact du lobe est essentielle dans l'analyse combinée des résultats. Avec les comptages galaxies corrigés, j'ai également fait une comparaison entre nos

observations et les prédictions provenant de diverses simulations et modèles semi-analytiques. La comparaison suggère une cohérence globale entre les observations et les prédictions. Cependant, la plupart des modèles sous-estiment le nombre de sources brillantes à 1.2 et 2 mm par un facteur de 2 à 4. Cela suggère probablement une sous-production de galaxies (massives) actives en formation d'étoiles dans ces simulations et modèles. D'autres possibilités, comme l'existence d'un nombre considérable de sources froides dont la SED de la poussière culmine à une plus grande longueur d'onde qu'anticipée, pourraient également conduire à une population plus importante que prévu de galaxies poussiéreuses brillantes millimétriques. Ces scénarios doivent encore être testés par de futures observations.

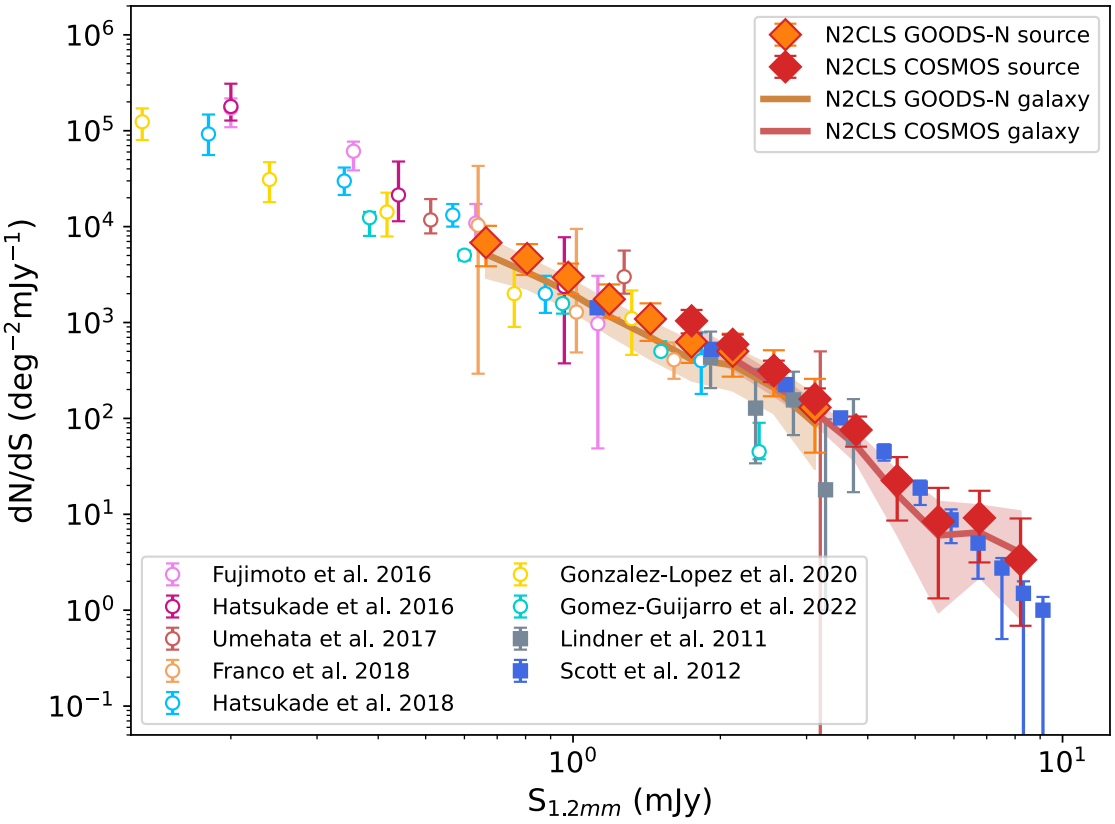

Figure 2 – Comptages de sources différentiels observés à 1.2 mm pour les champs N2CLS GOODS-N et COSMOS (losanges oranges et rouges) comparés aux mesures d'autres études à 1.1/1.2 mm. Tous les résultats des observations interférométriques sont présentés avec des symboles ouverts, et les mesures des observations de grands télescopes uniques sont présentées avec des symboles pleins. Les régions ombrées en jaune et en rouge montrent l'intervalle de confiance $\pm 1\sigma$ des comptages de galaxies N2CLS obtenus après correction des comptages de sources dans les champs GOODS-N et COSMOS, respectivement.

Les comptages en nombre de sources/galaxies dans (sub)millimétrique pourrait apporter des informations précieuses sur la formation et l'évolution des galaxies en les comparant aux modèles. Cependant, des études récentes ont également montré que les comptages de galaxies sont principalement dominés par les propriétés des sources à z=1-3, où la plupart des galaxies poussiéreuses brillantes en (sub)millimètre sont situées. L'information provenant des galaxies poussiéreuses à plus grand décalage vers le rouge (i.e. z>4) est donc diluée. Cependant, ces galaxies poussiéreuses apparaissent à l'aube cosmique et sont suggérées comme étant les progéniteurs manquants des galaxies massives quiescentes dans l'Univers jeune. Elles commencent donc à susciter l'intérêt d'un grand nombre d'études observationnelles et théoriques sur la formation et l'évolution des galaxies massives.

En plus des comptages, l'obtention du décalage vers le rouge individuel des sources (sub)millimétriques pourrait aider à identifier les premières galaxies poussiéreuses de l'Univers, à contraindre davantage les prédictions des modèles et à comprendre l'évolution cosmique des galaxies poussiéreuses et du taux de formation d'étoiles obscurci. Les études du chapitre 4 se concentrent sur les défis des mesures de décalage vers le rouge des galaxies poussiéreuses, qui constituent la première étape pour contraindre leur évolution cosmique. Ce travail commence par les observations pilotes de NIKA (précurseur de NIKA2) dans GOODS-N et les observations de vérification scientifique de NIKA2 autour d'une galaxie poussiéreuse lentillée à z=5.2 HLS J0918+5142 (HLS en abrégé). Dans ces deux observations profondes, nous identifions 7 galaxies candidates à haut redshift et (ou) fortement obscurcies. Ces sources sont sélectionnées parce qu'elles ont une émission millimétrique brillante tout en étant faibles à d'autres longueurs d'onde. Plus précisément, les quatre sources sélectionnées dans le champ HLS ont des SEDs "froides" dans l'IR lointain qui pourraient correspondre à des galaxies actives en formation d'étoiles à z=3-7, suggérant ainsi des grands décalages vers le rouge.

Dans cette étude, j'utilise les observations interférométriques de NOEMA pour obtenir le continuum et les spectres millimétriques des sources sélectionnées. La haute résolution angulaire et la haute sensibilité de l'interféromètre NOEMA nous aident d'abord à identifier les vraies contreparties des sources NIKA2 aux autres longueurs d'onde et à obtenir leur position précise et leur flux. A partir des données du continuum, nous trouvons les contreparties de six sources, tandis qu'une source dans GOODS-N est suggérée comme étant liée à des pics de bruit dans le premier relevé NIKA. Deux sources NIKA(2) de l'échantillon GOODS-N sont résolues en deux composantes. Au total, nous trouvons trois sources NOEMA associées à deux sources NIKA dans GOODS-N, et cinq sources NOEMA associées à quatre sources NIKA2 dans HLS.

Les décalages vers le rouge des sources dans GOODS-N et HLS sont obtenus par différentes approches. Pour les trois sources NOEMA associées à l'échantillon GOODS-N, nous croisons leurs coordonnées avec les catalogues de diverses observations

HST, Spitzer et en IR lointain pour obtenir la photométrie multi-longueur d'onde de ces sources. Avec les flux du proche UV au millimétrique, nous effectuons des modélisations de leur SED avec CIGALE et EAZY pour estimer leur décalage vers le rouge photométrique, qui est principalement contraint par les données optiques et infrarouges. Pour les sources HLS, le manque de données multi-longueurs d'onde autre que les observations Herschel dans l'infrarouge lointain empêche l'estimation du décalage vers le rouge par l'ajustement des SED optique-IR. Comme ces sources sont observées par des relevés spectraux NOEMA à large bande avec une couverture continue couvrant 31 GHz, nous estimons leur décalage vers le rouge spectroscopique directement en recherchant les raies d'émission CO/[CI] dans leurs spectres. Cependant, la faiblesse des raies, la large couverture des spectres et le bruit non uniforme posent des problèmes importants pour la recherche et l'identification des raies en aveugle. Pour identifier avec précision et efficacité les raies et mesurer le décalage vers le rouge des sources HLS, nous développons un nouveau cadre d'analyse. La méthode est conçue pour contraindre conjointement le décalage vers le rouge de la source en tenant compte des informations provenant à la fois de la photométrie multi-longueurs d'onde et des relevés spectraux NOEMA. En utilisant les résultats des ajustements de la SED, la méthode ne considère pas seulement la distribution de probabilité du décalage vers le rouge obtenue, mais convertit également la luminosité infrarouge (dépendant du décalage vers le rouge) en flux de raies attendus. Cette conversion utilise la corrélation mesurée entre la luminosité dans l'infrarouge lointain et les luminosités des raies CO/[CI]/[CII], et produit des spectres modèles attendus pour une large gamme de décalages vers le rouge. Nous effectuons ensuite la corrélation croisée des spectres modèles pour chaque décalage vers le rouge avec les spectres NOEMA et déterminons le meilleur décalage vers le rouge en utilisant le maximum de la probabilité.

Avec la méthode ci-dessus (analyse photométrique ou jointe photométrique/spectroscopique millimétrique), j'ai obtenu le redshift photométrique/spectroscopique de toutes les sources détectées par NOEMA. Dans GOODS-N, nous avons trouvé une source NOEMA avec un redshift photométrique de 2-3, et deux autres sources avec un redshift photométrique de ~4. L'une des sources de redshift 4 est associée à une source invisible en optique dans toutes les bandes d'observations HST, qui, comme suggéré par le redshift photométrique de EAZY, pourrait également être une galaxie poussiéreuse active en formation d'étoiles à z>6. Dans HLS, nous avons mesuré le décalage vers le rouge spectroscopique de quatre sources NOEMA sur cinq, localisées à z=5.241, z=5.131, z=3.123 et z=3.036.

La robustesse de la méthode d'analyse conjointe sous différentes conditions et hypothèses de modèle est discutée plus en détail dans la section 4.5.1 de ce chapitre, ce qui permet d'envisager positivement l'application de la méthode à d'autres projets de mesure de décalage vers le rouge. Il reste une source HLS sans détection de raie significative et sans solution de décalage vers le rouge. Pour cette source, prenons donc le décalage vers le rouge le plus probable obtenu grâce aux données en IR lointain-

millimétrique dans l'analyse qui suit. Des exemples d'identifications de décalage vers le rouge et de raies sur deux sources peuvent être trouvés dans la Fig. 3.

Avec le décalage vers le rouge de chaque source, je mesure ensuite leurs propriétés en matière de poussière, de gaz froid et de formation d'étoiles. Nous avons estimé la température de la poussière de ces galaxies en ajustant les données photométriques de l'IR lointain jusqu'au millimétrique avec un modèle de corps noir modifié. Deux des galaxies de l'échantillon HLS ont une température de poussière significativement plus froide que la moyenne des galaxies active en formation d'étoiles à leur décalage vers le rouge. Ceci ajoute des preuves à l'existence d'une population de galaxies poussiéreuses avec une SED apparemment froide. A partir de la modélisation de la SED, nous estimons également le taux de formation d'étoiles de chaque galaxie à partir de leurs luminosités infrarouges totales. Pour GOODS-N, en combinant avec la masse stellaire estimée à partir des données optiques-IR, nous trouvons que les trois sources sont toutes situées autour de la séquence principale des galaxies actives en formation d'étoiles à leur décalage vers le rouge, indiquant une activité normale de formation d'étoiles dans ces galaxies. Cependant, en utilisant la masse de gaz moléculaire dérivée du flux continuum à grande longueur d'onde, nous trouvons que deux des sources GOODS-N ont un temps d'épuisement du gaz assez court, jusqu'à quelques dizaines de millions d'années. Cela suggère un appauvrissement rapide et continu de leur réservoir de gaz froid, et donc de la formation d'étoiles. Le court temps d'épuisement du gaz et leur masse stellaire élevée suggèrent probablement que ces deux galaxies connaissent la dernière étape de leur évolution vers la quiescence. Au contraire, sur la base du taux de formation d'étoiles et des mesures de la masse de gaz moléculaire à partir de la SED dans l'infrarouge lointain et des raies du CO, les autres galaxies de GOODS-N et HLS montrent un temps d'épuisement du gaz un ordre de grandeur plus long. Cela suggère une évolution plus séculaire. En outre, avec la galaxie poussiéreuse lentillée à z=5.243 et les deux autres sources HLS NIKA2 à z=5.241 et z=5.131, je discute de la possibilité de l'existence d'une surdensité de galaxies poussiéreuses dans le champ HLS.

Enfin, je résume les résultats et présente quelques perspectives du relevé N2CLS et de mes recherches. Pour N2CLS, l'identification de galaxies poussiéreuses active en formation d'étoiles à grand décalage vers le rouge et les observations de suivi sont en cours. Les études correspondantes ont déjà commencé dans GOODS-N. Une observation de suivi avec NOEMA a été effectuée sur les sources N2CLS non identifiées par les observations aux autres longueurs d"onde. A partir des observations de suivi, nous avons déjà obtenu un échantillon de galaxies invisibles en optique et candidates pour être à grand décalage vers le rouge, qui ressemble à celui identifié dans l'échantillon GOODS-N au chapitre 4. Une analyse plus approfondie avec les données ancillaires et les observations JWST à venir et des spectres millimétriques supplémentaires nous aideront à construire un échantillon complet, sûr et non biaisé de galaxies poussiéreuses formant des étoiles dans GOODS-N dans un avenir proche. À partir de notre analyse des données N2CLS, j'ai également souligné l'importance

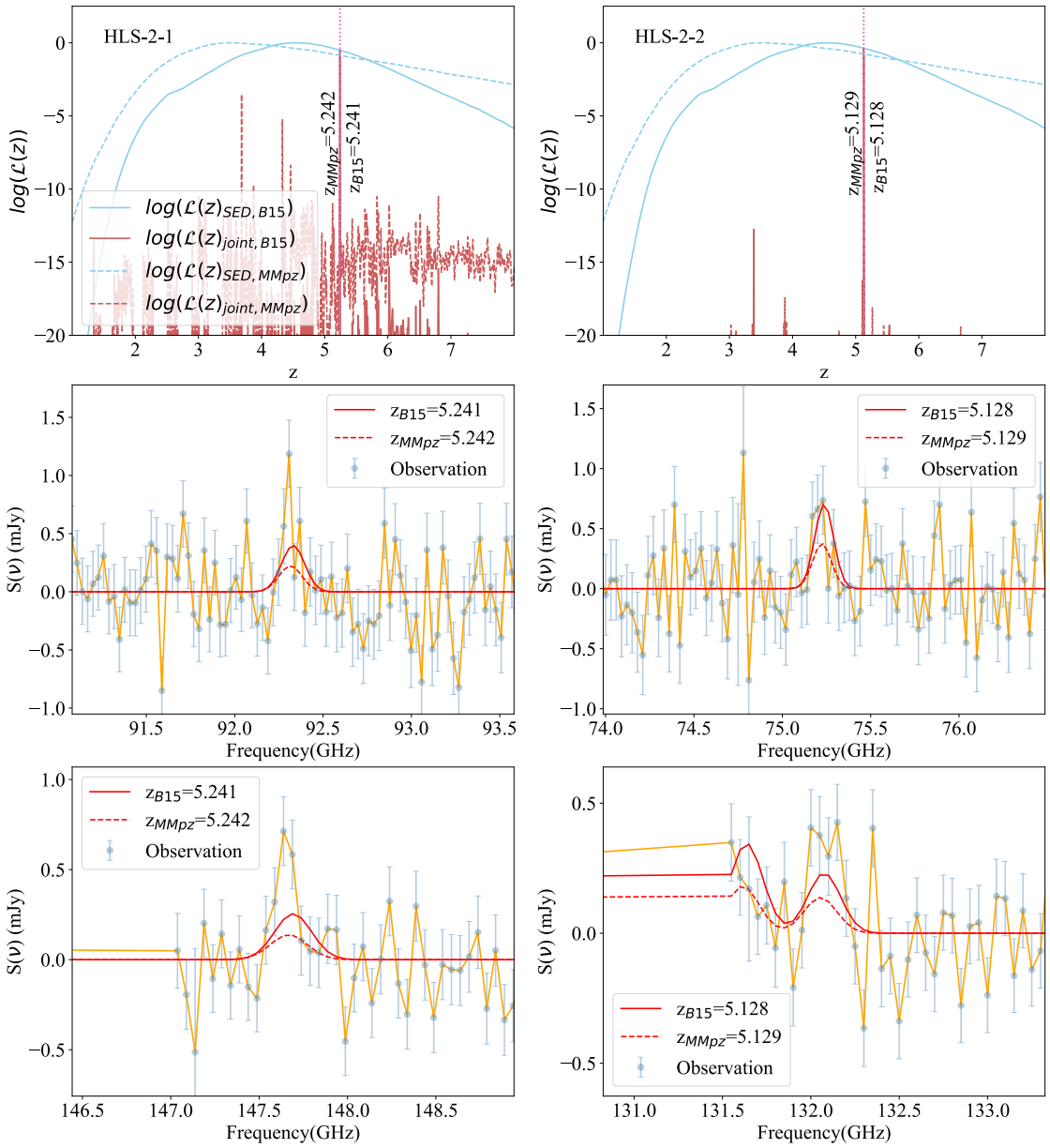

Figure 3 – Exemples du résultat de l'analyse conjointe photométrie+spectroscopie millimétrique sur deux sources HLS. La figure de la première ligne montre la vraisemblance obtenue par l'analyse conjointe en fonction du décalage vers le rouge. Les lignes bleues indiquent la vraisemblance en fonction du décalage vers le rouge basée uniquement sur la modélisation de la SED, et les lignes brunes montrent la vraisemblance conjointe obtenues avec les contraintes photométriques et spectroscopiques. Les lignes pointillées et les lignes pleines représentent la vraisemblance de l'analyse conjointe basée sur deux méthodes différentes de modélisation de la SED, en plus des données spectrales de NOEMA. Les meilleures solutions de décalage vers le rouge sont mises en évidence par le texte et les lignes verticales pointillées, et l'analyse conjointe avec deux techniques de modélisation de la SED montre des résultats cohérents. Les deuxième et troisième rangées montrent les raies d'émission millimétriques identifiées par la méthode. Les points bleus et les lignes orange montrent les spectres NOEMA extraits à la position de la source, et les lignes rouges illustrent le modèle aux décalages vers le rouge déterminés pour la source, qui correspondent le mieux aux spectres observés.

des simulations de bout en bout avec des modèles de ciel réalistes dans l'analyse des données pour les futurs relevés dans l'infrarouge lointain et le millimétrique. En outre, je discute également de l'application possible de l'analyse conjointe photométrie + spectroscopie millimétrique dans la recherche des décalages vers le rouge pour les futurs relevés.

Contents

Affidavit 2

Liste de publications et participation aux conférences 3

Résumé 4

Abstract 5

Acknowledgements 6

Long Résumé 7

Contents 17

List of Figures 20

List of Tables 28

Introduction 30

1 The Dusty Star-Forming Galaxies 32
- 1.1 General Picture of Galaxy Formation and Evolution . . . 32
  - 1.1.1 Galaxy Formation and Evolution Under Λ-CDM Cosmology . . 33
  - 1.1.2 Cosmic Evolution of Star-Formation Rate Density . . . 35
  - 1.1.3 Star-Formation in Galaxies across cosmic time . . . 36
- 1.2 Dusty Star-Forming Galaxies . . . 40
  - 1.2.1 Spectral Energy Distribution of Galaxies . . . 40
  - 1.2.2 Dusty Interstellar Medium in Galaxies . . . 43
  - 1.2.3 Selection of Dusty star-forming Galaxies . . . 48
  - 1.2.4 The Role of Dusty Galaxies in Galaxy Formation and Evolution . 52
  - 1.2.5 Open Questions and Limitations . . . 54
- 1.3 Observations of Dusty Galaxies . . . 56
  - 1.3.1 Space-Based Missions . . . 56
  - 1.3.2 Ground-Based Single-Dish Telescopes . . . 61
  - 1.3.3 Continuum Interferometric Observations . . . 65
  - 1.3.4 Spectroscopic Interferometric Observations . . . 69

2 New IRAM KIDs Arrays 2 (NIKA2) 72
- 2.1 Basic Information on NIKA2 . . . 72
  - 2.1.1 Design and General Aspects of NIKA2 . . . 72

2.1.2 Scientific Applications of NIKA2 . . . 75
2.2 NIKA and NIKA2 Deep Fields . . . 76
2.3 Observation with NIKA2 . . . 78
2.4 NIKA2 Data Reduction . . . 81
2.4.1 NIKA2 Data Calibration and Map Reconstruction with PIIC . . . 81
2.4.2 Source Extraction and the Effects To Be Corrected . . . 84
2.4.3 PIIC Simulations . . . 87

3 Millimeter Number Counts from NIKA2 Cosmological Legacy Survey 90
3.1 Introduction . . . 90
3.2 Survey Map, Source Extraction and Statistical Corrections . . . 92
3.2.1 Deepfield Maps from N2CLS . . . 92
3.2.2 Method of Source Extraction and Photometry . . . 95
3.2.3 Statistical Corrections and Analysis . . . 98
3.2.4 Flux Corrrection . . . 104
3.3 Source and Galaxy Number Counts . . . 105
3.3.1 Number Counts Estimation . . . 105
3.3.2 Validation of the number counts reconstruction from simulations 106
3.3.3 1.2 and 2 mm Number Counts . . . 108
3.3.4 Comparison with Models . . . 113
3.4 Discussion . . . 114
3.5 Summary . . . 117

4 Finding the high-redshift population of DSFGs 120
4.1 Introduction . . . 120
4.2 Sample, NOEMA Observations and Data Reduction . . . 122
4.2.1 Sample Selection . . . 122
4.2.2 NOEMA observations and data calibration . . . 124
4.2.3 NOEMA Source Identification and Continuum Flux Measurement 125
4.2.4 Extraction of NOEMA millimeter spectra . . . 129
4.2.5 Multiwavelength Photometry of the GOODS-N Sample . . . 129
4.3 Redshift of sources . . . 131
4.3.1 Photometric Redshift of GOODS-N Sources with Optical-IR Data 133
4.3.2 Far-IR Photometric redshift of HLS sources . . . 136
4.3.3 Joint Analysis of Photometric Redshifts and NOEMA Spectra . . . 139
4.3.4 Robustness of the Joint Analysis Method . . . 145
4.4 Physical Properties of Sources . . . 149
4.4.1 Kinematics and excitation of molecular gas of HLS sources . . . 149
4.4.2 Dust mass and dust temperature from modified black body fitting 153
4.4.3 Dust and stellar content of GOODS-N sample from SED modeling 157
4.4.4 Molecular gas properties . . . 161
4.4.5 A possible over-density of DSFGs . . . 165
4.5 Discussion . . . 166
4.5.1 Cross-validation and tension between different SED modeling . 166

4.5.2 Implications for the search and study on high-z DSFGs 167
4.6 Summary 168

Conclusions and Perspectives **170**

Bibliography **175**

List of Figures

1 Exemple du modèle de ciel basé sur la simulation SIDES/Uchuu (à gauche) injecté dans les données réelles de bruit en temps pour la simulation PIIC, et carte PIIC en sortie de simulation, après 5 itérations (à droite). Ces exemples sont des découpages du modèle et de la simulation réalisés pour les corrections de biais des observations N2CLS du champ GOODS-N à 1,2 mm. 9

2 Comptages de sources différentiels observés à 1.2 mm pour les champs N2CLS GOODS-N et COSMOS (losanges oranges et rouges) comparés aux mesures d'autres études à 1.1/1.2 mm. Tous les résultats des observations interférométriques sont présentés avec des symboles ouverts, et les mesures des observations de grands télescopes uniques sont présentées avec des symboles pleins. Les régions ombrées en jaune et en rouge montrent l'intervalle de confiance $\pm 1\sigma$ des comptages de galaxies N2CLS obtenus après correction des comptages de sources dans les champs GOODS-N et COSMOS, respectivement. 11

3 Exemples du résultat de l'analyse conjointe photométrie+spectroscopie millimétrique sur deux sources HLS. La figure de la première ligne montre la vraisemblance obtenue par l'analyse conjointe en fonction du décalage vers le rouge. Les lignes bleues indiquent la vraisemblance en fonction du décalage vers le rouge basée uniquement sur la modélisation de la SED, et les lignes brunes montrent la vraisemblance conjointe obtenues avec les contraintes photométriques et spectroscopiques. Les lignes pointillées et les lignes pleines représentent la vraisemblance de l'analyse conjointe basée sur deux méthodes différentes de modélisation de la SED, en plus des données spectrales de NOEMA. Les meilleures solutions de décalage vers le rouge sont mises en évidence par le texte et les lignes verticales pointillées, et l'analyse conjointe avec deux techniques de modélisation de la SED montre des résultats cohérents. Les deuxième et troisième rangées montrent les raies d'émission millimétriques identifiées par la méthode. Les points bleus et les lignes orange montrent les spectres NOEMA extraits à la position de la source, et les lignes rouges illustrent le modèle aux décalages vers le rouge déterminés pour la source, qui correspondent le mieux aux spectres observés. 15

1.1 An Illustration of the difference between halo mass function and galaxy mass function. The impact of stellar feedback at low mass end and AGN feedback at high mass end result in the inefficiency of stellar mass growth in low and high mass halos. Figure comes from Silk and Mamon (2012). 34
1.2 Left: redshift evolution of the cosmic SFRD based on rest-frame UV and IR observations. The black line presents the best-fit SFRD. Right: similar to the left plot, but showing the UV (unobscured) SFRD uncorrected by dust attenuation, in comparison with IR (obscured) SFRD. Figures come from Madau and Dickinson (2014). 36
1.3 A recent summary of cosmic SFRD measurements, which includes recent estimations at z~4 or higher redshift based on IR observations (orange points) on top of the UV-based SFRD measurements and the results from Madau and Dickinson (2014, blue points and dotted curve). The IR-based SFRD values from different studies span more than an order of magnitude at z=4-5. Figure from Khusanova et al. (2021). . . . 37
1.4 Left: redshift evolution of the cold gas density based on CO observations from Decarli et al. (2019) and Riechers et al. (2020), as well as the prediction based on SIDES model (Gkogkou et al., 2022). Right: similar to the left plot, but showing the comoving space density of black hole accretion rate based on X-ray (red curve and green shading from Shankar et al. (2009) and Aird et al. (2010)) and infrared (blue shading Delvecchio et al. (2014)) observations across cosmic time. The values are scaled up by a factor of 3300 to compare with the best-fit SFRD presented as the black solid line. Figure come from Madau and Dickinson (2014). 38
1.5 The SED of galaxies with different contributions of dust emission. I have obtained these SEDs by fitting the observed photometric data points with the code CIGALE (Burgarella et al., 2005; Noll et al., 2009; Boquien et al., 2019; Yang et al., 2020; Yang et al., 2022). The data points I used are coming from Dale et al. (2017) for the elliptical galaxy NGC4125, star-forming galaxy NGC3184, and starburst galaxy NGC3034. For the dusty starburst galaxy GN20, I used the multiwavelength photometric data from CANDELS (Barro et al., 2019), deblended photometry in mid and far-IR from Liu et al. (2018), and millimeter interferometric observations from PdBI (Daddi et al., 2009; Tan et al., 2014). 41
1.6 Extinction curves of the diffuse and dense clouds in our Galaxy, Large Magellanic Cloud and Small Magellanic Cloud from Gordon et al. (2003). 44
1.7 Infrared dust emission model from Compiègne et al. (2011), which models the dust emission by PAH (pink) dominating in mid-IR, small sized carbonaceous grains of ~10 nm (green) between mid and far-IR, and large sized silicate and carbonaceous grains of ~100 nm (red) dominating in far-IR. 45
1.8 Structure of the ISM and the distribution of carbon in CO molecule, neutral carbon and ionized carbon, as illustrated by Madden et al. (2020) 48

1.9 The negative k-correction effect in deep field observations in far-IR to millimeter, as illustrated by Casey et al. (2014b). At fixed galaxy SED, the detected flux from z=1 to z=10 almost remains constant for observations around 1 mm, and could even rises with increasing redshift for 2/3 mm observations. 50

2.1 Left: A scheme of the resonant circuit that constructs a KID. Right: An illustration of the resonant frequency of the KID before (solid line) and after (dotted lines) the superconducting inductor absorbs incoming photons. Figure extracted from Mazin et al. (2012) 73
2.2 Structure of the NIKA2 instrument and its cryostat. The dashed line marks regions cooled down to different temperatures. The figure comes from Adam et al. (2018) 74
2.3 An example of the output of quick look reduction on a pointing scan on MWC349 on the PIIC monitor. The pointing offsets in both direction in arc-seconds and the source size could be found from the text in the reduced image in the bottom-left of the panel. 79
2.4 An illustration of the origin of incompleteness and flux boosting using a detection with fixed S/N threshold. The histogram shows the distribution of the measured flux S_{out} of sources with fixed intrinsic flux at S_0 randomly added to N2CLS half-difference maps with a uniform Gaussian noise at σ_0. The x-axis on the top shows the corresponding S/N of sources measured on the half-difference maps. The dash-dotted line shows the intrinsic flux of the added sources. The dashed vertical line shows the detection threshold. Sources with measured S/N lower than this threshold are considered as undetected and could not be considered in the study. The dotted line marks the average flux of detected sources which is higher than the intrinsic flux, illustrating how the detection with fixed threshold is affected by flux boosting. 86
2.5 An Example of a sky model based on SIDES and Uchuu simulation injected into the half-differenced timeline for the PIIC simulation (left) and the output PIIC map from the corresponding simulation after 5 iterations (right). This example of simulation is made for the GOODS-N field. The output map is produced using the same data reduction parameters applied to N2CLS GOODS-N observations, as shown in Table 2.1. . . . 89

3.1 Signal-to-noise ratio (left panels) and instrumental noise (σ_{inst} in mJy, right panels) maps of the 1.2 mm N2CLS maps of the GOODS-N (upper panels) and COSMOS (lower panels) fields. The S/N maps are match filtered by the Gaussian beam at the corresponding wavelength. The regions enclosed in the red contours have a sufficient S/N to be analyzed by our source detection algorithm, and our catalogs and number counts are derived only in these areas (see Sect. 3.3.3). 93
3.2 Same as Fig. 3.1 but at 2 mm. 94

3.3 Pixel S/N distribution within the high-quality regions in the 1.2 and 2 mm maps shown in Figs. 3.1 and 3.2, as well as the average distribution of pixel S/N in 100 randomly generated half-difference maps for each field and waveband. The red shaded region illustrates the best fit normal distribution on the average histograms of the half-difference maps. . . 96
3.4 The purity of detected sources at different S/N_{corr} in the match-filtered map from the simulations at 1.2 and 2 mm in the GOODS-N and COSMOS field. 99
3.5 The ratio between source fluxes measured on the output map and source fluxes from the input blob catalog as functions of S/N_{corr} at 1.2 and 2 mm in GOODS-N and COSMOS. This is called effective flux boosting. The box at each S/N bin shows the ranges between 25% to 75% of the cumulative distribution and the upper and lower bound of bars present the 5% to 95% of the cumulative distribution. The dots show the position of outlier sources in the corresponding bins of S/N. The dots show the average trend in regions of different local noise (σ_{local}, see the values in labels). The red line in each panel presents the flux boosting derived by S2CLS (Geach et al., 2017) based on random injection and extraction of artificial sources on half-difference maps. 101
3.6 The completeness of sources in N2CLS as a function of f_{true}/σ_{local} at 1.2 and 2 mm in GOODS-N and COSMOS field. The completeness in the whole survey area and survey areas with different instrumental noise levels are presented as color-coded dots. The red line shows the best fit of the completeness function in the form of Eq. 3.3 on the completeness values in the whole survey area. 103
3.7 The comparison between input galaxy number counts from the SIDES-Uchuu catalogs (brown lines) and input source number counts (from the blob catalog, after applying the convolution of beam, shown as the pink lines), as well as the output source number counts derived from the detected sources in the simulated map (diamonds). The source number count from N2CLS is also shown as red diamonds, which are further described in detail in Sect. 3.3.3. The output source number counts are corrected for the purity, effective flux boosting and completeness based on the simulation, which is exactly the same as the corrections applied to the real N2CLS observations. The galaxy counts could be corrected from the source counts in the same tables by multiplying the correction factors in the corresponding bins. 107

3.8 The observed 1.2 mm differential source number counts of N2CLS GOODS-N and COSMOS survey (Orange and red diamonds) compared to the measurements of other surveys at 1.1/1.2 mm. All results from interferometric observations are presented with open symbols, and the measurements from single-dish observations are presented with filled symbols. The yellow and red shaded regions show the $\pm1\sigma$ confidence interval of the N2CLS galaxy number counts obtained after correction of the source number counts in the GOODS-N and COSMOS field, respectively. . . . 111
3.9 Similar to Fig. 3.8, but for the observed 1.2 (left) and 2 mm (right) cumulative number counts obtained from N2CLS and compared to measurements from the literature. 112
3.10 Comparison between the N2CLS differential galaxy number counts and the predictions of simulations and semi-analytic models (Béthermin et al., 2015; Schreiber et al., 2017; Lagos et al., 2020; Popping et al., 2020). The shaded regions show the $\pm1\sigma$ confidence interval of the combined GOODS-N+COSMOS galaxy number counts. 115

4.1 Cleaned images of NOEMA observation on our seven NIKA and NIKA2 sources. The effective beam size and shape of each map are shown in the bottom right of each panel. The contour levels from white to dark red correspond to -3, 3, 6, and 9× RMS of each map, respectively. The red crosses mark the position of detected NOEMA sources from the uv_-fit. The scale bars in the maps correspond to 5 arcseconds in the sky. The frequencies of the continuum data are presented in the upper right corner of each panel. 127
4.2 Spectrum of a source (HLS-2-1) extracted from the uv tables from 2 NOEMA programs, as well as the continuum model to be subtracted. . 130
4.3 Optical-IR counterparts of 3 NOEMA sources in GOODS-N. The background color images are produced by data from CANDELS survey. The observation using F814W, F125W and F160W filters are used as blue, green and red layer to produce the background images. The S-CANDELS data at 3.6 μm are shown with white contours, where different levels correspond to 0.005, 0.01, 0.02 and 0.04 MJy/sr, respectively. NOEMA continuum emission is shown with red contours, where the levels correspond to 3, 5 and 7 times of the RMS of the cleaned image. The yellow cross shows the position of NOEMA sources coming from the uv_fit results in Table 4.3. The images are 5"×5" and the scale bars in the images correspond to 1" length. 133
4.4 CIGALE (left) and EAZY (right) fitting on the 3 GOODS-N sources. From the top to bottom block in each plot: the redshift probability density distribution; the best-fit model, SED components (CIGALE only) and photmetric data; the residual of the photometric data relative to the best-fit. 135

4.5 The results of IR template fitting on 4 HLS sources with Béthermin et al. (2015) dust templates and MMPZ method, using the SPIRE, NIKA2 and NOEMA photometry. The plot in the first column shows the probability density distribution (normalized by the peak values) of each sources. The second column shows the evolution of weighted average infrared luminosity with the redshift. The third column shows best fit SED models with the observations. Sources from the top to the bottom are HLS-2, HLS-3, HLS-4 and HLS-22. 138
4.6 Joint analysis on the redshift of 4 HLS sources with the SED fitting based on (Béthermin et al., 2015) dust templates or MMPZ. The first column shows the normalized log-likelihood and the joint log-likelihood for each source. The second and third column show the cutout of spectra around candidate spectral lines at the best redshift solutions. The lines shown in the second column are detected in the earliest band1 spectral scans (W17EL and W17FA) and those in the third row are detected in the additional follow-up observations (W18FA and S20CL). The spectra models at the most probable redshift based on (Béthermin et al., 2015) or MMPZ IR luminosities are plotted as solid and dashed red lines. We emphasize that these models are not coming from parametric fitting but are generated using the estimate on the total infrared luminosity and the $L_{CO}(L_{[CI]})$-L_{IR} scaling relations. 144
4.7 Joint analysis on the redshift of 3 GOODS-N sources with the SED fitting results of CIGALE. The shape of the joint log-likelihood (red solid lines) of GOODS-N sources are significantly different from those of HLS sources in Fig. 4.6, which is due to the noncontinuous redshift coverage of considered spectral lines in the relatively narrow frequency range of the WideX spectra. The smooth parts of the joint log-likelihoods of GOODS-N sources correspond to the redshift ranges with no CO/[CI]/[CII] lines falling into the frequency coverage of the source spectrum. 145
4.8 First row: Joint log-likelihood of 4 HLS sources with models spectra with line widths of 300km/s, 500km/s and 800km/s. Second row: Comparison between the models of these 3 line widths at the corresponding redshift solution and the observed source spectra. 146
4.9 Comparison between the observed spectra of HLS-22 and the model spectra with FHWM of 300 km/s at the best redshift solution z=2.436. The features identified as an emission line is a strong noise spike in the data. 147

4.10 The result of joint analysis on the 4 HLS sources with spectroscopic redshifts derived in Sect. 4.3.3, using only the 31 GHz NOEMA spectral scans observed in 2018. The first row shows the likelihood from SED fittings and joint log-likelihood of photometric and spectroscopic data, using the SED fitting outputs with Béthermin et al. (2015) templates and MMPZ. The comparison between observed spectra and the model spectra predicted by the IR luminosities from the 2 SED fitting results are shown in the second and third rows. 148
4.11 NOEMA data and the best-fit model of all emission lines in the HLS sample listed in Table. 4.13. The name of the source and lines are labeled in each subplot. For the lines coming from the same source, their kinematics are tied to be the same during the fitting. A double-peaked Gaussian model is preferred by the lines from HLS-3 based on AIC, while the rest could be properly fit by single Gaussian models. 152
4.12 Example of modified black-body fitting on the far-IR to millimeter photometric data of one of our sample galaxies. (a) Photometric data and best-fit model. $\pm1\sigma$ and $\pm2\sigma$ uncertainties of the model are shown with blue shades of different transparency. (b) Corner plot on the posterior distribution of parameters in the fitting. The contours in the corner plots enclose the fraction of mass of the sample corresponding to 1, 1.5, and $2\,\sigma$ in the 2D histogram. 155
4.13 Dust temperature versus the redshift of high-z DSFGs in our sample, and DSFGs/LBGs from literature. The dust temperatures of these sources are all measured under the optically-thin modified black-body model. The corresponding references are listed in the legend. We also overlaid the average T_{dust}-z relation of main sequence galaxies derived by Schreiber et al. (2018) and Béthermin et al. (2015) based on observational data. The 3 sources with uncertain/discrepant photometric redshifts (HLS-4, 12646, and 13161) are further highlighted by red square enveloping the corresponding symbols, and we use dash-dotted grey lines to present the degeneracy between dust temperature and redshift in the plot. . . . 158
4.14 The stellar mass and SFR offset from the star forming main sequence in Speagle et al. (2014) at the indicated redshifts of 3 GOODS-N sources. M_* and SFR derived at different z_{fix} in Table 4.10 are presented and connected by dotted lines. Data points in the plot are color codded based on the corresponding z_{fix}. The dashed line in the plot shows the typical 0.3dex scatter of star formation main sequence. 160
4.15 Comparison of the dust masses derived by CIGALE and optically-thin modified black-body fitting. The results of the same source derived with different redshifts are listed in Tables 4.14 and 4.16 and are connected by dashed lines. 161

4.16 The molecular mass from Rayleigh-Jeans dust emission and the star formation rate of HLS and GOODS-N samples. The dashed lines show the location where molecular gas depletion time correspond to 20 Myr, 100 Myr and 500 Myr. Each source is color coded by the redshift and sources analysed under several ambiguous redshifts are connected with the dotted lines. 164
4.17 Examples of optically dark/faint sources identified by NOEMA follow-up observations on N2CLS sources in GOODS-N. The cleaned NOEMA data are illustrated by the red contour at levels of 4, 6, and 8 times the RMS of the cleaned images. The peak positions in the cleaned images are highlighted by cyan crosses. The flux distribution at 4.5 μm from Spitzer IRAC observations are shown as white contours between 0 to 0.320 MJy/sr in 9 levels uniformly separated with a logarithmic scale. The background images are generated using HST F814W, F125W, and F160W images in the blue, green, and red channels, respectively. The scale bars in each subplot have lengths of 1". 173

List of Tables

1.1 Summary of the basic information of mid-IR and far-IR surveys (10μm $< \lambda_{obs} < 500\mu$m) from space missions since 2000. 60
1.2 Summary of the basic information of sub-millimeter and millimeter surveys ($450\,\mu$m $< \lambda_{obs} < 2000\,\mu$m) from ground based single-dish telescopes since 2000. 64
1.3 Summary of the basic information of sub-millimeter and millimeter surveys in blank fields, as well as some compilation of data for serendipitous continuum detections (450μm $< \lambda_{obs} < 3000\,\mu$m) from ground based interferometers since 2013. 68

2.1 Summary on the setup of parameters used in the PIIC data reduction on N2CLS observations in GOODS-N and COSMOS. 84
2.2 Summary on the scan numbers, scan times of all N2CLS scans and properly reduced scans, as well as the 225 GHz atmospheric opacities (τ_{225}) of all, reduced and rejected scans in each field and band. 84

3.1 Comparison of N2CLS-May21 depth to other single-dish (sub)mm surveys in GOODS-N and COSMOS. For each survey, the root mean square (RMS) noise is normalized to 1.2 or 2mm assuming the average IR SED of star-forming galaxies at z=3 (Béthermin et al., 2015). 97
3.2 Differential and cumulative source number counts at 1.2 mm in GOODS-N and COSMOS. The galaxy counts could be corrected from the source counts by multiplying the correction factors at the corresponding fluxes. 109
3.3 Differential and cumulative source number counts at 2 mm in GOODS-N and COSMOS. The galaxy counts could be corrected from the source counts by multiplying the correction factors at the corresponding fluxes. 109
3.4 Combined differential and cumulative galaxy number counts at 1.2 and 2 mm from the observation on the two fields 115

4.1 Coordinates and millimeter fluxes of our sample from NIKA (GOODS-N) and NIKA2 (HLS) observations, and SPIRE far-IR photometry (HLS only). The fluxes of the 3 GOODS-N sources now measured with NIKA2 are given in brackets. The 1-sigma flux uncertainty of SPIRE undetected HLS sources are in parenthesis. The NIKA2 and SPIRE fluxes presented in the table only accounts for the uncertainties coming from flux measurements. The SPIRE fluxes of the GOODS-N sources will be described in Table 4.5 123
4.2 Information on NOEMA follow-up observations. 125

4.3 NOEMA continuum source positions and best-fit sizes 128
4.4 Continuum fluxes from PdBI/NOEMA observations 128
4.5 Multi-wavelength photometry of three GOODS-N sources. Non-detections in Liu et al. (2018) are presented with 1σ uncertainties from their catalog in parentheses. The NIKA2/NOEMA fluxes of these 3 sources are given in Table 4.1 and Table 4.4. 132
4.6 Choice of CIGALE Parameters for photometric redshift analysis 134
4.7 Photometric redshift of GOODS-N sources. 134
4.8 Photometric redshift of HLS sources 137
4.9 Parameters of the log-linear scaling relation between strong far-IR to millimeter lines and far-IR/total IR luminosity used to generate model spectra for our analysis. The parameters of the scaling relations come from Greve et al. (2014), Liu et al. (2015), Valentino et al. (2018) and De Looze et al. (2014) 141
4.10 Summary on the redshifts of NOEMA sources, including the optical-IR photometric redshift from CIGALE and EAZY (z_{OIR}), far-IR photometric redshift from the fitting with Béthermin et al. (2015) template and MMPZ (z_{FIR}), the best spectroscopic redshift solution from our joint analysis (z_{joint}) and the redshift values which we fixed to in the measurement of source physical properties (z_{fix}). 143
4.11 Redshift of HLS sources from the joint-analysis with models of different line width 146
4.12 Redshift of HLS sources from the joint-analysis with the 31 GHz continuous spectra observed in 2018 148
4.13 Emission line fluxes, luminosities and widths of 4 sources in HLS field 151
4.14 Dust properties of NIKA2 sources and HLS J0918+5142 from optical-thin modified black-body fitting. For the fit on all sources, their redshifts are fixed to z_{fix} in Table. 4.10. The dust mass, far-IR luminosity, and SFR of HLS J0918+5142 are corrected by a lensing magnification of 11, as reported by Combes et al. (2012). 156
4.15 Choice of CIGALE parameters for the fitting with "dl2014" model . . . 159
4.16 Dust and Stellar Properties of GOODS-N Sample from Full SED Fitting 159
4.17 Molecular gas properties of GOODS-N and HLS sources. 163

Introduction

In the past centuries, people witnessed a dramatic expansion of our view on the Universe. Although our horizon was limited to the solar system and nearby stars until a few hundred years ago, today we are able to observe billions of galaxies containing billions of stars. Moreover, due to the finite speed of light, observations in the distant Universe not only see the faint and distant objects, but also provide a perspective to reconstruct the history of the Universe and the galaxies therein.

Nowadays, ground-based and space-based observatories image all or part of the sky across the electromagnetic spectrum. These surveys allow to uncover representative samples of millions of galaxies since the first few hundred million years of cosmic times. Each wavelength provides different information on the physical properties of galaxies. The stellar emission dominates the light we observe in UV, optical and near infrared, where the emission from young stellar population dominates at the short wavelengths and aged stars dominate at the long wavelengths. At longer wavelength in mid- and far-infrared, the emission from galaxies are mostly produced by dust heated by starlight. The accreting black holes, or active galactic nuclei, also produces characteristic emission across the electromagnetic spectrum (e.g. in X-rays and radio).

In particular, deep observations at rest-frame UV and optical wavelengths dramatically improved our understanding on the galaxy formation and evolution in the past three decades. However, the existence of dust could dim these emissions from early massive galaxies and lead to bias in the statistical studies on early galaxy evolution and cosmic star formation. Observations in the far infrared (far-IR) to millimeter allow to probe the emission of the cold interstellar medium causing the dimming of starlight and tracing the birth place of stars. These observations thus provide highly complimentary information to the optical observations by directly probing the dust emission, as well as some key molecules like CO, from galaxies in the early Universe.

Systematic deep millimeter surveys over large cosmological volume have been constrained by the observing capability for a long time. The recent emergence of new facilities and instruments open new capabilities. High resolution, sensitive (sub)millimeter interferometry has been widely applied to observing faint but representative dusty galaxies in the distant Universe with unprecedented details. The single-dish telescopes, although with much worse spatial resolution, provide large field-of-view continuum observing capability. This makes single dish telescopes still highly complimentary in making census of dusty galaxies over large area and cosmic volume, which could be inapplicable to the interferometer surveys with much nar-

rower field-of-view. Only by combining these two sets of observations could we have a complete picture on the dusty galaxy population in the Universe over a wide range of luminosity, mass, environment and redshift.

This thesis focus on the studies of high-z dusty galaxies and obscured star formation using New IRAM KIDs Array2 (NIKA2), a recent continuum camera, installed on the IRAM 30m telescope, observing at 1.2 and 2 mm. With its large field-of-view and high sensitivity, NIKA2 presents unprecedented capability for deep and wide surveys in the millimeter to probe the dust emission from high-redshift galaxies.

After a detailed introduction on the dusty star-forming galaxies, I will first describe the NIKA2 instrument, its science, and the NIKA2 data reduction and interpretation framework in Chapter 2. The new features to more completely consider the biases in data reduction, source detection and flux measurement will be highlighted. With this new framework, I am presenting in Chapter 3 new measurements of the 1.2 and 2 mm number counts obtained from the NIKA2 Cosmological Legacy Survey (N2CLS), which has unprecedented large coverage at its depth and wavelength. The number counts over an order of magnitude in flux are also fairly compared with previous observations and models, with the impact of beam resolution accounted for for the first time.

Chapter 4 focus on challenges of redshift measurements of dusty galaxies, which is required to constrain their cosmic evolution and obscured star formation rate. We develop a new method to jointly constrain the source redshift with the information from photometry and spectroscopy obtained from NOEMA follow-up observations of NIKA2 galaxies. The method takes information from far-IR spectral energy distribution fitting to generate model spectra at a wide range of redshifts and find the best match with the data. I verified the effectiveness and robustness of the method on five NIKA2 sources and highlight the possible application of this highly automatic method to large millimeter data sets. With the derived source redshifts, I further analyse the dust, molecular gas and star formation properties. From the sample, we identified two sources that are possibly under the transition from star-forming to quiescence, as indicated by their normal star formation rate and short gas depletion time. Star-forming galaxies with significantly colder than average dust temperature, as well as a possible z=5.2 overdensity of dusty galaxies, are also noticed from the analysis.

Finally, I summarise the results and present some perspectives of the N2CLS survey and my research. For the N2CLS survey, we plan to make redshift and source property analysis on the complete N2CLS sample. The corresponding studies has already started in GOODS-N, with the ancillary data, recently completed by NOEMA follow-up observations, and upcoming JWST observations. The requirements of end-to-end simulation in recovering the fluxes and number counts also bring insights into the design and data analysis for future single-dish blank field surveys. I also briefly describe the possible application of the joint analysis framework in the redshift searching follow-up observations of future surveys.

1 The Dusty Star-Forming Galaxies

Sommaire

1.1 General Picture of Galaxy Formation and Evolution 32
1.1.1 Galaxy Formation and Evolution Under Λ-CDM Cosmology . . 33
1.1.2 Cosmic Evolution of Star-Formation Rate Density 35
1.1.3 Star-Formation in Galaxies across cosmic time 36
1.2 Dusty Star-Forming Galaxies 40
1.2.1 Spectral Energy Distribution of Galaxies 40
1.2.2 Dusty Interstellar Medium in Galaxies 43
1.2.2.1 Dust Extinction 43
1.2.2.2 Dust Emission in Infrared 44
1.2.2.3 Other Emission from the Dusty ISM 46
1.2.3 Selection of Dusty star-forming Galaxies 48
1.2.3.1 Mid-IR Selection 49
1.2.3.2 Far-IR Selection 49
1.2.3.3 Near-IR Dropout Selection 51
1.2.4 The Role of Dusty Galaxies in Galaxy Formation and Evolution . 52
1.2.5 Open Questions and Limitations 54
1.3 Observations of Dusty Galaxies 56
1.3.1 Space-Based Missions 56
1.3.2 Ground-Based Single-Dish Telescopes 61
1.3.3 Continuum Interferometric Observations 65
1.3.4 Spectroscopic Interferometric Observations 69

1.1 General Picture of Galaxy Formation and Evolution

Modern astronomy describes galaxies as gravitationally bound systems that consist of stars, gas, dust, and dark matter. These components construct complex ecosystems. Their building, deconstruction, and(or) interaction with each other shape the formation and evolution of galaxies through physical processes from microscopic to cosmological scales. In this section, we will summarize the modern theory and studies of galaxy formation and evolution, specifically focusing on star formation across cosmic time.

1.1.1 Galaxy Formation and Evolution Under Λ-CDM Cosmology

The current paradigm of structure formation in the Lambda- Cold Dark Matter (Λ-CDM) cosmological framework suggests galaxies form from the collapse of dark matter overdensities and grow through the accretion of both baryons and dark matter (Benson, 2010). In the classical picture of galaxy formation (Rees and Ostriker, 1977; White and Rees, 1978), the gas falls into the dark matter halo from the intergalactic medium (IGM). During this process, the gas is first shock-heated to the virial temperature of the halo, then cools and settles down into the center of the halo. The further supply of gas to galaxies is contributed by both accretion and galaxy mergers. On larger scales, the primordial perturbation in the density field grows into structures of different densities in walls, sheets, filaments, and voids revealing the galaxy and dark matter distribution in the Universe, which has been observed by redshift surveys in the past decades (Geller and Huchra, 1989; Springel et al., 2006).

The growth of galaxies through accretion and mergers, in return, could also act as a preventive process of galaxy growth. Suppression or quenching of the star formation in galaxies happens in processes both internal and external to the gas reservoir. In low mass and high redshift dark matter halos, filamentary structures from the IGM enter the galaxy along cold streams without being heated, and thus feed the gas reservoir for star formation. However, at lower redshift, as dark matter halo mass grows to above $\sim 10^{12}$ $M_\odot$ with the accretion, the infalling gas could get heated by shock and its availability to delay star formation is set by the cooling time (Dekel et al., 2009; Nelson et al., 2015). Other internal processes in galaxies, including the active galactic nuclei (AGN), supernovae and massive young stars that feed by or reside in the gas reservoir, could also induce ejection and heating of gas in galaxies through their released energy and momentum (Fabian, 2012; Heckman and Best, 2014; Hopkins et al., 2014; Harrison, 2017). The various feedback process are suggested to contribute to the inefficiency and variation of star formation in dark matter halos across a wide mass range, as illustrated by Fig. 1.1.

Although the growth of dark matter structures is only driven by gravity, proper treatment on baryonic processes, including gas heating and cooling, feedback, accretion and chemical enrichment, is crucial to reproduce the observed galaxy properties (Nelson et al., 2019). However, the large range of scales these interactions act on could be numerically expensive to be covered by one single simulation. For cosmological simulations, these processes are usually considered and treated using sub-grid prescriptions (Kim and Ostriker, 2018; Nelson et al., 2019). The predictions on the cosmic evolution of galaxy properties are thus strongly dependent on the implementations of these sub-grid models in cosmological simulations and may not be able to capture how different physical mechanisms shapes the evolution of galaxies (Naab and Ostriker, 2017; Vogelsberger et al., 2020). Modern zoom-in simulations provide high resolution at a few to a few tens of parsec to understand the baryonic processes from the scale of star clusters to the whole galaxy (Wetzel et al., 2016; Feldmann et al., 2017; Dekel et al., 2020). However, these simulations are mostly carried out on small number

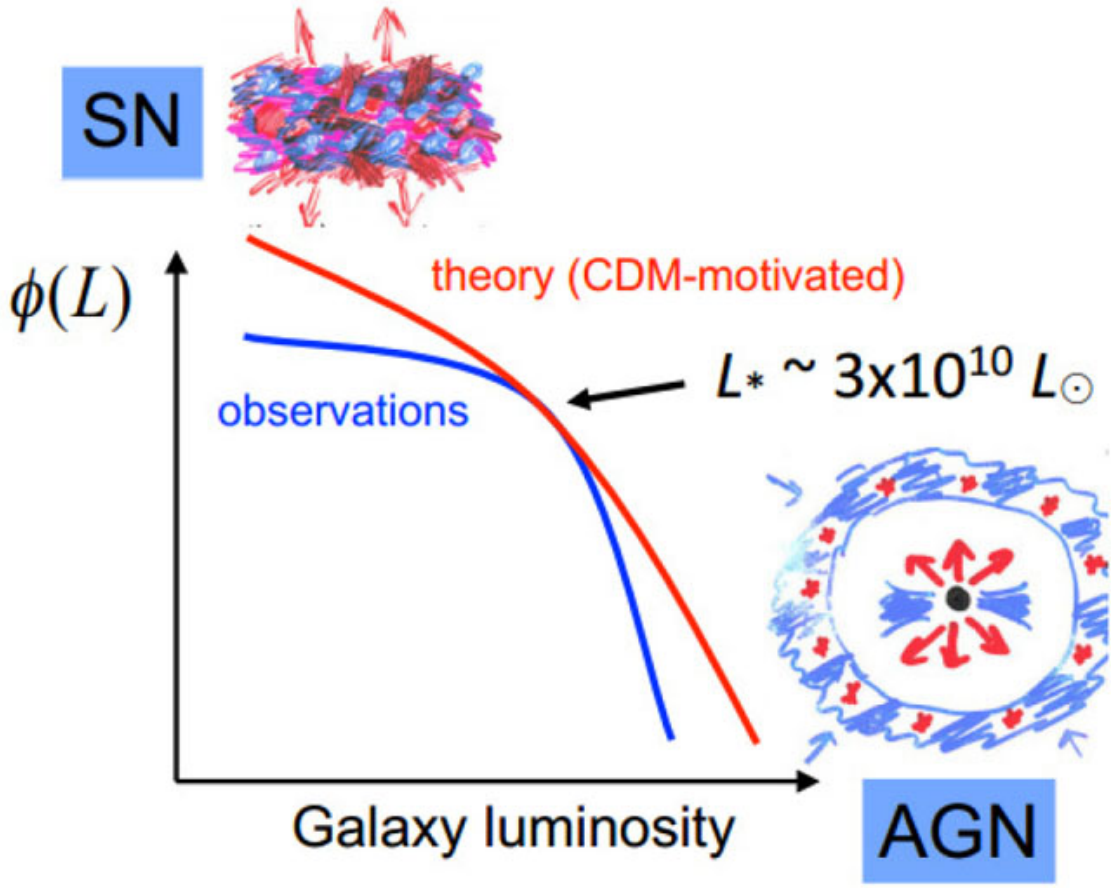

Figure 1.1 – An Illustration of the difference between halo mass function and galaxy mass function. The impact of stellar feedback at low mass end and AGN feedback at high mass end result in the inefficiency of stellar mass growth in low and high mass halos. Figure comes from Silk and Mamon (2012).

of individual dark matter halos, which could only provide implications on the details of galaxy evolution in a limited parameter space at once.

1.1.2 Cosmic Evolution of Star-Formation Rate Density

In the past decades, the rapid development of ground and space-based facilities significantly advanced the measurement of galaxy formation and evolution properties across cosmic time. Among all of the quantitative assessments, the estimation of cosmic star formation rate density (SFRD) comes to attention in both observational and theoretical studies. Cosmic SFRD describes the amount of stellar mass formed in unit comoving volume at a given cosmic time or redshift, which is normally given in the unit of solar mass per year per cubic comoving cubic megaparsec ($M_\odot/yr/cMpc^3$).

Measurements on the cosmic SFRD rely on the observations of characteristic emissions associated with young stars that trace the ongoing star formation. The dominance of luminosity from massive stars in the young stellar population, as well as their high temperature, makes the luminosity of continuum emission from ultra-violet (UV) a primal and direct quantitative indicator of star formation rate in galaxies. The SFRD measurements based on rest-frame UV observations have been made from the local Universe up to the reionization era at z~10, where the youngest galaxies are discovered (Oesch et al., 2016; Jiang et al., 2021). However, UV emission is also sensitive to the attenuation caused by dust in the interstellar medium (ISM), which makes the observed luminosity lower than the intrinsic luminosity and thus biases the estimated star formation rate. The correction on the attenuated emission is made either using the slope of UV spectral energy distribution (SED) (Calzetti, 1997; Meurer et al., 1999) or through the alternative observations in infrared (IR), which directly trace the emission from dust heated by the massive young stars (Kennicutt, 1998). In the following part of the thesis, we will note this part of star formation and SFRD as obscured star formation and obscured SFRD.

The measurements on cosmic SFRD provide a crucial global perspective in understanding galaxy formation and evolution. The left panel in Fig. 1.2 presents the redshift evolution of cosmic SFRD based on attenuation-corrected ultraviolet (UV) and infrared (IR) data from Madau and Dickinson (2014). These observations reveal star formation comparable to the current level already exists by the end of reionization and quickly reaches a maximum of cosmic SFRD at redshift 2. This indicates a rapid assembly of galaxies in the first few billion years of the Universe, and after this era, the activity of star formation in the Universe gradually declines. The right panel in Fig. 1.2 shows the contribution of UV-based, or unobscured SFRD, relative to the obscured SFRD traced by IR emission. It reveals the dominance of obscured star formation from the local Universe to the peak of cosmic star formation, suggesting the richness of dust in galaxies at these epochs. When going to the higher redshift, a decline of the contribution of unobscured SFRD as traced by UV data could be observed. However, the lack of measurements in IR at z>4 lead to the ambiguity on the transition time of ISM from transparent to opaque to the UV-optical emission from young stars, and recent results from ALMA or VLA seem to indicate still controversial results for the

obscured SFRD (see Fig. 1.3 for a summary from Khusanova et al. (2021), also see e.g. Maniyar et al. (2018), Zavala et al. (2021), Casey et al. (2021) and van der Vlugt et al. (2022), for other measurements based on IR/radio).

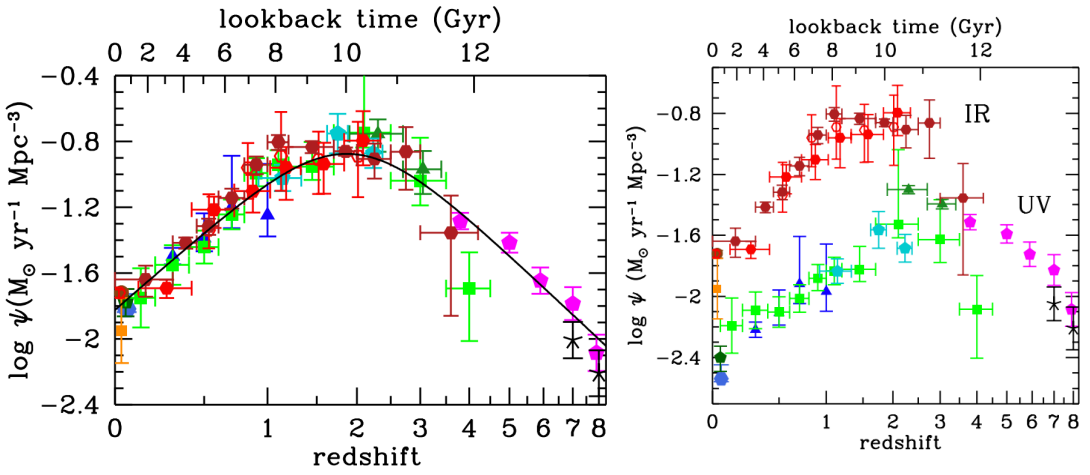

Figure 1.2 – Left: redshift evolution of the cosmic SFRD based on rest-frame UV and IR observations. The black line presents the best-fit SFRD. Right: similar to the left plot, but showing the UV (unobscured) SFRD uncorrected by dust attenuation, in comparison with IR (obscured) SFRD. Figures come from Madau and Dickinson (2014).

Apart from the cosmic evolution of obscured and unobscured SFRD themselves, studies also seem to indicate coordination of the cosmic evolution between SFRD and other observable. In Fig. 1.4, we present the measurements of cold gas mass density across cosmic time (Decarli et al., 2019; Riechers et al., 2020) and the black hole accretion history (Madau and Dickinson, 2014), in comparison with the scaled cosmic star-formation rate density. Despite the large uncertainties in the measurements, the two groups of comparison both reveal similar trend of the cosmic evolution of star-formation with the amount of cold gas and the black hole accretion rate, suggesting close coordination or co-evolution between each other through self-regulation in galaxies or external processes. These measurements on the global integrated properties of galaxies also set key baselines for calibrating and comparing baryonic physics in large volume cosmological simulations to understand the roles different processes play in galaxy formation and evolution (Pillepich et al., 2018).

1.1.3 Star-Formation in Galaxies across cosmic time

The observations from the local Universe to high redshift reveal significant cosmic evolution of the space density of star-forming activity, as described in the previous section. Such variation in star formation properties could also be observed in individual galaxies, while some statistical features of the galaxy population are strikingly

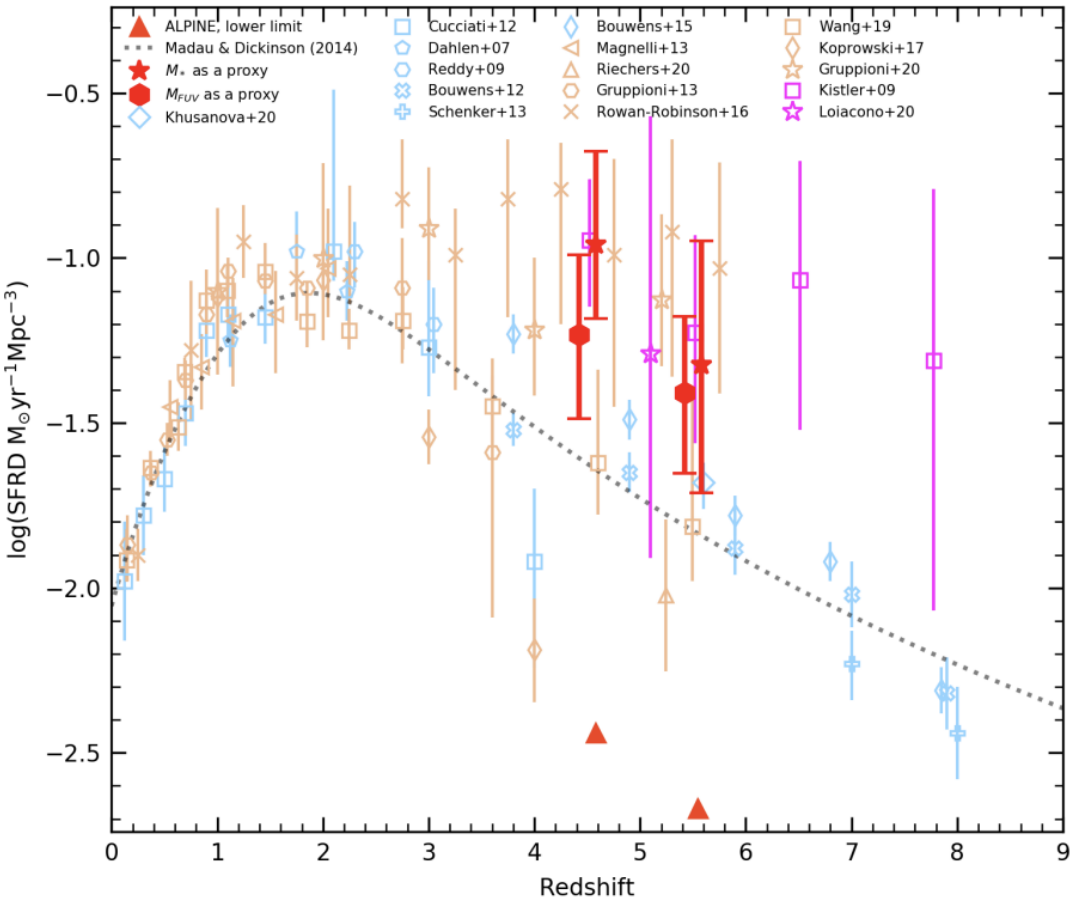

Figure 1.3 – A recent summary of cosmic SFRD measurements, which includes recent estimations at z~4 or higher redshift based on IR observations (orange points) on top of the UV-based SFRD measurements and the results from Madau and Dickinson (2014, blue points and dotted curve). The IR-based SFRD values from different studies span more than an order of magnitude at z=4-5. Figure from Khusanova et al. (2021).

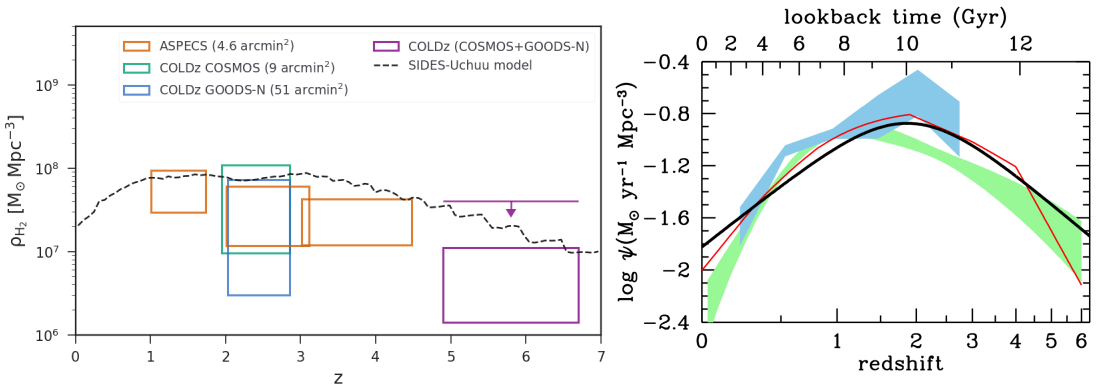

Figure 1.4 – Left: redshift evolution of the cold gas density based on CO observations from Decarli et al. (2019) and Riechers et al. (2020), as well as the prediction based on SIDES model (Gkogkou et al., 2022). Right: similar to the left plot, but showing the comoving space density of black hole accretion rate based on X-ray (red curve and green shading from Shankar et al. (2009) and Aird et al. (2010)) and infrared (blue shading Delvecchio et al. (2014)) observations across cosmic time. The values are scaled up by a factor of 3300 to compare with the best-fit SFRD presented as the black solid line. Figure come from Madau and Dickinson (2014).

preserved across cosmic time. One of the most notable universal features is that the majority of star-forming galaxies at similar redshifts follow a well-defined correlation between their stellar mass (M_*) and SFR, which is known as the main sequence of star-forming galaxies.

The main sequence of star-forming galaxies was first noticed in the local Universe from Sloan Digital Sky Survey on nearby galaxies (Brinchmann et al., 2004) and soon after in the deep field observation on galaxies at higher redshift (Elbaz et al., 2007; Daddi et al., 2007). The basic functional form of the main sequence could be described as a linear correlation between log(SFR) and log(M_*) of galaxies across the mass range of the star-forming galaxies observed at/around a given redshift, as given by Eq. 1.1. Current studies suggest the tight main sequence over a large range of stellar mass and redshift reflects the self-regulation of star-formation activity by cooling, accretion, and feedback (Matthee and Schaye, 2019; Nelson et al., 2021). Some recent observations also suggest a flattening of star formation main sequence at the high mass end at around or below redshift 2, which indicates a mass-related suppression of star formation associated with the growth of dark matter halo (Schreiber et al., 2016; Tomczak et al., 2016). The comparison between the main sequence at different redshifts an increase of the specific star formation rate (sSFR), the SFR per unit stellar mass, by around two orders of magnitude, which could be explained by the increased fraction of cold gas feeding the star formation in galaxies (Genzel et al., 2015; Scoville et al., 2016).

$$\log(\mathrm{SFR}/\mathrm{M}_{\odot}\mathrm{yr}^{-1}) = \alpha\log(\mathrm{M}_{*}) + \beta \tag{1.1}$$

Quantitatively, the general population of star-forming galaxies distributes close to the main sequence with a scatter of 0.3 dex in star formation rate. However, among all galaxies with active star formation, there are still a small fraction of galaxies with SFR up to several tens of times above the main sequence, which are known as starburst galaxies. At low redshift, there is also a notable population of galaxies with little recent star formation lying below the star formation main sequence. This population is known as quiescent galaxy, which is found to be already in place at redshift 3-4 (Hill et al., 2016; Schreiber et al., 2018) at the high mass end and gradually populates much wider range of mass afterwards (Faber et al., 2007; Stefanon et al., 2013).

When looking at individual galaxies from these populations at low redshift, studies notice clear distinctions between their morphology and dynamics. The galaxies residing in the star-forming main sequence usually show extended rotating disk morphology with spiral arms and newborn star clusters visible across their disk with blueish color. The quiescent galaxies, however, generally show more centrally-peaked and featureless radial light profiles with more reddish colors, as well as larger contributions of random motion in stellar dynamics and almost absence of molecular gas (Emsellem et al., 2011; Young et al., 2011; Graham et al., 2018). The starburst galaxies, however, show more disturbed morphology, indicating a much higher fraction of interacting galaxies and galaxy mergers among this population. Some of the trends could also be noticed in high-z galaxies, While crucial differences with respect to galaxies at low redshift are also observed. A considerable fraction of normal star-forming galaxies at high redshift show disturbed and clumpy morphology compared to their low-z siblings (Förster Schreiber et al., 2009; Daddi et al., 2010b; Tadaki et al., 2018). These features might originate from the disk instability, which could be induced by a higher gas fraction from gas accretion and (or) more frequent interaction with other galaxies (Dekel et al., 2009; Ceverino et al., 2010).

The arise of quiescent galaxies since z=3-4 and their growing fraction from high to low redshift suggests an evolution from star-forming to quiescence in the life of galaxies. In the past decades, a large number of studies have provided evidence of the possible mechanism that contributed to this transition. Observations on the cold gas in merging starburst galaxies reveal that the vigorous star formation in these systems could consume their cold gas at a rate several times faster than normal star-forming galaxies (Genzel et al., 2010). The high frequency of luminous AGN in merger and merger remnants (Sanders and Mirabel, 1996; Comerford et al., 2015; Ellison et al., 2019), as well as the strong evidence of outflow found in these systems (Heckman and Best, 2014; González-Alfonso et al., 2017; Liu et al., 2022), suggests a further path of consuming the gas reservoir and reach to quiescence in galaxy mergers. The observations at high redshift also reveal a population of compact star-forming galaxies, which have starlight distributions similar to the compact quiescent galaxies at comparable redshifts (Barro et al., 2013). In addition to their unique morphology, these galaxies are also found to have short gas depletion timescale under normal

or starbursting SFR, making them promising candidates for tracing the transition of massive galaxies from star-forming to quiescence at high redshift (Barro et al., 2016; Gómez-Guijarro et al., 2022b). The low-mass quiescent galaxies in the local Universe, however, are found to have a strong bias to the dense environment like galaxy clusters (Dressler, 1980; Kauffmann et al., 2004; Peng et al., 2010). During the infall of low-mass galaxies to massive galaxy clusters, the ram pressure of hot intergalactic medium could remove the gas from low-mass galaxies and thus quench their star formation (Boselli et al., 2022).

1.2 Dusty Star-Forming Galaxies

Multi-wavelength observations over several decades reveal the prevalence of dust in galaxies across cosmic time. As the product of metals produced and released by the dying stars, it is also striking to find the existence of dust in young galaxies in the reionization era (Knudsen et al., 2017; Bakx et al., 2020; Bakx et al., 2021; Sugahara et al., 2021; Laporte et al., 2021; Fudamoto et al., 2021; Inami et al., 2022; Ferrara et al., 2022; Dayal et al., 2022), as well as a considerable population of dust-rich galaxies in the very early Universe from recent observations (Daddi et al., 2009; Riechers et al., 2013; Cañameras et al., 2015; Strandet et al., 2017; Zavala et al., 2018; Marrone et al., 2018; Casey et al., 2019; Reuter et al., 2020; Jin et al., 2022). The early and prevalent arise of these dusty star-forming galaxies (DSFGs) provides crucial tests and challenges on the theory of galaxy formation and evolution in the first billion years of the Universe (Marrone et al., 2018; Wang et al., 2019; Nanni et al., 2020). Under broader aspects, the measurement of emissions from the dust and the closely associated molecular and atomic lines from galaxies also provide important measurements of the gas and star formation in modern observational studies. In this section, we will discuss the different ingredients of the dusty ISM in galaxies, as well as the production and properties of their electromagnetic emissions. We will also summarize the methods to select dusty galaxies from the observations and the difference in source properties of the sample from various selection methods.

1.2.1 Spectral Energy Distribution of Galaxies

Multi-wavelength observations from the local Universe to the high redshift reveal a large diversity of the spectral energy distribution (SED) of galaxies. Fig. 1.5 shows some examples of rest-frame galaxy SED of different types from observations across optical, infrared, and millimeter bands. These include three nearby galaxies (NGC4125, NGC3184 and NGC3034) of different star-forming activities from KINGFISH sample (Kennicutt et al., 2011) and a z=4.05 prototype dusty starburst galaxy, GN20 (Pope et al., 2006; Daddi et al., 2009; Tan et al., 2014). From the comparison, we could notice several features in common, while the relative intensity and shape of SEDs at different wavelengths vary significantly between different examples.

The SED of all galaxies shows a strong cutoff at 91.2 nm. This is called the Lyman

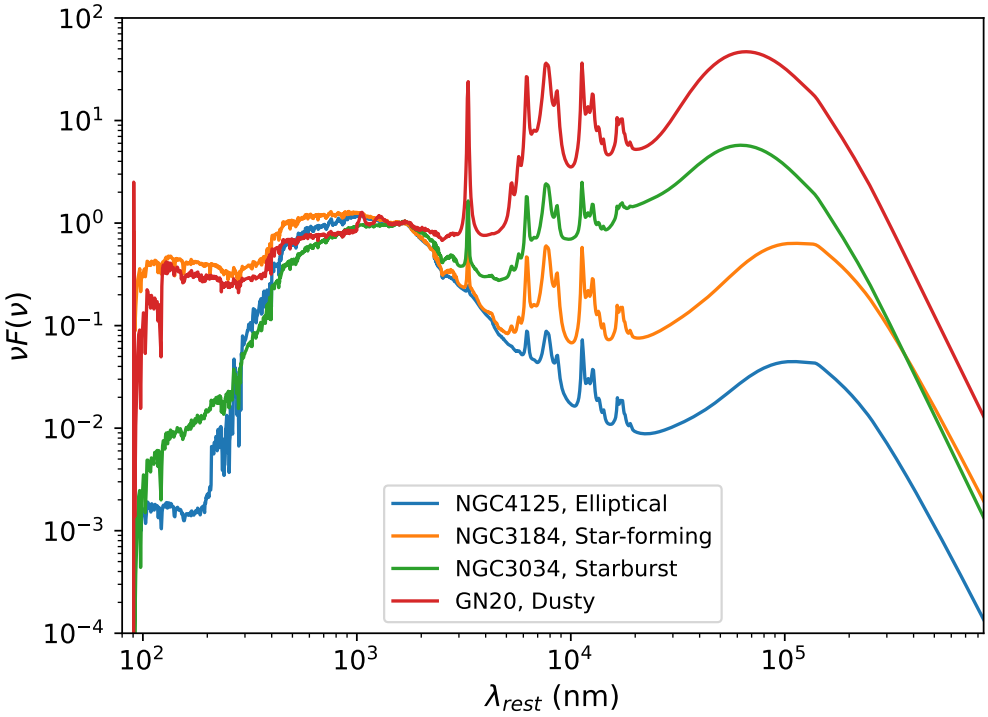

Figure 1.5 – The SED of galaxies with different contributions of dust emission. I have obtained these SEDs by fitting the observed photometric data points with the code CIGALE (Burgarella et al., 2005; Noll et al., 2009; Boquien et al., 2019; Yang et al., 2020; Yang et al., 2022). The data points I used are coming from Dale et al. (2017) for the elliptical galaxy NGC4125, star-forming galaxy NGC3184, and starburst galaxy NGC3034. For the dusty starburst galaxy GN20, I used the multiwavelength photometric data from CANDELS (Barro et al., 2019), deblended photometry in mid and far-IR from Liu et al. (2018), and millimeter interferometric observations from PdBI (Daddi et al., 2009; Tan et al., 2014).

break (Steidel et al., 1995), which corresponds to the absorption of photons from the photosphere of stars in galaxies by atomic hydrogen at the fundamental quantum level n=1. This break has been widely applied in the selection of galaxies at different redshifts and the census on unobscured star formation (see Sect. 1.1.3). A second cut around 0.4 µm is called the Balmer break, which corresponds to transitions from the quantum level n = 2 of hydrogen atoms and is also mostly contributed by stellar light. The optical to near-IR spectrum presents a maximum of around 1.6 μm, which is mostly due to the significant decrease of attenuation in the infrared (see Sect. 1.2.2.1 for a more detailed explanation) and emission from old stellar populations. When going to longer wavelengths, another 2 common features among these example SEDs arise. All galaxies show similar emission bands in mid-IR at 3μm and 8-20μm, as well as a common broad peak of emission in far-infrared to millimeter, with the maximum of SEDs appearing at around 50-100 μm. Both of these features are produced by dust, although by different ingredients in the dust composition. The mid-IR continuum and emission bands come from the small hot dust grains and excited polycyclic aromatic hydrocarbon molecules (the so-called PAHs), and the continuum peaked in far-IR is dominated by the thermal emission of bigger dust grains (See Sect. 1.2.2.2 for a detailed discussion).

Although different types of galaxies share the common features described above, it is also clearly revealed in Fig. 1.5 that the relative intensity of emission from different wavelengths varies significantly between different types of galaxies. The elliptical galaxy NGC4125 shows the weakest infrared emission from dust, which has minimal contribution to the total luminosity of the galaxy. On the contrary, a dusty starburst galaxy (GN20) could emit more than 50% of its total luminosity in infrared through the dust. Here the infrared means the large domain of emission between 8-1000 μm. The dusty star-forming galaxies were also called IR galaxies in the early days, as they were discovered by IRAS, which was discovered at IR bands in 12, 25, 60, and 100μm (see Sect. 1.3.1 for a more detailed summary on the IR observations). Normal star-forming and starburst galaxies fall in the middle of the two extreme cases, where infrared emission from dust has luminosity comparable to the stellar emission in optical and near-IR. From the studies over the past decades, we have already understood that the differences in SED shape and the intensity of infrared emission reflect the prevalence or the lack of young stellar populations, as well as the amount of dust and gas in the galaxies. The related physical processes reshape the SED and produce emissions from the dusty ISM that will be discussed in more details in Sect. 1.2.2.2.

Apart from the component described above, the emission from the accretion disk and dusty torus of active galactic nuclei could also contribute to the UV, optical and infrared emission of galaxies (Edelson and Malkan, 1986). In observations, the signature of AGN could be uniquely identified through the high X-ray luminosity (Elvis et al., 1978) and features in optical-IR emission lines (Kewley et al., 2006). Apart from that, mid-IR (Lacy et al., 2004) and radio (Smolčić et al., 2008) observations could also be used to identify the AGNs in galaxies but with less robustness or(and) completeness (Griffith et al., 2011; White et al., 2000). Previous studies notice that ~20% of bright submillimeter galaxies could host X-ray detected AGNs, while their

contribution to the infrared SED is mostly insignificant under the high star-formation rate (Georgantopoulos et al., 2011; Wang et al., 2013; Johnson et al., 2013). In the studies throughout the thesis, we do not account for the AGN composition in our SED analysis, assuming it to be negligible with respect to the contribution due to star formation.

1.2.2 Dusty Interstellar Medium in Galaxies

1.2.2.1 Dust Extinction

Although the emission from the dusty ISM has little contribution in the optical bands, observations nearly a century ago could already reveal the impact of dust through its extinction properties. In the 1910s and 1920s, photographic observations already caught more than 300 dark nebulae over the dense stellar background close to the galactic plane, indicating the existence of material significantly absorbing starlight along some sight lines. The first conclusive demonstration of the interstellar absorption by dust came from the statistical study on the open clusters in our Galaxy. It found the slower decrease of angular diameter compared to observed brightness, as well as the increase of reddening on the observed color of member stars, suggesting the dimming and reddening come from the scatter of grains (Trumpler, 1930).

The development of photoelectric detectors advanced the accurate estimate of the impact of dusty ISM on the background starlights through multi-wavelength observations. These observations along different sight lines provide benchmark measurements on the extinction curves in various environments. Fig. 1.6 shows the extinction curves in magnitudes normalized to V band from UV to near-IR, as measured in our Milky Way and the Large and Small Magellan Clouds (Gordon et al., 2003), where R_V is defined as the ratio between V-band extinction (A_V) and color excess between B and V band (E(B-V)), both in magnitudes:

$$R_V = \frac{A_V}{E(B-V)} \tag{1.2}$$

From Fig. 1.6 we could find several similarities among the different extinction curves. First, all extinction curves have a steeply rising relative strength of extinction with the decrease of wavelength, suggesting the emissions from short wavelengths like UV are more significantly absorbed than those from optical and near-IR. The stronger extinction at short wavelength cause the reddening of the starlight seen in the observations. The shape of the extinction is dominated by the absorption of dust grains of a wide range of sizes spanning from ~0.01μm to ~0.1μm to produce the wavelength-dependent extinction (Weingartner and Draine, 2001). Besides, apart from the extinction curve from the Small Magellanic Cloud, all curves show a strong bump of extinction centered on 2175 Å. Studies suggest that this bump is mainly contributed by the carbonaceous materials in the interstellar medium, while the exact origin is still under debate (Joblin et al., 1992; Li and Draine, 2001; Bradley et al., 2005; Steglich et al., 2010). The variation of the 2175 Å bump in different galaxies is suggested

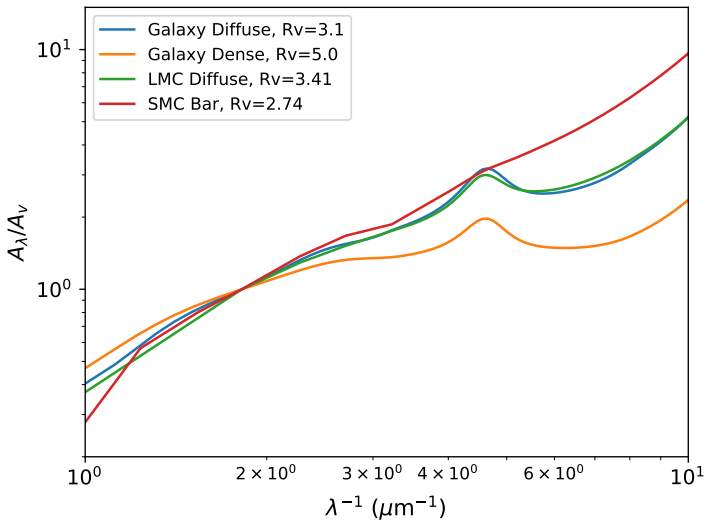

Figure 1.6 – Extinction curves of the diffuse and dense clouds in our Galaxy, Large Magellanic Cloud and Small Magellanic Cloud from Gordon et al. (2003).

to be related to the relative abundance of very small carbonaceous materials, which is further regulated by the grain production, growth, destruction, coagulation, shattering, and possible selective removal by galactic winds under different environments (Yan et al., 2004; Gall et al., 2011; Inoue, 2011; Ormel et al., 2009; Bekki et al., 2015).

1.2.2.2 Dust Emission in Infrared

The extinction curves in Fig. 1.6 quantitatively describe the selective processing of the interstellar medium to the starlight, which is dominated by the absorption of photons by dust grains of different sizes and components. The energy carried by these absorbed photons, in return, heats the dust grains and excites the large hydrocarbon molecules, producing most of the infrared emission we see in the spectra of galaxies from mid-infrared up to the millimeter at the rest frame.

Due to the complex components of dust itself, the absorbed energy from stars is also re-emitted by the dust through various physical processes, producing the different features in the galaxy spectra starting from mid-IR. Fig. 1.7 shows the IR emission model of dust from Compiègne et al. (2011), which suggests 3 main components of dust emission contributing to the total IR SED.

Around certain wavelengths in mid-IR, such as 3.3, 6.2, 7.7, 8.6, 11.3, and 12.7 μm, the spectra show broad emission peaks. These features trace the characteristic emission from PAH, a population of large complex interstellar hydrocarbon molecules (Li, 2020). Due to their small physical size, the stochastic excitation by single photons from the radiation background dominates the heating of the PAH particles. PAHs are also suggested to be an important contributor to the absorption feature at 2175 Å

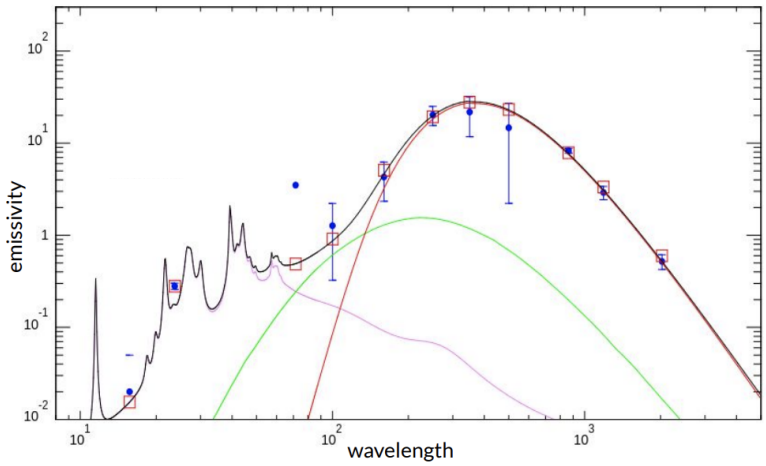

Figure 1.7 – Infrared dust emission model from Compiègne et al. (2011), which models the dust emission by PAH (pink) dominating in mid-IR, small sized carbonaceous grains of ~10 nm (green) between mid and far-IR, and large sized silicate and carbonaceous grains of ~100 nm (red) dominating in far-IR.

(Joblin et al., 1992; Mennella et al., 1998; Steglich et al., 2010) and diffuse interstellar bands in optical and near-IR (Duley and Kuzmin, 2010). The vibrational transitions of PAH molecules bearing the radiation field produce the characteristic photons at the wavelength of observed prominent mid-IR emission features (Draine and Li, 2007). In the studies on normal star-forming galaxies in the local Universe, the PAH emission is found to be able to contribute to the total IR luminosity by a few percent (Draine et al., 2007). Studies also found PAH emission to be sensitive to the UV radiation field. Observations find their deficiency in starburst galaxies, possibly due to the deconstruction of PAH by hard and intense UV radiation in these galaxies (Murata et al., 2014; Maragkoudakis et al., 2017).

When going to longer wavelengths from a few tens of microns to one millimeter, the SED of dust emission starts to be dominated by dust grains of a wide range of sizes. The small grains of ~10 nm produce thermal continuum emission peaked around 50μm. Due to their small sizes, their heating by UV radiation is not uniform and evolves rapidly with time (Desert et al., 1986). The grains with larger sizes under thermal equilibrium produce the continuum emission peaking at 100μm, which dominates the total infrared emission of dust in galaxies. This part of thermal emission, in practice, could be well modeled by a modified black body model, which accounts for the frequency variation of dust emissivity. The modified blackbody model, as well as the frequency-dependent dust emissivity, could be described as Eq. 1.3 and Eq. 1.4, where β in Eq. 1.3 represents the power law index of the dust emissivity over the wavelength, B(ν, T) represents the black body emission at given tempature T, $\kappa(\nu)$ is the emissivity of dust and κ_0 is the dust emissivity at frequency ν_0 (also see Sect. 4.4.2 for further details in our application):

$$S(\nu) \propto k(\nu) B(\nu, T_{\rm dust}) \tag{1.3}$$

$$k(\nu) = k_0 \left(\frac{\nu}{\nu_0}\right)^{\beta} \tag{1.4}$$

In normal star-forming galaxies like the Milky Way, the dust temperatures T_{dust} measured from the far-IR photometry through modified black body model fall around 20 K (Sodroski et al., 1997). Higher dust temperatures are found in starburst galaxies at low and high redshift, which could be explained by the larger heating by the more intense radiation from the more numerous young massive stars (Béthermin et al., 2015; Schreiber et al., 2018). Moreover, there are indications of T_{dust} increasing with redshift (e.g. Béthermin et al., 2015; Sommovigo et al., 2020).

In star-forming galaxies, the UV radiation from the young stars dominates the heating source of dust. This suggests that the dust emission from galaxies could also probe the star formation in galaxies, in addition to the UV emission that directly traces the young stellar populations. It could not only trace the energy emitted from the young stars under weak or moderate attenuation but also probe the energy budget from the star formation that is so heavily obscured by dust that could not be detected in rest-frame UV observations. In practice, the total infrared luminosity of galaxies has been proved and well-calibrated to be a tracer of star formation rate in galaxies, and has been widely applied either independently or in addition with other tracers. In this thesis, Eq. 1.5 is applied to estimate the star-formation rate of galaxies from the measurement of their total infrared luminosity at 3-1000 μm, according to the results in Kennicutt and Evans (2012) calibrated to Chabrier initial mass function (Chabrier, 2003). L_{IR} should be given in the unit of ergs s^{-1}

$$\log \mathrm{SFR}\,(M_\odot/\mathrm{yr}) = \log L_{\rm IR} - 43.41 \tag{1.5}$$

1.2.2.3 Other Emission from the Dusty ISM

Under metal-enriched conditions, The surface of dust grains in the ISM is suggested to be the place to catalyze the formation of molecular hydrogen (H_2) (Cazaux and Tielens, 2002). In normal galaxies like the Milky Way, cold molecular gas occupies very limited spaces but contains ~50% of the total mass of ISM in our Galaxy and nearby normal star-forming galaxies (Gordon and Burton, 1976; Leroy et al., 2008), tracing the part of ISM with the highest density and most closely related to the star-formation process. The mass of cold molecular gas is dominated by molecular hydrogen. However, the lack of electric dipole of symmetric hydrogen molecule prohibits transitions at the ground state, making it impossible to make direct observational measurements on the cold molecular gas through emission from molecular hydrogen.

Except for hydrogen, carbon monoxide is the most important and widely observed molecule in the interstellar medium. As the next most abundant molecule after H_2 in metal-enriched ISM, CO has bright characteristic emission lines in millimeter and

far-IR. Because of its low effective critical density and easily accessible condition of excitation, low J (e.g., J=1-0, J=2-1, or J=3-2) CO emission has been widely used as a tracer of the distribution, mass, and kinematics of molecular gas in the Milky Way and other galaxies for several decades. In practice, studies usually convert the observed CO luminosity to molecular gas mass following Eq. 1.6, where the CO luminosity and molecular gas mass are in units of M (K km/s/pc^2)$^{-1}$ and M$_\odot$, respectively.

$$M_{\rm H2} = \alpha_{\rm CO} \times L_{\rm CO} \tag{1.6}$$

The conversion factor $\alpha_{\rm CO}$ has measured values around 4.36 in our Galaxy (Strong and Mattox, 1996; Dame et al., 2001) and this value is also widely applied in the studies of metal-rich star-forming galaxies from the local Universe to the high redshift. However, there is ample evidence that $\alpha_{\rm CO}$ is highly varying under different extreme conditions in local and high redshift Universe. Comparing to the $\alpha_{\rm CO}$=4.36 M$_\odot$ (K km/s/pc^2)$^{-1}$ in the Milky Way, local galaxies with intense starburst show low $\alpha_{\rm CO}$ value of around 1 M$_\odot$ (K km/s/pc^2)$^{-1}$ (Downes and Solomon, 1998; Papadopoulos et al., 2012), while studies on low metallicity dwarf galaxies (Israel, 1997; Leroy et al., 2011) suggests high $\alpha_{\rm CO}$ values of >10 M$_\odot$ (K km/s/pc^2)$^{-1}$. Thus the application of a given $\alpha_{\rm CO}$ must be conservative considering its dependence on the gas conditions and metallicity.

The far-UV radiation field in star-forming galaxies could penetrate into the dusty ISM and destroy the CO to neutral and ionized carbon through photo-dissociation (Madden et al., 2020). The cosmic ray accelerated by the shocks of supernovae or jets could also dissociate the CO molecule in star-forming and starburst galaxies and produce reservoirs of neutral and ionized carbon (Dalgarno, 2006; Gaches et al., 2022). The balance of dissociation and formation of CO in different regions of molecular clouds by the external far-UV radiation and cosmic rays leads to a layered structure of distribution of different states of carbon in the cold ISM, which is illustrated in Fig. 1.8 (Madden et al., 2020).

The neutral carbon ([CI]) emission at 492 GHz and 809 GHz at rest-frame have critical densities comparable to low-J CO emission, which, in principle, provide an alternative tracer of cold molecular gas. Given their high luminosity and high frequency compared to low-J CO emission, [CI] starts to draw more attention in the studies on the molecular gas reservoirs on high-z galaxies, where the two lines start to fall into the more transparent atmospheric windows in (sub)millimeter (Valentino et al., 2018; Valentino et al., 2020; Jiao et al., 2019). Observations on the two [CI] lines altogether also provide a measurement of the temperature of the cold ISM, assuming optically thin emission and thermal equilibrium of gas (Cortzen et al., 2020).

The further photo-ionization of neutral carbon produces ionized carbon in the outskirt of molecular clouds. Ionized carbon could produce fine structure line emission at 158μm, which is the strongest emission line from the metal-enriched interstellar medium under normal conditions. The brightness and high frequency of [CII] fine structure line make it the best probe of ISM in galaxies at redshift higher than 4, which has been widely used for redshift measurement, kinematical modeling,

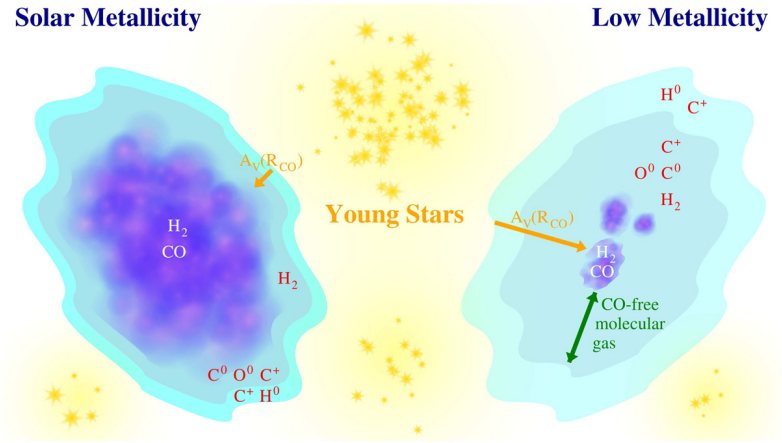

Figure 1.8 – Structure of the ISM and the distribution of carbon in CO molecule, neutral carbon and ionized carbon, as illustrated by Madden et al. (2020)

and neutral/molecular gas measurement on high-z galaxies in the past decades (e.g. Béthermin et al., 2020; De Breuck et al., 2014).

Apart from these emission features relative to carbon in the ISM, previous studies have also probed the distribution, mass, and physical condition of the ISM using emissions from many other molecules, atoms, and ions. These include emission from HCN molecules with higher critical density, which probes the dense molecular gas most closely related to the ongoing star formation (Gao and Solomon, 2004). Besides, the far-IR fine-structure lines from [NII] and [OIII] are also being used for redshift searching, ISM excitations, temperature, density, and gas-phase metallicity measurements (Herrera-Camus et al., 2018; De Breuck et al., 2019; Tadaki et al., 2022; Bouwens et al., 2022).

1.2.3 Selection of Dusty star-forming Galaxies

Since the first infrared survey by IRAS satellite in the 1980s, observations have already detected the dust emission from galaxies from the local Universe to the reionization era, including a population of galaxies with a large fraction of their total luminosity emitted by the dust. The most prevalently used method to select and build statistical samples of these dusty galaxies is making direct detection in the data observed at mid-IR to (sub)millimeter wavelengths, where the dust emission from galaxies dominates the emission. The multi-wavelength observations covering different parts of the SED of the dusty galaxies also result in the variation of source properties selected from these datasets.

1.2.3.1 Mid-IR Selection

The observation at the shortest wavelengths used in selecting dusty galaxies through their dust emission is the observation at around 24μm. At redshift at z 2 or smaller, 24μm observations mainly cover the PAH emission from star-forming regions in galaxies, making them a proper method for selecting star-forming galaxies. However, compared to the observations at longer wavelengths, the 24μm observation is much less sensitive to the high redshift dusty galaxies due to not only the dimming at larger luminosity distance but also the k-correction, especially when comparing to the evolution of (sub)millimeter observations (see Fig. 1.9 and Sect. 1.2.3.2 for further discussion). Follow-up studies on 24μm selected sources confirm the majority of the sample is populated by low to intermediate redshift sources at z<1, while also including luminous high redshift source at z=2-5 (Le Floc'h et al., 2005; Desai et al., 2008; Fiolet et al., 2010). Besides, the emission from hot dust in the torus region of obscured AGNs could have a significant contribution in mid-IR, which also requires careful decomposition by panoramic SED fitting to account for its contribution in the statistical studies related to star formation rates.

Using the observations at around 24μm by Spitzer, a population of Dust Obscured Galaxies, or DOGs (Dey et al., 2008) have been identified, with a mean redshift at $< z > \sim 2$. DOGs are selected by their very red color between the optical R-band and 24μm. The DOG population is made of mid-infrared bright dusty galaxies of various natures, while about 50% containing obscured AGNs. The rest of DOGs includes pure starbursts and very luminous PAH emitters. Besides, using the shallower near and mid-IR all-sky survey of WISE, studies also identified hot dust obscured galaxies (HOTDOGS) with red color between 12/22μm and 3.4/4.6μm (Eisenhardt et al., 2012; Wu et al., 2012). Compared to DOGs, these HOTDOGs show hyper-luminous infrared luminosities (10^{13} $L_\odot$) with significant contribution of hot dust emission in their mid-IR SED. Follow-up observations reveal their massive gas reservoir, disturbed gas kinematics, and possible outflows therein, suggesting that these galaxies could be mergers with AGNs radiating around the Eddington limit(Wu et al., 2018).

1.2.3.2 Far-IR Selection

Compared to the mid-IR selected samples, the dusty galaxies selected from far-IR and millimeter observations have fewer biases to the AGN contamination, as the emission from this wavelength range probes the thermal dust emission with much less AGN contribution in galaxies with active star formation. The observation from 100 to 500 μm can better sample the peak of the far-IR SED of galaxies across a wide range of redshift. Both model predictions and observations reveal that the wavelength and the depth of selection of dusty galaxies in far-IR to millimeter could lead to varied average properties of the samples.

Although not the only determinant, it has been shown that observations at longer

wavelength favor in general the detection of dusty galaxies at higher redshift. The 70-160 μm selected sample in extragalactic deep fields shows redshift distribution peaked at slightly below 1 (Elbaz et al., 2011; Gruppioni et al., 2013). In comparison, the 850 μm to 1.2m m selected sample in deep surveys by ground-based single-dish telescopes results in a slightly higher average source redshift at z=2-3 (Chapman et al., 2005; Smolčić et al., 2012; Stach et al., 2019; Simpson et al., 2020; Gómez-Guijarro et al., 2022a) or slightly above (Gruppioni et al., 2020), and the sources selected from 2 mm observations have an average redshift of z=3.6 (Casey et al., 2021), which is the highest among all deep far-IR to millimeter surveys. The favor of high redshift sources in sub-millimeter and millimeter observations could be explained by the negative k-correction effect in cosmological observations. As illustrated by Fig. 1.9, in the (sub)millimeter observations on high-z dusty galaxies, the dimming of observed fluxes due to larger luminosity distance and the shift of the far-IR SED peak to the observed frequency almost cancels out with each other.

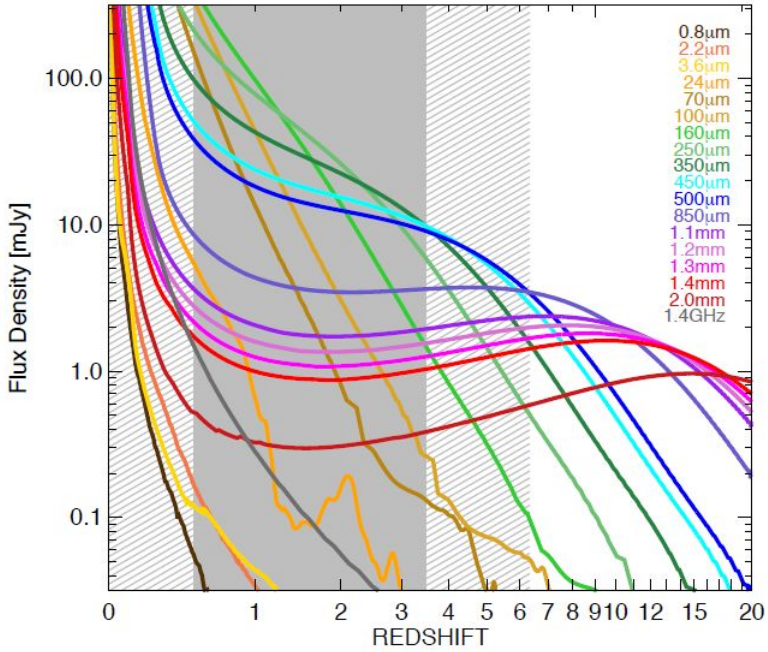

Figure 1.9 – The negative k-correction effect in deep field observations in far-IR to millimeter, as illustrated by Casey et al. (2014b). At fixed galaxy SED, the detected flux from z=1 to z=10 almost remains constant for observations around 1 mm, and could even rises with increasing redshift for 2/3 mm observations.

As illustrated by Fig. 1.9, for a galaxy with typical far-IR SED of dusty galaxies, the observed fluxes could almost remain unchanged between z=1-10 in submillimeter, or even rising in the millimeter observations at 2-3 mm. This also indicates that submillimeter and millimeter selected samples by single surveys could have similar limits in far-IR luminosity and thus star formation rate.

Apart from the wavelength dependence of the average redshift of far-IR to millimeter selection, studies also reveal a dependence of source properties on the sensitivity of observations. The deep 1.2 mm survey from Aravena et al. (2016) reveals higher contribution of intermediate redshift sources at z=1-2 among their sample, while the complete follow-up studies from Smolčić et al. (2012) on samples selected from shallower 1.1 mm observations show higher average redshift at z>3 (Scott et al., 2008; Younger et al., 2009). This could be associated with the higher SFR and IR luminosity of high redshift star-forming/starburst galaxies at fixed stellar mass, considering the redshift evolution of star formation main sequence. Having the negative k-correction in mind, we could expect more significant contribution of high-z dusty galaxies with more intense star formation in samples with brighter (sub)millimeter fluxes. Meanwhile, this also naturally results in a lower SFR of sources selected by the deep surveys compared to shallower blind observations.

The brightest sources selected from the wide-area surveys in far-IR and millimeter covering hundreds to thousands of square degrees have more distinct properties compared to the other samples described above. At fluxes above 25 mJy at 870 μm, the sources selected from SPT-SZ survey 1.3 mm catalogs are predominantly gravitational lensed galaxies, with the rest of the samples consist of galaxy mergers and high-z protoclusters (Reuter et al., 2020). Mass follow-up studies on these bright sources reveal that these systems have the highest redshift (z~3.9 on average with highest redshift at 6.9 for the SPT-SZ sample, see Marrone et al. (2018) and Reuter et al. (2020)) and intrinsic IR luminosity (>10^{13} $L_{\odot}$) among the highest of all far-IR and millimeter selected dusty galaxy sample Cañameras et al. (2015), Strandet et al. (2016), Reuter et al. (2020), and Neri et al. (2020). The higher average redshift of bright sources detected by wide-area blind surveys is also consistent with the predictions by various models. (see Béthermin et al. (2015) as an example, and Hodge and da Cunha (2020) for a summary)

1.2.3.3 Near-IR Dropout Selection

Apart from the selection using the observations on the dust emission, the significant attenuation on the starlight also leaves features in the optical and infrared SED of dusty galaxies, leading to the development of near-IR dropout selection. These galaxies are identified using deepfield observations from the CANDELS survey. Showing detections with high significance in Spitzer IRAC 3.6/4.5 μm observations with 5-sigma depth of 26.5 AB magnitudes, these source remains undetected in the deep optical and near-IR observations up to H and K band (1.6/2.2μm) with 5-sigma depth of 25-27 AB magnitudes (Wang et al., 2016; Wang et al., 2019; Smail et al., 2021). The submillimeter follow-up observations and SED modeling on such samples confirm the dust-rich nature of some of them. This suggests that their faintness in the H/K band and brightness at longer wavelengths could not only be explained by the large dust attenuation but also could be due to their high redshift (Wang et al., 2019). With a high average redshift of z~4, the H-band observations target the rest-frame UV emission at around 320 nm, while the IRAC observations probe the rest-frame optical emission at

700-900 nm from these H-dropout galaxies. With the existence of a large amount of dust, the rest-frame UV emission seen by H-band is subject to much stronger attenuation than the rest-frame optical emission probed by IRAC observations, resulting in the dropout features in deep H/K band observations.

The selection of such galaxies could be blended with foreground sources due to the much worse spatial resolution of current Spitzer IRAC observations (2") compared to HST (0.1"). This could add complexities in estimating the completeness of optically-dark dusty galaxies (Franco et al., 2020). This problem would be overcome by the JWST observations with almost ten times better spatial resolution at above 2 μm compared to the previous datasets. The unprecedented depth of JWST observations could also help complete the identification of these dusty galaxies at lower mass and higher redshift, and make a more efficient selection of samples with different levels of attenuation using more quantitative color-color/color-magnitude selection criteria.

1.2.4 The Role of Dusty Galaxies in Galaxy Formation and Evolution

In the local Universe, galaxies with the highest dust attenuation and infrared luminosity are dominated by major mergers and interacting systems. These galaxies are also classified as (Ultra-)Luminous Infrared Galaxies (ULIRGs and LIRGs), with total IR luminosity higher than 10^{12} $L_{\odot}$ and at 10^{11} to 10^{12} $L_{\odot}$, respectively. The high IR luminosity indicates efficient star formation even when considering the possible contribution of AGNs, and the observations on their molecular gas tracers (i.e. CO(1-0)) further reveal the difference of their star-formation compared to normal star-forming galaxies in the local Universe. it has been shown that local ULIRGs show 5 times faster depletion of their molecular gas, suggesting highly efficient star formation. Such systems could consume the gas reservoir of these galaxies in about 100 million years (Daddi et al., 2010a; Genzel et al., 2010; García-Burillo et al., 2012). The rapid consumption of gas and active star formation could be explained by the result of compression and accretion of cold gas into the center of galaxies through merger and galaxy interactions, which is also indicated by the higher dense gas fraction traced by HCN (Solomon et al., 1992). These dustiest local galaxies are also suggested to trace the short-lived transition phase in galaxy evolution from star-forming to quiescent systems in the local Universe.

The connection between quiescent galaxies and major mergers with dusty starbursts seems to be direct from the observations on the local ULIRGs. However, we should be aware that the observed quiescent galaxies in the local Universe already ceased their star formation for more than 1 Gyr. Thus, to build the connection in evolution between dusty, infrared-millimeter bright galaxies and quiescent galaxies, statistical studies on both populations across cosmic time should be carried out. In the past decades, it has been a challenge to reproduce the observed number of galaxies already in quiescence at redshift 3-4 (Glazebrook et al., 2017; Schreiber et al., 2018). However,

recent studies reveal the missing number of quiescent high-z galaxies are likely to be evolved from the dusty galaxies at z>4 missed by optical observations (Wang et al., 2019; Smail et al., 2021; Fudamoto et al., 2021). The deep sub-millimeter observations reveal the dusty nature of the majority of these optically-dark galaxies, while also revealing their fainter dust emission than bright sub-millimeter galaxies found from shallow surveys and suggest less extreme values of SFR in these galaxies. Panoramic SED analysis combining observations from optical-IR to (sub)millimeter suggests that these optically dark dusty galaxies dominate the massive end of star-formation main sequence at the corresponding redshifts (Wang et al., 2019; Fudamoto et al., 2021). These galaxies are found to have an order of magnitude higher number density than z>4 massive Lyman break galaxies, suggesting their dominance in the possible progenitors of massive quiescent galaxies arise after z=4.

Among the dusty galaxies in the early Universe, a large diversity in the possible physical process of the regulation and quenching of star formation has been observed. Using different approaches with optical-IR or (and) sub-millimeter observations, studies reveal rich dust content in high-z compact star-forming/starburst galaxies. In contrast to their active star formation, these galaxies show sizes and light profiles that resemble the compact quiescent galaxies (Barro et al., 2013; Barro et al., 2016; Popping et al., 2017). Some other studies also reveal compact dusty and possibly gas-rich cores in galaxies around cosmic noon, selected from sub-millimeter interferometric observations (Calabrò et al., 2018; Puglisi et al., 2019; Gómez-Guijarro et al., 2022a). These sources have compact sizes of dust distribution comparable to the compact dusty galaxies, while their optical emission could have extended disk-like profiles, in contrast to their compact dust and gas reservoir. At the same time, observations find prevalent short gas depletion time, down to a few tens of million years, in these high-z galaxies with compact dusty structures, which indicates rapid gas consumption and quenching of star formation in these galaxies. These properties suggest that these galaxies are likely to be the progenitors of the high-z massive compact quiescent galaxies, and the compact gas reservoir to be consumed by the star formation might trace the final stage of the stellar bulge formation in these galaxies.

However, dynamical analysis of the cold gas in some high-z dusty galaxies suggests the dominance of regular rotation on a few kiloparsec scales. Specifically, observations at kiloparsec resolution reveal cold gas kinematics in high-z submillimeter galaxies (Rizzo et al., 2020; Lelli et al., 2021; Fraternali et al., 2021; Xiao et al., 2022). These galaxies show both high circular motion and low velocity dispersion, which could be even more dynamically cold than the normal star-forming galaxies at similar redshift. Moreover, observations of bright submillimeter galaxies down to a few hundred parsecs reveal clumpy or spiral arm structures in dust and gas emission, suggesting their star formation is likely to be triggered by the disk instability (Hodge et al., 2012; Tadaki et al., 2018; Hodge et al., 2019; Tsukui and Iguchi, 2021). Although the evidence of cold dynamics and disk instability regulated star formation could not rule out the scenario of gas-rich mergers, more secular processes like gas accretion or minor merger under

gas-rich conditions at high redshift could reproduce similar properties as those found in observations (Dekel et al., 2020; Kretschmer et al., 2021). This is significantly different from the dusty galaxies found in the local Universe, which have significant overlap with the starbursting galaxy major mergers of (U)LIRG luminosity. Compared to the local dusty galaxies like ULIRGs, this indicates the non-monotonic nature of the dusty galaxy population in the general picture of massive galaxy formation and evolution in the early Universe.

1.2.5 Open Questions and Limitations

Studies on the evolution of cosmic SFRD bring a general picture of galaxy formation and evolution across cosmic time and set a crucial baseline for galaxy formation and evolution models. In the past decades, advancements in the ground and space-based optical and near-IR observations have provided consistent estimates on the cosmic SFRD. With additional IR observations, studies also revealed the dominance of dust-obscured star formation in the total cosmic SFRD up to the peak of cosmic star formation at redshift 2-3 (Madau and Dickinson, 2014). During the census of cosmic star formation, the long-wavelength observation of the dust emission is found to be necessary, not only because it could recover the ultraviolet light from young, massive stars absorbed by dust and re-radiated, but also because the conditions of the ISM, the environments of star formation and the viewing angle of observers could tremendously impact the obscuration of the starlight and thus significantly affect whether they could be selected and counted by existing surveys (Casey et al., 2014a; Whitaker et al., 2017).

However, compared to the advance of UV observations, the statistical studies of the absolute value and relative importance of star formation in dusty galaxies in the early Universe have not kept pace. There are still only limited measurements on the obscured star formation rate density at z>4 until now, and the analysis published in recent years also show differences of an order of magnitude (Gruppioni et al., 2020; Dudzevičiūtė et al., 2020; Khusanova et al., 2021; Zavala et al., 2021). This not only limits our understanding of the assembly of galaxies in the first few billion years of the Universe, but also further limits our understanding of the enrichment of metals in the ISM that the formation of different ingredients of dust rely on.

The first limitation of the current studies on high-z dusty star-forming galaxies comes from the difficulties of covering statistically significant samples. Deep surveys covering small areas have low efficiency in searching high-z DSFGs of low space density. Their statistics on bright sources could also be affected by the increased cosmic variance. On the other hand, large area surveys also suffer from the limitation of the shallow depth, which could mostly cover only the extreme star-forming systems at high redshift. Apart from that, the samples from very wide and shallow surveys have significant contributions from lensed galaxies (Reuter et al., 2020). Their fluxes and distribution are related to the geometry of the foreground sources unknown by the blind survey itself, making them less clean samples for statistical study on the space

density and the cosmic star formation from DSFGs.

The combination of analysis of surveys with tiered depth could overcome the issues on the coverage of high-z dusty star-forming galaxies. However, it is still difficult to properly identify the dusty galaxies at redshift above 4, especially for the wide and shallow surveys carried out by low-resolution single-dish telescopes. As the far-IR SED of galaxies follows the form of a modified black body, the degeneracy between dust temperature and redshift makes them highly dependent on the assumption, which could only provide very uncertain estimates on source redshift. The optical-IR SED analysis could provide more accurate photometric redshifts to identify high-z dusty star-forming galaxies. However,single-dish observations covering bright sources have beam sizes of tens of arcseconds up to arc minutes, leading to confused identification alone. Counterpart identification using mid-IR or radio data could help in searching for optical-IR counterparts by pre-selecting sources with active star formation at higher resolution and lower source density, while this method still has drawbacks in the incompleteness of identification, especially for high-z sources with mid-IR/radio emission undetected (Hodge et al., 2013; Chen et al., 2016).

High-resolution (sub)millimeter observations provide the most complete and robust way to locate the multiwavelength counterparts of dusty galaxies from surveys and construct the source SED to obtain source redshifts (Hodge et al., 2013; Stach et al., 2019; Simpson et al., 2020). The modern optical-IR photometric redshift analysis has good performance on large statistical samples, but the identification of high-z dusty galaxies with these methods could still suffer from the large uncertainties in photometric redshift introduced by the lack of detection in optical and some bands in near-infrared (Casey et al., 2021; Manning et al., 2022; Fudamoto et al., 2021). Besides, in the most widely used Spitzer data, the counterpart identification and photometry in the near and mid-IR images of a few arcseconds could still be affected by source blending.

For the identification of high redshift dusty galaxies in highly confused regions, as well as the analysis of the clustering and local environments of high-z dusty galaxies, the more accurate spectroscopic redshift will be needed or preferred. However, it is also known by the practices in the past decades that measuring the spectroscopic redshift of high-z dusty galaxies could be extremely time-consuming. Even with the high sensitivity and large bandwidth of ALMA/NOEMA, it still requires several hours to obtain reliable detections on at least 2 bright far-IR/millimeter emission lines on a bright, unlensed high-z dusty galaxy (Jin et al., 2019; Jin et al., 2022; Chen et al., 2022). Other attempts to observe strong optical-IR emission lines with large ground-based telescopes have also been carried out in the past studies (Casey et al., 2017; Cowie et al., 2017), while the rich atmospheric emission and absorption in near-IR could significantly affect the efficiency and completeness of these redshift searching methods. All of these issues discussed above make the spectroscopic redshift searching on large and complete samples of dusty galaxies extremely challenging.

Some recent studies also introduce forward modeling methods to estimate the

global evolution of cosmic star-formation rate density up to the reionization era (Casey et al., 2018; Zavala et al., 2021). These studies only use number counts from multi-wavelength observations in far-IR to millimeter as the observables to constrain the analysis. Notice that the differential number counts describe the density of sources per unit flux in the sky, and cumulative number counts describe the density of sources above a certain flux. Unlike the luminosity function describing the space density of sources with given luminosity at a given redshift, number counts only provide measurements of the 2D density of sources across the cosmic time projected on the sky. With assumptions on IR SEDs and the form of IR luminosity functions at different redshifts, these studies manage to derive the cosmic evolution of obscured star formation that could reproduce the observed number counts at different wavelengths. They suggest that long wavelength observations, such as 2-3 mm, could be most distinguishable on predictions with high and low high-z obscured SFRD. However, the number counts measured at these wavelengths were very limited at the starting time of this thesis.

Such analysis is also dependent on the assumptions on the parameters that determine the shape of far-IR SED, such as the dust temperature. Although earlier statistical studies with far-IR observations shows generally consistent cosmic evolution of dust temperature in high-z star-forming galaxies (Béthermin et al., 2015; Schreiber et al., 2018), recent observations also discover sources with apparently cold SED (Jin et al., 2019; Cortzen et al., 2020; Jin et al., 2022). With the search of these sources limited to the brightest (sub)millimeter samples, their contribution to the general population of dusty galaxies also remains uncertain. Besides, a recent analysis from Viero et al. (2022) suggests much higher T_{dust} and warm SED compared to previous studies at redshift above 5, which could result in large discrepancies in the estimate of the obscured SFRD in this era.

1.3 Observations of Dusty Galaxies

Since the 1980s, observations across the infrared and millimeter wavelengths have revealed dusty galaxies from the local Universe up to the reionization era, and with a large variety of luminosity and evolutionary stages. The increased angular resolution and sensitivity of facilities also help reveal more details on the structure and distribution of dust in such sources beyond the local Universe. In this section, I will summarize the past, ongoing and upcoming missions and surveys that target dusty galaxies across cosmic time, with a specific focus on the most recent decade.

1.3.1 Space-Based Missions

The discovery of dusty galaxies in the Universe starts from the all-sky survey of IRAS satellite at 4 bands in mid to far-IR at 12, 25, 60, and 100 μm (Neugebauer et al., 1984). With an angular resolution of 0.5-2.0', the IRAS all-sky survey reveals ~170000 sources at more than 10 degrees away from the galactic plane (Moshir et al., 1990).

These sources have typical fluxes above 0.5 Jy at 12, 25, and 60 μm and above 1.0 Jy at 100 μm. The sources with an extragalactic origin from the IRAS survey are dominated by galaxies and active galactic nuclei at z<0.5, with infrared luminosities of 10^{11} to 10^{13} $L_\odot$, while a small fraction of sources at higher redshift (up to 3) with hyper luminous apparent luminosity, above 10^{13} $L_\odot$ (Saunders et al., 2000; Wang et al., 2014). Better sensitivity and resolution in the mid to far-IR were achieved by the ISOPHOT instrument on the Infrared Space Observatory (ISO), reaching 11" resolution at 25 μm, and 44" resolution at 100 μm. Various blank field surveys have been carried out by ISO. The survey in the Lockman Hole cover 1 deg^2 with sensitivity of 16 mJy (Rodighiero and Franceschini, 2004), FIRBACK survey in three fields of 4 deg^2 in total down to the confusion limit at 45 mJy (Dole et al., 2001), and the larger ELAIS survey cover 10 deg^2 with a sensitivity of 100 mJy at ~100 μm (Oliver et al., 2000). At shorter wavelengths, ISO also made blind surveys with ISOCAM at shorter wavelength of 15μm with spatial resolution of 12" (Cesarsky et al., 1996). In the observations on ELAIS fields, the survey detected sources down to 3mJy with in 12 deg^2 (Oliver et al., 2000). The multi-tiered ISOCAM Guaranteed Time Extragalactic Surveys cover multiple fields, including the Lockman Hole, Marano Field, as well as the Hubble Deep Field North and South. Each of these fields covers area ranging from ~30 to ~1900 arcmin^2, and reachs 80% completeness on sources ranging from 0.1 to 1 mJy (Elbaz et al., 1999).

In the most recent two decades, several new generations of space missions perform deep observations on blank fields in mid-IR and far-IR and provide the widely used legacy data in the studies on star formation, dust, and ISM in galaxies beyond the local Universe. Many of these observations are coordinated with the extragalactic deep fields firstly observed by several projects of the Hubble Space Telescope, such as GOODS (Giavalisco et al., 2004), COSMOS (Scoville et al., 2007) and CANDELS (Koekemoer et al., 2011), which are also covered by rich multiwavelength deep observations.

`AKARI`: Although mostly focused on its all-sky surveys, the AKARI satellite also performed deep integrations on 2 fields, AKARI-NEP and AKARI Deep Field South (ADFS) (Matsuhara et al., 2006). The AKARI deep survey in the North Ecliptic Pole (NEP) field covers a circular region of 0.67 deg^2 in 9 photometric bands at 2-24 μm, with the resolution of 2"-3" and 5σ sensitivity on point sources at 5-120 μJy (Wada et al., 2008; Takagi et al., 2012). In total, 7284 sources are included in the mid-IR catalog from the AKARI-NEP deep survey in Takagi et al. (2012). Compared to the observation in NEP, the survey in ADFS targets the far-IR emission at 65, 90, and 140 μm, to take the advantage of low galactic cirrus in the survey area. The slow-scan observation covers ~15 deg^2 and reaches 5σ point source sensitivity of 28, 13 and 121 mJy at spatial resolution of 26" to 54" (Shirahata et al., 2009; Murakami et al., 2007).

`Spitzer`: The Spitzer Space Observatory launched in 2003 provides 2 instruments for continuum imaging through near to far-IR in seven photometric bands. The IRAC instrument performs continuum observations at 3.6, 4.5, 5.8, and 8.0 μm with spatial resolutions of 2" over a 5'×5' field of view (Fazio et al., 2004). The other instrument, MIPS, provides mid to far-IR continuum imaging capability at 24, 70 and 160 μm

with spatial resolutions of 6", 18" and 40", respectively, over a field of view of 5'×5' (Rieke et al., 2004). Observations in the 4 IRAC bands and MIPS 24 μm have been heavily involved in the studies on galaxies at cosmological distances, while the IRAC observations predominately trace stellar emission at high redshift. Thus, we limit the descriptions and summary on Spitzer blank-field observation to those carried out by MIPS at 24 μm.

Before the consumption of coolant, Spitzer carried out various imaging surveys on blank fields with MIPS at 24 μm. The deep observations in GOODS-N and GOODS-S field reach 3σ depth of 20 μJy within 160 arcmin^2 in each field and detected sources up to the first billion years of the Universe (Elbaz et al., 2011). Another series of observations were carried out in the COSMOS field under the S-COSMOS survey, with a larger coverage of 3.4 deg^2 and shallower 1σ point source sensitivity of 18 μJy (Sanders et al., 2007; Le Floc'h et al., 2009). With the relatively high spatial resolution and good sensitivity on dust emission from high-z sources, these observations have also been applied as a prior catalog for the identification of the counterparts and analysis on SEDs for sources detected by far-IR and (sub)millimeter observations of much worse spatial angular resolution (Elbaz et al., 2011; An et al., 2018).

Apart from the deep field observations, MIPS has also carried out wider and shallower blank field observations, such as the SIMES survey with a coverage of 7.7 deg^2 and 1σ point source depth of 20 μJy (Baronchelli et al., 2016; Baronchelli et al., 2018).

`Herschel:` The Herschel Space Observatory launched in 2009 provides 2 far-IR instruments for far-IR continuum imaging in six photometric bands. The PACS provides the capability of 70, 100 and 160 μm continuum observations with spatial resolutions of 5", 7" and 12" over a field of view of 3.5'× 1.75' (Poglitsch et al., 2010). During the lifetime of Herschel, PACS performed deep field observations in mostly 100 μm and 160 μm with multi-tiered coverage and depth. The typical small area and deep surveys in extragalactic deep fields, such as GOODS-Herchel (Elbaz et al., 2011), covered 160 arcmin^2 in GOODS-N and GOODS-S. The observations in GOODS-N reach a 3-σ point source sensitivity of 1.1 and 2.7 mJy at 100 and 160 μm, respectively. For the observations in GOODS-S, the 3σ point source sensitivities are 0.8 mJy, and 2.4 mJy at 100 and 160 μm, respectively. Surveys in larger deep fields, such as the observation of PEP (Lutz et al., 2011) in the COSMOS field, covers 2 deg^2 with 5σ point source sensitivity of 7.5 mJy and 16.4 mJy at 100 and 160 μm. PACS also performed some wide area observations. In Herschel Astrophysical Terahertz Large Area Survey (H-ATLAS), PACS observations covers ~600 deg^2 and reach 1-σ depth of 44 mJy and 49 mJy at 100 μm and 160 μm, respectively, in the GAMA fields (Eales et al., 2010; Valiante et al., 2016).

Apart from PACS, the Herschel also provide continuum imaging capability at 250, 350 and 500 μm by SPIRE, with spatial resolutions of 18", 26" and 36", respectively (Griffin et al., 2010). The larger format detectors of SPIRE provide a field of view of 4×8 arcminutes, making it more capable for wide area mapping in the far-IR than PACS. During the lifetime of Herschel, SPIRE carried out multi-tiered blank extragalactic observations ranging from confusion-limited small area observations to very wide area

surveys (Oliver et al., 2012). The typical deep small area survey includes the mapping on GOODS-N/S and COSMOS with typical coverage of 0.25-2 deg^2 and with a 5σ noise level of 8.1, 6.7 and 9.7 mJy at 250, 350 and 500 μm, respectively. SPIRE surveys in larger extragalactic deep fields, such as the HerMES observation in XMM-LSS (Oliver et al., 2012), cover 18.9 deg^2 with 5σ depth of 25.8, 21.2 and 30.8 mJy. On larger scales, SPIRE also conducted the HerMES Large Mode Survey (HeLMS) (Oliver et al., 2012) and H-ATLAS survey (Eales et al., 2010; Valiante et al., 2016). These surveys cover 280 and 600 deg^2 in the sky, with typical 5σ noise levels of 64/45, 53/57, and 77/53 mJy.

`WISE`: The WISE satellite launched in 2009 carried out an all-sky survey in 4 near and mid-IR photometric bands at 3.4, 4.6, 12 and 22 μm (Wright et al., 2010). Specifically, the mid-IR observations at 12 and 22 μm have been used to trace the hot dust emission and PAH from galaxies in the local Universe and at high redshift, and lead to the discovery of Hot Dust Obscured Galaxies (HotDOGs) (Eisenhardt et al., 2012; Wu et al., 2012). These 12 and 22 μm observations have spatial resolutions of 6.5" and 12", and 5σ noise levels of 0.67 and 5.1 mJy, respectively.

A summary of the observing wavelength, coverage, and sensitivities of these surveys in the mid-IR and far-IR photometric bands can be found in Table. 1.1.

Table 1.1 – Summary of the basic information of mid-IR and far-IR surveys ($10\mu\text{m} < \lambda_{\text{obs}} < 500\mu\text{m}$) from space missions since 2000.

Instrument	Name	λ_{obs} μ m	Coverage	Resolution	Depth 5σ	References
AKARI	NEP	2-24	0.67deg^2	2-3"	5-120μJy	1,2
–	ADFS	65/90/140	15deg^2	26-54"	28/13/121mJy	3,4
WISE	allWISE	3.4/4.6/12/22	all-sky	6.5"-12"	0.08/0.11/1/6mJy	5
MIPS24	GOODS-N/S	24	0.044deg^2	6"	20μJy(3σ)	6
–	COSMOS	24	3.4deg^2	6"	18μJy(1σ)	7,8
PACS	GOODS-N/S	100/160	0.044deg^2	7"/12"	1.1/2.7mJy	6
–	PEP	100/160	2deg^2	7"/12"	7.5/16.4mJy	9
–	H-ATLAS	100/160	600deg^2	7"/12"	44/49mJy	10
SPIRE	GOODS-N/S	250/350/500	0.25deg^2	18"/26"/36"	8.1/6.7/9.7mJy	6,11
–	COSMOS	250/350/500	2deg^2	18"/26"/36"	8.1/6.7/9.7mJy	11
–	XMM-LSS	250/350/500	18.9deg^2	18"/26"/36"	26/21/31mJy	11
–	HeLMS	250/350/500	280deg^2	18"/26"/36"	64/53/77mJy	11
–	H-ATLAS	250/350/500	600deg^2	18"/26"/36"	45/57/53mJy	10

Notes. [1] Wada et al. (2008) [2] Takagi et al. (2012) [3] Shirahata et al. (2009) [4] Murakami et al. (2007) [5] Wright et al. (2010) [6] Elbaz et al. (2011) [7] Sanders et al. (2007) [8] Le Floc'h et al. (2009) [9] Lutz et al. (2011) [10] Valiante et al. (2016) [11] Oliver et al. (2012)

1.3.2 Ground-Based Single-Dish Telescopes

The ground-based observations of the dust emission from galaxies are mainly carried out in the continuum at wavelengths corresponding to several atmospheric transmission windows in the sub-millimeter and millimeter, including 450 μm, 850 μm, 1.1-1.3 mm, ~2 mm and ~3 mm. The early blank field observations at these wavelengths were mostly carried out by single-dish telescopes equipped with large-format bolometer arrays. Although millimetric interferometers could provide better sensitivity on point sources and orders of magnitude higher spatial resolutions, the capability of large format continuum detectors on single-dish telescopes in wide area surveys is still irreplaceable to the current statistical study on high-z dusty galaxies.

`Sub-mm deep surveys:` The first series of deep surveys on dusty galaxies in sub-millimeter were carried out by SCUBA on the James Clerk Maxwell Telescope (JCMT) (Holland et al., 1998; Smail et al., 1998; Barger et al., 1998; Hughes et al., 1998). These observations have spatial resolutions of 15" and reach sensitivity (1-σ) of ~2mJy over a few arcmin^2 at 850μm. Some of these observations also target massive galaxy clusters at z=0.3-0.5 to benefit from the magnification of sub-millimeter emission by gravitational lensing on any background dusty galaxies along the same sight line. These observations, combined with Hubble imaging, reveal dusty star-forming galaxies at cosmological distances, which have been suggested to be the main contributor to the cosmic infrared background.

The SCUBA was decommissioned from JCMT and substituted by SCUBA-2 in 2011. With ~ 10000 pixels, SCUBA-2 offers 5-10 times better mapping speed than SCUBA at 450 and 850 μm, with spatial resolution similar to SCUBA (7" at 450 μm and 15" at 850 μm) (Holland et al., 2013). The largest completed SCUBA-2 survey is S2CLS, which covers over 5 deg^2 in total in 7 deep fields all over the sky (Geach et al., 2017) with a sensitivity of 1.2 mJy/beam in most of the surveyed area. Additional observations have been done on GOODS-N, GOODS-S, and Extended Groth Stripe (EGS), reaching down to 0.2 (0.28/0.56 in GOODS-N/S) mJy/beam and 1.2 (1.14/1.86 in GOODS-N/S) mJy/beam at 850μm and 450μm over 70-100 arcmin^2 in each field (Cowie et al., 2017; Barger et al., 2022; Zavala et al., 2017). Besides, observations of STUDIES (Wang et al., 2017) also take the advantage of significantly improved survey efficiency and sensitivity at 450 μm to make deep surveys down to 0.6-1 mJy/beam in ~75 arcmin^2 in the COSMOS CANDELS stripe. The observations of S2COSMOS also complement the data from S2CLS in COSMOS field (Simpson et al., 2019). It produces a more complete coverage over 1.6 deg^2 in COSMOS footprint, with a more uniform sensitivity of 1.2 mJy/beam, as well as an additional 1 deg^2 coverage with a sensitivity of 1.7 mJy/beam.

Recent and ongoing 850μm large surveys by SCUBA2 include North Ecliptic Pole SCUBA-2 survey (NEPSC2) and SCUBA-2 Large eXtragalactic Survey (S2LXS). NEPSC2 is designed to cover 4 deg^2 with a sensitivity of 1.7 mJy/beam in the planned Euclid

NEP deep field, while S2LXS plans to map 10 deg^2 each in E-COSMOS and XMM-LSS fields with a sensitivity of 2 mJy/beam. Besides, another 450 μm project, AWESOME, is proposed to study sources beyond the confusion limit of JCMT by taking the advantage of lensing magnification through the observations on a sample of carefully selected clusters at 0.8-0.9 mJy/beam sensitivity.

Apart from SCUBA and SCUBA2 on JCMT, in the southern hemisphere, the Atacama Pathfinder EXperiment (APEX) telescope is also equipped with LABOCA, a large bolometer array operating at 870 μm (Siringo et al., 2009). LABOCA had a beam size of 19", similar to that of SCUBA on JCMT, while it also had a much larger field of view of 11.4 arcmin^2. LABOCA carried out deep and uniform blank field observation in the Chandra Deep Field South called LABOCA ECDFS Submillimetre Survey (LESS) (Weiß et al., 2009), which reached a sensitivity of 1.2 mJy/beam over 900 arcmin^2.

`Millimeter deep surveys:` At longer wavelengths of about 1.2 mm, the blank field deep surveys start from the commissioning of MAMBO on IRAM-30m telescope in 1998 and its successor, MAMBO-2, in 2002. MAMBO-2 provides 150 arcmin^2 mapping with 0.8 mJy/beam sensitivity in both ELAIS-N2 and the Lockman Hole (Greve et al., 2004). These observations were followed by a 0.7 mJy/beam depth survey over 287 arcmin^2 in GOODS-N (Greve et al., 2008), as well as a 400 arcmin^2 survey with 1 mJy RMS in COSMOS (Bertoldi et al., 2007). The MAMBO-2 survey in the Lockman Hole was further extended and complimented by more observations and finally reach 0.75 mJy RMS over 566 arcmin^2 (Lindner et al., 2011).

Apart from MAMBO, another 144-element bolometer array, AzTEC, also carried out several surveys at 1.1 mm before its final commissioning on the Large Millimeter Telescope (LMT). It first made surveys on the JCMT, with a spatial resolution of 19". These observations include a 0.3 deg^2 survey in COSMOS field (Scott et al., 2008), a 0.08 deg^2 survey in GOODS-N (Perera et al., 2008) and a survey in the Lockman Hole with 0.3 deg^2 coverage (Austermann et al., 2010). All of these surveys reached similar depths of 1.3 mJy/beam. After that, AzTEC was moved to the 10m ASTE telescope in Chile and operated with a spatial resolution of 28". During this period, three surveys on GOODS-S, ADF-S, and SXDF field down to 0.5 mJy/beam were carried out, covering 0.08 and 0.20 deg^2, respectively (Scott et al., 2010; Hatsukade et al., 2011). Another survey in COSMOS surpassed the one made on JCMT, with a wider coverage of 0.72 deg^2 and a comparable depth of 1.3 mJy/beam (Aretxaga et al., 2011).

At 2 mm, the only single dish surveys with published results by 2019 were carried out by the GISMO bolometer camera on IRAM-30m telescope. At a spatial resolution of 24", GISMO made two series of blank field observations in GOODS-N and COSMOS. The GOODS-N observation covered ~40 arcmin^2 with a sensitivity of 0.135-0.27 mJy/beam (Staguhn et al., 2014), and the COSMOS survey covered 250 arcmin^2 with a sensitivity of 0.23 mJy/beam (Magnelli et al., 2019).

`Wide area surveys:` Apart from the single-dish telescopes for the use of general astrophysical studies, there are also several millimeter instruments dedicated to the cosmic microwave background that contribute to the studies on bright dusty galaxies, such as the South Pole Telescope (SPT). The SPT survey initially aimed at the detection of clusters through the Sunyaev-Zel'dovich effect covers 2500 deg^2 with 20.4, 5.8, and 9.8 mJy sensitivity at 4.5σ on point source and 1.0', 1.2' and 1.7' angular resolution at 1.3, 2 and 3 mm, respectively (Everett et al., 2020). From the 4845 sources detected by SPT-SZ, 506 sources are classified as SMG, and 81 have been confirmed with the spectroscopic redshift surveys to date (Reuter et al., 2020).

`On-going and upcoming surveys and facilities:` In recent years, the development of techniques related to kinetic inductance detectors leads to the construction and application of larger format continuum detectors in new and upcoming ground-based millimeter and sub-millimeter observations. The first application of the KIDs instrument in millimeter observations comes from the NIKA and NIKA2 installed on the IRAM-30m telescope in 2010 and 2015, which finally fills the full 6.5' diameter field of view of the telescope with thousands of detectors operating at 1.2 and 2 mm. The upcoming TolTEC instrument observing at 1.1, 1.4 and 2 mm on the 50m LMT (Bryan, 2018), the 850 GHz camera (Chapman et al., 2022) of the Fred Young Survey Telescope (FYST/CCAT-prime), and the future upgrade of SCUBA-2 at 450 and 850 μm on JCMT (Wang et al., 2020) are also designed to equip KIDs detector arrays.

The observing wavelength, coverage and sensitivities of these surveys in the (sub)mm are summarized in Table. 1.2.

Instrument	Name/Region	λ_{obs} μm	Coverage	Resolution	Depth mJy/beam	References
SCUBA2	S2CLS	850	~5 deg^2	15"	1.2	Geach et al. (2017)
–	GOODS-N	450/850	175 arcmin^2	10"/15"	1.14/0.28	Cowie et al. (2017) and Barger et al. (2022)
–	EGS	450/850μm	70 arcmin^2	10"/15"	1.2/0.2	Zavala et al. (2018)
–	S2LXS	850μm	~10 deg^2	15"	2	JCMT
–	NEPSC2	850μm	4 deg^2	15"	1.7	Shim et al. (2020)
–	STUDIES	450μm	151 arcmin^2	10"	0.91	Wang et al. (2017)
–	AWSOME	450μm	cluster	10"	0.9	JCMT
LABOCA	ECDFS	870	900 arcmin^2	19"	1.2	Weiß et al. (2009)
MAMBO-2	Lockman-H	1200	566 arcmin^2	11"	0.75	Lindner et al. (2011)
–	COSMOS	1200	400 arcmin^2	11"	1	Bertoldi et al. (2007)
–	GOODS-N	1200	287 arcmin^2	11"	0.7	Greve et al. (2008)
AzTEC(J)	GOODS-N	1100	0.08 deg^2	19"	1.3	(Perera et al., 2008)
–	COSMOS	1100	0.3 deg^2	19"	1.3	Scott et al. (2008)
–	Lockman-H	1100	0.3 deg^2	19"	1.3	Austermann et al. (2010)
AzTEC(A)	COSMOS	1100	0.72 deg^2	28"	1.3	Aretxaga et al. (2011)
–	ADFS	1100	0.20 deg^2	28"	0.5	Hatsukade et al. (2011)
–	GOODS-S	1100	0.08 deg^2	28"	0.5	Scott et al. (2010)
GISMO	GOODS-N	2000	40 arcmin^2	24"	~0.2	Staguhn et al. (2014)
–	COSMOS	2000	250 arcmin^2	24"	0.23	Magnelli et al. (2019)
SPT	SPT-SZ	1300/2000	2500 deg^2	1.0'/1.2'	4.5/1.3	Everett et al. (2020)

Table 1.2 – Summary of the basic information of sub-millimeter and millimeter surveys (450 μm < λ_{obs} < 2000 μm) from ground based single-dish telescopes since 2000.

1.3.3 Continuum Interferometric Observations

The emergence of millimeter interferometers like ALMA and NOEMA in the past decade enhances the capability of surveying and studying dusty galaxies with unprecedented depth and detail. The blind ALMA continuum observations at 1.1-1.3 mm reach μJy sensitivity and a few to sub-arcsecond resolution within a few to several tens of arcmin^2. These observations provide samples of less massive faint high-z dusty star-forming galaxies with normal star formation rates, which is highly complementary to the bright sub-millimeter galaxies more properly sampled by wide but shallow single-dish observations. Deep interferometric continuum surveys have also been performed in cluster lensing fields, which could cover samples with ~10 times fainter flux than ordinary blind observations in blank fields, tracing the contribution to the cosmic infrared background.

Currently, most of the interferometric continuum surveys on blank fields are carried out at 1.1 to 1.3 mm, which corresponds to the coverage of ALMA band6. The first few ALMA blank field surveys cover small area of 2 arcmin^2 SXDF (Hatsukade et al., 2016) and 1 arcmin^2 ASPECS-pilot survey in HUDF (Aravena et al., 2016) with 1σ sensitivity of 55 μJy and 13 μJy respectively. These observations detected 25 sources of >4σ detection from SXDF and 9 sources of >3.5σ detection from HUDF, respectively. With these samples, they brought 1.1/1.2 mm number counts measurements from 0.03 mJy to 1 mJy in continuous fields.

The high resolution of ALMA observation helps locate the optical-IR counterparts of the detected sources in HUDF and reveals an average photometric redshift of 1.5, which is smaller than the brighter sample from the single-dish surveys. The extension of ASPECS-pilot covered 4.6 arcmin^2 with comparable depth to the pilot survey, which further constrained the faint end of number counts and showed flattening of 1.2 mm cumulative number counts below 0.1 mJy (González-López et al., 2020). This suggests an almost complete recovery of faint galaxies contributing to the cosmic infrared background (Popping et al., 2020).

These first blank field ALMA surveys, in addition to the earlier surveys targeting the serendipitous detections in ALMA observation (Karim et al., 2013; Ono et al., 2014; Carniani et al., 2015; Fujimoto et al., 2016) and further observations of similar coverage in other fields (Dunlop et al., 2017; Umehata et al., 2017), provide the first number counts measurements at around 1.2 mm below 1 mJy. However, their limited field coverage also makes the results affected by significant cosmic variance, especially on bright sources. Thus, various ALMA blind surveys further extended the coverage to constrain the number density and study the physical properties of dusty galaxies with less bias. The surveys and studies on bright sources were complemented by ASAGAO and GOODS-ALMA. In the HUDF field, ASAGAO covered 26 arcmin^2 with a sensitivity of 60 μJy/beam and obtained number counts measurements from 0.2 to 2 mJy with 45 sources detected at >4.5σ (Hatsukade et al., 2018). In comparison, the GOODS-ALMA survey covers ~70 arcmin^2, providing the best statistics on bright

1.2 mm sources from a single ALMA survey. It was initially observed with a sensitivity down to 0.18 mJy/beam, with the map tapered from 0.3" original resolution to 0.6" (Franco et al., 2018). Then the survey was complimented by additional low-resolution data, reaching to a combined sensitivity of 68.4 μJy/beam at 0.5" resolution after combining all the data (Gómez-Guijarro et al., 2022a). From the combined data sets, 88 sources are identified, where half of the sources come from blind detection above 5σ significance, and the rest have 3.5-5σ detection with matched priors in multi-wavelength data sets. This sample extended the estimate of source number counts at 1.1/1.2 mm from high-resolution ALMA surveys to ~3 mJy. Apart from these band6 observations, ALMA has also performed its widest area blind survey with continuous coverage of 184 arcmin^2 with ~ 90 μJy at 2mm in COSMOS field under the MORA survey (Zavala et al., 2021; Casey et al., 2021). These long wavelength observations provide unique constraints on the bright end of 2 mm galaxy number counts with high spatial resolution, using the 13 sources detected with flux above 5σ. Thanks to the favor of selection on high redshift sources at this long wavelength, the MORA sample is also suggested to contain a large fraction of candidate high-z dusty galaxies, including a dusty galaxy with confirmed redshift at z=5.85 (Casey et al., 2019; Jin et al., 2019).

In parallel to the blank field surveys, millimeter interferometers have also carried out observations on massive galaxy clusters to benefit from the ~10 times magnification at most. These surveys could cover faint dust emission of ~10 μJy after lensing correction and thus more completely reveal the nature of sources that contributed to the cosmic infrared background. A most complete compilation of number counts from lensing cluster survey can be found in (Muñoz Arancibia et al., 2022), which reach a flux limit of 0.01 mJy.

After over ten years of observations, the ALMA observatory also gradually accumulated a large number of archival observations targeting different types of extragalactic sources. Apart from the detection of signals on the target sources, a considerable number of serendipitous detections are also found, which also consist of a unique blindly selected sample for statistical studies on high-z dusty galaxies. The earliest attempts to study these serendipitous sources brought the first few number counts measured by ALMA (Karim et al., 2013; Ono et al., 2014; Carniani et al., 2015; Fujimoto et al., 2016), even before the start of blind surveys in continuous fields. Recent studies with serendipitous sources from single or multiple projects extend the sample and number counts measurements to previously much less explored frequencies and flux ranges (Zavala et al., 2018; Klitsch et al., 2020; Béthermin et al., 2020; Zavala et al., 2021), and further extended the measurements on IR luminosity function to redshift above 4 (Gruppioni et al., 2020). The currently largest compilation of ALMA archival data, A3COSMOS (Liu et al., 2019), already got ~100 arcmin^2 coverage with sensitivity better than 0.1 mJy/beam at 1.1 mm in its most recent data release in only the COSMOS field, suggesting the high value and large potential of these archival data in statistical studies on high-z dusty galaxies.

A summary of the ALMA surveys in blank fields is given in Table 1.3.

Table 1.3 – Summary of the basic information of sub-millimeter and millimeter surveys in blank fields, as well as some compilation of data for serendipitous continuum detections ($450\mu\text{m} < \lambda_{\text{obs}} < 3000\ \mu\text{m}$) from ground based interferometers since 2013.

Instrument	Name/Region	λ_{obs} μm	Coverage arcmin^2	Resolution	Depth μJy/beam	References
ALMA B6	ASPECS	1200	4.6	1.3"	9.3	1,2
–	SXDF	1200	2	0.5"	55	3
–	HUDF	1300	4.5	0.7"	35	4
–	SSA22	1100	6	0.7"	60	5
–	ASAGAO	1200	26	0.5"	61	6
–	GOODS-ALMA	1100	72	0.5"	68	7,8
–	ALCS	1200	88	~1"	80	9
–	ALMA-FF	1100	20	~1"	55-71	10
ALMA B6+7	ALMACAL	var	69PB	<1"	~30	11
ALMA B7	ALPINE	870	25	~0.7"	30	12
ALMA B4	MORA	2000	184	~1.6"	90	13
ALMA B3	various	3000	~200	>1.0"	10-100	2,13,14

Notes. (1) Aravena et al. (2016) (2) González-López et al. (2020) (3) Hatsukade et al. (2016) (4) Dunlop et al. (2017) (5) Umehata et al. (2017) (6) Hatsukade et al. (2018) (7) Franco et al. (2018) (8) Gómez-Guijarro et al. (2022a) (9) Muñoz Arancibia et al. (2022) (10) Kohno (2019) (11) Oteo et al. (2016) (12) Béthermin et al. (2020) (13) Zavala et al. (2021) (14) Zavala et al. (2018)

1.3.4 Spectroscopic Interferometric Observations

Apart from the blind continuum surveys, the high sensitivity of modern (sub)millimeter interferometers also opens the possibility of massive spectroscopic surveys on the cold gas in star-forming galaxies across cosmic time. These observations primarily target two types of spectral lines. Surveys and observations at relatively low frequencies, such as 3 mm, primarily target multiple low and mid-J CO emissions tracing the cold molecular gas in high-z galaxies. Using four frequency setups on ALMA or two frequency setups on NOEMA, observations could have continuous spectral coverage over ~30 GHz. These setups could cover two or even more CO emission lines from galaxies at a wide range of redshifts, which allows accurate measurement of the spectroscopic redshift and estimate of the molecular gas mass of these galaxies. Besides, some other observations target the [CII] 158 μm and [OIII] 88 μm emission, which are predicted to be the brightest fine structure lines accessible to ALMA observation at and above the frequency of band6. Even a single detection of these lines could be used to obtain the spectroscopic redshift of high-z galaxies with additional constraints from photometric redshifts. Surveys targeting these bright emission lines also bring a wealth of information on the neutral/ionized gas distribution in the galaxy and circumgalactic medium, as well as their dynamics, in galaxies up to the epoch of reionization.

`ASPECS`: The initial observation of ASPECS pilot program surveyed 1 arcmin^2 region in the Hubble Ultra Deep Field with one pointing down to 1σ sensitivity at 3.8 and 12.7 μJy/beam at 3 and 1 mm continuum and ~ 2×10^9 K km/s pc^2 on CO emission (Walter et al., 2016; Decarli et al., 2016b; Decarli et al., 2016a). The spatial resolution of the ASPECS-pilot 3 mm observation is 2.8". The project was followed by the ASPECS-LP, extending the coverage to 4.6 arcmin^2 with sensitivity comparable to the pilot program (Decarli et al., 2019) and a slightly better spatial resolution of 1.8". Both of these observations cover the frequency range between 84 and 115 GHz continuously. The combination of a wide spectral coverage with a high sensitivity maximizes the efficiency of covering a large redshift range with various CO lines and probes the constraints up to the knee of the CO luminosity function. 613 line candidates with SNR >5.0 are detected in the ASPECS-LP in total. The study reveals the factor of 3-7 rise of molecular gas density from the local Universe to the peak of cosmic star formation at z=1-3, while it also shows tension with the predictions of various semi-analytic models on the CO luminosity function, especially at the bright end.

`COLDz`: The COLDz survey was carried out by the Very Large Array with lower frequency observation (Pavesi et al., 2018b). The survey aims to census the CO(1-0) emission and CO(2-1) emission to constrain the cosmic density of molecular gas at the peak of cosmic star formation and in the first billion years of the Universe. The survey is of two tiers, including a small area and deep integration on ~9 arcmin^2 in COSMOS field with 7 pointings and cover 31 to 39 GHz with 5σ sensitivity of 8×10^9 K km/s pc^2 on CO lines, as well as a wide and shallow mapping on 51 arcmin^2 within GOODS-N field with 57 pointings and cover 30 to 38 GHz with 5σ sensitivity of 3×10^{10}

K km/s pc^2 on CO lines. 26 sources are identified by COLDz observation in COSMOS and 32 are identified by the observation in GOODS-N. These candidates have at least one emission line detected at SNR >5.25 and 5.5 in COLDz COSMOS and GOODS-N observations, respectively. The wide area of COLDz survey provides more stringent constraints on the bright end of the CO luminosity function and finds consistency in the CO luminosity function and cosmic evolution of molecular gas density with ASPECS up to the peak of cosmic star formation (Riechers et al., 2019). The survey also confirms 3 dusty star-forming galaxies at z>5 in the total survey area, which suggests a higher density of this population of galaxies with respect to previous studies (Riechers et al., 2020).

Apart from blind surveys, there are also a large number of dedicated spectroscopic observation programs that target the emissions from high-redshift galaxies. These projects pre-select their sample with accurate spectroscopic or photometric redshift constraints to make targeted observations on bright emission lines in sub-millimeter and millimeter frequencies.

One of the first dedicated spectral line surveys by ALMA is ALPINE, an ALMA large program targeting the [CII] 158 μm emission from 118 normal star-forming galaxies (Le Fèvre et al., 2020). The samples are selected based on their bright UV luminosity $L_{UV} > 0.6\ L^*$ and with spectroscopic observations to obtain accurate redshift and exclude type-I AGNs. The sources have redshift between z=4.4 and z=5.9 and make [CII] emission accessible through the ALMA band7 (~870μm) observation, while no sources fall into the redshift range of z=4.65-5.05, which avoids an opaque atmospheric window.

The ALMA band7 observations were carried out with spatial resolution >0.7" to optimize the line detection. From the observations, 75 sources have their [CII] emission detected with SNR >3.5 (Béthermin et al., 2020) at a sensitivity of 0.4×10^8 $L_\odot$ on [CII] emission of 235km/s width. Apart from the primary target of the survey, 12 more candidate serendipitous [CII] detections are also identified within a total area of 0.41 arcmin^2 within the primary beam (Loiacono et al., 2021). The [CII] observation of ALPINE have contributed to various topics on the studies of high-z star-forming galaxies, including the [CII] luminosity function (Yan et al., 2020; Loiacono et al., 2021), the cosmic evolution of $L_{[CII]}$-SFR scaling relation (Schaerer et al., 2020), gas kinematics (Jones et al., 2021) and the extended gas halos in high-z star-forming galaxies (Fujimoto et al., 2020).

REBELS, a more recent ALMA spectroscopic survey, is observing 40 massive star-forming galaxies at higher redshift than ALPINE, at z>6.5 (Bouwens et al., 2022). Similar to ALPINE, the survey also selects the sample based on their UV brightness. Uniquely, the REBELS sample is also selected to have the highest UV luminosity over 7 deg^2, making them a representative sample of the most massive and active star-forming galaxies in the early Universe. The observations are designed to cover either

[CII] 158 μm or [OIII] 88 μm emission, while the redshift information mainly comes from the accurate photometric constraints.

To maximize the efficiency, the REBELS survey targets the [CII] line through spectral scans for sources at z=6.5-8, with a limiting luminosity (5σ) of 2×10^8 $L_\odot$. For sources with z>8, the survey observes [OIII] though spectral scans at 5σ sensitivity of 7×10^8 $L_\odot$. With the survey data on emission lines, the study reveals little size evolution of [CII] emission from z=4 to z=7, in comparison with the ALPINE sample (Fudamoto et al., 2022).

The accurate measurement of the spectroscopic redshift of high-z dusty star-forming galaxies has been a challenge for decades. Given their high dust attenuation in optical and UV, the blind search of far-IR and millimeter emission lines through interferometric spectroscopy provides a less biased way of obtaining the redshift of a statistical sample of such dusty galaxies. Normally, such studies require multiple line detections to obtain robust redshift, while the high sensitivity requirements limited the systematical blind line searching to only the brightest (sub)millimeter selected sources from large blind observations of several deg^2, such as the observation of 18 SMG sample in Chen et al. (2022), which have 850μm fluxes higher than 12 mJy and reach to the sensitivity of 0.33 mJy/beam per 15.8 MHz and determine the spectroscopic redshift of 17 sources. The sample dominated by gravitational lensing from a very wide area survey of hundreds to thousands deg^2 (Weiß et al., 2013; Cañameras et al., 2015; Neri et al., 2020; Reuter et al., 2020) are more completely surveyed by ALMA/NOEMA, which also identified sources with the highest redshift selected from millimeter and sub-millimeter (Marrone et al., 2018).

Similar to the cases in the studies on continuum, spectral lines from non-target sources of interferometric observations could also be detected by chance, providing precious sample for case studies or statistical studies. Although continuum follow-up observations on single-dish detected sources are normally carried out with low sensitivity, the resulting RMS in the low resolution spectra before combination could still satisfy the sensitivity requirements of detecting bright emission lines like [CII]. In (Mitsuhashi et al., 2021), the authors report 5 possible serendipitous detections of [CII] in the ALMA band7 follow-up observation of S2COSMOS sources. With the additional spectroscopic information on other sources in the COSMOS field, they report a candidate large scale structure at z~4.6 over 10 comoving Mpc. Besides, the brightness of calibrators used in ALMA observations also opens the possibility of detecting CO absorptions in the foreground line of sight. Systematical studies on these absorption features in the ALMA calibration data has also contributed to the constraints on the cosmic evolution of molecular gas mass density (Klitsch et al., 2019).

2 New IRAM KIDs Arrays 2 (NIKA2)

Sommaire

2.1 Basic Information on NIKA2 72
2.1.1 Design and General Aspects of NIKA2 72
2.1.2 Scientific Applications of NIKA2 75
2.2 NIKA and NIKA2 Deep Fields 76
2.3 Observation with NIKA2 78
2.4 NIKA2 Data Reduction 81
2.4.1 NIKA2 Data Calibration and Map Reconstruction with PIIC . . . 81
2.4.2 Source Extraction and the Effects To Be Corrected 84
2.4.3 PIIC Simulations 87

In this thesis, we primarily focus on the scientific studies on high-z dusty star-forming galaxies brought or initiated by New IRAM KIDs Array 2, or NIKA2 in short, installed on the IRAM 30m telescope. As a representative new generation (sub)millimeter continuum camera, NIKA2 brings significantly improved capability in a wide range of observations compared to previous instruments at its working frequencies, while it also poses new challenges in the reduction and analysis. This section will give a brief introduction to the general design and goals of NIKA2, as well as details on the design, observation, and data reduction of the extragalactic deep fields carried out with NIKA2 and its prototype instrument, NIKA, in the past years.

2.1 Basic Information on NIKA2

2.1.1 Design and General Aspects of NIKA2

The NIKA2 instrument makes sensitive millimeter photon detection through the application of kinetic inductance detectors or KIDs. The basic design of a KID consists of a superconducting inductor and a capacitor, which make up a resonant circuit. When photons illuminate the superconducting inductor, they could break Cooper pairs of electrons produced under superconducting temperature, create excess quasi-particles and change the kinetic inductance of the superconducting material. As a result, the incoming photons alter the resonant frequency and amplitude of the circuit, which could be measured, and quantitatively constrain the flux of incoming emission. An illustration of the resonant circuit and the impact of photon illumination on the resonant frequency can be found in Fig. 2.1

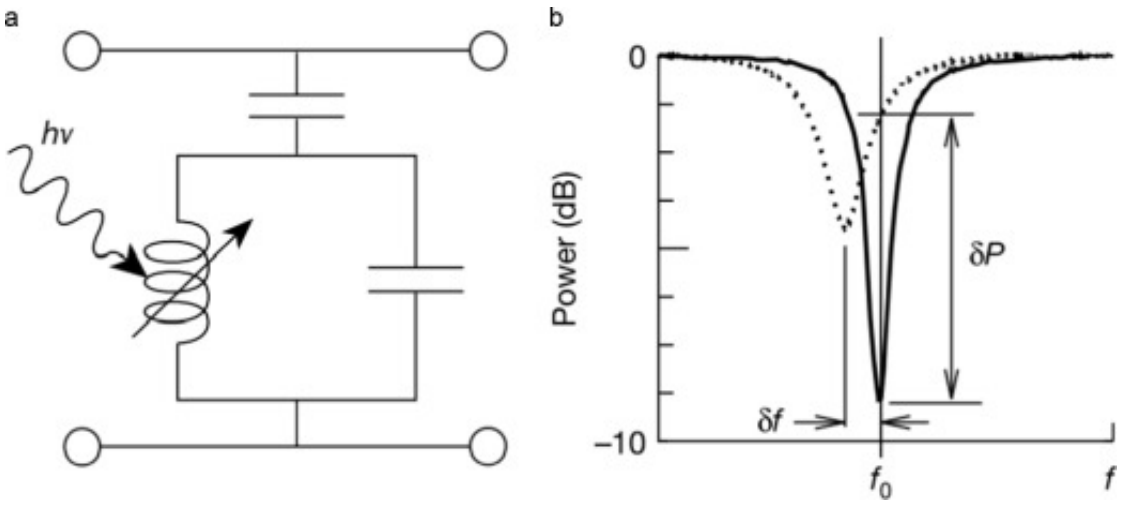

Figure 2.1 – Left: A scheme of the resonant circuit that constructs a KID. Right: An illustration of the resonant frequency of the KID before (solid line) and after (dotted lines) the superconducting inductor absorbs incoming photons. Figure extracted from Mazin et al. (2012)

The high sensitivity to faint emission With its simple design and the principle of photon detection, a large number of KIDs could be fabricated with similar structures with slightly different resonant frequencies. Up to a few hundred KIDs could be connected to a single readout system, where their slightly different resonant frequency ensures limited interference between the frequency signal from each detector during the processing of these data under ideal conditions. Compared to the other type of detectors in (sub)millimeter detectors like the transition-edge sensor (TES), the advantages of the simple construction of detectors and readout system make KIDs a more capable choice for large field-of-view, high multiplex (sub)millimeter continuum detector arrays on ground-based single dish telescopes.

In Fig. 2.2, we present a scheme of the structure of the NIKA2 instrument. The design of NIKA2 consists of 3 KIDs arrays as the core instrument to detect the millimeter emission collected by the telescope. Among the three KIDs arrays, two of them (Array 1 and Array 3) work at ~260 GHz (1.2mm) with bandwidths of ~50 GHz, while the other array (Array 2) works at ~150 GHz (2.0mm) with a bandwidth of ~40 GHz. The incoming emission collected by the 30m telescope is separated by a dichroic mirror to separate ~260GHz from ~150 GHz emission to Array 2, and the ~260 GHz emission further passes a grid polarizer, which guides horizontal and vertical polarized light to Array 1 and Array 3, respectively. Each of the arrays working at 260 GHz consists of 1140 KIDs connected to 8 feed-lines for signal readout, and Array 2 working at 150 GHz is made of 616 KIDs connected to 4 feed-lines. These detectors on each array fill the 6.5' diameter field of view of the IRAM 30m telescope, for 260 GHz, and 150 GHz observations, respectively. Due to the superconducting working condition, the whole

system on the KIDs array, the dichroic mirror, and the polarizer is cooled down to 150 mK during the operation. Outside of the core part of the detectors, multiple stages of cooling and filters are applied to minimize the illumination of unwanted off-band emission on the detectors.

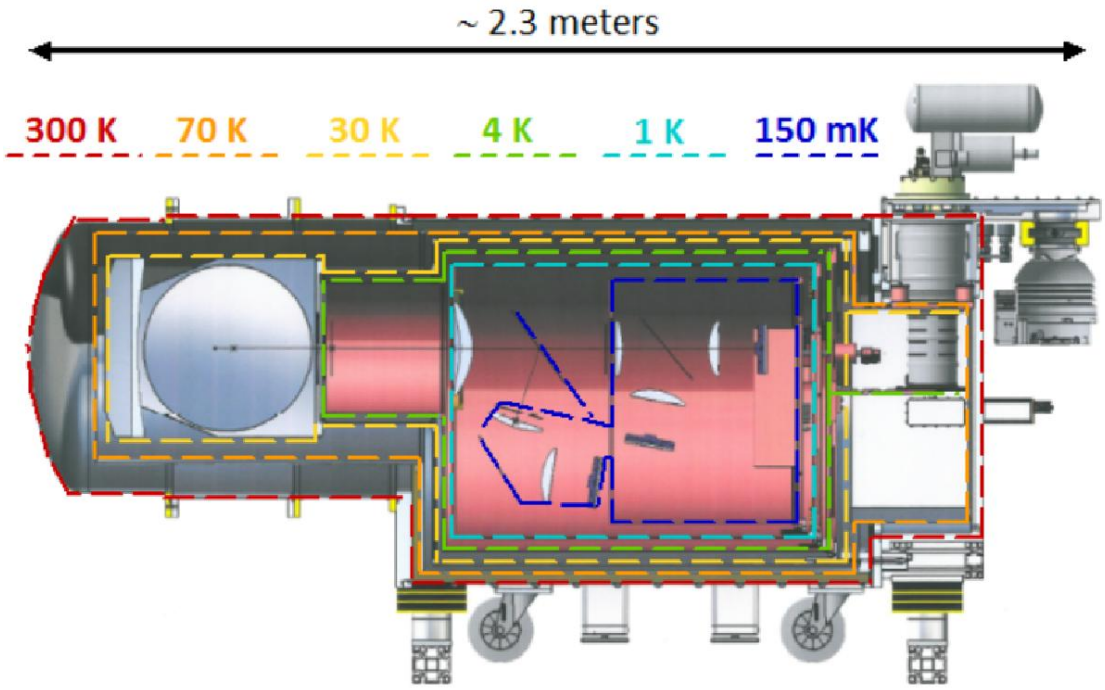

Figure 2.2 – Structure of the NIKA2 instrument and its cryostat. The dashed line marks regions cooled down to different temperatures. The figure comes from Adam et al. (2018)

Due to the imperfect fabrication, not all of the KIDs could be properly used in practical observations. The beammap observations (see Sect. 2.3 for an introduction) on bright point-like sources in Perotto et al. (2020) reveal a 84% validity on Array 1 and 3, and a 90% validity of KIDs on Array 2. Based on these observations, Perotto et al. (2020) also measured the main beam full-width half maximum of the NIKA2 continuum observations at 260 GHz and 150 GHz to be 11.1"±0.2" and 17.6"±0.1", and the main beam efficiency of 47%±3% and 64%±3%, respectively, on the IRAM 30m telescope. The repeated observation of flux calibrator MWC349 suggests a stable recovery of its flux with an absolute flux calibration uncertainty of 5%.

To quantify the on-sky sensitivity of continuum detector arrays like NIKA2, we use the noise equivalent flux density (NEFD). The NEFD is the 1σ error on the flux density of a point source in one second of integration time by a given instrument at zero atmospheric opacity, with a unit of mJy $s^{1/2}$. It further defines the mapping speed of continuum instrument (M_s, usually presented in the unit of $arcmin^2/mJy^2/h$), which

describes the sky area $A_{\rm scan}$ that can be mapped at a variance level of 1 mJy^2 in an integration time of one hour, through Eq. 2.1. Note that $d_{\rm FOV}$ = 6.5' is the FOV diameter, and η is the fraction of valid KIDs for an observation.

$$M_s = \eta \frac{\pi}{4} d_{\rm FOV}^2 \frac{1}{\rm NEFD^2} \tag{2.1}$$

The NEFD and the mapping speed of NIKA2 are measured from the deep integration on a high-z lensed dusty galaxy, HLS J0918+5142, though the variation of flux-density uncertainties as a function of the effective integration time on each array. From these data, Perotto et al. (2020) measured NEFD in of 30.1 mJy s$^{1/2}$ and 111 mJy s$^{1/2}$, at 260 GHz and 150 GHz, respectively. With various observing campaigns, they also obtained the mapping speed of NIKA2 at 260 GHz and 150 GHz of 1388 arcmin^2/mJy^2/h and 8.8 arcmin^2/mJy^2/h.

2.1.2 Scientific Applications of NIKA2

With the combination of the large aperture of the 30m telescope and the large field of view of the KIDs array, NIKA2 provides the best deep millimeter continuum mapping capability available to the community to date. Since 2017, NIKA2 has carried out various science observation projects, which cover a wide range of research topics in astrophysics.

The observations on galactic sources and galaxies in the local Universe with NIKA2 primarily trace the long wavelength Rayleigh-Jeans tail of the thermal dust emission, with the possible contribution of free-free emission. The sensitive observations of NIKA2 also measure the millimeter emission from dust in the debris disk of young stars, providing constraints on the dust size distribution, composition, and dynamical states in this late stage of protoplanetary disk evolution.

Apart from the protoplanetary disk around young stars, NIKA2 also targets the star-forming regions in our Galaxy to observe the cold dust emission from them. These observations provide unique constraints on the dust emissivity from different star-forming environments, and also probe the cold and low mass cores down to the mass regime of brown dwarves in the nearby star-forming regions. These surveys and studies could improve the estimate of the core mass distribution in the early stage of star formation and thus shed light on the measurement of initial mass function and its environmental dependence.

In the observations on nearby galaxies, NIKA2 probes a similar part of SED compared to the galactic observations. Thus, these data also provide the constraints on the spatially resolved dust emissivity in nearby galaxies, as well as its variation with galaxy type and environment. The improved dust emissivity constraints, in return, reduce the uncertainty of dust mass distribution and dust-to-gas ratio measurements. Besides, the 2 mm observation traces a transition part of SED where both thermal dust

emission and free-free emission contribute to the observed flux. The inclusion of these data in SED modeling could help the decomposition of free-free emission in galaxies, which has been proposed as a powerful and less biased tracer of both obscured and unobscured star formation accessible by the upcoming Square Kilometer Array (SKA).

At higher redshift, there has been a large amount of NIKA2 observations invested in the measurements of the Sunyaev–Zeldovich (SZ) effect in distant galaxy clusters. Originating from the inverse Compton scattering of cosmic microwave background (CMB) photon by the hot gas in the intergalactic medium (IGM) in massive galaxy clusters, the SZ effect produces negative signals relative to the background at frequencies below 218 GHz and positive signals above this frequency. It has been used as a powerful tool in studying the cluster thermal and dynamical states, mass distribution, as well as constraints of crucial cosmological parameters. The small beam size of NIKA2 on the 30m telescope allows the observations to properly resolve cluster SZ signal at both low and high redshift ($z < 1$).

Apart from the SZ effects, NIKA2 millimeter observations also cover the thermal dust emission from high redshift star-forming and starburst galaxies. With the assistance of the negative k-correction in the millimeter observation of high-z galaxies, the large field of view, high sensitivity, and relatively good spatial resolution of NIKA2 make it a suitable survey engine for the census on dusty star-forming galaxies (DSFGs) from the cosmic noon to the reionization era. The following part of this thesis will particularly focus on the studies on high-z DSFGs from NIKA2 observations and the details of these NIKA2 deep field observations could be found in the following sections.

2.2 NIKA and NIKA2 Deep Fields

The first deep field observation with KIDs instrument on IRAM 30m telescope was made in under the proposal 230-14 with the NIKA pathfinder. This series of observation cover a small 3.5'×2.5' field centered on AzGN10 (Penner et al., 2011) at (RA, Dec)=(12:36:27, 62:12:18) in the GOODS-N field, which was initially identified as a z~6.5 candidate galaxy (Liu et al., 2018). The observation was carried out under weather conditions with a zenith opacity of 0.39 at 1.2 mm, which is not satisfactory for deep continuum mapping. With 6.5 hours on-sky, we reach 1σ sensitivity of 0.6 and 0.2 mJy at 1.2 and 2 mm respectively at the center of the field. These early NIKA data were reduced following Adam et al. (2014).

During the commissioning of NIKA2, deep integrations on selected sources have been made to verify the sensitivity, stability, and capability of recovering fluxes of both bright and faint sources of the instrument. In this thesis, we use the observations centered on the gravitational-lensed DSFG HLSJ0918+5142 at z=5.24 (Combes et al., 2012) to initiate the research in Chapter 4. As part of the NIKA2 Science Verification (NIKA2 SV), observations on HLSJ0918+5142 took place in February 2017.

An area of 185 arcmin^2 centered on HLSJ0918+5142 was covered for an on-source time of about 3.5 hours at the center of the map. This allowed us to reach 1σ sensitivities of about 0.3 mJy at 1.2 mm and 0.1 mJy at 2 mm in the central region of the map.

Since October 2017, NIKA2 deep field observations from our team have been devoted to the NIKA2 Cosmological Legacy Survey (N2CLS), an IRAM guaranteed time large program investing 300 hours in NIKA2 observations in GOODS-N and COSMOS fields. The N2CLS observation was designed to have good statistics on both faint and bright sources, through a narrow and deep survey in the GOODS-N field and a wider and shallower observation in the COSMOS field. The survey time in GOODS-N was chosen to approach the confusion limit of the IRAM 30m telescope on a relatively narrow area of ~160 arcmin^2. In COSMOS, N2CLS covers a much larger area of ~1100 arcmin^2 with a shallower depth, to get a larger sample of bright sources and very high redshift DSFGs Béthermin et al. (2015). Thanks to the capability of dual-band coverage of NIKA2, we are simultaneously obtaining 1.2 mm and 2 mm data. The observations at these relatively long wavelengths are also expected to favor the selection of DSFGs at higher redshift (Blain et al., 2002; Lagache et al., 2004; Casey et al., 2014b; Béthermin et al., 2015).

N2CLS observations started in October 2017 and are still ongoing, under project ID 192-16. In the corresponding research works for this thesis, we use 179.4 h of observations in total that were conducted from October 2017 to March 2021. These observations consist of 92.2 h data obtained in GOODS-N and 87.2 h obtained in COSMOS. In the observation on GOODS-N, we executed two groups of 12'×6.3' and 6.5'×12.3' scans in orthogonal directions in GOODS-N centered on RA:12:36:55.03 Dec:62:14:37.59. For the COSMOS field, we carried out two groups of 27'×34.7' and 35'×28' orthogonal on-the-fly scans centered on RA:10:00:28.81 Dec:02:17:30.44. The two groups of orthogonal scans in both fields were taken at equal times. In the GOODS-N field, we made the two groups of scans with a speed of 40 and 35 arcsec/sec, and position angles of -40^o and -130^o in the RA-DEC coordinate system of the telescope. For COSMOS observations, the two groups of scans were observed with a speed of 60 arcsec/sec at position angles of 0^o and +90^o in the RA-DEC coordinate system of the telescope.

By the end of March 2021, a total number of 760 scans for GOODS-N and 390 scans for COSMOS from each array were observed by the N2CLS. During the observations, 225 GHz sky opacities measured by the IRAM 30-m taumeter $\tau_{225\,GHz}$ varied from 0.06 to 0.40, with a mean value of 0.20. These scans will pass through a quality evaluation by the data reduction pipeline, where the scans that do not satisfy the preset requirements or encounter fatal errors in the processing will be removed. A summary of the scan removal and the statistics on the conditions and qualities of scans kept in our final data reduction could be found in Sect. 2.4.

2.3 Observation with NIKA2

Most of the NIKA2 projects are scheduled as pool observations at the 30m telescope. Compared to assigning projects to fixed blocks of time, this significantly increases the flexibility of NIKA2 observations with the source availability and different demands on weather quality. During the observations, most of the NIKA2 observing scans are on-the-fly (OTF) raster scans, which consist of a series of scans at two orthogonal directions, mostly in altitude-azimuth or right ascension-declination. These observations could be carried out at the observatory on Pico de Veleta in Granada, Spain, or remotely through internet connections. In total, I participated in 32 days of pool observations with NIKA2.

The observation campaign over a whole day consists of three or four shifts, with different groups of observers taking the control of the telescope commands. The observatory provides facilities for observers to plan their observations and monitor the observing conditions. A quick look reduction script based on PIIC, the IRAM official data reduction pipeline for NIKA2, keeps refreshing the database and reducing the calibration and scientific observations. It also presents the maps and, if the scan is identified as pointing or focus calibrations (see descriptions below), the automatic measurements on calibrator position and shape. An example could be found in Fig. 2.3. The observers can also choose to use the similar quick reduction pipeline written in IDL to make similar measurements by manually launching the script. The observer should also frequently monitor the weather conditions through the tau meter at the observatory, which gives the real-time atmospheric opacity at 225 GHz (τ_{225}). For N2CLS observation, the satisfactory condition should have τ_{225} below 0.2, while slightly higher but stable opacity at 0.2-0.3 is still acceptable. The observatory also provides XEphem, the software that records the information of project targets and calibrators, and tracks the position of astronomical sources and telescope pointing in the sky.

The complete pool observations consist of five major parts that are required to be carried out. Apart from the science observations, the rest four parts include the focus scans, pointing scans, beam map scans, and skydips, which are all required for proper scanning, map reconstruction, and flux measurements.

`Focus`: The observation of each pool normally starts with a group of short focusing scans. This procedure consists in performing a series of five successive one-minute raster scans of a bright point source (above a few Jy) at five axial offsets of the secondary mirror (M2) along the optical axis. Possible sources for focusing can be found in the XEphem. As the scan size is 1'×5', the main contribution to each map mainly comes from the KIDs located in the central part of the FOV. Elliptical Gaussian fits on the five maps provide estimates of the flux and FWHM along minor and major axes for each focus. The best axial focus in the central part of the array is then estimated as the maximum of the flux or the minimum of the FWHM using parabolic fits of the five

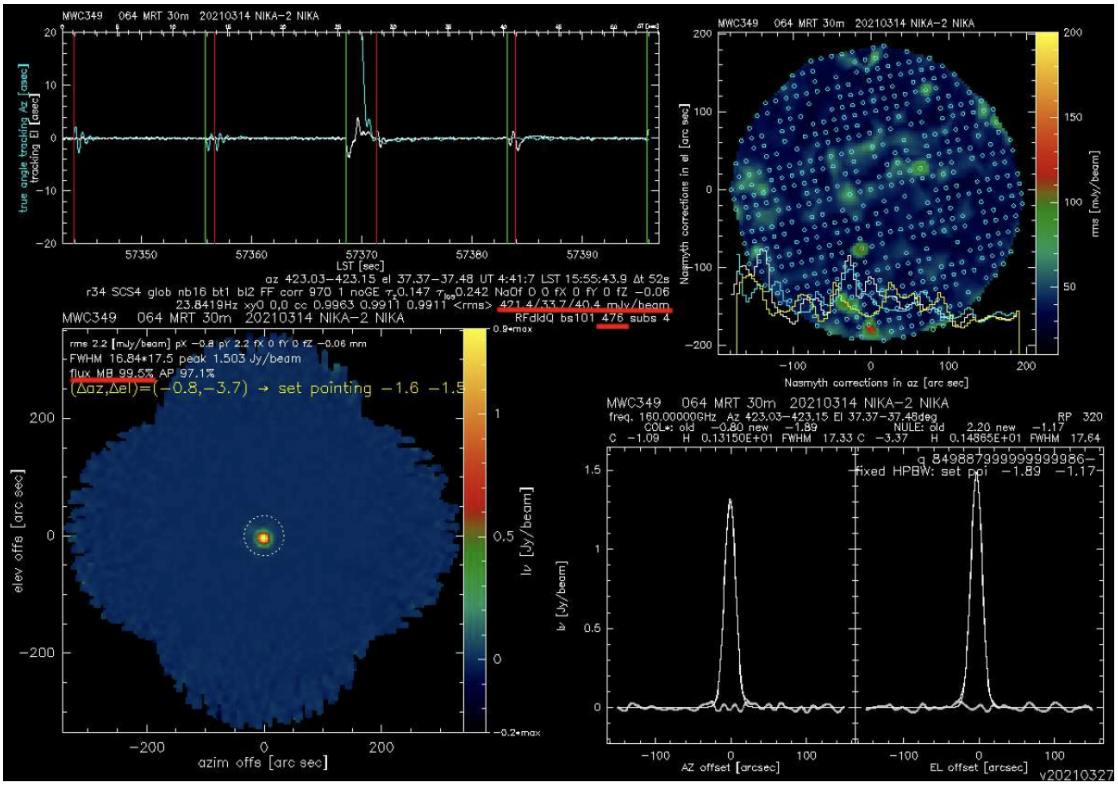

Figure 2.3 – An example of the output of quick look reduction on a pointing scan on MWC349 on the PIIC monitor. The pointing offsets in both direction in arc-seconds and the source size could be found from the text in the reduced image in the bottom-left of the panel.

measurements. With the dense sampling of the NIKA2 FOV, it is possible to map a source in such a short integration time and measure its shape variation at different M2 positions. As shown by Perotto et al. (2020), the focus surface of the full system is not flat across the full FOV but slightly bowl-shaped. Thus, a -0.2 mm offset relative to the best axial focus in the central part of the array is added in the tuning of telescope focus in practice to optimize the average focus across the FOV.

During the pool observations, the axial focus offsets are measured every hour during the daytime and are systematically checked after sunrises and sunsets to account for the deformation of the system due to sunlight and temperature changes. During the night normally with a more stable atmosphere and temperature, the focus is checked every two or three hours.

`Pointing:` Once the instrument is correctly focused, or the science observation on one project is about to start, the observers of the pool shift will need to estimate pointing corrections. The pointing of the 30m telescope is carried out by a group of cross-type scans on point sources. During the pointing observation, the telescope executes a back-and-forth scan in azimuth and a back-and-forth scan in elevation, both of which are centered on the observed source. After taking the pointing scans, the real-time reduction procedures fit Gaussian profiles from the timelines of the reference detector, which is chosen as a valid detector located close to the center of Array 2, to derive the current pointing offsets. The target sources of pointing scans should also be bright point-like sources to the 30m telescope. These sources are usually radio sources more suitable to observe at 150 GHz by NIKA2, which leads to our choice of a valid detector Array 2 as the reference.

For these pointing sources, we have less strict requirements on the brightness than the focusing sources, as they will only be observed at or close to the focus. However, it is much more favorable to find a pointing source close to the upcoming science target with similar elevations at the time to increase the accuracy of offset determination. The pointing offset returned by the real-time reduction is given in arc-seconds in azimuth and elevation. After recording them to the observing system, this correction is propagated to the following scans. The pointing is recommended to be monitored on an hourly basis.

`Beammap:` A beammap scan is a raster scan in azimuth-elevation coordinates mapping a bright compact source, in most cases, a planet. The sources in beammap scans are observed with steps of 4.8", which are small enough to ensure a half-beam sampling for each KID. In the beammap observation, the target source is scanned over a series of 13arcmin×7.8arcmin sub-scans with the telescope continuous slews at either fixed elevation or fixed azimuth.

The beammap observations are designed to determine the beam shape and KIDs positions of NIKA2 observations. The designed fixed-elevation scanning in beammap observations has the advantage of suppressing the air-mass variation across a sub-scan, while the fixed-azimuth scanning offers an orthogonal scan direction to the former: the combination of both gives a more accurate estimate of the side lobes.

With the large scan size, the map from each KID out to the edges of the array could be produced, and it also allows for properly correlated noise subtraction. During sub-scans, the telescope moves at 65 arcsec/s . Under the NIKA2 nominal acquisition rate of 23.8 Hz, this satisfies the threshold of high-fidelity sampling of the 11" beams of Array 1/3 observation along the scan direction, which requires a minimum of 2.7 samples per beam. Each sub-scans in the beammap observations last 12 s, and the entire scan lasts about 25 min.

Beammaps provide the key scans in NIKA2 observations, which is used in multiple steps of data reduction, including KIDS relative positions and relative photometric calibration. During the NIKA2 pool observations, beammap scans are normally performed once or twice per day.

`Skydip:` A skydip scan consists of a step-by-step sky scan along a large range of elevations. In NIKA2 observations, the skydip includes 11 steps in the elevation range from 19^o to 65^o, which are regularly spaced in air mass. Twenty seconds of data are acquired at each step to ensure a precise measurement. The KIDs are tuned at the beginning of each constant elevation sub-scan. During the scan, the KIDs are used as total power detectors to estimate the emission of the atmosphere and thus, the opacity of the atmosphere at the time of observation. Therefore, NIKA2 skydips serve to calibrate the KID responses with respect to the atmospheric background for atmospheric opacity derivation. Skydips are typically performed every eight hours, or normally once per shift, to cover a wide range of atmospheric conditions during an observation campaign.

2.4 NIKA2 Data Reduction

During the observation of sources, the detectors in the NIKA2 KIDs array scans across the sky and records the signal with various origin over time. These signals include the celestial emission with the astrophysical origin and the background emission dominated by the atmosphere, which varies with time and telescope pointing. From the KIDs raw data, a time series of quantities proportional to the KID frequency shift are computed, following the principles described in Perotto et al. (2020). These data collected by the observation of each KID constitute the KID time-ordered information (TOI), which will be further calibrated and reduced by the NIKA2 data reduction pipeline.

2.4.1 NIKA2 Data Calibration and Map Reconstruction with PIIC

In this thesis, the N2CLS observations are calibrated and reduced with PIIC, the official IRAM data reduction pipeline for NIKA2 [1] (Zylka, 2013). Our analysis is based

1. https://www.iram.fr/ gildas/dist/piic.pdf

on the may-21 version of PIIC, which contains all the calibration information for the observations we reduce. Each distribution of PIIC contains a calibration database (called DAFs) with calibration files to be used in data reduction. These files are produced for each NIKA2 pool by the supporting team. It contains five different main types of files: calibration files (CAL) defining the response of KIDs for flux calibration, deleted receiver pixels (DRP) files listing those KIDs that are known to be defective, frequency files (NKFR) listing the natural resonance frequencies of all KIDs, receiver pixels parameters (RPP) listing the position of each KID in the field of view of NIKA2 for different sweeps, and atmospheric conditions overall observing runs (TAU files) containing the values of the atmospheric opacity produced by the observatory's tau meter. We also note that only the calibration files for observations after October 2017 are publicly available. As a result, the data reduction of NIKA2 SV observation on HLS J0918+5142 was carried out by the IRAM team and the resulting maps are analyzed following slightly different procedures compared to the N2CLS reduction described in the following text. Details could be found in Chapter 4.

The data reduction by PIIC could be carried out following the procedures and commands provided in a template data reduction script associated with each distribution. There are minor differences between the PIIC data reduction of observations on different source types with the script, and we will only touch on the details about the reduction of deep field survey data like N2CLS.

The goal of PIIC data reduction is to extract astrophysical signals from the sky signal and its low-frequency noise, as well as the instrumental instabilities in the timeline data. The initiation of the PIIC data reduction after loading the scans list assigns sky positions to each KID, performs main-beam flat-fielding, and excludes known problematic KIDs from the scans.

After this initiation, the PIIC goes into an iterative process to extract faint source signals from the timeline data. The 0th iteration in PIIC starts with no prior information on source positions at the beginning, which is only recorded after the end of the 0th iteration on sources above a certain SNR threshold. The source position will be updated and propagated to the following iterations, where masks are generated to protect the source signal in the operations of fitting and baseline subtraction.

The first step of each iteration is to transform the KIDs signal into flux density and calibrate it to physical units of mJy/beam from Hz, which initially records the resonant frequency of KID illuminated by the incoming emission. After a further flat fielding on sky-noise, the PIIC data reduction software computes the correlation coefficient of each KID to all others and derives the r.m.s of the signal from each KIDs along the timeline. The KIDs with bad correlation statistics and the highest noise levels are rejected. Then the pipeline subtracts sky noise from the signals from the pre-defined number of best-correlated KIDs, with the data from the position of masked sources ignored. This step is followed by a baseline correction on each timeline to remove instabilities

that could not be dealt with during sky-noise subtraction. After the application of extinction correction, PIIC distributes the signal of all KIDs onto the final pixel grid, using the appropriate kernel linking the NIKA2 PSF and KIDs size to the grid, which finalizes one iteration. The sources in the map of the current iteration are identified, and the positions of pixels above a given threshold are used to generate/update the mask applied to the following iterations.

To reduce the N2CLS observations and generate proper deep field maps for further analysis, a few parameters in the script are needed to be adjusted. The parameter values applied in the data reduction of this thesis are listed Table. 2.1. The parameter deepField clarifies if the data to be reduced is a blind survey of the blank field with only faint sources. In our case, it is set to "yes", and the pipeline will not request for a pre-defined source polygon mask, and baselines are computed over the whole area with sources included. The activation of deepField also automatically propagates weakSou to yes, making the pipeline optimized for the recovery and detection of sources invisible in single scans. As we do not aim to observe negative signals like the SZ effect from galaxy clusters, the parameter souSign is set to "+". The parameter nIterModel set the number of iterative loops for recovering the source signal. For the reduction of observations on faint point-like sources like in N2CLS, the practice of the PIIC developing team suggests that the recovered source flux could converge after about 3 iterations. Thus we conservatively set this value to 5 for both fields. The snrLevel determines the S/N threshold above which pixel positions in the map products are selected to create the source mask in further iterations on the timeline data. The last parameter in the table is directly related to the production of survey maps, with blOrderOrig, defining the order of polynomial function to fit the baseline of each sub-scan in the baseline correction. To have proper fits and produce map products with smooth backgrounds, we apply a larger value of blOrderOrig=17 to the COSMOS field with a large survey area and a smaller value of blOrderOrig=10 to the reduction on GOODS-N with smaller sizes. The final products of the data reduction consist of 2 crucial maps for our further analysis. These include a signal map that stores the fluxes in the surveyed area recovered from the PIIC iterative data reduction, as well as a weight map storing the inverse variance across the surveyed area. The last parameter in the table, wrIndMaps, is related to the production of half-difference maps, which will be introduced separately in Sect. 2.4.3.

Due to the strong instabilities, bad weather and failure of the files themselves, some of the scans could not be properly calibrated and reduced by the pipeline. These scans are either automatically filtered by the default setups on the noise level in the data reduction script, or produce fatal errors in the data reduction, which are later removed manually from the scan list. For the observations used in the thesis, we obtain 390 scans on COSMOS field and 760 scans on GOODS-N field from each array, and the total number of scans for each field and each band are listed in Table. 2.2. The number of 1.2mm scans includes those coming from array 1 and 3, thus the total number is twice of the number of 2.0mm scans. Following the criteria described above, we

Parameter Name	Value
deepField	yes
weakSou	yes
souSign	+
nIterModel	5
snrLevel	4
blOrderOrig	17(COSMOS),10(GOODS-N)
wrIndMaps	yes

Table 2.1 – Summary on the setup of parameters used in the PIIC data reduction on N2CLS observations in GOODS-N and COSMOS.

generate the list of proper scans to be passed in the data reduction.

In Table. 2.2 we summarize the total time of observed scans and those kept in the reduction, as well as the average τ_{225} during their observation, in comparison with the complete scan list and the rejected scan list. For each field, we have a small fraction of lose of observing time at 14% on average, and the scan selection mostly rejects data taken at conditions worse than average. In this case, we conclude that N2CLS follows an efficient strategy of deep field observation during its operation.

Field	Band	$N_{\rm total}$	$N_{\rm keep}$	$t_{\rm total}$	$t_{\rm keep}$	$\tau_{225,\rm total}$	$\tau_{225,\rm keep}$	$\tau_{225,\rm rej}$
COSMOS	1.2 mm	780	700	87.2	78.7	0.20	0.19	0.25
COSMOS	2 mm	390	351	87.2	79.0	0.20	0.19	0.26
GOODS-N	1.2 mm	1520	1281	92.2	78.0	0.20	0.20	0.24
GOODS-N	2 mm	760	599	92.2	72.8	0.20	0.20	0.23

Table 2.2 – Summary on the scan numbers, scan times of all N2CLS scans and properly reduced scans, as well as the 225 GHz atmospheric opacities (τ_{225}) of all, reduced and rejected scans in each field and band.

2.4.2 Source Extraction and the Effects To Be Corrected

In the N2CLS survey, we follow the general strategy of other blind surveys to make source detection on the maps. The signal and noise maps from each field and band are first convolved by a Gaussian kernel to obtain the beam match-filtered signals. The kernels have their full-width half maximums (FWHMs) equal to the beam size of the corresponding band and the peak values of unity, which preserves the value in the match-filtered map equivalent to a measurement on the point-source flux at the position of each pixel. Then, we divide the match-filtered signal maps with the

corresponding match-filtered noise maps to obtain the match-filtered S/N maps. The match-filtered noise maps are derived according to the sqrt of noise square during the matching filter process. The source detection of each map is made on the match-filtered S/N maps afterwards, using a fixed threshold in S/N which is different for each map. The source fluxes are also measured by fitting 2D Gaussian functions at the position of detection.

This source detection and flux measurement framework, however, is also known to have several issues and biases in the recovery and flux measurements, which are subject to corrections in the statistical studies on source properties.

`Purity corrections:` In the source extraction, we use a fixed S/N threshold to determine if a certain peak in the match-filtered S/N map is considered to be a source. However, this could not distinguish noise peaks with S/N above the threshold from the real sources, making the selected sources unavoidably contaminated by spurious sources. The source purity is thus defined as the fraction of true sources from the detection. Under the assumption of Gaussian noise, the purity of detection is estimated in bins of S/N, where we expect 100% purity at high S/N and a lower purity with the decrease of S/N The estimate of purity of detection versus S/N will not only correct for the contamination of spurious sources in the statistical analysis with the sample from blind detection, but also help setup the S/N threshold for studies with different levels of purity. A detailed follow-up study may request a sample above a certain S/N corresponding to a high purity of 95% to minimize the time loss due to false detections. For the statistical analysis on number counts in this work we only request a sample above a given S/N corresponding to high purity of 80%.

`Completeness corrections:` As described previously, the blind source detection in practice is made on N2CLS maps consisting of both source signal and noise. For sources of fixed flux added in a map with uniform Gaussian noise, their S/N of detection and measured flux at the input position is expected to be positively or negatively affected, which is illustrated in Fig. 2.4. With a fixed S/N threshold of detection, we will inevitably encounter situations that a fraction of faint source close to the S/N threshold fall into valleys in the noise-only maps, making them having biased low S/N in our measurements and remain undetected in the map. The statistical analysis with faint sources is affected by this loss, and the real number of faint sources is also subject to a correction on this incomplete detection. Under a Gaussian noise assumption, the impact of noise valley on source detection is affected by the true flux of sources, the local noise level around their position and the S/N threshold of source detection. As the source is firstly determined by the requirement on purity, we only account for the other two quantities in the analysis and corrections of completeness. The details of our analysis for N2CLS data are presented in Chapter 3.

`Flux corrections:` Apart from the spurious source and incompleteness, the noise and the data reduction algorithm could also add distortions to the measured

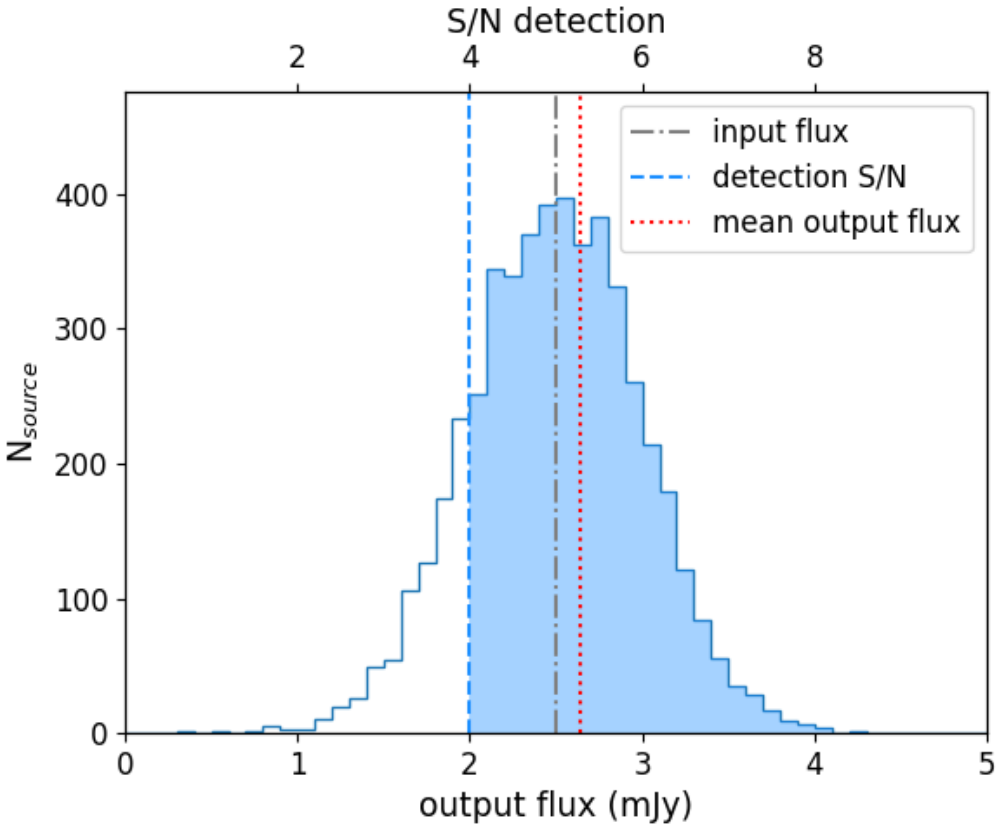

Figure 2.4 – An illustration of the origin of incompleteness and flux boosting using a detection with fixed S/N threshold. The histogram shows the distribution of the measured flux S_{out} of sources with fixed intrinsic flux at S_0 randomly added to N2CLS half-difference maps with a uniform Gaussian noise at σ_0. The x-axis on the top shows the corresponding S/N of sources measured on the half-difference maps. The dash-dotted line shows the intrinsic flux of the added sources. The dashed vertical line shows the detection threshold. Sources with measured S/N lower than this threshold are considered as undetected and could not be considered in the study. The dotted line marks the average flux of detected sources which is higher than the intrinsic flux, illustrating how the detection with fixed threshold is affected by flux boosting.

source fluxes from two different aspects. As described in the origin of incompleteness, for a given set of sources of same flux in an uniform map, the measured-at-peak method of source detection and flux estimate could be biased to the sources on the positive noise peaks. Despite of the incompleteness, this also makes the average flux of detected sources biased high compared to their input flux, as illustrated in Fig. 2.4. Apart from this "bias-to-peak" effect, the higher density of faint sources also causes the well-known Eddington bias, which not only overestimates the number of rarer bright sources from raw number counts, but also in turn contributes to this flux boosting effect. The combination of these two effects is usually called as flux boosting in literature (Geach et al., 2017). In addition to the flux boosting, the data reduction of NIKA2 data requires several fit on the global and local variations of TOI from each KIDs to subtract the contribution of sky noise and correct the instability. This, although with source masks defined during the iterative process, have an uncertain impact on the source flux recovery, especially when the source confusion starts to be non-negligible in the deep GOODS-N observations. Besides, for the relative low resolution single-dish observations, the blending of sources at sight line close to each other, either due to the clustering or coincidence, could also bring additional boosting of the measured flux (Béthermin et al., 2017).

2.4.3 PIIC Simulations

In previous studies, the contamination of spurious sources, the incompleteness of detection, and the flux boosting described above are quantitatively accounted for through randomly injecting sources on noise maps. The noise maps are generated using half-difference methods, which are produced by randomly inverting the fluxes from half of the individual scans in the data reduction. Through these operations, the source signals from individual scans are canceled out, while the noise features are still preserved. By randomly injecting sources on thousands of half-difference maps following reasonable flux distributions, these studies estimate the purity, completeness, and flux boosting due to the noise features in the map and correct for the source flux and source number counts measurements.

In the ordinary data reduction of NIKA2 observations, the setup in Table 2.1 only produces the signal and weight maps with all of the reduced data cumulated. To obtain the signal of individual scans, we further activate the parameter in wrIndMaps to 'yes' during the data reduction. This allows us to save cumulative signal and weight maps following the order of the scan list. With these additional data products, we could derive the signal map from individual scans for the production of half-difference maps in our study, following Eq. 2.2:

$$S(i) = \frac{C(i) - C(i-1)}{W(i) - W(i-1)} \tag{2.2}$$

where S(i), C(i) and W(i) correspond to the individual scan map from the i-th scan, as

well as the cumulative signal and weight up to i-th scans in the reduced scan list. For each simulation, additional randomization on the order of the scan list is also made to ensure the production half-difference maps is fully randomized.

However, as shown by our discussion in Sect. 2.4.2, the impact of source flux recovery by the pipeline, as well as the source clustering and blending, could not be accounted for by the half-difference simulation framework in the literature alone. In the PIIC pipeline, a simulation feature has been introduced since the release of may-21 version. It allows a model of sources to be injected into the half-difference timeline and passed through the complete data reduction procedure after the calibration. The injected source models are required to be produced under the same beam size of NIKA2 observation and should be given in fits format with world coordinate system (WCS) information and pixel value units of mJy/beam. During the simulation process, the source models are subject to the same kind of distortion by the pipeline, beam, and noise as the real observations. Thus, the impact of these effects on source detection and flux measurements could be more completely estimated and self-consistently accounted for in our analysis of source flux and number counts.

To apply the simulations in practice, we set the key parameters, addSource, and nullMap, to 'yes' and produce the path to the deep field sky model to the script. The deep field sky model in our work comes from the SIDES models based on Uchuu dark matter simulation described by Gkogkou et al. (2022). This work generate sky models at the two NIKA2 bands over 117 blocks of 1 deg^2 light cones, producing the adequate size of maps and number of sources to empirically correct for the biases in NIKA2 source detection and flux measurements. For each dark-matter halo, galaxy properties are generated following scaling relations measured empirically. The 1.2 mm and 2 mm NIKA2 fluxes are then derived by convolving the SED templates by the NIKA2 transmission curve, and maps are produced based on the fluxes and the positions. With these setups and the original scan list, the PIIC pipeline produces simulated observations on the model sky. As the positions of sources are assigned based on light cones of dark matter simulations, the sky model naturally includes the clustering and is generally in good agreement with CIB anisotropies, redshift distribution, luminosity function, and number counts.

Before being injected into the timeline, the original model map of 2" pixel sizes are first smoothed to the resolution of NIKA2 observation at the corresponding wavelength, as required by the PIIC simulation described above. With these models and processing procedures, we obtain simulated sky maps with realistic galaxy clustering between sources, which is not accounted for in the techniques used in most of the previous studies. A total of 117 independent tiles of 1 deg^2 are used to produce the input sky model at 1.2 mm and 2 mm simulating the GOODS-N and COSMOS fields, which later produce 117 independent simulated N2CLS observations at the two wavelengths on the two fields. A comparison between the input model and output simulated observations by the framework can be found in Fig. 2.5.

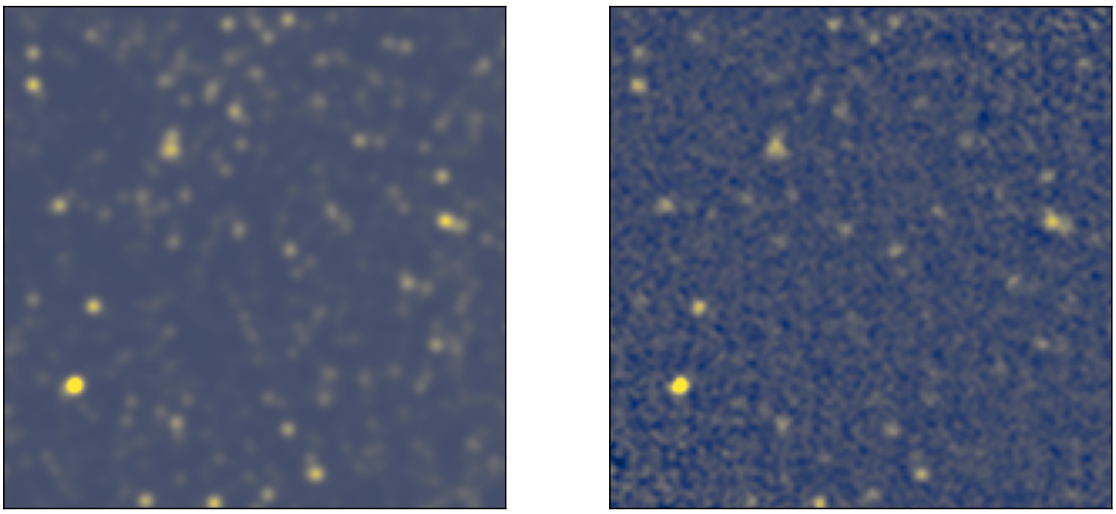

Figure 2.5 – An Example of a sky model based on SIDES and Uchuu simulation injected into the half-differenced timeline for the PIIC simulation (left) and the output PIIC map from the corresponding simulation after 5 iterations (right). This example of simulation is made for the GOODS-N field. The output map is produced using the same data reduction parameters applied to N2CLS GOODS-N observations, as shown in Table 2.1.

From the 117 input sky models for each field and band, we also obtain two sets of catalogs. The "galaxy catalogs" record the fluxes assigned to each simulated galaxy, no matter if they are blended or not with close-by galaxies in the NIKA2 beam. From the noiseless beam match-filtered model map, we also identify all peaks above a certain peak flux and record their position and peak fluxes in the "blob catalogs". The peak flux thresholds are set to 0.15/0.05 mJy for GOODS-N and 0.45/0.15 mJy for COSMOS for input maps of simulation at 1.2/2 mm. The resulting catalogs extracted from noiseless maps are thus much deeper than the real NIKA2 ones. In the analysis of completeness, purity, and flux correction, we will use the input "blob catalog" as the reference, which is subject to the same source blending at the same NIKA2 angular resolution. The galaxy catalogs will be used to correct the impact of source blending itself on the number counts. Details on the further operations to make consistent detection and analysis of the observation and simulations can be found in the next chapter.

3 Millimeter Number Counts from NIKA2 Cosmological Legacy Survey

Sommaire

3.1 Introduction . . . 90
3.2 Survey Map, Source Extraction and Statistical Corrections . . . 92
3.2.1 Deepfield Maps from N2CLS . . . 92
3.2.2 Method of Source Extraction and Photometry . . . 95
3.2.3 Statistical Corrections and Analysis . . . 98
3.2.3.1 Spurious Sources and Purity . . . 98
3.2.3.2 Effective Flux Boosting . . . 99
3.2.3.3 Completeness . . . 102
3.2.3.4 Effective Survey Area . . . 103
3.2.4 Flux Corrrection . . . 104
3.3 Source and Galaxy Number Counts . . . 105
3.3.1 Number Counts Estimation . . . 105
3.3.2 Validation of the number counts reconstruction from simulations 106
3.3.3 1.2 and 2 mm Number Counts . . . 108
3.3.4 Comparison with Models . . . 113
3.4 Discussion . . . 114
3.5 Summary . . . 117

3.1 Introduction

Blind far-IR to millimeter observations have dramatically improved our understanding of the massive dusty galaxies in the early Universe. It became one of the fundamental means of searching and studying the high-z dusty galaxies since the start of ground-based (sub)millimeter observations (Barger et al., 1998; Ivison et al., 2007; Hodge et al., 2013; Simpson et al., 2020; Dudzevičiūtė et al., 2020). Compared to targeted follow-up observations on pre-selected samples, the dusty galaxy samples from blind far-IR to (sub)millimeter surveys that come from continuous sky areas are much less affected by a complex selection function. These advantages make blind far-IR to millimeter observations most unbiased in statistical studies on massive and(or) dust-obscured star-forming systems at high redshift. These sources are believed to

be the progenitors of massive quiescent galaxies in dense environments that later emerged at lower redshift (Toft et al., 2014; Spilker et al., 2019; Valentino et al., 2020; Gómez-Guijarro et al., 2022b), and the study on the early phase of their formation and evolution provide crucial tests on the theory of galaxy and structure formation and evolution (Liang et al., 2018; Lovell et al., 2021; Hayward et al., 2021).

The negative k-correction lead to almost unevolved (sub)millimeter fluxes of dusty galaxies of fixed IR luminosity at redshift above 1. This could make both low and high redshift dusty galaxies uniformly probed by blind millimeter surveys of certain depths (Casey et al., 2014b). From the blind surveys alone, studies could directly make measurements on the source number counts, which describe the variation of the number density of sources with the source fluxes at given wavelengths. With limited information on individual sources, the number counts still provide constraints on the integrated number density of sources of different flux across the cosmic time and the selection function is relatively simple to be accounted for in the analysis. However, although semi-analytic models with simplified assumptions could have successful predictions on the source number counts, hydrodynamical simulations have been struggling in reproducing this simple observable a few years ago (Hayward et al., 2013; McAlpine et al., 2019) and still shows tension with observation within certain flux ranges in most recent works (Lovell et al., 2021; Hayward et al., 2021). This indicates detailed studies on the smaller scale physics, including the geometry of dust and stars, the burstiness of star formation, as well as the initial mass function in (sub)millimeter bright dusty galaxies, are still highly essential in understanding the formation and evolution of high-z dusty galaxies (Hodge and da Cunha, 2020; Popping et al., 2020)

Due to the limitation of sensitivity or field of view, it is difficult for one blind survey alone to detect a statistically large sample of (sub)millimeter sources over a wide range of fluxes and make a complete measurement of the number counts. In practice, the measurement on the number counts of bright millimeter sources above a few mJy at 1.2 mm are dominantly contributed by single-dish observations (e.g. Lindner et al., 2011; Scott et al., 2012). On the contrary, ALMA brings most of the constraints on faint end number counts at the sub-mJy regime, where single-dish surveys start to be limited by their sensitivity and source confusion (e.g. Fujimoto et al., 2016; González-López et al., 2020; Gómez-Guijarro et al., 2022a). Most of the previous studies directly combine the two different classes of observations in the interpretation, fitting, and model comparison. However, it has also been known for years that fluxes from single-dish and interferometers do not provide completely equivalent flux measurements. The high resolution of interferometers makes the fluxes of detected sources almost strictly contributed by individual galaxies, while the large beam of single-dish observations could introduce additional contribution from close-by faint galaxies to the measured fluxes on the brightest "isolated" galaxy in the beam (Béthermin et al., 2017). Previous studies lack realistic estimation based on real data from blind surveys. The impact source clustering and blending in single dish number counts measurements and comparison with interferometric number counts are seldom considered.

In this chapter, we will present the new 1.2 and 2 mm number counts measurement based on the tiered N2CLS observations over >1000 arcmin^2 in GOODS-N and COSMOS. Our measurements cover an unprecedentedly wide range of source fluxes from one single-dish instrument and consider the impact of the beam in number counts measurements for the first time. Sect. 3.2 will present the reduced N2CLS map, the method of source extraction and photometry, and the framework of correcting bias in source detection and flux measurement due to noise, pipeline, and large beam. Sect. 3.3 will present the source catalog, as well as the 1.2/2.0mm source number counts measurements based on the catalog and corrections on biases due to noise and pipeline. Sect. 3.3 will also present the galaxy number counts after additional correction on the effect of the large beam, as well as a direct comparison with predictions of semi-analytic models. The discussion on the results and conclusion will be presented in Sect. 3.4 and Sect. 3.5.

3.2 Survey Map, Source Extraction and Statistical Corrections

3.2.1 Deepfield Maps from N2CLS

Following the data calibration and reduction procedures and setups by PIIC in Chapter 2, we obtain the 1.2 and 2 mm maps of GOODS-N and COSMOS fields from the N2CLS observations. In Fig. 3.1 and Fig. 3.2, we show the 1.2 and 2 mm signal-to-noise ratio (S/N) maps of the N2CLS survey in GOODS-N and COSMOS match-filtered by the beam in the corresponding band. The instrumental noise maps are also generated from the weight maps produced along with the signal maps, and are also presented in Fig. 3.1 and Fig. 3.2 for 1.2 and 2 mm observations, respectively. Our study on the number counts is restricted to the high-quality regions with low instrumental noise delimited by the red lines in Fig. 3.1 and Fig. 3.2, which exclude the noisy edges of the map that could introduce artifacts to the number counts during the corrections in Sect. 3.2.3. These regions are defined as having an instrumental noise (σ_{inst}) smaller than 3 and 1.6 times the minimal value at the center of the GOODS-N and COSMOS field, respectively.

The high-quality regions used in our analysis, as enclosed by the red contours in Fig. 3.1 and Fig. 3.2 , cover 159 arcmin^2 and 1010 arcmin^2 in GOODS-N and COSMOS, respectively. In Fig. 3.3, we present the distribution of the pixel values of the S/N map within the high-quality region of each field and each band. The S/N histograms of all fields and bands reveal tails of high S/N pixels, which indicates that sources are detected by the N2CLS survey. In Table 3.1, we provide the noise level in the high-quality regions of maps for each field and band after removing the pixels with S/N>5 or S/N<-5.

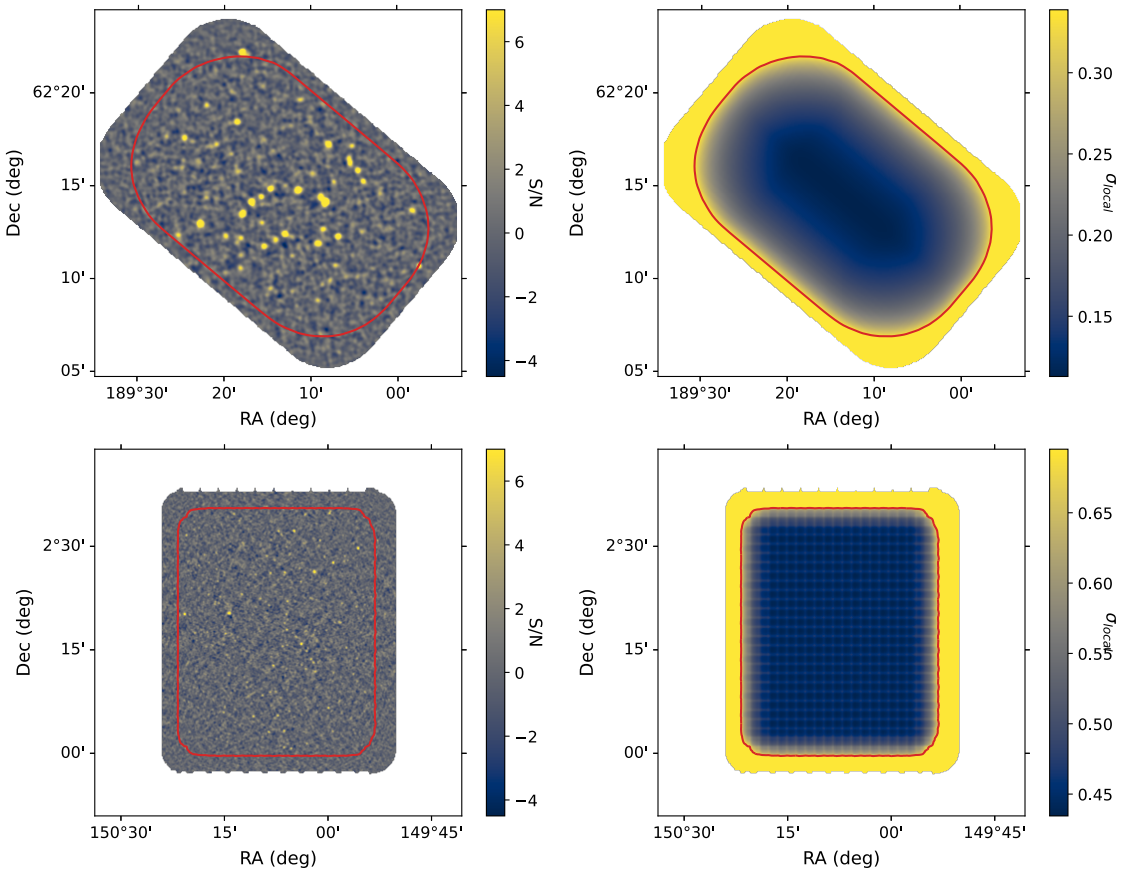

Figure 3.1 – Signal-to-noise ratio (left panels) and instrumental noise (σ_{inst} in mJy, right panels) maps of the 1.2 mm N2CLS maps of the GOODS-N (upper panels) and COSMOS (lower panels) fields. The S/N maps are match filtered by the Gaussian beam at the corresponding wavelength. The regions enclosed in the red contours have a sufficient S/N to be analyzed by our source detection algorithm, and our catalogs and number counts are derived only in these areas (see Sect. 3.3.3).

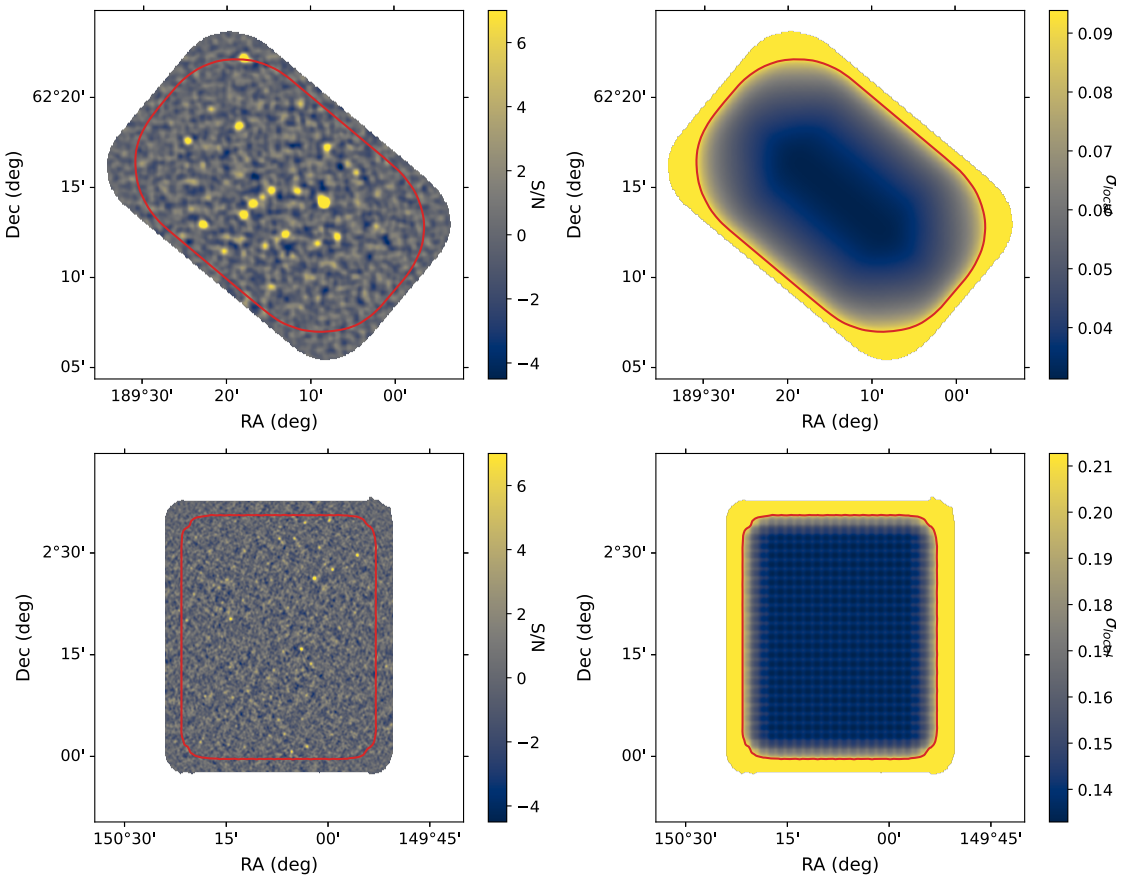

Figure 3.2 – Same as Fig. 3.1 but at 2 mm.

In Table.3.1, we list the depth of N2CLS surveys and other single-dish surveys (in RMS) in the GOODS-N or COSMOS field at similar wavelengths. To compare the noise level with surveys at different wavelengths than the N2CLS, we rescale the depth of other surveys assuming a far-IR SED template of typical star-forming galaxies at z~3 (Béthermin et al., 2015). In GOODS-N, N2CLS is already surpassing the depth of any other single-dish millimeter surveys (AzTEC (Perera et al., 2008), MAMBO (Greve et al., 2008) and GISMO (Staguhn et al., 2014)). It currently matches the deepest submillimeter survey by SCUBA2 at 850 μm (Cowie et al., 2017). As for COSMOS, N2CLS is about twice deeper than AzTEC (Aretxaga et al., 2011) and MAMBO (Bertoldi et al., 2007) at 1.1/1.2 mm, respectively, and being slightly deeper than GISMO at 2 mm (Magnelli et al., 2019). It is still slightly shallower than S2COSMOS (Simpson et al., 2019) at 850 μm, while the remaining observations in the COSMOS field are expected to make the final depth comparable to S2COSMOS.

To obtain realistic realizations of the instrumental noise, we generate half-difference maps from the original scans by reverting half of the individual scans generated from the procedures described in Sect. 2.4.3. This process removes the astrophysical signal and preserves the instrumental noise properties if the noise is symmetric. The PIIC software does not produce the individual scan maps and their associated weights. However, they can be recovered from the cumulative signal and weight maps, which are produced and saved each time a new scan is processed. The individual scan maps can be recovered using Eq. 2.2. The distribution of S/N in half-difference maps is shown in Fig. 3.3 along with its best fit by a normal distribution. The S/N values in the N2CLS data and half-difference maps are normalized and corrected for any global offsets, following the procedures described in Sect. 3.2.2. The fit on the distribution from half-difference maps are excellent with reduced χ^2 around 1. This demonstrates that the noise is Gaussian.

3.2.2 Method of Source Extraction and Photometry

The source detection of N2CLS survey is made on the match-filtered PIIC map produced by the dedicated python package "nikamap". For the match-filter, the kernels are fixed to circular 2D Gaussian with a FWHM equal to the corresponding beam sizes. An histogram of S/N in each 3"/4" pixel for 1.2/2 mm maps is generated after the match-filtering, and we perform a Gaussian fitting on the histogram values between -3 and 1.5. The cut of fitting range on the positive S/N side avoid strong contamination by the true detections, which could overestimate the noise. The best-fit parameters provides the global offset of background and the fluctuations of the pixel values, which are measured by the center ($\mu_{S/N}$) and the width ($\sigma_{S/N}$) of the best-fit Gaussian function to the S/N histogram. We further use the $\mu_{S/N}$ and $\sigma_{S/N}$ values to the noise and S/N maps to removing the background offset and renormalize the S/N used for source detection, following Eq. 3.1 and Eq. 3.2. The noise and S/N before

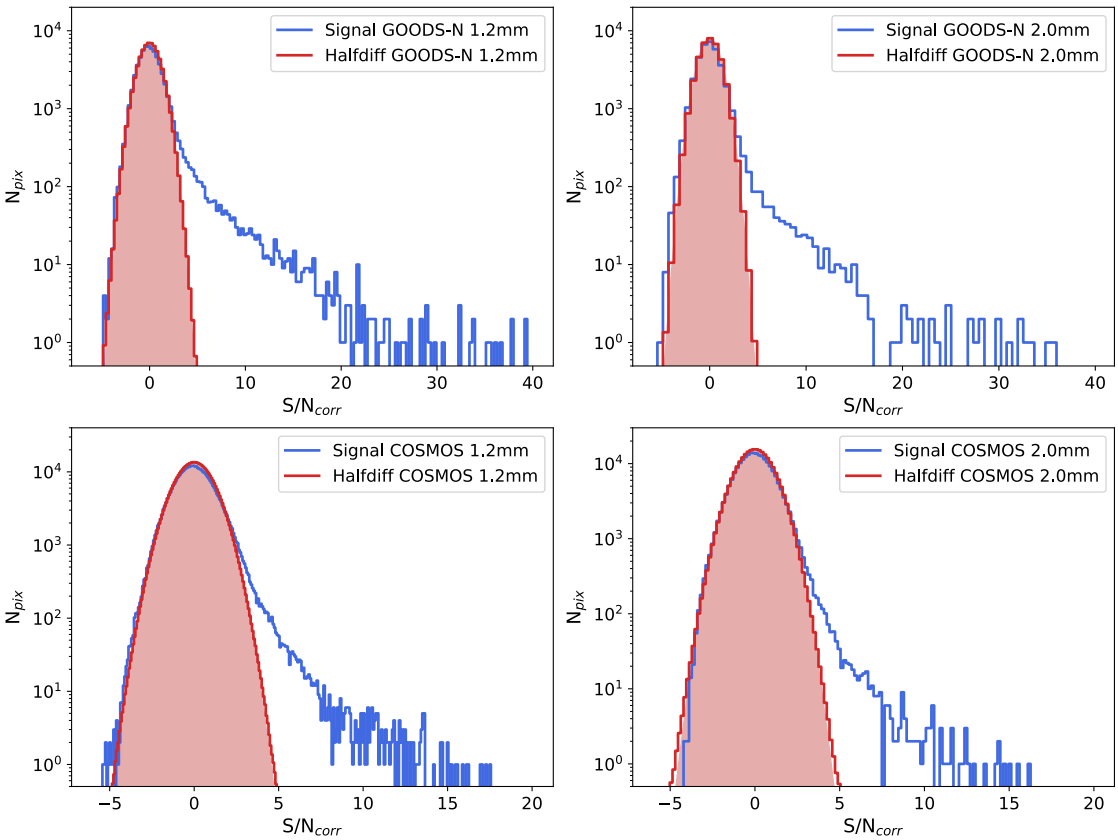

Figure 3.3 – Pixel S/N distribution within the high-quality regions in the 1.2 and 2 mm maps shown in Figs. 3.1 and 3.2, as well as the average distribution of pixel S/N in 100 randomly generated half-difference maps for each field and waveband. The red shaded region illustrates the best fit normal distribution on the average histograms of the half-difference maps.

Table 3.1 – Comparison of N2CLS-May21 depth to other single-dish (sub)mm surveys in GOODS-N and COSMOS. For each survey, the root mean square (RMS) noise is normalized to 1.2 or 2mm assuming the average IR SED of star-forming galaxies at z=3 (Béthermin et al., 2015).

Field	Survey	ν_{obs} (GHz)	Area (arcmin^2)	RMS (mJy/beam)
GOODS-N 0.85/1.2 mm	AzTEC	273	245	1.06
	SCUBA2	353	~140	~0.16
	N2CLS-May2021	255	160	0.19
GOODS-N 2 mm	GISMO	150	38	0.14
	N2CLS-May2021	150	160	0.057
COSMOS 0.85/1.2 mm	AzTEC-ASTE	273	2592	1.26
	MAMBO	255	400	1.00
	S2COSMOS	353	5760	~0.47
	N2CLS-May2021	255	1100	0.55
COSMOS 2 mm	GISMO	150	250	0.23
	N2CLS-May2021	150	1100	0.18

the correction are labeled by σ_{ori} and S/N$_{ori}$, and the corresponding quantities after correction are marked as σ_{corr} and S/N$_{corr}$.

$$\sigma_{corr} = \sigma_{ori} \times \sigma_{S/N} \tag{3.1}$$

$$S/N_{corr} = \frac{S/N_{ori} - \mu_{S/N}}{\sigma_{S/N}} \tag{3.2}$$

In absence of noise, a match-filtered S/N map of an isolated point source is maximal at the position of the source. The "nikamap" package incorporates the "find_peak" algorithm from the astropy photutils package (Bradley et al., 2022), which identifies peaks above certain threshold within every box of 5×5 pixels in the match-filtered S/N maps. The resulting pixel values in the match-filtered signal maps at the peak positions also measure the source fluxes (flux_peak). With the source position obtained, we then perform PSF-fitting photometry on the original PIIC map with the center fixed to the peak positions. During the photometry, the sources are first grouped by DAOGroup under photutils according to their positions and then fitted by BasicPSFPhotometry from photutils. The PSFs used in this process have the same FWHMs as the HPBW in the PIIC map at the corresponding wavelength. The median backgrounds of the full maps are estimated at first by MedianBackground under photutils and removed during the analysis.

For the source detection in the N2CLS observations, we further refine the choice of detection threshold in the both fields and both bands according to the purity analysis

presented in Sect. 3.2.3.1. We use the source fluxes from the PSF fitting in the following analysis, which provide more robust flux measurements on slightly blended sources than the peak flux. As for the flux uncertainties from the measurements, we provide the pixel value of the noise map after corrections in Eq. 3.1, which accounts for the correlations between nearby pixels.

3.2.3 Statistical Corrections and Analysis

As described by Sect. 2.4.2, the source detection and photometry in blind millimeter surveys by single-dish telescopes could be affected by several systematical effects and biases due to noise, pipeline, and the instrument. To obtain adequate source properties for further study on source number counts and follow-up observations, we need to quantitatively estimate the impact of source purity, completeness, and the bias in flux measurements, and apply the corresponding constraints and corrections to the exact procedure of source detection and raw measurements on the N2CLS maps.

The source extraction and photometry in the simulated maps from the PIIC simulation with the SIDES+Uchuu sky model follow the same methods we applied to the N2CLS observation to preserve the consistency between them. The source detection in the simulated maps is initially made with the S/N threshold at 2, which takes the best effort to cover the low S/N to quantify the evolution of purity. After fixing the detection thresholds of each map based on the purity analysis in Sect. 3.2.3.1, we perform the PSF photometry to the detected source in simulated maps above this S/N and use their photometry to compare with the input blob catalogs, the sources identified on beam match-filtered noiseless model maps (see Sect. 2.4.3), in the following analysis.

3.2.3.1 Spurious Sources and Purity

We first use the 117 simulated observations to determine the purity of sources detected at a given S/N on each field and each wavelength. The purity is measured, as a function of S/N, by the fraction of detections in the output map from the simulations that could be matched with the input blob catalog. The matching radii are set to be 0.75 times the FWHM of the Gaussian beam we used to match-filter the model, which is consistent with the distance threshold used in previous studies (Geach et al., 2017). This threshold of source cross-matching is also used in the estimation of source completeness (see Sect. 3.2.3.3), which ensures the two effects are consistently accounted for in the following estimate of source number counts.

We present the true detection rate, or purity, as a function of S/N in functional form from the spline fitting in Fig. 3.4. The spline fits are made using the "UnivaraiteSpline" interpolation module in scipy with the smoothing factor parameter set to 0.005 and

0.002 at 1.2 and 2 mm, respectively. In COSMOS, the purity at 1.2 and 2.0 mm reaches 80% at S/N=3.9 and S/N=3.8, respectively, and is >95% at S/N>4.6. In GOODS-N, as the observations are designed to approach the confusion limit, the higher source density at the faint end results in higher purity than COSMOS at fixed S/N. The purity reaches 80% at S/N=3.0 and S/N=2.9, at 1.2 and 2.0 mm respectively, and go up to >95% at S/N>4.2 and S/N>4.1. In the following analysis, we set the S/N threshold of sources to the S/N of 80% purity for the corresponding field and wavelength, which compromises the spurious source fraction and depth.

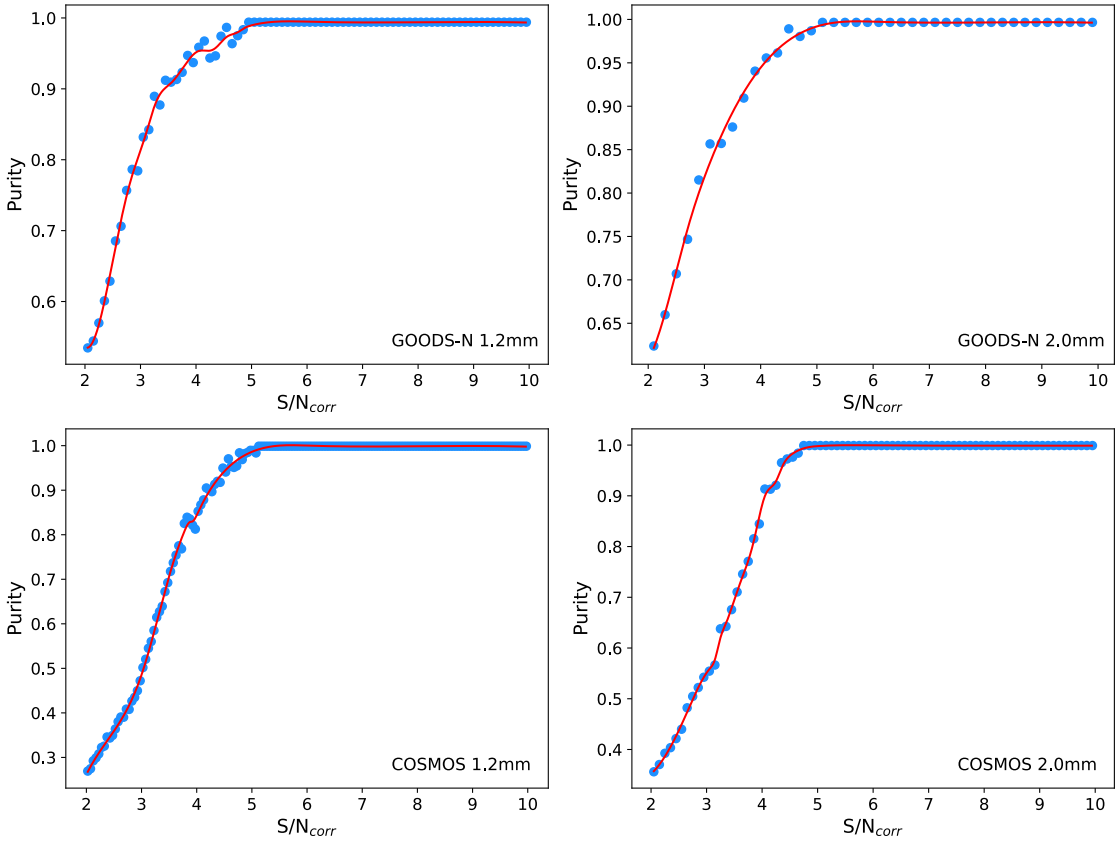

Figure 3.4 – The purity of detected sources at different S/N$_{corr}$ in the match-filtered map from the simulations at 1.2 and 2 mm in the GOODS-N and COSMOS field.

3.2.3.2 Effective Flux Boosting

We evaluate the impact of noise and pipeline on the measured source fluxes as a function of S/N of detection. As described by Sect. 2.4.2, the difference between the true flux and the measured flux from the map is subject to several effects related to the detection and flux measurement with noise, as well as the filtering effect in data reduction with the PIIC pipeline. As described in Sect. 2.4.2, the blind source

detection and the flux measurement with noise could introduce bias-to-peak effect and Eddigton bias, which could result in a positive bias on the flux of low S/N sources. The possible filtering of faint signal in the timeline during the data reduction, on the contrary, could work negatively on source fluxes.

The proper correction of the combined effect on source flux measurement is crucial for the estimate of source number counts, while the detailed individual analysis of these two effects is beyond the scope of this work. Here we directly measure the ratios between fluxes measured in the simulated maps and those in the input blob catalogs and estimate the variation of the ratios with S/N. Both the flux boosting and the pipeline filtering contribute to the deviation between input and output fluxes, and we name this output over input flux ratio as effective flux boosting. To estimate the effective flux boosting of source detection for each field and at each wavelength, we cross-match the input blob catalogs to the sources detected on the output map of the simulation. An input blob is considered to be recovered by our detection if any source above the S/N of 80% purity in the detected source catalog could be found within 0.75×FWHM to its position. This threshold is set to be the same as the one used in purity analysis, to preserve the consistency of the definition of true sources across the whole analysis process. We only keep the sources with detections on the simulated map in the following analysis. If multiple matches on an input blob are found, we keep the one closest to it as the best match. This cross-matching catalog will also be used in the completeness analysis in Sect. 3.2.3.3.

The distributions of the effective flux boosting are presented in Fig. 3.5. The mean values are also linearly interpolated and compared with the functional flux boosting curve from the S2CLS survey (Geach et al., 2017). As shown by Fig. 3.5, the mean effective flux boosting at both bands in the COSMOS field is mostly above one, suggesting that it is dominated by the flux boosting from Eddington bias and the "bias-to-peak" effect (see Sect. 2.4.2). The mean effective flux boosting curve also well matches the correction from the S2CLS survey, which only accounts for the typical flux boosting in their simulation. Contrary to the properties in COSMOS data, the mean effective flux boosting in the GOODS-N field drops below one already at relatively high S/Ns and reaches ~0.7-0.8 at the S/N of detection limit in both bands. This suggests a much stronger filtering on source flux during the data reduction in these deep observations approaching the confusion limit.

From the barplot in Fig. 3.5, we also notice a significant scatter in the effective flux boosting for some S/N bins. The span of the effective flux boosting within the central 50% of the distribution could be as high as 50% at the bins of S/N~4, and drops to less than 10% at S/N>20. This scatter is another source of uncertainties in addition to the uncertainties from the flux measurement on the map, to be considered in estimating the source number counts. The details of this correction process is described in Sect. 3.2.4.

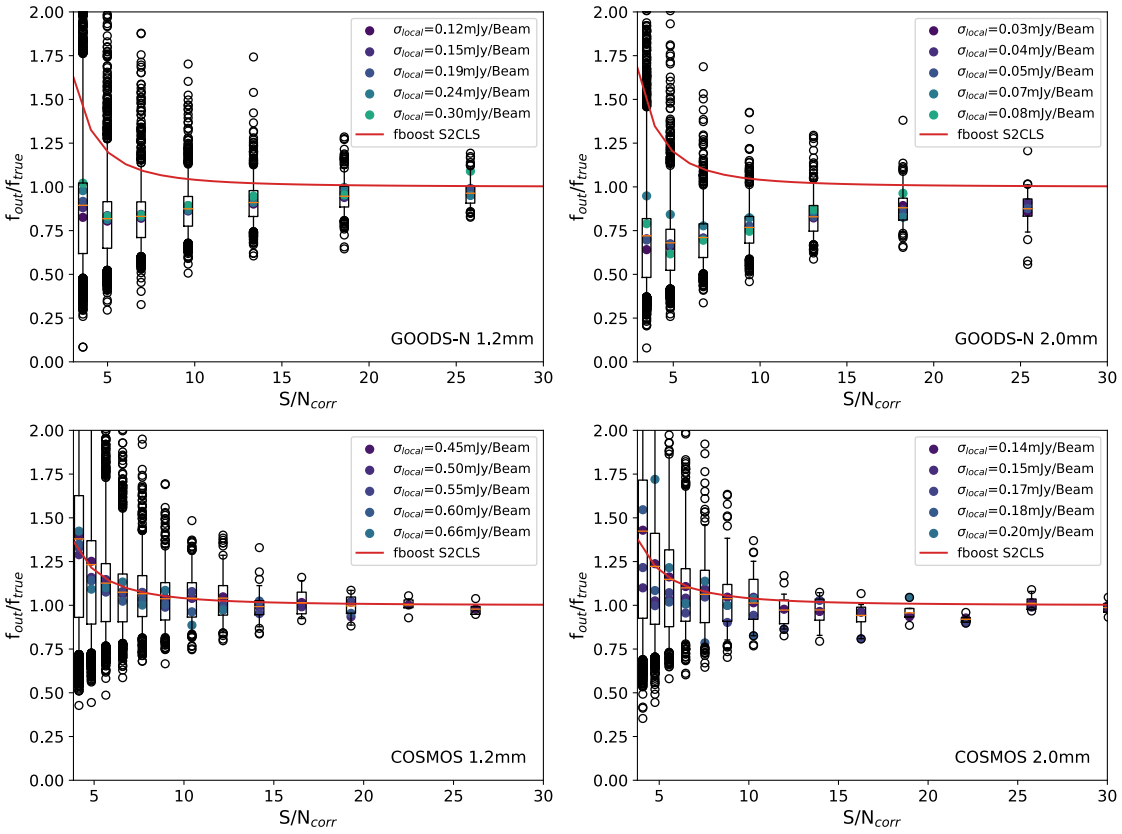

Figure 3.5 – The ratio between source fluxes measured on the output map and source fluxes from the input blob catalog as functions of S/N$_{corr}$ at 1.2 and 2 mm in GOODS-N and COSMOS. This is called effective flux boosting. The box at each S/N bin shows the ranges between 25% to 75% of the cumulative distribution and the upper and lower bound of bars present the 5% to 95% of the cumulative distribution. The dots show the position of outlier sources in the corresponding bins of S/N. The dots show the average trend in regions of different local noise (σ_{local}, see the values in labels). The red line in each panel presents the flux boosting derived by S2CLS (Geach et al., 2017) based on random injection and extraction of artificial sources on half-difference maps.

The corrected fluxes of sources above the 80% purity threshold from each realization of the Monte-Carlo simulation are further propagated to the estimation of completeness and effective survey area in Sect. 3.2.3.3 and Sect. 3.2.3.4. The estimation of intrinsic fluxes and flux uncertainties of sources with S/N above 80% purity are also derived and presented in Sect. 3.2.4 based on the results of the Monte-Carlo simulation.

3.2.3.3 Completeness

With the cross-matching between input blob catalogs and detected sources in the simulated map, we can simultaneously evaluate the completeness of source detection. The completeness is defined by the ratio of recovered sources to the total number of input sources. It is evaluated as a function of model blob flux densities and noise at the input sky coordinates of the sources in the output map of the PIIC simulations. Mathematically, we expect the completeness approaches zero at low flux and unity at high flux, while the evolution of completeness is not only dependent on the flux but also on the noise level in the map. This adds complexity to the completeness correction in the N2CLS survey, especially for the GOODS-N sample, which comes from a small field with significant variation in depth due to non-uniform survey coverage (see the maps of noise levels in Fig. 3.1 and Fig. 3.2).

From the practices on the ALMA blind selected samples in ALPINE survey (Béthermin et al., 2020), an functional form of completeness curve in the form of Eq. 3.3 is summarized, which could consistently reproduce the completeness function of sources in non-uniform maps with Gaussian noise. The completeness function follows a step model with an error function. The C, f_{true}, and σ_{local} represent the completeness, intrinsic fluxes of source (blobs) from the beam match-filtered model and the noise level at the source position in the map, and f_0 in the function modulate the turning position of the completeness curve.

$$C = 0.5 \times \left[1 + \mathrm{erf}\left(\frac{f_{true}}{\sigma_{local}} - \frac{f_0}{\sigma_{local}}\right)\right] \tag{3.3}$$

In this thesis, the completeness corrections on sources are made following the completeness curve in the form of Eq. 3.3 based on our analysis. By normalizing the intrinsic blob flux by the local noise, we find good consistency between the completeness curves obtained from the simulation using sources in regions of the different noise levels in the map. The consistency after normalization is illustrated in Fig. 3.6 between the blue dots of different darkness. Thus, we make an additional estimation on the completeness of all sources in the high-quality regions within 5 bins on f_{true}/σ_{local} between 2 to 10 in each field and band, as illustrated by the orange diamonds in Fig. 3.6. The modeling of these completeness data over the whole high-quality area is made under the form of Eq. 3.3 using the python package "lmfit".

With the fit on the completeness curve of each field and band, the completeness of each detected source in N2CLS survey are then estimated by applying the corresponding best fit parameter to Eq. 3.3. The correction factor for each source is estimated using the fluxes corrected by the effective flux boosting from each Monte-Carlo simulations (see Sect. 3.2.4 for details), $f_{deboost}$, as the true source fluxes to be assigned to f_{true}. The quantity of σ_{local} are set to be the pixel values at the positions of detected sources in the N2CLS maps.

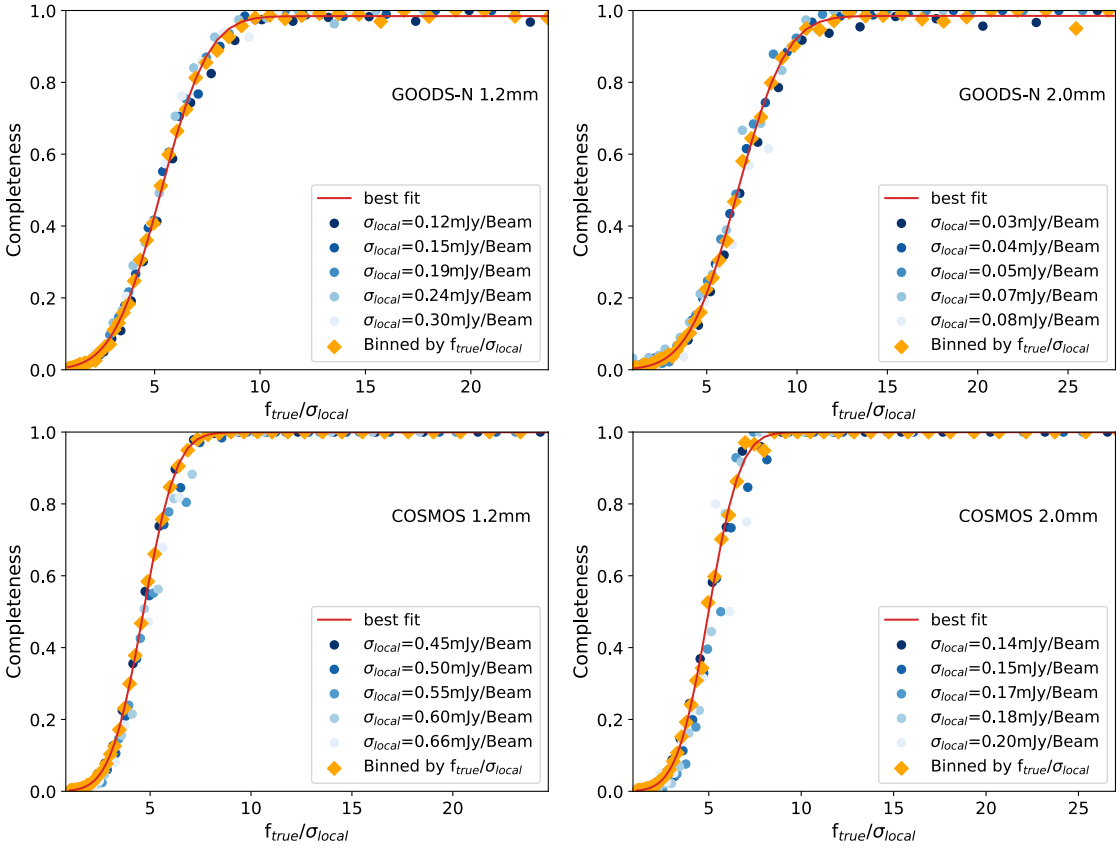

Figure 3.6 – The completeness of sources in N2CLS as a function of f_{true}/σ_{local} at 1.2 and 2 mm in GOODS-N and COSMOS field. The completeness in the whole survey area and survey areas with different instrumental noise levels are presented as color-coded dots. The red line shows the best fit of the completeness function in the form of Eq. 3.3 on the completeness values in the whole survey area.

3.2.3.4 Effective Survey Area

To further derive the surface density of sources, we need to know the effective surface area of our survey as a function of the source fluxes. Effective survey area describes the detectability of sources over the survey area considered in the number

counts analysis. In our N2CLS survey, it depends on the source fluxes, since the brightest sources are more likely to be detected on the noisier edges of the survey area compared to fainter sources.

The effective surface area as a function of source flux is derived from the completeness at one position in the map. In our pixelized data set, the effective surface area of a source at a given flux, $\Omega_{\rm eff}$, could be described as the sum of the area of each pixel ($\Omega_{\rm pix}$) weighted by the expected completeness at these positions $C(F_{\rm deboost}/\sigma_i)$, as shown by Eq. 3.4. The resulting format of the effective area of a given source is equivalent to the total survey area weighted by the expected completeness of sources in different regions over the map:

$$\Omega_{\rm eff} = \sum_{i=1}^{n} \Omega_{\rm pix} \times C\left(\frac{F_{\rm deboost}}{\sigma_i}\right) \tag{3.4}$$

With the effective area assigned to each source, the following calculation of number counts in the next section will naturally account for the variation of source completeness over the N2CLS maps due to the non-uniform depth. This is especially crucial for our number counts analysis in the GOODS-N field with 3 times variation in survey depth across the region considered for number counts analysis.

3.2.4 Flux Corrrection

We make source detection and measure their fluxes following the procedures described in Sect. 3.2.2. In the source detection on each field and band, the threshold of S/N are fixed to the corresponding 80% purity obtained by the analysis on simulated observations, and the purity of each source are also estimated based on the analysis presented in Sect. 3.2.3.1. We correct for the raw fluxes from the PSF fitting ($S_{\rm raw}$) to derive the corrected flux of each source ($S_{\rm corr}$), following the effective flux boosting curve and scatter in Sect. 3.2.3.2 and Fig. 3.5.

In the flux correction process, we sample the distribution of the effective flux boosting by Monte-Carlo simulations to make proper corrections on the source fluxes. We first obtain the cumulative distribution of the effective flux boosting for each S/N bin. Then, we generate random numbers between zero and one, representing the percentile of the cumulative distribution to be assigned to each source in the simulation. With the detection S/N of sources, we derive the effective flux boosting values at the random percentile within the two adjacent S/N bins above and below the detection S/N values. The effective flux boosting values assigned to the sources are then estimated by linear interpolation using the pair of values. Apart from the scatter in the effective flux boosting curve itself, we also consider the uncertainties of raw fluxes of sources measured on the map. In each Monte-Carlo simulation, we add an additional random scatter to the measured source fluxes before the correction of effective flux boosting. The random scatter on each source is drawn from a Gaussian distribution centered on zero and with the scatter (σ) of the flux uncertainty from the

source catalog.

Following the procedures described above, the uncertainties of both effective flux boosting values at given S/N and the measurement on S_{raw} are taken into account in the corrected flux (S_{corr}) uncertainties. From the N2CLS GOODS-N observations, we detect 120 and 67 source with at purity better than 80% at 1.2 and 2 mm, respectively. For COSMOS field, the numbers of sources with > 80% purity are 195 and 76 at 1.2 and 2 mm, respectively.

3.3 Source and Galaxy Number Counts

3.3.1 Number Counts Estimation

Following the procedures in Sect. 3.2.4, we obtain 100 realizations of "true" source fluxes from the simulation and corresponding corrections. We also used the “true” flux to derive the effective survey area of each source in each realization following the definition in Sect. 3.2.3.4. With the "true" flux, effective area, and the corresponding purity at the S/N of detection, we derive the differential source number counts at 1.2 and 2 mm for each realization following Eq. 3.5 at each flux bin centered on flux S. Here n counts the number of source within each flux bin for each realization, $\Omega_{\mathrm{eff},i}$ represents the effective area of the i-th source within the flux bin, and ΔS is the width of the flux bin:

$$\frac{dN(S)}{dS} = \sum_{i=1}^{n} \frac{1}{\Omega_{\mathrm{eff},i} \times \Delta S} \tag{3.5}$$

We also derive the corresponding cumulative source number counts. They are defined as the surface density of sources with flux density higher than a given value. They are estimated in the same flux bins as the differential source number counts and following Eq. 3.6. Similar to Eq. 3.5, here m counts the number of sources above flux S for each realization, $\Omega_{\mathrm{eff},j}$ represents the effective area of the j-th source with flux above S:

$$N(>S) = \sum_{j=1}^{m} \frac{1}{\Omega_{\mathrm{eff},j}}. \tag{3.6}$$

The derived differential and cumulative number counts are further truncated at the faint end to the flux with ~50% completeness in the corresponding N2CLS map. This ensures the values presented by the research are not subject to large correction on the incompleteness, which could significantly enlarge any bias in the estimation and introduce large uncertainties to the faint end number counts. While the various corrections are applied to recover the source number counts from observations, it is important to confirm if there is any systematic bias remains in our framework based on the simulations and analysis. To examine this, we applied the correction on purity and flux boosting to each source detected by the same threshold in the simulated observations of each field, derive the effective area of each detected source, and

estimate the output differential source number counts of the simulated observations in each band and field. These differential number counts are then compared with the input source counts from the peak detection in the beam match-filtered map (blob catalog), which checks the validity of the recovery of source fluxes and number counts by our method. The corresponding results are presented in Sect. 3.3.2. We also compare the output source number counts with the galaxy counts directly obtained from the input SIDES-Uchuu catalog. The ratios between the two counts give the impact of resolution on the number counts (Béthermin et al., 2017) and are also applied in the comparison between number counts from low-resolution single-dish observations and high-resolution interferometric observations in Sect. 3.3.4.

3.3.2 Validation of the number counts reconstruction from simulations

Before making further analysis, we first follow the same procedures as Sect. 3.2.3 to check if our simulation and analysis framework could properly recover the statistical properties of the input model. We make a direct comparison between the input differential blob counts and the differential source counts recovered from the output of simulation at 1.2 mm for GOODS-N and COSMOS. Both input and output differential counts are estimated under the same flux bins considered for the N2CLS survey data. In Fig. 3.7, the average value of output differential source number counts across the 117 simulated observations on each field is presented as blue diamonds. The shaded blue area shows the span of the 1-sigma upper and lower limit of the output differential source counts of individual simulated GOODS-N/COSMOS fields, illustrating the uncertainties from the cosmic variance in the input SIDE+Uchuu model. The average value input differential blob counts are presented as pink lines, which are generally consistent with the output differential number counts within 1-sigma uncertainty of cosmic variance. As the output differential source number counts are derived using the same detection and correction method as we did on the N2CLS survey data, the consistency with the input differential blob counts suggests that the full framework described in Sect. 3.2.3 could recover the fluxes of sources in real N2CLS observations properly for statistical analysis.

In Fig. 3.7, we also present the input galaxy number counts from the SIDES-Uchuu catalog to compare with the raw source number counts measured from the output of the simulations. The raw source counts are subject to beam smoothing at the resolution of the 30 m telescope, while the galaxy counts are directly coming from the SIDES-Uchuu catalog, and thus are input intrinsic models not affected by the beam. The comparison reveals systematically higher raw source counts recovered from the simulated maps compared to the input galaxy counts within the considered flux ranges. As the input blob number counts in the beam smoothed models match well with the output source number counts derived on the beam smoothed maps, their offsets relative to the input intrinsic galaxy counts suggest that large beam in the single-dish observation is introducing systematical biases on the measurement

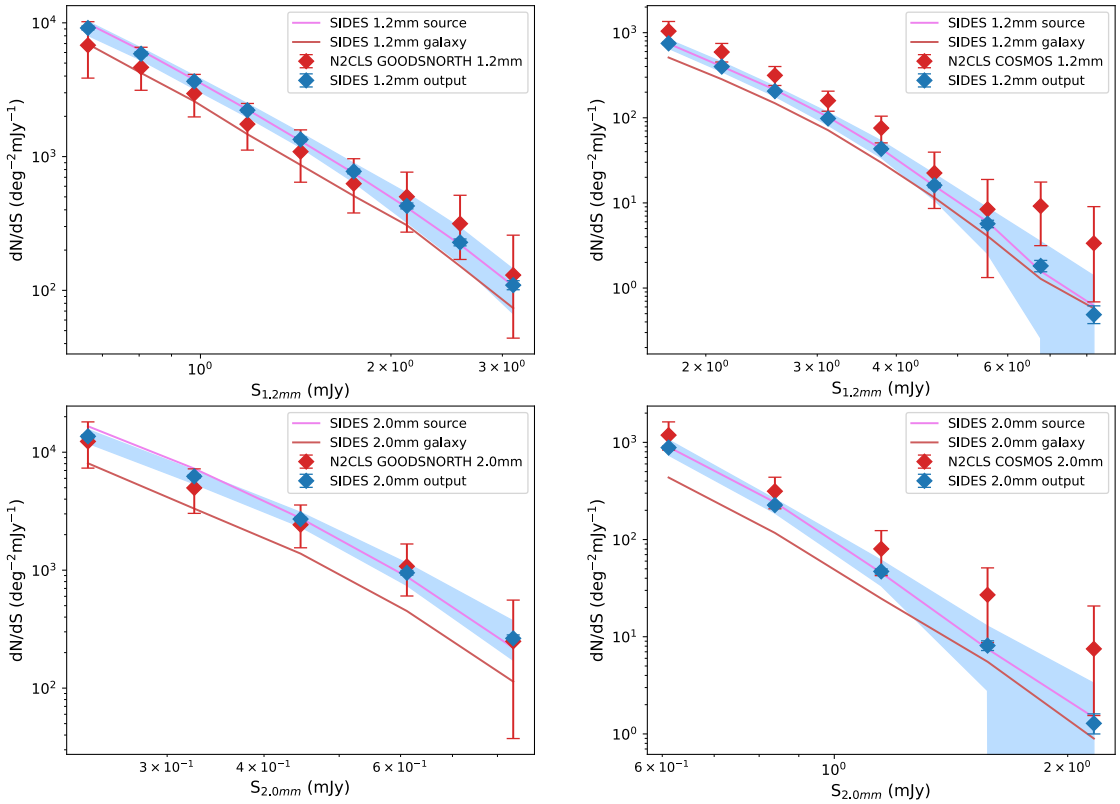

Figure 3.7 – The comparison between input galaxy number counts from the SIDES-Uchuu catalogs (brown lines) and input source number counts (from the blob catalog, after applying the convolution of beam, shown as the pink lines), as well as the output source number counts derived from the detected sources in the simulated map (diamonds). The source number count from N2CLS is also shown as red diamonds, which are further described in detail in Sect. 3.3.3. The output source number counts are corrected for the purity, effective flux boosting and completeness based on the simulation, which is exactly the same as the corrections applied to the real N2CLS observations. The galaxy counts could be corrected from the source counts in the same tables by multiplying the correction factors in the corresponding bins.

of the intrinsic flux distribution of (sub-)millimeter galaxies. As a result, this bias needs to be considered before comparing the single-dish source number counts with the high resolution interferometric measurements and empirical or theoretical model predictions. Thus, we further derive the galaxy-to-source ratio for differential and cumulative counts in each field at each flux bin, based on the analysis on the simulation input and output data. These ratios are noted as R_{diff} and R_{cum} to correct the differential and cumulative source number counts ($dN_{sou}(S)/dS$ and $N_{sou}(>S)$) to the corresponding galaxy counts ($dN_{gal}(S)/dS$ and $N_{gal}(>S)$), following Eq. 3.7 and Eq. 3.8.

$$\frac{dN_{gal}(S)}{dS} = \frac{dN_{sou}(S)}{dS} \times R_{diff}(S) \tag{3.7}$$

$$N_{gal}(>S) = N_{sou}(>S) \times R_{cum}(S) \tag{3.8}$$

The galaxy counts could be corrected from the source counts by multiplying the correction factors at the corresponding fluxes.

3.3.3 1.2 and 2 mm Number Counts

From the 100 realizations described in Sect. 3.2.3 and Sect. 3.3.1 on each field and band, we take the mean number counts as the results to be presented and compared with other observations and models. We further estimate 1σ upper and lower limits of the differential source number counts at each flux bin by 16% and 84% quantile of the distribution from the 100 realizations. These values, in addition to the Poisson error, are used to derive the uncertainty of the source number counts by adding them quadratically. For the computation of source number counts, the lower bound of deboosted 1.2 and 2 mm fluxes are set to 0.60 and 0.20 mJy, respectively. This flux truncation ensures a completeness of ~50% or higher in the analysis in the GOODS-N field. We also set the maximal flux at 9.0 and 2.5 mJy, at 1.2 and 2 mm, which encloses the brightest source in the N2CLS survey in both bands. With the upper and lower bound of source fluxes, we generate 14 and 8 flux bins with uniform logarithmic sampling for 1.2 and 2 mm analysis. The calculations in the GOODS-N field at 1.2/2 mm are limited to the 9/5 bins with the lowest fluxes, while in the COSMOS field the analysis is limited to the 9/5 bins with the highest fluxes. The values and uncertainties of the differential and cumulative number counts in the 2 fields at 1.2 mm are presented in Table 3.2, and the results at 2 mm are listed in Table 3.3. The 2.0 mm survey of N2CLS, for the first time, covers a wide range of flux density from 0.2mJy to 2.0 mJy with reasonable completeness (~50% or higher) on source detected down to the faint end. At 1.2mm, we are also the first single-dish survey that extend the number counts measurements well into the sub-mJy flux densities, which enables direct comparison between interferometric observations.

We present our measurement of 1.2 and 2 mm differential and cumulative source number counts from N2CLS COSMOS and GOODS-N data in Fig. 3.8 and Fig. 3.9,

GOODS-N						COSMOS					
S mJy	dN(S)/dS $deg^{-2}mJy^{-1}$	R_{diff}	S_{min} mJy	N(>S) deg^{-2}	R_{cum}	S mJy	dN(S)/dS $deg^{-2}mJy^{-1}$	R_{diff}	S_{min} mJy	N(>S) deg^{-2}	R_{cum}
0.66	6799^{+3398}_{-2938}	0.76	0.60	3598^{+448}_{-534}	0.71	1.75	1041^{+312}_{-272}	0.68	1.57	948^{+108}_{-102}	0.70
0.81	4650^{+1918}_{-1518}	0.72	0.73	2727^{+345}_{-389}	0.69	2.12	592^{+155}_{-140}	0.71	1.92	597^{+69}_{-69}	0.72
0.98	2960^{+1157}_{-981}	0.71	0.88	2005^{+276}_{-311}	0.68	2.57	315^{+85}_{-76}	0.72	2.32	355^{+48}_{-48}	0.72
1.19	1748^{+747}_{-630}	0.66	1.07	1447^{+229}_{-286}	0.66	3.12	159^{+47}_{-40}	0.73	2.82	199^{+34}_{-31}	0.72
1.44	1089^{+495}_{-446}	0.64	1.30	1047^{+196}_{-243}	0.66	3.79	$75.8^{+28.7}_{-25.0}$	0.69	3.42	103^{+25}_{-25}	0.71
1.75	627^{+337}_{-248}	0.66	1.58	745^{+176}_{-200}	0.67	4.59	$22.5^{+17.0}_{-13.9}$	0.72	4.15	$47.7^{+18.2}_{-15.6}$	0.74
2.12	501^{+264}_{-229}	0.72	1.92	533^{+160}_{-187}	0.69	5.58	$8.41^{+10.45}_{-7.09}$	0.72	5.04	$27.8^{+15.1}_{-11.9}$	0.76
2.57	315^{+198}_{-145}	0.66	2.32	328^{+148}_{-177}	0.66	6.76	$9.18^{+8.41}_{-6.03}$	0.71	6.11	$18.8^{+13.2}_{-9.4}$	0.83
3.12	130^{+128}_{-86}	0.67	2.82	172^{+162}_{-154}	0.66	8.21	$3.35^{+5.69}_{-2.67}$	1.19	7.42	$6.81^{+11.31}_{-5.90}$	0.95

Table 3.2 – Differential and cumulative source number counts at 1.2 mm in GOODS-N and COSMOS. The galaxy counts could be corrected from the source counts by multiplying the correction factors at the corresponding fluxes.

GOODS-N						COSMOS					
S mJy	dN(S)/dS $deg^{-2}mJy^{-1}$	R_{diff}	S_{min} mJy	N(>S) deg^{-2}	R_{cum}	S mJy	dN(S)/dS $deg^{-2}mJy^{-1}$	R_{diff}	S_{min} mJy	N(>S) deg^{-2}	R_{cum}
0.24	12340^{+5732}_{-5009}	0.59	0.20	2073^{+378}_{-385}	0.55	0.61	1186^{+438}_{-352}	0.49	0.52	358^{+73}_{-70}	0.51
0.33	4981^{+2243}_{-1951}	0.53	0.27	1157^{+237}_{-240}	0.51	0.84	314^{+124}_{-107}	0.51	0.71	131^{+33}_{-32}	0.53
0.45	2428^{+1140}_{-880}	0.51	0.38	650^{+168}_{-182}	0.49	1.14	$80.1^{+43.4}_{-37.6}$	0.53	0.97	$48.4^{+18.9}_{-16.1}$	0.58
0.61	1077^{+590}_{-473}	0.47	0.52	311^{+122}_{-118}	0.47	1.57	$27.0^{+24.1}_{-18.3}$	0.68	1.33	$19.6^{+14.0}_{-9.9}$	0.73
0.84	249^{+308}_{-212}	0.43	0.71	104^{+105}_{-100}	0.46	2.16	$7.50^{+13.21}_{-5.96}$	0.70	1.82	$6.28^{+10.82}_{-5.37}$	0.82

Table 3.3 – Differential and cumulative source number counts at 2 mm in GOODS-N and COSMOS. The galaxy counts could be corrected from the source counts by multiplying the correction factors at the corresponding fluxes.

together with the other number counts at similar wavelengths from various single-dish (Lindner et al., 2011; Scott et al., 2012; Staguhn et al., 2014; Magnelli et al., 2019), and interferometric surveys (Oteo et al., 2016; Fujimoto et al., 2016; Hatsukade et al., 2016; Aravena et al., 2016; Umehata et al., 2017; Franco et al., 2018; Hatsukade et al., 2018; González-López et al., 2020; Zavala et al., 2021; Gómez-Guijarro et al., 2022a). In order to compare the number counts from observations of slightly different wavelengths, the literature results at 1.1 mm in Fig. 3.8 and Fig. 3.9 need to be corrected. We obtain the 1.2-to-1.1 mm flux ratio from the main-sequence SED template from Béthermin et al. (2015), at the median redshift (z=2.5) of 1.1 mm detected source in GOODS-ALMA survey (Gómez-Guijarro et al., 2022a). This finds a 1.2-to-1.1 mm flux ratio of 0.8. The fluxes where the 1.1mm differential and cumulative number counts measured in literature are multiply by 0.8 to adjust to 1.2mm. The differential number counts are further divided by 0.8 to accounts for the difference of the corresponding flux bin widths accordingly.

The flux ranges we use to derive the number counts in GOODS-N and COSMOS fields overlap in 4 bins (1.7 mJy to 3.12 mJy) and 2 bins(0.61 mJy and 0.84 mJy) at 1.2 mm and 2 mm, which provides an independent check in the field to field variance in source number counts within N2CLS survey. From our results in Table 3.2 and Table 3.3, and as illustrated by Fig. 3.8 and Fig. 3.9, we find general consistency between the source number counts from GOODS-N and COSMOS in this overlapped flux range. Similar consistency could also be found in the 2 overlapped flux bins in 2 mm number counts in the two fields. In addition to the consistency with other surveys covering various fields, this indicates an insignificant contribution of cosmic variance compared to the current uncertainties of sources number counts measurements at 1.2 mm and 2 mm.

As shown by Fig. 3.8 and Fig. 3.9, the bright end of 1.2 mm differential and cumulative number counts from N2CLS survey well match with the results from the 1.1 mm AzTEC survey covering multiple fields including COSMOS and GOODS-N (Scott et al., 2012). The MAMBO survey in the Lockman Hole (Lindner et al., 2011) found slightly lower number counts than us, while both measurements are still consistent with each other within the uncertainties. The differential and cumulative source counts from our single-dish blind survey, on a non-lensing field, are generally consistent with the AzTEC results in the sub-mJy regime, where they are mainly derived from observations on cluster lensing fields (Scott et al., 2012).

The GOODS-N observation also reaches the flux regime covered by deep ALMA surveys and allows a direct comparison between the number counts from low-resolution single-dish observations and high-resolution interferometric surveys. From the 1.2 mm cumulative and differential number counts below 2 mJy, we notice that although our source number counts are still consistent with the other ALMA 1.1/1.2 mm surveys with narrow coverage and larger uncertainties, they are systematically higher than the galaxy counts values from GOODS-ALMA, which have a larger sky coverage

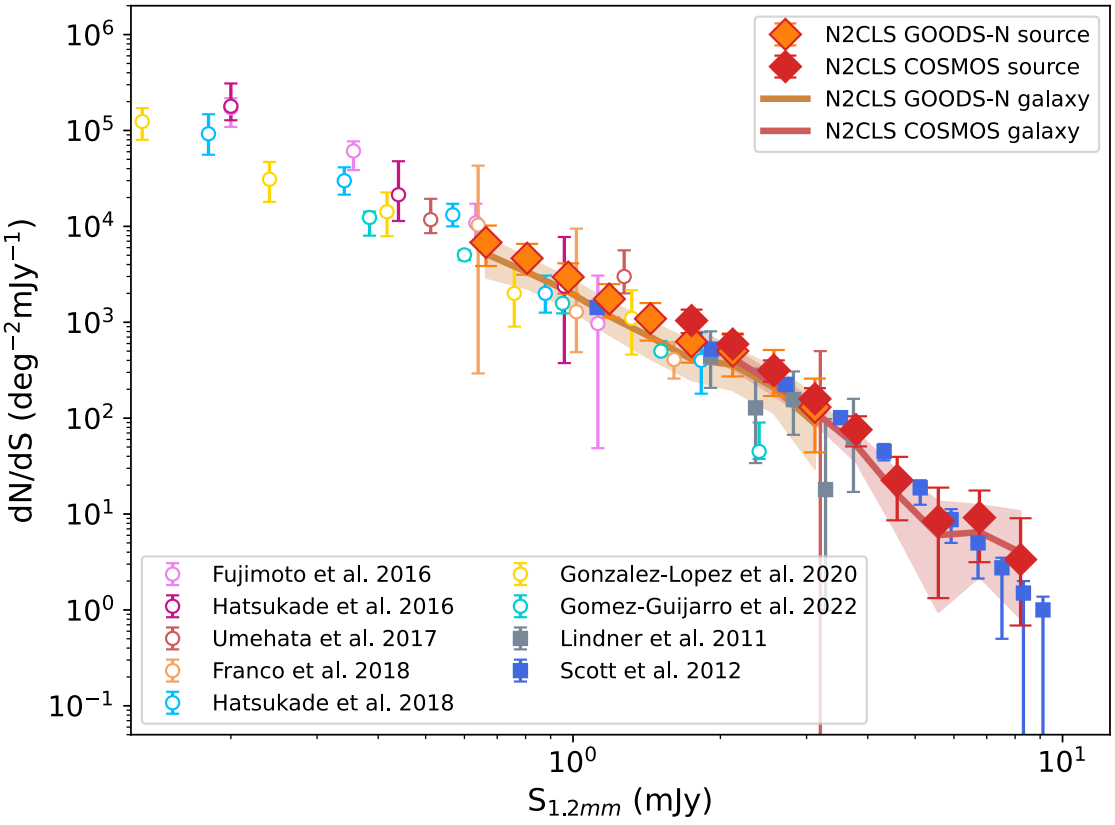

Figure 3.8 – The observed 1.2 mm differential source number counts of N2CLS GOODS-N and COSMOS survey (Orange and red diamonds) compared to the measurements of other surveys at 1.1/1.2 mm. All results from interferometric observations are presented with open symbols, and the measurements from single-dish observations are presented with filled symbols. The yellow and red shaded regions show the $\pm 1\sigma$ confidence interval of the N2CLS galaxy number counts obtained after correction of the source number counts in the GOODS-N and COSMOS field, respectively.

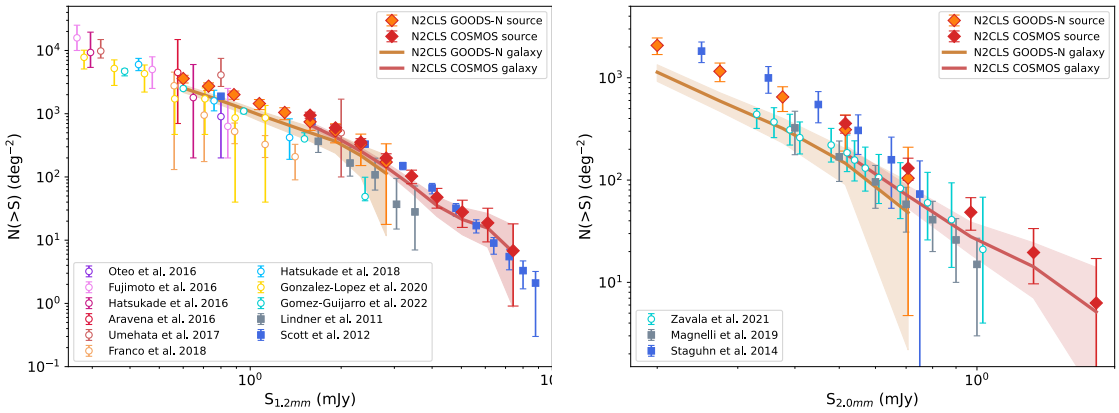

Figure 3.9 – Similar to Fig. 3.8, but for the observed 1.2 (left) and 2 mm (right) cumulative number counts obtained from N2CLS and compared to measurements from the literature.

of ∼40% of our survey. The source-to-galaxy number counts corrections based on Table. 3.2, however, put the N2CLS galaxy differential and cumulative number counts to values slightly lower than the corresponding source number counts. These corrected galaxy number counts match well with all measurements from ALMA blind surveys, including most of the measurements of GOODS-ALMA, which suggests an intrinsic consistency of interferometric number counts with our single-dish measurements.

In the past decades, only a few blind surveys at around 2.0 mm has been carried out, and the majority of them give the cumulative source/galaxy number counts. For the 2 mm results of N2CLS, we show the cumulative 2 mm source number counts in COSMOS and GOODS-N field in Fig. 3.9, and compare them with the results from the IRAM GISMO surveys in GOODS-N (Staguhn et al., 2014) and COSMOS (Magnelli et al., 2019), as well as the ALMA MORA 2 mm survey mostly overlaps with the CANDELS stripe in COSMOS (Zavala et al., 2021). Although the GISMO survey in GOODS-N covers a very limited area of ∼ 40 arcmin^2, we find good consistency between their source counts and our measurements almost covering the entire GOODS-N CANDELS stripe. Our measurement in COSMOS shows larger cumulative source counts compared to GISMO COSMOS and MORA, while the 3 measurements are still consistent with each other within the 1σ uncertainties. According to the results in Table 3.3, the 2 mm cumulative source number counts are subject to more significant source-to-galaxy counts corrections. We applied this correction and also present the galaxy number counts in Fig. 3.9 by the yellow and red solid lines. The corresponding confidence intervals within 1σ uncertainties are illustrated by the shaded areas of the color close to the lines. This shows an even better match between the corrected cumulative galaxy counts of our surveys and the MORA survey with overlapped coverage, as indicated by the comparison between shaded area and open cyan circles, which also indicates the reliability of our source-to-galaxy counts correction based on simulations.

3.3.4 Comparison with Models

Apart from the other observations, we can also compare our new measurements with number counts predictions from various models of galaxy evolution, including the predictions from the SIDES model(Béthermin et al., 2017), the Empirical Galaxy Generator (Schreiber et al., 2017), the SHARK semi-analytic model (Lagos et al., 2020) and the semi-empirical model described in Popping et al. (2020). The SIDES and the Empirical Galaxy Generator start from the stellar mass function and the evolution of the star-forming main sequence from observations to predict infrared and (sub-)millimeter fluxes. They also separately accounts for the emission from main-sequence and starbursts galaxies by different SEDs, while the IR SEDs in these two models follow different evolution with redshift. The SHARK predictions starts from the default suite of model parameters in Lagos et al. (2018) to predict the amount and distribution of gas in the galaxies. With these predictions on gas, as well as metallicity, the dust emission and (sub-)millimeter fluxes of galaxies are further modeled under the framework described in Lagos et al. (2019) and Lagos et al. (2020). The semi-empirical model in Popping et al. (2020) assigns star formation rate in given dark matter halos following the SFR-halo relation from the UNIVERSEMACHINE (Behroozi et al., 2019), then use empirical relations to estimate the dust mass and obscured star-formation and predict the millimeter fluxes correspondingly. Our work empirically accounts for the impact of lower spatial resolution in single dish observations, providing the first estimate on 1.2 mm and 2 mm galaxy number counts that could be directly compared with the predictions of these models.

To compare our measurements with the models, we first combine the number count measurements in the two fields from the source counts and corrections in Table 3.2 and Table 3.3. We derive the mean of the galaxy number counts in the overlapped flux range in the two fields using the inverse-variance weighted average of the estimate in each field. For the bright and faint end, we directly use the measurements in COSMOS and GOODS-N fields, respectively. The values and uncertainties of the combined 1.2 and 2 mm galaxy number counts are given in Table 3.4.

We use the differential galaxy number counts in the comparison between our observations and model predictions, which directly probe the number density of sources at given fluxes. Among the models used in the comparison, the predictions of SHARK (Lagos et al., 2020) and empirical model in Popping et al. (2020) are originally given in cumulative number counts. To make use of these predictions, we calculate the differential number counts from their cumulative number counts at given flux $dN(S_i < S < S_{i+1})/dS$, following the Eq. 3.9. We also make a correction on the prediction of Popping et al. (2020) to account for the slightly different wavelength (1.1 mm) compared to our 1.2 mm observation, using the same factors as in Sect. 3.3.3.

$$\frac{dN(S_i < S < S_{i+1})}{dS} = \frac{N(> S_i) - N(> S_{i+1})}{S_{i+1} - S_i}. \tag{3.9}$$

Fig. 3.10 shows the comparison between the combined differential galaxy number counts and model predictions. At 1.2 mm, we could find good consistency of the predictions of SIDES (Béthermin et al., 2015; Gkogkou et al., 2022), Empirical Galaxy Generator (Schreiber et al., 2017) and Popping et al. (2020) model with the N2CLS galaxy number counts at the faint end (<1.5 mJy) of the coverage of our analysis. However, compared to our observations, all of these models predict smaller number densities of sources at 2-3 mJy and the bright end of the coverage of the N2CLS survey by a factor of two. On the contrary, the prediction of SHARK model (Lagos et al., 2020) at 1.2 mm is generally consistent with the N2CLS results on bright sources above 2mJy, while it produces about a factor of two higher density of sources at the faint end. As for the comparison at 2 mm, we find a similar trend as the comparison at 1.2 mm. For the SIDES and Empirical Galaxy Generator, we find well-matched predictions with the galaxy number counts from N2CLS measurements below 0.6 mJy. However, at higher fluxes, we start to see the underprediction on the number density of sources by a factor of two to four compared to N2CLS observations. The underprediction of bright source densities in the Empirical Galaxy Generator is more significant than SIDES in most except for the brightest flux bins above 0.6 mJy. On the other hand, the SHARK model provides number counts prediction consistent with the observations within the uncertainties in most but the faintest flux bins below 0.4 mJy.

From the comparisons, we clearly reveal two families of models in their performance. The SHARK model matches with our observations on bright sources, but predicts slightly larger density of faint sources. The rest three models have better performance on faint sources number density but underpredicts the number of bright sources. From the comparison in Fig. 3.10, we could also find all models shows a relatively consistent slope in most flux bins expect for the bright end, where SHARK predicts the highest source number density across the flux coverage of N2CLS among all. Thus, we suggest that the two different trend seen in the comparison with these models could likely be consistently explained as a shallower slope of observed galaxy number counts within the flux coverage of N2CLS. This, as a result, indicates a larger contribution of bright millimeter sources to the general population of 1.2 and 2 mm sources than the predictions of current models.

3.4 Discussion

One important aspect of our work, as demonstrated by our simulations and observations, is the intrinsic difference between the number counts viewed by high-resolution, interferometric observations and low-resolution, single-dish observations. In interferometric observations, the blindly detected (sub-)millimeter sources ~1 arc-second resolution properly trace the emission from individual galaxies. The flux and number counts measurement, thus, could be more directly compared with the model predictions on the statistical properties of galaxies. However, at the low resolution of single-dish observations like N2CLS, the results of our end-to-end simulation suggests

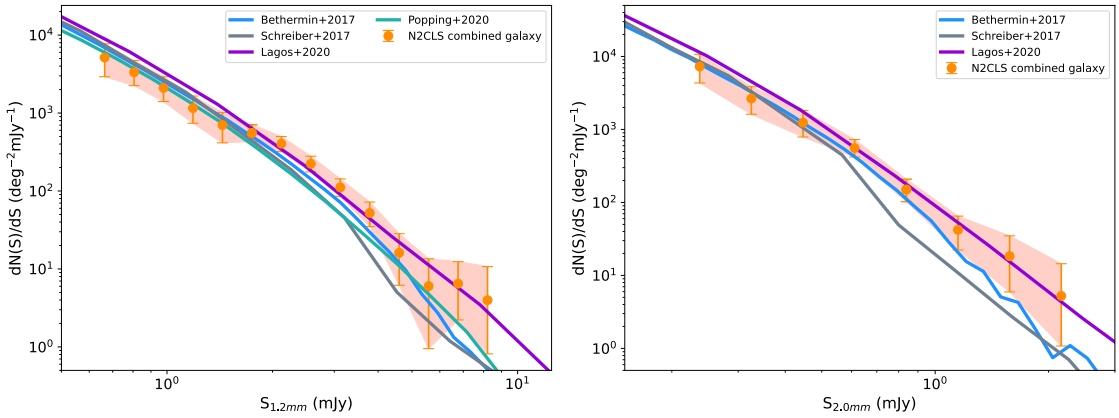

Figure 3.10 – Comparison between the N2CLS differential galaxy number counts and the predictions of simulations and semi-analytic models (Béthermin et al., 2015; Schreiber et al., 2017; Lagos et al., 2020; Popping et al., 2020). The shaded regions show the $\pm 1\sigma$ confidence interval of the combined GOODS-N+COSMOS galaxy number counts.

1.2 mm				2 mm			
S mJy	dN(S)/dS deg^{-2}mJy^{-1}	S_{min} mJy	N(>S) deg^{-2}	S mJy	dN(S)/dS deg^{-2}mJy^{-1}	S_{min} mJy	N(>S) deg^{-2}
0.66	5153^{+2575}_{-2227}	0.60	2546^{+317}_{-378}	0.24	7294^{+3388}_{-2961}	0.20	1134^{+207}_{-211}
0.81	3337^{+1377}_{-1090}	0.73	1879^{+238}_{-268}	0.33	2653^{+1195}_{-1039}	0.27	593^{+121}_{-132}
0.98	2100^{+821}_{-696}	0.88	1358^{+187}_{-211}	0.45	1237^{+581}_{-449}	0.38	320^{+83}_{-89}
1.19	1157^{+494}_{-417}	1.07	959^{+152}_{-189}	0.61	556^{+171}_{-137}	0.52	171^{+31}_{-30}
1.44	702^{+319}_{-287}	1.30	695^{+130}_{-161}	0.84	150^{+58}_{-48}	0.71	$67.3^{+16.5}_{-15.9}$
1.75	554^{+154}_{-123}	1.58	624^{+64}_{-63}	1.15	$42.1^{+22.8}_{-19.8}$	0.97	$28.0^{+10.9}_{-9.3}$
2.12	405^{+95}_{-85}	1.91	418^{+45}_{-46}	1.58	$18.4^{+16.5}_{-12.5}$	1.33	$14.2^{+10.1}_{-7.2}$
2.57	224^{+56}_{-48}	2.32	252^{+33}_{-33}	2.16	$5.24^{+9.23}_{-4.16}$	1.82	$5.15^{+8.86}_{-4.39}$
3.12	111^{+32}_{-26}	2.82	142^{+24}_{-22}				
3.79	$52.2^{+19.8}_{-17.3}$	3.42	$73.2^{+17.8}_{-17.7}$				
4.59	$16.1^{+12.2}_{-9.9}$	4.15	$35.2^{+13.4}_{-11.5}$				
5.58	$6.02^{+7.48}_{-5.07}$	5.04	$21.3^{+11.5}_{-9.1}$				
6.76	$6.48^{+5.93}_{-4.26}$	6.11	$15.5^{+10.9}_{-7.8}$				
8.21	$3.98^{+6.74}_{-3.16}$	7.42	$6.46^{+10.73}_{-5.60}$				

Table 3.4 – Combined differential and cumulative galaxy number counts at 1.2 and 2 mm from the observation on the two fields

contamination of a few tens of percent from close-by galaxies on the flux measurement of detected galaxies. The impact of spatial resolution on flux measurements in single-dish observation has been discussed in previous modelings. Our work, for the first time, quantitatively estimate and correct for this effect in real single-dish blind surveys, as revealed by the comparison between output source number counts and input galaxy number counts in our simulation in Sect. 3.3.2. The consistency between the input and output source number counts in Sect. 3.3.2 suggests the observed difference is unlikely to be introduced by the pipeline or imperfect correction, but mostly due to angular resolution effects. As shown in Table 3.2 and Table 3.3, the differences between the galaxy number counts and source number counts in N2CLS observations could be up to a factor of two at 2 mm, and are almost constant in all bins except for the bright end. The differences are also already significant compared to the uncertainties in the number counts measurements.

Current (sub)millimeter interferometric observations mostly have spatial resolutions of a few to sub-arcseconds (see Table 1.3). The beam size of these observations corresponds to 4-10 kpc at z=2-3, which could adequately separate the (sub)millimeter emission of one galaxy from close-by sources. This makes the number counts derived from the ALMA blind surveys close to the definition of galaxy number counts in Sect. 3.3.4, which counts the number density of point sources around or above certain fluxes directly associating with dark matter halo/subhalos in simulations. However, the intrinsic difference of single-dish source number counts (like the ones we obtained from N2CLS) with these ALMA/simulated galaxy number counts stress the importance of making additional source-to-galaxy correction before comparing the measured/simulated number counts of significant different spatial resolution.

The source-to-galaxy correction below unity (see Table. 3.2 and Table. 3.3) is expected to put the galaxy number counts after correction lower than the raw source number counts from the N2CLS survey. However, we still find a higher number density of bright galaxies than most of the model predictions at 1.2 and 2 mm after this correction. A possible explanation for this discrepancy could be the under-prediction of galaxies with intense but obscured star formation by current models. These models, such as SIDES Béthermin et al. (2017), set a conservative upper limit of the star formation rate of galaxies ($1000 M_{\odot}$/yr) and a fixed fraction of starburst galaxies at redshift higher than 1(3%). From various model predictions, we notice the brightest sources are expected to be more contributed by high redshift sources, galaxies with intense obscured star-forming activities, and (or) massive star-forming systems the more considerable number of any of these populations, in reality, could explain the excess of bright (sub)millimeter galaxies relative to models like Béthermin et al. (2015), Schreiber et al. (2017), and Popping et al. (2020). Besides, some of the models with underestimated number counts also rely on the assumption of far infrared SED of high-z galaxies following an evolution of dust temperature. However, recent studies also discovers starburst/star-forming galaxies with far infrared SED peaked at significantly longer wavelengths than normal star-forming galaxies (Jin et al., 2019). At a fixed

star formation rate, sources with these apparently cold SEDs naturally have higher millimeter fluxes. As these cold SEDs have not been accounted for in these models, the existence of a considerable population of starburst/star-forming galaxies with cold SEDs could also contribute to the higher number density of bright millimeter sources compared to the model predictions.

As indicated by the comparison between input and output source number counts in Fig. 3.7 from the simulation, the full framework we developed to correct bias and pipeline effects can properly recover the input source number counts from the observations. However, the correction factors to be applied to source fluxes and completeness also depend on the galaxy number count of the input model, as already revealed by previous works. As a result, the slight inconsistency of the SIDES input model and the measured number counts of N2CLS could also pose possible issues with the flux correction in our analysis. As illustrated by the effective flux boosting in Fig. 3.7, fainter sources detected at lower S/N will be subject to more significant corrections back to their intrinsic fluxes. As an example, under a steeper slope/higher density of faint sources, the positive effective boosting at the faint end, such as the case in the COSMOS field will naturally put the apparent flux of a more considerable number of faint sources to brighter fluxes. This, in return, will result in larger effective boosting factors at a given raw flux or S/N of detection, and will thus make the flux correction and the corresponding completeness correction in Sect. 3.2.3 not completely compatible with our simulation. However, although we obtained a higher value of galaxy number counts compared to SIDES (see Fig. 3.7), the faint end slope of source counts from our GOODS-N and COSMOS observation and the SIDES simulation are still generally consistent. This suggests that the relative number density distribution of faint sources subject to the most significant flux corrections is still consistent with models. Thus, we could still expect a milder impact on the flux correction factors derived from the simulation and number counts measurements due to the slight discrepancy between the models and observed number counts.

3.5 Summary

In this work, we describe and present the first results of the NIKA2 Cosmological Legacy Survey (N2CLS), a large blind millimeter survey in GOODS-N and COSMOS fields with NIKA2 on the IRAM 30m telescope. The survey reaches an unprecedented combination of depth at similar wavelengths and sky coverage in the two fields. Our analysis and result summarize as follow:

1. We develop a framework to accurately correct the instrument and statistical effect on source detection and flux measurements in N2CLS data. This new framework takes advantage of the new simulation features in the IRAM official PIIC pipeline, which accepts realistic sky simulations as input models to be injected into the half-difference NIKA2 timeline data. The lower average detected

flux relative to input flux in GOODS-N field demonstrate the importance of the simulation, which allows us to account both for the pipeline filtering and the clustering/blending of sources for the first time in single-dish observations, in addition to the source completeness, purity and flux boosting. We find good reproduction of input source number counts from the detected source in the simulations using our framework, which validates its accuracy in correcting the systematic properties of sources in N2CLS observations.

2. We make new measurements of the source number counts at 1.2 and 2 mm in the two fields. With the largest single-dish sample at 1.2 and 2 mm and the robust corrections on bias and systematics from the simulation, we derive the differential and cumulative number counts in GOODS-N and COSMOS field, covering the largest range of flux from a single blank field survey. We find consistent number counts in GOODS-N and COSMOS field in the overlapped flux ranges. We also find consistent number counts with most of the previous single-dish measurements at similar wavelengths.
3. We derive galaxy number counts directly comparable to the model predictions from a low-resolution single-dish survey for the first time. Using the simulation framework and realistic input sky models, we derive the ratios between the differential/cumulative number counts calculated from input galaxy catalogs and estimated from the detected sources in the simulated observations, R_{diff} and R_{cum}, in each flux bins. We further apply these counts correction factors to remove the impact of large beams of the singe-dish telescope on the source number counts and derive the galaxy number counts. This, for the first time in single-dish surveys, provides number count estimates directly comparable to the high-resolution ALMA observations and number counts predictions from simulation/semi-analytic models.
4. We combine the galaxy number counts from the 2 fields in N2CLS survey and compare them to models predictions from SIDES (Béthermin et al., 2015), Empirical Galaxy Generator (Schreiber et al., 2017), SHARK (Lagos et al., 2020) and Popping et al. (2020) models. The comparison reveals up to a factor of four higher galaxy counts from N2CLS compared to all except for the predictions of SHARK above 2mJy and 0.6mJy at 1.2 and 2 mm, respectively. The SHARK prediction itself, on the contrary, produces up to a factor of two higher number density of faint sources in our observations. This provides the first comparisons to models at the bright end of millimeter number counts that correct for the impact of larger beams on observed number counts in single-dish observations.

The larger galaxy number counts from N2CLS survey relative to various model predictions indicates an underproduction of massive galaxies with active star formation in current simulations and models, and (or) the lack of account for a considerable population of starburst/star-forming galaxies with apparently cold dust emission at high redshift. The upcoming follow-up observations with NOEMA/ALMA will pinpoint the location of DSFGs contribution to the observed N2CLS sources. The rich ancillary data and ongoing JWST observations like COSMOS-Webb will help iden-

tify the multi-wavelength counterpart of these millimeter sources, construct their full SED, determine the redshift distribution and physical properties of this unique long-wavelength selected N2CLS DSFG sample and will provide more strengthen observational test on the models and simulations. This research also reveal the non-negligible impact of beam on the number counts from single-dish survey. We stress the importance of end-to-end simulation like us in the comparison of various results and model predictions.

4 Finding the high-redshift population of DSFGs

Sommaire

4.1 Introduction . . . 120
4.2 Sample, NOEMA Observations and Data Reduction . . . 122
4.2.1 Sample Selection . . . 122
4.2.2 NOEMA observations and data calibration . . . 124
4.2.3 NOEMA Source Identification and Continuum Flux Measurement 125
4.2.4 Extraction of NOEMA millimeter spectra . . . 129
4.2.5 Multiwavelength Photometry of the GOODS-N Sample . . . 129
4.3 Redshift of sources . . . 131
4.3.1 Photometric Redshift of GOODS-N Sources with Optical-IR Data 133
4.3.2 Far-IR Photometric redshift of HLS sources . . . 136
4.3.3 Joint Analysis of Photometric Redshifts and NOEMA Spectra . . 139
4.3.4 Robustness of the Joint Analysis Method . . . 145
4.3.4.1 Robustness under Different Line Widths . . . 145
4.3.4.2 Robustness under Narrower Spectral Coverage . . . 147
4.4 Physical Properties of Sources . . . 149
4.4.1 Kinematics and excitation of molecular gas of HLS sources . . . 149
4.4.2 Dust mass and dust temperature from modified black body fitting 153
4.4.3 Dust and stellar content of GOODS-N sample from SED modeling 157
4.4.4 Molecular gas properties . . . 161
4.4.5 A possible over-density of DSFGs . . . 165
4.5 Discussion . . . 166
4.5.1 Cross-validation and tension between different SED modeling . 166
4.5.2 Implications for the search and study on high-z DSFGs . . . 167
4.6 Summary . . . 168

4.1 Introduction

It is well known that in the (sub-)mm, larger area and relatively deep surveys can efficiently find high-redshift dusty star-forming galaxies (DSFGs) (Béthermin et al., 2015), thanks to the negative k-correction (Casey et al. (e.g. 2014b), also see Fig. 1.9), combined with the shape of the luminosity functions. Such large-area deep surveys are conducted with single-dish telescopes, as with the SCUBA2 instrument on the

JCMT (Holland et al., 2013) or the NIKA2 instrument on the IRAM 30m (Adam et al. (2018) and Perotto et al. (2020), also see Sect. 2.1). The census of dusty star-forming galaxies at high redshift, especially at z>4, is also one of the primary goals of the N2CLS survey.

One of the drawback of (sub)millimeter single dish survey is the the relatively poor angular resolutions. As for N2CLS, the angular resolution of 11.3" and 17.0" at 1.2 and 2 mm makes it difficult to unambiguously identify the multi-wavelength counterparts of the selected sources and to search for the high-redshift population. As already shown by the follow-ups of SCUBA2 sources with ALMA (e.g. Simpson et al., 2020), the combination of single-dish and interferometer surveys is by far the most efficient way of constraining the dusty star formation at $2 < z < 6$. Indeed, the high angular resolution and sensitivity of (sub-)mm interferometers can provide accurate position measurement on DSFGs and thus the identification of their multi-wavelength counterparts.

However, getting photometric redshift from optical-IR is complicated by the lack of sufficiently deep homogeneous multi-wavelength data to analyze large samples. Moreover, DSFGs are subject to significant optical extinction (some of them are even optically dark, see Franco et al. (2018), Williams et al. (2019), and Manning et al. (2022)) which impacts the quality and reliability of photometric redshift estimates and prevents optical/near-infrared spectroscopic follow-up, especially before the delivery of infrared observations from JWST. Photometric redshifts from far-IR/mm broad-band photometry are even more uncertain as the spectral energy distributions (SEDs) in the far-IR/mm do not show any spectral features (but a broad peak), and there is often only few data points on the SEDs to constrain the model. In addition, there is a strong degeneracy between dust temperature and redshift in distant dusty galaxy, which limits the usefulness of simple photometric redshifts (e.g. Blain, 1999). Finally, in the modelling of the FIR emission, optically thin or thick solutions are heavily degenerate. Indeed, the same SED could arise from either cold and optically thin or a warm and optically thick FIR dust emission with no robust way to discriminate between the two by using continuum observations (Cortzen et al., 2020). This often leads to an overestimate of the FIR photometric redshifts because of an apparent colder dust temperature derived from optically-thin emission in high-redshift, starbursting DSFGs.

For the optical and near-IR faint, highly obscured galaxies, spectral scans in the millimeter can be the only way of getting the spectroscopic redshift, as shown in e.g. Walter et al. (2012), Fudamoto et al. (2017), Strandet et al. (2017), and Zavala et al. (2018). The success rate of measuring the redshift using millimeter spectral scans can be very high, being >70% (Weiß et al., 2013; Strandet et al., 2016) and even up to >90% (Neri et al., 2020). Such success is obtained on large samples in a reasonable amount of telescope time but for bright DSFGs. For example, with a total time of 22.8 hours on 13 DSFGs with average 850μm fluxes of 32 mJy, Neri et al. (2020) measured the redshift of 12/13 sources with NOEMA. Weiß et al. (2013) obtained a ~90% detection rate for

sources with $S_{1.4\,mm} > 20$ mJy.

To reach the goal of constraining the obscured SFRD at $z > 4$, we need first to obtain the redshift of N2CLS sources. Although blind spectral scans demonstrate the high success rate of obtaining accurate redshift of bright (sub)millimeter selected high-z galaxies, our N2CLS sample contains many faint fluxes compared to most of the sources in previous research. Considering the overall cosmic evolution of obscured star formation, we also expect a significant number of interlopers with redshift around z=2, on top of the high-z population of our interest. These possible issues suggest that a framework of high-z candidate selection and efficient spectroscopic follow-up is ultimately required for the follow-up studies of the N2CLS survey.

This chapter describes our explorations on the identification and efficient follow-up observations on high-z DSFGs in N2CLS/NIKA2 observation. As a pilot program to try to identify the high-redshift population, we selected 7 high-redshift candidates detected at 1.2 and 2 mm. Four have been selected from their far-IR/mm SEDs photometric redshift in the HLS J0918+5142 field observed with NIKA2. Three have been detected in a small deep field centered around a z ~6.5 candidate in GOODS-N ID12646, Liu et al., 2018 first observed with the NIKA pathfinder (Adam et al., 2014; Catalano et al., 2014), and further observed with NIKA2 (Adam et al., 2018; Perotto et al., 2020) as part of the N2CLS program. This paper presents the spectral scans and (or) continuum obtained with NOEMA on the 7 sources. It is organized as follows. In Sect 4.2, we present the sample, describe the NOEMA observations and data reduction, the extraction of continuum fluxes and spectral scans, and the source identification. In Sect. 4.3, we extensively discuss the redshifts. In particular, we develop a new method that combines both photometric data and spectral scans to measure the redshift. Source properties, such as their dust mass and temperature, kinematics, and excitation of molecular gas, are given in Sect. 4.4. This section also presents the potential discovery of a DSFG over-density at z=5.2 in the HLS field. Section 4.5 give more details on the method of redshift measurements and its validation and discusses the implications of our findings for the search and study on high-z DSFGs. Conclusions are given in Sect. 4.6. Throughout the paper, we adopt the standard flat ΛCDM model as our fiducial cosmology, with cosmological parameters as given by Planck Collaboration et al., 2020.

4.2 Sample, NOEMA Observations and Data Reduction

4.2.1 Sample Selection

Our millimeter sources were selected as high-z candidates from the HLS field observed in the framework of science verification observations with NIKA2 centered on lensed dusty star-forming galaxy HLS J0918+5142and from the GOODS-N field

Table 4.1 – Coordinates and millimeter fluxes of our sample from NIKA (GOODS-N) and NIKA2 (HLS) observations, and SPIRE far-IR photometry (HLS only). The fluxes of the 3 GOODS-N sources now measured with NIKA2 are given in brackets. The 1-sigma flux uncertainty of SPIRE undetected HLS sources are in parenthesis. The NIKA2 and SPIRE fluxes presented in the table only accounts for the uncertainties coming from flux measurements. The SPIRE fluxes of the GOODS-N sources will be described in Table 4.5

.

Source	RA	Dec	F_{250}	F_{350}	F_{500}	$F_{NIKA(2)-1.2}$	$F_{NIKA(2)-2.0}$
12646	12:36:27.5	62:12:18.0	–	–	–	2.8±0.6	0.96±0.20
						[2.20±0.12]	[0.36±0.03]
13161	12:36:36.8	62:11:55.9	–	–	–	1.2±0.6	0.84±0.08
						[1.79±0.12]	[0.27±0.03]
1160047	12:36:21.7	62:12:39.3	–	–	–	2.3±0.6	0.6±0.3
						[N/A]	[N/A]
HLS-2	09:18:17.2	51:41:25.1	(6.1)	11.3±6.1	17.4±6.1	2.9±0.3	0.42±0.07
HLS-3	09:18:23.3	51:42:51.9	(6.1)	(6.1)	(6.3)	2.4±0.3	0.60±0.06
HLS-4	09:18:24.3	51:40:49.7	(6.1)	8.9±6.1	8.9±6.1	1.9±0.3	0.28±0.07
HLS-22	09:18:34.9	51:41:44.9	(6.1)	(6.1)	(6.1)	1.7±0.3	0.36±0.06

observed with NIKA. The details of the NIKA2 and NIKA observations could be found in Sect. 2.2.

From the combined 1.2+2mm signal-to-noise ratio map of the NIKA deep field, we identified three candidates with S/N of 3.4, 3.7, and 4.1. Based on their photometric redshift based on full SED modeling with optical , IR and sub-mm data (see Liu et al. (2015) for the details), these sources were all z∼6 galaxy candidates and identified as: one massive dusty main-sequence galaxy (12646), one clumpy disk-like below-main-sequence galaxy (13161), and one case of a 1.2/2 mm (NIKA) and 500 μm tentatively detected galaxy with neither IRAC nor radio counterpart (1160047; a "dark" IR galaxy). These are ∼1.2-2.8 and ∼0.6-1 mJy sources at 1.2 and 2 mm, respectively, in the NIKA pathfinder observations (Table 4.1).

These sources also fall within the footprint of N2CLS in GOODS-N. N2CLS data have already reached a much smaller noise level, and thus we also provide in table 4.1 the 1.2 and 2 mm fluxes as measured by N2CLS. The N2CLS data have been reduced with the IRAM NIKA2 PIIC software. ID 1160047 is not detected in the deeper N2CLS maps.

We built the first NIKA2 catalog using NIKA2 data reduced using the collaboration pipeline (Ponthieu et al., in prep). Based on the source catalog in the field, we also measured their fluxes in Herschel SPIRE observations at 250, 350, 500 μm, which fully overlaps with the NIKA2 coverage. The SPIRE flux were measured using FASTPHOT [1]

1. https://www.ias.u-psud.fr/irgalaxies/downloads.php

(Béthermin et al., 2010). Other data around this field, including PACS, IRAC, and HST images, cover only a very small part of the field on the west side (where NIKA2 observations have lower signal-to-noise ratios). Thus only SPIRE data were used to select high-z candidates.

From this SPIRE+NIKA2 photometric catalog, we selected four sources detected at both 1.2 and 2 mm with high signal-to-noise ratio (between 5.7 and 9.7) and for which there is a faint (at the level of confusion noise) or no SPIRE counterparts, as to bias the sample towards the highest redshift candidates. Indeed, rough sub-millimeter photometric redshifts, obtained by fitting empirical IR SED templates from Béthermin et al., 2015 to our SPIRE+NIKA2 data, were $z_{phot} \sim 5-7$. These sources are named HLS-2, HLS-3, HLS-4, and HLS-22. Using a new data reduction with PIIC, we measured fluxes between 1.7 and 2.9 mJy at 1.2 mm and 0.28 and 0.60 mJy at 2 mm (see Table 4.1). Although HLS J0918+5142in the center of the field is close to the z=0.22 cluster Abell 773, it is likely lensed by a galaxy at z∼0.63 rather than the cluster itself. For our NIKA2 sources, the magnification by the galaxy cluster is <10%. Therefore, we do not expect the NIKA2 sources to be highly magnified (E. Jullo, private communication).

In total, 3 NIKA sources and 4 NIKA2 sources were selected as high-z DSFG candidates for follow-up observations with PdBI and NOEMA.

4.2.2 NOEMA observations and data calibration

We made follow-up observations using PdBI/NOEMA on these NIKA2 selected candidate high-z galaxies from 2016 to 2020 with 6 different programs. The 3 sources in GOODS-N were observed using the WideX correlator in band3 with the D configuration (project W16EE) of the PdBI. Source 12646 was further followed-up by project E16AI at band1 with D configuration by the PdBI. The rest 4 sources in the HLS field were all observed by NOEMA with the PolyFiX correlator within 4 different programs, which have larger instantaneous bandwidth of 7.7 GHz in each sideband to cover a wider range of spectra. The sample sources were initially targeted by project W17EL (HLS-2/3/4) and W17FA (HLS-22) using 2 setups that continuously cover the spectra from 71 GHz to 102 GHz with the D configuration in band1. HLS-22 was further observed in project W18FA with the A configuration in band1 and HLS-2 and HLS-3 were further observed in project S20CL with the D and C configurations in band2. The total on-source time of all of the proposals above is 63.3 hours. The details of the observations on each source are summarized in Table. 4.2.

NOEMA observations are first calibrated using CLIC and imaged by MAPPING under GILDAS3. Radio sources 3C454.3, 0716+714, 1156+295, 1055+018, 0851+202, and 0355+508 are used for bandpass calibrations during these observations, and the source fluxes are calibrated by LHKA+101 and MWC349. With the calibrated data, we further generate the uv table with the original resolution of 2 MHz. We also produce the continuum uv table of each source by directly compressing all the channels in

Table 4.2 – Information on NOEMA follow-up observations.

Source Name	Setup	ν GHz	$\sigma_{\rm cont}$ μJy/beam	$\sigma_{\rm 2MHz}$ mJy/beam	On-source time hour
12646	W16EE	255.0	215.1	1.58	0.6
	E16AI	108.8	14.8	0.12	13.6
1316113207	W16EE	255.0	99.3	0.76	2.9
1160047	W16EE	255.0	137.2	1.09	1.3
HLS-2	S20CL001	137.5	16.3	0.14	12.0
	W17EL002	84.25	24.4	0.36	0.6
	W17EL001	76.50	13.4	0.24	4.4
HLS-3	S20CL002	144.2	21.4	0.25	2.4
	W17EL002	84.25	22.7	0.36	0.6
	W17EL001	76.50	14.7	0.23	4.5
HLS-4	W17EL002	84.25	21.6	0.36	0.6
	W17EL001	76.50	13.4	0.24	4.5
HLS-22	W18FA001	114.0	7.9	0.20	5.2
	W17FA002	84.25	12.3	0.19	5.4
	W17FA001	76.50	15.0	0.28	4.7

the corresponding lower sideband (LSB) and upper sideband (USB) data with the uv_compress function in MAPPING.

4.2.3 NOEMA Source Identification and Continuum Flux Measurement

We identify the counterparts of our sample in the NOEMA continuum data. We first generate the continuum dirty map with MAPPING and then clean the continuum image of each source with the Clark algorithm within MAPPING. We blindly search for candidate sources by identifying all of the peaks above 4×RMS within the NOEMA primary beam. For each NIKA2 source with observations from several NOEMA projects, we pick the combined continuum uv table from the projects reaching the highest S/N of detection and(or) the best spatial resolution as the reference uv table for source detection and flux measurements. The cleaned image of each source from the reference continuum uv table is shown in Fig. 4.1. In these reference uv tables, the accurate positions and source models are derived with the uv_fit function in MAPPING with the peak positions as the prior position of the fitting and point source as the model. After that, the continuum fluxes at the other frequencies are estimated with source models and positions fixed to that from the sources in the reference uv table.

The continuum fluxes are measured using uv_fit and the same models as given in Table 4.3. We further make primary beam corrections on the source fluxes derived from the uv_fit to account for the reduced response due to the offsets from the phase

center. The corrections are made following Eq. 4.1.

$$S_{cont} = \frac{S_{raw}}{C_{pb}} \tag{4.1}$$

The correction factor of each source, C_{pb}, as a function of the offset from phase center d_{off} is derived following Eq. 4.2, assuming a Gaussian response within the primary beam of the interferometer.

$$C_{pb} = \exp\left(-\frac{{d_{off}}^2}{2{\sigma_{pb}}^2}\right). \tag{4.2}$$

The full-width half maximum (FWHM) of the Gaussian primary beam of each observation, which corresponds to $2.35\times\sigma_{pb}$, is derived following Eq. 4.3, assuming it has the same size as the FWHM of the Airy disk of a circular aperture of the same diameter of every single antenna. The diameter of every single antenna (D) and the wavelength of observation (λ) should be provided with the same unit. For NOEMA, D should be set to 15 meters.

$$\mathrm{FWHM}(") = 2.5 \times 10^5 \times \frac{\lambda}{D} \tag{4.3}$$

The 4 sidebands in the 2 setups of W17EL and W17FA are combined to generate continuum uv tables centered on 3.6 mm, given the low SNR of continuum emission at such a long wavelength. When data are available, the continuum fluxes at higher frequencies are measured both sidebands by sideband and on the combined LSB+USB uv-table. The continuum fluxes are listed in Table 4.4.

We detect 8 NOEMA continuum sources above the S/N threshold in at least one continuum uv table: 3 NOEMA sources are detected in the observations on 2 NIKA2 sources in GOODS-N. For the HLS sample, 5 NOEMA sources are found to be associated with the 4 HLS sources. We further checked the residual RMS on the map with source models more complex than point sources. This does not improve the level of residuals in all but 2 sources. For these 2 sources, HLS-2-1 and HLS-3, the favored simplest models are a circular Gaussian model and an elliptical Gaussian model, respectively. The position and preferred models of each GOODS-N and the HLS sources are listed in Table 4.3, and we note that the position of these sources does not change significantly depending on the model.

In GOODS-N, we cross-matched the coordinates of the detected sources with the source catalog from CANDELS/S-CANDELS survey (Ashby et al., 2015; Barro et al., 2019). The radii of cross-matching are set to 0.85", the half-width of the synthesized beam size of NOEMA observations. We identified the optical-IR counterparts of the 3 NOEMA sources, that are coincident with the counterparts ID12646, ID13161, and ID13207, identified in the super-deblended catalog of Liu et al. (2018). NOEMA observation on 1160047 only reveals low SNR continuum sources that are not coincident

with optical/IR sources from CANDELS/S-CANDELS or radio sources from deep JVLA survey at 1.4 GHz (Owen, 2018). In addition, this NIKA source is not detected in the much deeper data from the NIKA2 Cosmological Legacy Survey (N2CLS), suggesting that 1160047 is very likely to be a noise spike in the original NIKA data. In the following studies on the GOODS-N sample, we discard source 1160047 and only focus on the rest of the sample.

For HLS, we detect 5 continuum sources with NOEMA. Similar to 13161/13207, the NIKA2 source HLS-2 is also resolved into a double source in our high-resolution NOEMA observation with SNR~10. The rest of the NIKA2 sources are all associated with 1 single NOEMA source.

For the 4 NIKA/NIKA2 sources (12646, HLS-3, HLS-4, and HLS-22) with a single NOEMA counterpart, we compare their positions in the NOEMA and NIKA/NIKA2 observations. The maximum offset is found in HLS-3 with a value of 1.9 arcsec. The average offset is 0.9 arcsec among these 4 sources, which suggests a high positional accuracy of NIKA/NIKA2 for locating sources with relatively high S/N.

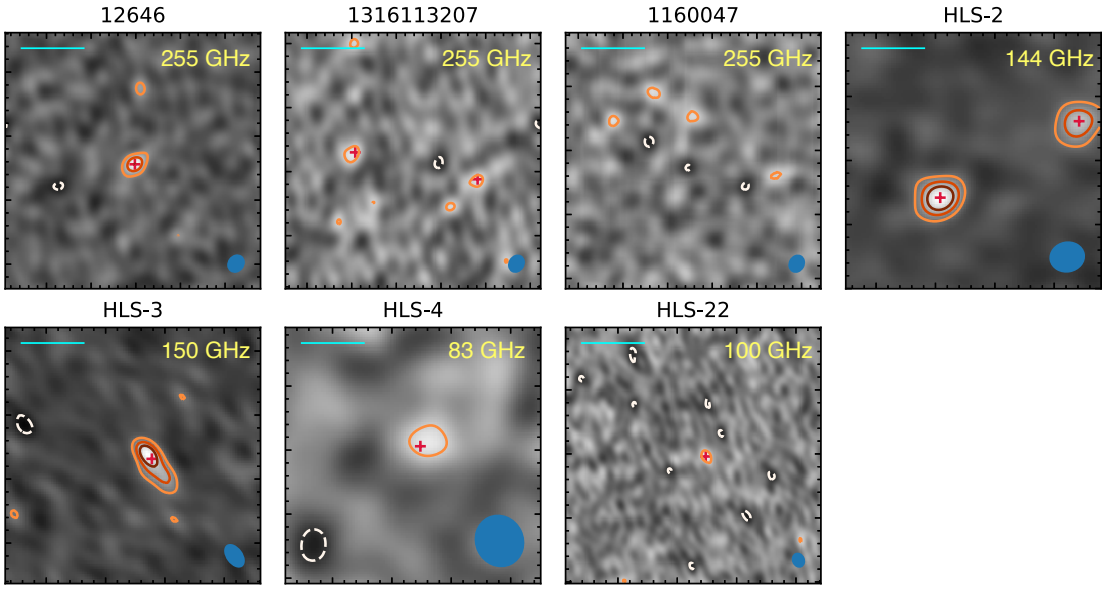

Figure 4.1 – Cleaned images of NOEMA observation on our seven NIKA and NIKA2 sources. The effective beam size and shape of each map are shown in the bottom right of each panel. The contour levels from white to dark red correspond to -3, 3, 6, and 9× RMS of each map, respectively. The red crosses mark the position of detected NOEMA sources from the uv_fit. The scale bars in the maps correspond to 5 arcseconds in the sky. The frequencies of the continuum data are presented in the upper right corner of each panel.

Table 4.3 – NOEMA continuum source positions and best-fit sizes

Name	RA	Dec	FWHM(")
12646	12:36:27.5	62:12:17.8	point
13161	12:36:37.5	62:11:56.5	point
13207	12:36:36.1	62:11:54.4	point
HLS-2-1	09:18:16.3	51:41:28.1	1.2
HLS-2-2	09:18:17.5	51:41:22.1	point
HLS-3	09:18:23.1	51:42:51.6	2.8×0.7
HLS-4	09:18:24.26	51:40:50.3	point
HLS-22	09:18:34.76	51:41:44.8	point

Table 4.4 – Continuum fluxes from PdBI/NOEMA observations

Name	Sideband	ν_{cont} [GHz]	S_{cont} [μJy]	SNR
12646	full	255.0	1660.3±191.2*	8.7
–	full	108.8	144.3±13.2	10.9
13161	full	255.0	621.2±114.0*	5.4
13207	full	255.0	530.1±128.8*	4.1
HLS-2-1	LSB+USB	143.7	238.9±29.5*	8.1
–	LSB+USB	82.5	41.6±15.4	2.7
HLS-2-2	LSB+USB	143.7	231.2±12.9*	17.9
–	LSB+USB	82.5	44.1±12.7	3.5
HLS-3	LSB+USB	150.0	417.5±43.7*	9.6
–	LSB+USB	82.5	32.3±14.2	2.3
HLS-4	LSB+USB	82.5	48.4±10.0*	4.8
HLS-22	USB	113.7	58.0±16.2	3.6
–	LSB	100.3	45.1±10.1*	4.5
–	LSB+USB	81.9	<41.5	N/A

Notes. $^{(*)}$ Datasets and fluxes derived with free parameters on source position and shape in uv_fit. The fluxes at the other frequencies on a specific source are fitted with positions and shapes fixed to the same as marked dataset, which are given in Table 4.3.

For all but HLS-4 and HLS-22, our NOEMA observations measure their continuum fluxes at a frequency close to the representative frequencies of NIKA2 1.2/2 mm bands. Compared to the NIKA2 1.2 mm fluxes in Table 4.4, the total PdBI 255 GHz fluxes of 12646 and 13161 are about 30% lower. As for the ~150 GHz fluxes from NOEMA observation of 2 NIKA2 HLS sources, the NOEMA and NIKA2 fluxes are consistent for HLS-3. The total NOEMA fluxes of the 2 components of HLS-2 are 50% higher than that measured by NIKA2, while still being consistent with each other within 3 σ uncertainties.

4.2.4 Extraction of NOEMA millimeter spectra

We extract the millimeter spectra of NOEMA continuum sources from the full uv table. The uv tables are first compressed by the uv_compress function in MAPPING, which makes averages within several channels to enhance the efficiency of line searching with higher SNR per channel and smaller loads of data. For observations in band1, we set the number of channels to average to 15 while the observations in band2 and band3 are averaged every 25 channels, which corresponds to channel widths of 107km/s, 100km/s and 59km/s at 84 GHz, 150 GHz and 255 GHz, respectively. Given the typical line width (a few hundred to one thousand km/s) for sub-millimeter galaxies (Spilker et al., 2014), the compression of uv tables could still ensure Nyquist sampling by 2-3 channels on the emission line profiles and preserve the accuracy of line center and redshift measurement.

To extract the spectra, we perform uv_fit on the compressed spectral uv table with the position and source model fixed to the same as those given in Table 4.3. For the observations of the W17EL002 setup, we flagged the visibilities associated with one antenna significantly deviating from the others. Given the relatively low angular resolution of most of our data on HLS sources (~5" in band1 and ~2" in band2), these galaxies are unlikely to be significantly resolved, thus the uv_fit at fixed positions on the uv tables should be able to uncover the majority of their line emission.

We further remove the continuum in the extracted spectra, assuming a fixed spectral index of 4. This is equivalent to a modified black-body spectrum with a fixed emissivity at 2, and is generally consistent with the dust emissivity we derived in Sect. 4.4.2. We use these continuum subtracted NOEMA spectra for redshift searching and emission line flux measurement (see Sect. 4.3.3 and Sect. 4.4.1). An example of extracted spectra and continuum model to be removed is shown in Fig. 4.2.

4.2.5 Multiwavelength Photometry of the GOODS-N Sample

Based on the source identification in Sect. 4.2.3, we compile optical-to-near-IR photometry of the 3 continuum sources detected in our NOEMA observations on the GOODS-N sample from Barro et al. (2019). The catalog contains multiwavelength photometry from near UV to infrared bands of Spitzer IRAC observation for sources

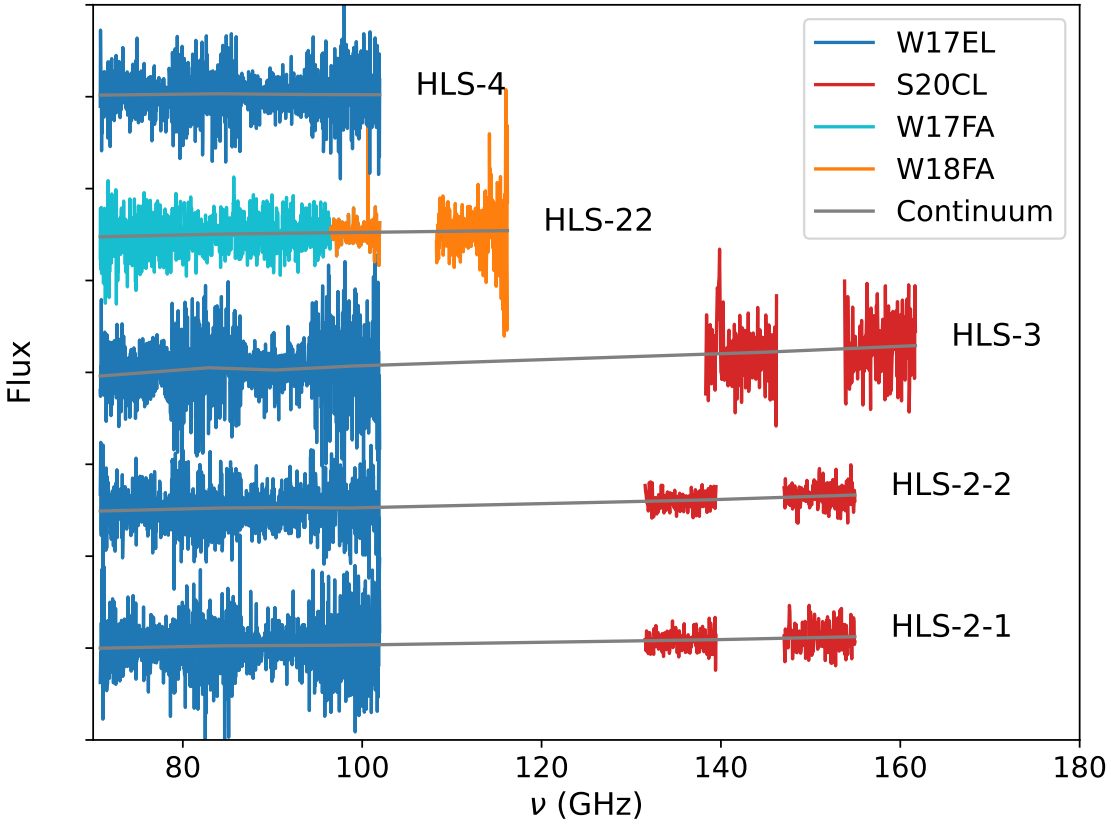

Figure 4.2 – Spectrum of a source (HLS-2-1) extracted from the uv tables from 2 NOEMA programs, as well as the continuum model to be subtracted.

detected in the H-band data of the HST CANDELS survey. Apart from Barro et al. (2019) data, we further added the S-CANDELS catalog from Ashby et al. (2015) to include any near-IR dropout sources, which are expected to be at high redshift and with high dust extinction. We further obtained the deblended fluxes of Spitzer MIPS 24 μm, Herschel PACS/SPIRE, and SCUBA2 observations of these 3 sources from Liu et al. (2018). We cross-match our sources with these catalogs using the coordinates given in Table 4.3. The distance threshold is fixed to 0.85", which corresponds to the half-width of the NOEMA beam size. The photometric information of these 3 sources are listed in Table 4.5 and are used in the following analysis on source SEDs in Sect. 4.3.1.

Figure 4.3 shows the RGB color images of the optical-IR counterparts for the 3 GOODS-N sources, as well as NOEMA source positions. Source 12646 does not have a clear counterpart in HST CANDELS images, which is consistent with its absence in the catalogs of Barro et al. (2019). This also makes 12646 an "HST-dark" galaxy, indicating that it might be a high-redshift or (and) heavily obscured source. The rest two sources, 13161 and 13207 are detected in both deep HST and Spitzer IRAC images. As for 13207, its optical-IR counterpart shows 2 slightly blended peaks in HST images, while Barro et al. (2019) treated them as a single source in their photometric catalog. This could be an ongoing galaxy merger or 2 galaxies aligned along the same line of sight by chance. We also notice a ~0.2" offset between the optical-IR peaks in HST and the NOEMA continuum positions of 13207. This offset probably suggests that the rest-frame UV/optical emission and FIR emission could be dominated by different regions of the galaxy, as already seen in some high-z starburst galaxies (Hodge et al., 2016; Gómez-Guijarro et al., 2018), although the expected position uncertainties of the NOEMA counterpart at its SNR and synthesized beam size is still comparable to the observed offset (see Eq.1 in Reid et al. (1988)). Both issues discussed above would challenge the basic assumptions on the energy balance of CIGALE SED fitting on 13207 in Sect. 4.3.1 and introduce some difficulties during the analysis.

4.3 Redshift of sources

Accurate redshift is a prerequisite to the accurate estimate of the physical properties of high-z galaxies. However, accurate and systematic determination of the redshifts of DSFGs has been challenging for decades, due to their faintness in optical-IR and the degeneracy between far-IR colors, dust temperature, and redshift. In this section, we describe the different methods and summarize the results of the redshift measurements on our sample, with both photometric and spectroscopic data described in Sect. 4.2. Specifically, we introduce a new joint analysis framework to determine the redshifts of NIKA2 sources combining the probability distribution function of photometric redshifts with the corresponding IR luminosities and blind spectral scans, which helps us identify the low SNR spectral lines in the NOEMA spectra.

Table 4.5 – Multi-wavelength photometry of three GOODS-N sources. Non-detections in Liu et al. (2018) are presented with 1σ uncertainties from their catalog in parentheses. The NIKA2/NOEMA fluxes of these 3 sources are given in Table 4.1 and Table 4.4.

Band	12646 flux [μJy]	13161 flux [μJy]	13207 flux [μJy]
F435W[1]	—-	0.028±0.019	0.034±0.019
F606W[1]	—-	—-	0.133±0.016
F755W[1]	—-	0.018±0.013	0.340±0.022
F814W[1]	—-	0.046±0.035	0.334±0.037
F850LP[1]	—-	0.034±0.015	0.396±0.021
F105W[1]	—-	0.054±0.013	0.398±0.015
F125W[1]	—-	0.144±0.013	0.470±0.014
F140W[1]	—-	0.213±0.055	0.568±0.036
F160W[1]	—-	0.443±0.029	0.714±0.024
MOIRCS_K[1]	—-	1.63±0.03	1.28±0.02
CFHT_Ks[1]	—-	1.55±0.10	1.72±0.09
IRAC1[1]	1.36±0.21	8.45±0.05	4.90±0.07
IRAC2[1]	2.49±0.30	13.7±0.1	6.65±0.06
IRAC3[1]	4.50±0.15	19.0±0.5	9.21±0.55
IRAC4[1]	9.20±0.18	18.6±0.5	14.2±0.5
IRS16[2]	6.44±9.76	24.4±8.3	14.0±6.4
MIPS1[2]	15.6±4.4	151±7	21.8±3.4
PACS100[2]	511±413	803±627	(561)
PACS160[2]	612±829	(1958)	3621±1146
SPIRE250[2]	2367±1268	$(10.3\pm4.8)\times10^3$	6239±2208
SPIRE350[2]	4827±1705	$(15.0\pm2.4)\times10^3$	9176±2094
SPIRE500[2]	(2435)	$(12.7\pm4.3)\times10^3$	8348±3749
SCUBA2[2]	4800±370	2480±880	1920±770

Notes. [(1)] Barro et al. (2019) [(2)] Liu et al. (2018)

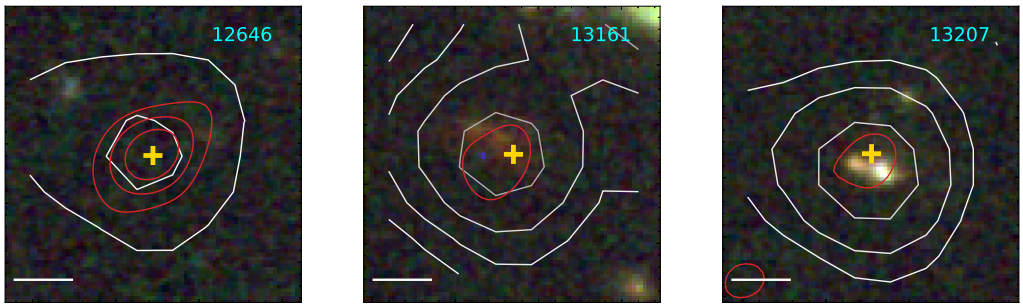

Figure 4.3 – Optical-IR counterparts of 3 NOEMA sources in GOODS-N. The background color images are produced by data from CANDELS survey. The observation using F814W, F125W and F160W filters are used as blue, green and red layer to produce the background images. The S-CANDELS data at 3.6 μm are shown with white contours, where different levels correspond to 0.005, 0.01, 0.02 and 0.04 MJy/sr, respectively. NOEMA continuum emission is shown with red contours, where the levels correspond to 3, 5 and 7 times of the RMS of the cleaned image. The yellow cross shows the position of NOEMA sources coming from the uv_fit results in Table 4.3. The images are 5"×5" and the scale bars in the images correspond to 1" length.

4.3.1 Photometric Redshift of GOODS-N Sources with Optical-IR Data

With the optical to millimeter photometric data given in Table 4.1 (only for the single source 12646 at 2mm), Table 4.4 and Table 4.5, we perform full SED modeling on the 3 GOODS-N sources using CIGALE. It models the stellar and ISM emissions simultaneously and considers energy balance in the reprocessing of stellar emission by the dust (Burgarella et al., 2005; Noll et al., 2009; Boquien et al., 2019). For the SED fit, we use the BC03 model with solar metallicity (Bruzual and Charlot, 2003), Chabrier initial mass function (Chabrier, 2003), and a star formation history (SFH) of one initial starburst and one delayed starburst with exponential decays (sfh_delayed) to model the stellar emissions. The dust extinction law from Charlot and Fall (2000) is used to account for the absorption of stellar emission from ISM. As for the modeling of dust emission from IR to the millimeter, we use the IR SED template from Dale et al. (2014). We also make the redshifts as a free parameter in the fit to determine the photometric redshift from the output probability distribution.

The grid of key free parameters associated with the stellar population, extinction, dust, and redshift in our fit are listed in Table 4.6. As most of our sources do not have rest-frame UV detections to constrain the age of young stellar populations, we made the fit with the e-folding time of the recent starburst set to be much longer than the burst age, assuming a nearly constant SFR in the most recent starburst to reduce the

Table 4.6 – Choice of CIGALE Parameters for photometric redshift analysis

Parameter	Values
age_main	500, 1000, 2500
tau_burst	10000
age_burst	10, 30, 100
f_burst	0.0, 0.003, 0.01, 0.03, 0.1, 0.3, 1
Av_ISM	0.3, 0.6, 1.0, 1.5, 2.0, 2.5, 3.0, 3.5, 4.0, 5.0
slope_ISM	-1.3, -1.0, -0.7, -0.4, -0.1
slope_BC	-1.3
dust.alpha	0.125 to 3.625, step 0.5
redshift	1.0 to 7.5, step 0.1

Table 4.7 – Photometric redshift of GOODS-N sources.

Name	z_{CIGALE}	z_{EAZY}	$z_{Barro19}$	z_{Liu18}	z_{3D-HST}
12646	$3.7^{+2.1}_{-0.3}$	$7.3^{+1.1}_{-1.2}$	N/A	$6.8^{+1.0}_{-1.0}$	N/A
13161	$2.3^{+0.1}_{-0.3}$	$2.8^{+0.1}_{-0.1}$	$4.8^{+0.2*}_{-0.2}$	$5.0^{+0.5}_{-0.5}$	$5.1^{+0.1}_{-0.3}$
13207	$4.3^{+0.2}_{-0.1}$	$4.3^{+0.2}_{-0.2}$	$3.6^{+0.1}_{-0.1}$	$4.1^{+0.3}_{-0.3}$	$4.3^{+0.1}_{-0.1}$

Notes. (*) Failed SED fitting according to the information in Rainbow Navigator

number of models to be fitted.

CIGALE returns the best-fit model, the probability density distribution of the parameters, and the χ^2 of each combination of parameters considered in the fit. For the 3 sources in GOODS-N, the comparison between photometric data and the best fit model, and the probability density distribution of the source redshift are shown in Fig. 4.4. The best fit, median, and $\pm1\sigma$ uncertainties of the photometric redshifts are listed in Table 4.7.

We also analyze the optical and near-IR data only with EAZY (Brammer et al., 2008) to independently derive the photometric redshift of the 3 sources and cross-check with the results from CIGALE. The photometric data are fitted with the default setting of EAZY with the redshift range set to be 0.01 to 9.00 with a spacing of 0.01. Apart from our own photometric redshift analysis, we also checked the photometric redshift values based on the super-deblended technique described in Liu et al. (2018), as well as the redshifts from Barro et al. (2019) and 3D-HST (Skelton et al., 2014; Momcheva et al., 2016). The best-fit models and redshift probability distributions from the EAZY fitting are also presented in Fig. 4.4. All photometric redshift measurements are listed in Table 4.7 for comparison.

For source 12646, the SED fitting using CIGALE returns a poorly constrained photometric redshift, with a primary peak in probability density distributions at $z \sim 3.7$ and

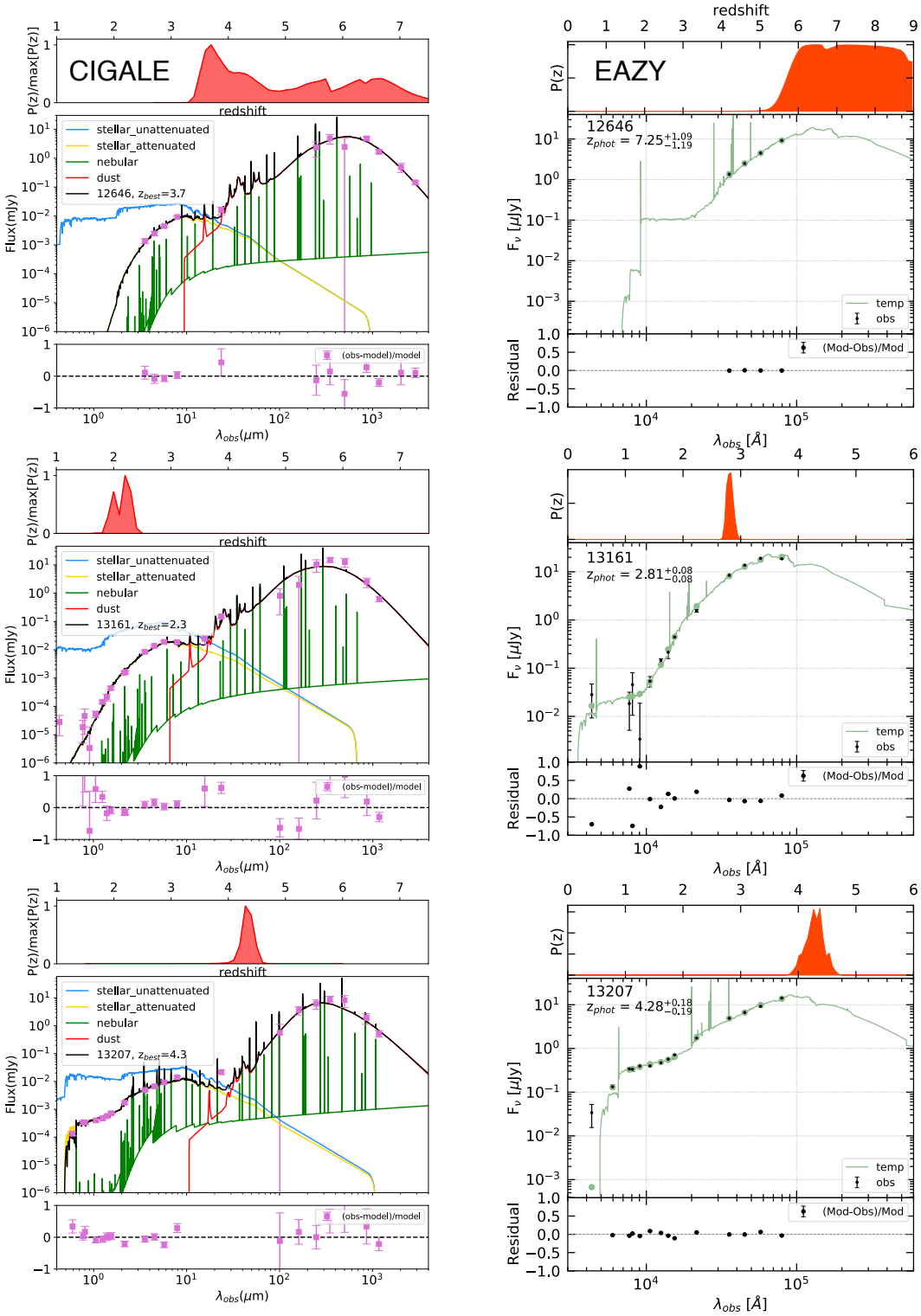

Figure 4.4 – CIGALE (left) and EAZY (right) fitting on the 3 GOODS-N sources. From the top to bottom block in each plot: the redshift probability density distribution; the best-fit model, SED components (CIGALE only) and photmetric data; the residual of the photometric data relative to the best-fit.

a secondary peak around z=6. The results from EAZY and Liu et al. (2018) favor a very high redshift at $z > 5.5$, and largely exclude the possibility of being at $z = 3-5$. From the photometric redshifts, as derived with the above-listed methods, we conclude that 12646 is unlikely to be at $z < 3$, which is consistent with the redshift distribution of massive galaxies that remain undetected in HST CANDELS observations in the H band (Wang et al., 2019).

The redshifts of the other two sources are more precisely constrained with their better-sampled optical-IR SEDs. The CIGALE SED fitting returns the best redshift solutions at $z = 2.3$ and $z = 4.3$, respectively. For source 13207, we find 3 in the other 4 redshift measurements are highly consistent with the CIGALE results at $z = 4.3$. Thus, we take this value in the following. For source 13161, which is a redder and optically fainter source, the different results are in tension. Our CIGALE and EAZY fitting return low redshift, between $z = 2-3$, while the rest 3 methods suggest a much higher redshift at around z=5. We double-checked the output of Barro et al. (2019) and 3D-HST, through the Rainbow Navigator [2] and found that their best-fit model is inconsistent with the data, suggesting an occasional failure of their fit on this source. Furthermore, the high redshift from 3D-HST leads to a best fit stellar mass of $10^{12.4}M_{\odot}$, which becomes nonphysical for an unlensed source. Thus, we keep the 2 lower redshift solutions (z=2.3 and 2.8) in the following analysis on star formation rate, stellar mass, molecular gas mass, and dust mass in Sect. 4.4.

4.3.2 Far-IR Photometric redshift of HLS sources

The HLS field of NIKA2 science verification observation is not covered by deep optical and infrared ancillary data, making it impossible to do a full SED modeling as we did on GOODS-N sources. Apart from NIKA2 observations, this field was observed by SPIRE with the Herschel Lensing Survey (Egami et al., 2010), which adds photometric data at 250, 350, and 500 μm covering the peak of FIR SED of high-redshift galaxies.

We fit the far-IR SED with dust emission templates to estimate the redshifts and IR luminosities of these sources. Given the poor angular resolution of the FIR data, we are not able to obtain the fluxes of every single component resolved by NOEMA observations on HLS-2. Thus we only fit with the integrated fluxes under the assumption that the 2 components blended within the beam of SPIRE and NIKA2 are located at the same redshift.

We used 2 sets of FIR dust templates: the synthetic infrared SED templates from Béthermin et al. (2015) and the MMPZ framework (Casey, 2020) using parametrized dust templates from Casey (2012).

Béthermin et al. (2015) templates could be described as a series of empirical dust

2. http://arcoirix.cab.inta-csic.es/Rainbow_navigator_public/index.php?

Table 4.8 – Photometric redshift of HLS sources

Name	z_{B15}	z_{MMPZ}
HLS-2	$4.6^{+0.8}_{-0.7}$	$3.5^{+1.5}_{-0.8}$
HLS-3	$5.9^{+1.2}_{-0.9}$	$4.6^{+2.5}_{-1.4}$
HLS-4	$4.3^{+1.0}_{-1.0}$	$3.3^{+0.6}_{-0.6}$
HLS-22	$4.7^{+1.3}_{-1.0}$	$3.1^{+4.6}_{-1.4}$

SEDs of galaxies at different redshifts. The dust SEDs are produced based on the deep observational data from infrared to millimeter. It considers 2 populations of star-forming galaxies, starburst and main-sequence galaxies, and produces the 2 sets of empirical SED templates correspondingly. We fit our photometric data points with the templates of main-sequence galaxies, which consist of 13 SEDs at each redshift. These templates include the average SED and the SEDs within $\pm 3\sigma$ uncertainties with steps of 0.5σ. The estimated redshift, as well as the 1σ uncertainties are listed in Table 4.8.

Casey (2012) describes the intrinsic FIR dust emission of galaxies using a generalized modified black-body model in far-IR plus a power-law model at mid-IR. For the SED fitting with Casey (2012) template, we work within the framework of the MMPZ algorithm Casey (2020). It considers the intrinsic variation of dust SED at different IR luminosity, as well as the impact of rising CMB temperature at high redshift. The default set of IR SEDs fixes the mid-infrared spectral slope to 3 and dust emissivity β to 1.8. The template SED also considers the transition from optically thin to optically thick when going to higher frequencies, where the frequency of unity opacity ($\tau(\lambda)$=1) is fixed to 200 μm. The redshift, the total infrared luminosity, and the corresponding wavelength at the peak of IR SED are the main parameters to be considered for the fit. The empirical correlation between the latter two parameters is also taken into account during the fit.

The process returns the probability density distribution of source redshifts, the probabilities of each combination of the templates and redshifts, as well as the corresponding infrared luminosity. Estimated redshifts are listed in Table 4.8. From the probabilities of each combination of parameters, we also derive the weighted average of the total infrared luminosity of each redshift using a similar procedure as given by Eq. 4.4.

From the results in Fig. 4.5 and Table 4.8, we find that MMPZ returns systematically slightly lower redshifts than the template fitting using (Béthermin et al., 2015), although the two redshifts are still consistent within their uncertainties. The infrared luminosities returned by MMPZ are also systematically lower by ~0.3 dex, especially at redshifts beyond 3 The faintness and large uncertainties on these sources in the 3 SPIRE bands make the constrain on the peak of their IR SEDs much worse than for brighter/lensed high-z sources, which leads to large uncertainties on the estimated

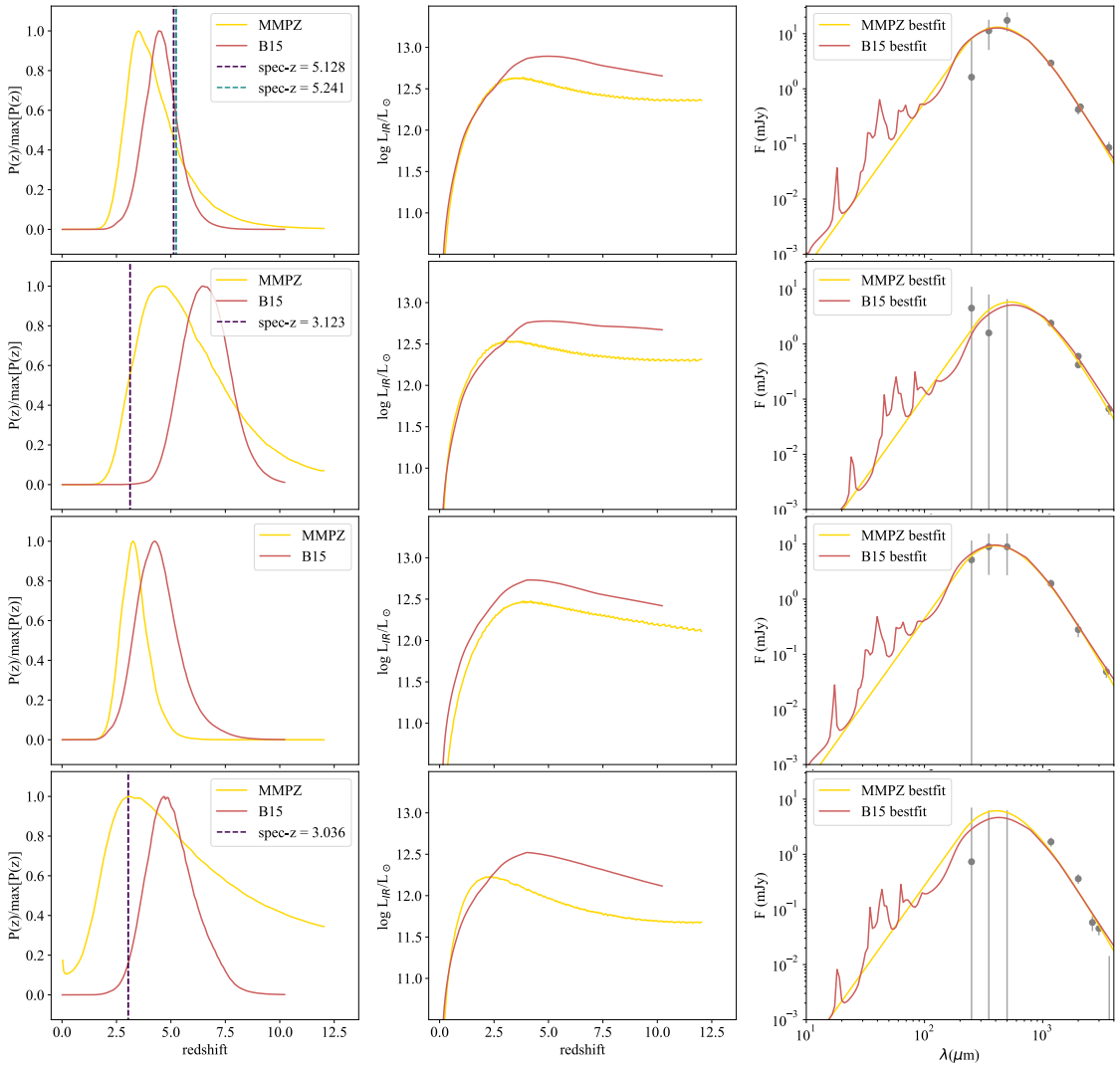

Figure 4.5 – The results of IR template fitting on 4 HLS sources with Béthermin et al. (2015) dust templates and MMPZ method, using the SPIRE, NIKA2 and NOEMA photometry. The plot in the first column shows the probability density distribution (normalized by the peak values) of each sources. The second column shows the evolution of weighted average infrared luminosity with the redshift. The third column shows best fit SED models with the observations. Sources from the top to the bottom are HLS-2, HLS-3, HLS-4 and HLS-22.

total IR luminosity. Compared to the template fitting with Béthermin et al. (2015), MMPZ further takes the CMB heating and dimming (da Cunha et al., 2013) into consideration. Although this could affect the dust emissivity index β and, as a result of β-T degeneracy, the dust temperature and IR luminosity, the β values are all fixed to 2 in these 2 templates. Thus we consider that the inclusion of the CMB effect is not the major contributor to the differences between the results of the two template fitting

methods.

The difference in the estimated total IR luminosities will be propagated to the joint photometric and spectral analysis on source redshift in Sect. 4.3.3. In order to test the stability of the following analysis and make cross validation between the two methods, we keep and use the SED fitting results from both methods in the global redshift solution search in Sect. 4.3.3.

4.3.3 Joint Analysis of Photometric Redshifts and NOEMA Spectra

Optical-IR photometric redshift codes, such as EAZY (Brammer et al., 2008) and LePhare (Arnouts and Ilbert, 2011), have been applied to large extragalactic surveys from the local universe to the cosmic noon. Their accuracy largely relies on our knowledge on the stellar emission in UV, optical and near-IR, while high-z DSFGs could be completely dark at these wavelengths due to their heavy dust obscuration. The uncertainties on the photometric redshift from CIGALE SED fitting, δz/(1+z), could still be as large as 45% for 12646 in GOODS-N with only IRAC photometry included. For the HLS sources without deep optical-IR observations, we could only rely on the more uncertain dust SED models, which lead to even larger uncertainties on the photometric redshift.

The most precise and unbiased approach to get the redshift of heavily obscured, sub-mm bright galaxies is searching for FIR-millimeter spectral lines with blind millimeter spectral scans. In a continuous spectrum, 2 to 3 lines detected at high significance are required for getting unambiguous redshift solution. However, given the faintness of spectral lines at high redshift and the sparseness of these lines relative to the instantaneous bandwidth of current heterodyne receivers, it could be extremely time-consuming to satisfy such criteria in spectral scans made by current millimeter interferometers.

Limited by the sensitivity and frequency coverage of spectral scans, we failed to detect any lines in 4 of the PdBI/NOEMA continuum sources (12646, 13161, 13207, and HLS-4) in our observations in 2016 and 2017. The rest of the sources have one significant/tentative line detection, which, in principle, could be consistent with several possible redshift solutions when assuming different line species/transitions.

Moreover, in our research, the full SED fitting and the FIR template fitting in Sect. 4.3.1 and Sect. 4.3.2 could not only estimate the source redshift but also give constraints on the total infrared luminosities at any sampled redshift in the SED fitting. From the output χ^2 and IR luminosities of all models at one given redshift, we could derive the weighted average value of total infrared luminosity of the source at this redshift using Eq. (4.4):

$$L_{\mathrm{IR,avg}}(z) = \frac{\sum_{j=1}^{n} L_{\mathrm{IR,j}}(z) \times \exp\{[\chi^2(z,j) - \sigma(j)^2]/2\}}{\sum_{j=1}^{n} \exp\{[\chi^2(z,j) - \sigma(j)^2]/2\}}. \tag{4.4}$$

The $\sigma(j)$ in Eq. (4.4) is a weighting term to account for the deviation of the 13 model SEDs from the median of star-forming galaxies at given redshift in Béthermin et al. (2015), which include 1 median SED and 12 SEDs within $\pm3\sigma$ uncertainties with a spacing of 0.5σ. When using these templates, the values of $\sigma(j)$ are between -3 and +3 with a step of 0.5. Otherwise, the $\sigma(j)$ will be set to 0 when using the output from MMPZ or CIGALE.

With a series of average IR luminosity over the redshift grid in the SED fitting, we linearly interpolate the IR luminosity at any given redshift in between. We further use the IR luminosity to constrain the fluxes of strong FIR-millimeter emission lines at any given redshifts based on the well-defined, almost redshift invariant L_{FIR}-L_{line} relations in the form of Eq. 4.5:

$$L_{\rm line} = N \times log(L_{\rm FIR}) + A. \tag{4.5}$$

With the estimated fluxes of different line species at given redshifts, we generate a model spectrum in the frequency range of the NOEMA spectral scans and compare this model with the observations. The luminosities and fluxes of the ^{12}CO lines of J(1-0) to J(12-11), two transitions of [CI], and the [CII] line at 158 μm are predicted based on various scaling relations found in the literature. The detailed information is listed in Table 4.9 and references therein.

We note that this framework aims to find the redshift solution. According to the current test with different line widths (see the Appendix), the result is not very sensitive to the height of the peak, thus we could expect adding the information on the scatter of L_{IR}-L_{line} scaling relation will not significantly change the solution found by the code (even if we just use the 31 GHz band1 spectra). Besides, if we account for these, a series of templates need to be generated, which will dramatically increase the time of execution.

When generating the model spectra, we assume the emission lines have Gaussian profiles. We fix the FWHM of the Gaussians to 500 km/s[3]. As the redshifts directly sampled during the SED fitting could be too sparse (e.g. $\delta z = 0.1$ for CIGALE) to cover the possible spectroscopic redshift of the sources, we also linearly interpolate the $L_{FIR,med}$-z relations from IR template fitting to a finer redshift grid and generate the corresponding model spectra to be compared with observations. The spacing between adjacent redshifts in the resampled grid satisfies Eq. 4.6, which is equivalent to a fixed spacing in velocity (Δv) between adjacent redshifts:

$$\Delta z = \frac{\Delta v(1+z)}{c}. \tag{4.6}$$

We fixed the Δv to be 1/3 of the chosen FWHM, making the emission line profile to be Nyquist-sampled by the predicted line centers at corresponding redshifts in the new grid. This ensures that emission lines in the spectra and their corresponding redshift solutions will not be missed in our analysis due to poor redshift sampling. The goodness of the model prediction at a given redshift is evaluated by log-likelihood $\ln(\mathscr{L}_{\rm spec}(z))$ from the χ^2 between the model spectra and the data, as given below in

3. The line width assumption on the robustness of the method is discussed in Sect. 4.3.4.1

Table 4.9 – Parameters of the log-linear scaling relation between strong far-IR to millimeter lines and far-IR/total IR luminosity used to generate model spectra for our analysis. The parameters of the scaling relations come from Greve et al. (2014), Liu et al. (2015), Valentino et al. (2018) and De Looze et al. (2014)

Line Name	Rest Frequency [GHz]	N	A
CO(1-0)[1]	115.27120	0.99	1.90
CO(2-1)[1]	230.53800	1.03	1.60
CO(3-2)[1]	345.79599	0.99	2.10
CO(4-3)[2]	461.04077	1.06	1.49
CO(5-4)[2]	576.26793	1.07	1.71
CO(6-5)[2]	691.47308	1.10	1.79
CO(7-6)[2]	806.65181	1.03	2.62
CO(8-7)[2]	921.79970	1.02	2.82
CO(9-8)[2]	1036.9124	1.01	3.10
CO(10-9)[2]	1151.9855	0.96	3.67
CO(11-10)[2]	1267.0145	1.00	3.51
CO(12-11)[2]	1381.9951	0.99	3.83
[CI](3P1-3P0)[3]	492.16065	1.28	0.00
[CI](3P2-3P1)[3]	809.34197	1.28	0.61
[CII][4]	1900.5369	1.01	2.84

Notes. [1] Greve et al. (2014) [2] Liu et al. (2015) [3] Valentino et al. (2018) [2] De Looze et al. (2014)

Eq. 4.7 and Eq. 4.8:

$$\mathscr{L}_{\rm spec}(z) \propto \exp\left(-\chi^2_{\rm spec}(z)/2\right), \tag{4.7}$$

$$\chi^2_{\rm spec}(z) = \sum_{\nu_i} \frac{[f_{\nu_{i,obs}} - f_{\nu_{i,model}}(z)]^2}{\sigma_{\nu_i}(z)^2}. \tag{4.8}$$

In addition to the goodness of match between spectra and models, we further account for the goodness of SED fitting at given redshifts, $\chi^2_{\rm SED}$(z) (CIGALE or SED template fitting), which is defined in the same form as Eq.(4.8). The joint log-likelihood at each sampled redshift reads as:

$$\mathscr{L}_{joint}(z) \propto \mathscr{L}_{\rm spec}(z) \times \exp\left[-\chi^2_{\rm SED}(z)/2\right]. \tag{4.9}$$

As the template fitting relies on the FIR to millimeter data with relatively poor angular resolutions, one issue needed to be further considered for the HLS sources is how to estimate the contribution to the total infrared luminosities by multiple sources within one NIKA2 beam. HLS-2 is an example of this case in our sample, which has 2 components detected at high SNR in NOEMA band2 data separated by 12.4". Since we do not have further information from high-resolution optical and infrared data, we assume that they have similar redshifts and share the same FIR SED. Based on the contribution of each component to the total NOEMA flux, we allocate the total infrared luminosities from the template fitting to each component of HLS-2 and derive their final joint-likelihood of redshift

We search for the most probable redshift solutions of the 8 NOEMA sources using the joint redshift analysis framework described above, using the output from SED fitting and spectra extracted at NOEMA positions. The results of joint log-likelihood of redshift from photometry+spectral scan analysis on 3 GOODS-N sources and 5 HLS sources are shown in Fig 4.6 and Fig 4.7, respectively. For each source, we normalize the $\mathscr{L}_{\rm spec}(z)$ to the peak value, which helps us quantitatively compare the relative goodness of match between model predictions and observed spectra of our samples at different redshifts. We select all the peaks in $\ln(\mathscr{L}_{\rm spec}(z))$ with an amplitude larger than -10 and width larger than 3 samples in the applied redshift grid as the possible redshift solutions of our sources, using the "find_peaks" algorithm in SciPy. Considering the large uncertainties on total infrared luminosity of HLS sources, we further cross validate their possible redshift solutions by repeating the joint likelihood analysis using the output IR luminosity at different redshifts from MMPZ fitting, and apply the same algorithm to record the possible redshift solutions.

Compared to the log-likelihood of redshift with photometric constraints only, the joint analysis helps us to highlight significant isolated peaks for the redshift of HLS-2-1, HLS-2-2, HLS-3, and HLS-22 at z=5.241, 5.128, 3.123 and 3.036, respectively. The redshift with maximum log-likelihood value is also not sensitive to the choice of IR templates. As shown in Fig 4.6, for these 4 sources, (Béthermin et al., 2015) IR template and MMPZ find almost the same redshift where the joint log-likelihood value reaches the maximum, which further confirms their redshift solutions as listed above. For HLS-4, although having the best constrained photometric redshift from IR template

Table 4.10 – Summary on the redshifts of NOEMA sources, including the optical-IR photometric redshift from CIGALE and EAZY (z_{OIR}), far-IR photometric redshift from the fitting with Béthermin et al. (2015) template and MMPZ (z_{FIR}), the best spectroscopic redshift solution from our joint analysis (z_{joint}) and the redshift values which we fixed to in the measurement of source physical properties (z_{fix}).

Name	z_{OIR}	z_{FIR}	z_{joint}	z_{fix}
HLS-2-1	N/A	$4.6^{+0.8}_{-0.7}$, $3.5^{+1.5}_{-0.8}$	5.241	5.241
HLS-2-2	N/A	$4.6^{+0.8}_{-0.7}$, $3.5^{+1.5}_{-0.8}$	5.128	5.128
HLS-3	N/A	$5.9^{+1.2}_{-0.9}$, $4.6^{+2.5}_{-1.4}$	3.123	3.123
HLS-4	N/A	$4.3^{+1.0}_{-1.0}$, $3.3^{+0.6}_{-0.6}$	N/A	4.3, 3.3
HLS-22	N/A	$4.7^{+1.3}_{-0.9}$, $3.1^{+4.6}_{-1.4}$	3.036	3.036
12646	$3.7^{+2.1}_{-0.3}$, $7.3^{+1.1}_{-1.2}$	N/A	N/A	3.7, 7.3
13161	$2.3^{+0.3}_{-0.1}$, $2.8^{+0.1}_{-0.1}$	N/A	N/A	2.3, 2.8
13207	$4.3^{+0.2}_{-0.1}$, $4.3^{+0.2}_{-0.2}$	N/A	N/A	4.3

fitting, the lack of emission line detection in the band1 spectral-scan observations makes our analysis fail to find prominent peaks in the joint log-likelihood and thus no reliable redshift solution is found for this source.

For the 3 GOODS-N sources, we also derive the joint log-likelihood with the CIGALE fitting and spectral scans and present them in Fig 4.7. The limited spectral coverage of the WideX leads to noncontinuous redshift coverage when using the emission line catalog in Table 4.5, which is also reflected in the joint log-likelihood of the 3 sources. For these 3 sources, although we could find some peaks based on the criteria described above, all of them are coincident with the noise spikes on the edges of WideX spectra. Thus, we conclude that the observations failed to detect any emission line and high significance in the spectra of 3 GOODS-N sources and no secure redshift can be obtained. Given their probability distribution of photometric redshift, it is likely that the narrow spectral coverage of our earlier PdBI observations missed all strong spectral lines in these 3 sources.

In Table 4.10, we summarize the redshifts from the joint analysis method (z_{joint}), as well as the optical-IR (z_{OIR}) and far-IR (z_{FIR}) photometric redshifts from our SED analysis for comparison. Our estimate of source properties in the following sections will fix the redshift to the values indicated in the last column (z_{fix}) of Table 4.10. These redshifts come from the joint analysis, if a best redshift solution is found, or their photometric redshifts from the SED fitting. For 12646, 13161, and HLS-4 with ambiguous photometric redshifts from two different methods (CIGALE/EAZY, or B15/MMPZ), we will use the bestfit redshifts of both in the analysis and provide two different measurements in the tables of summary.

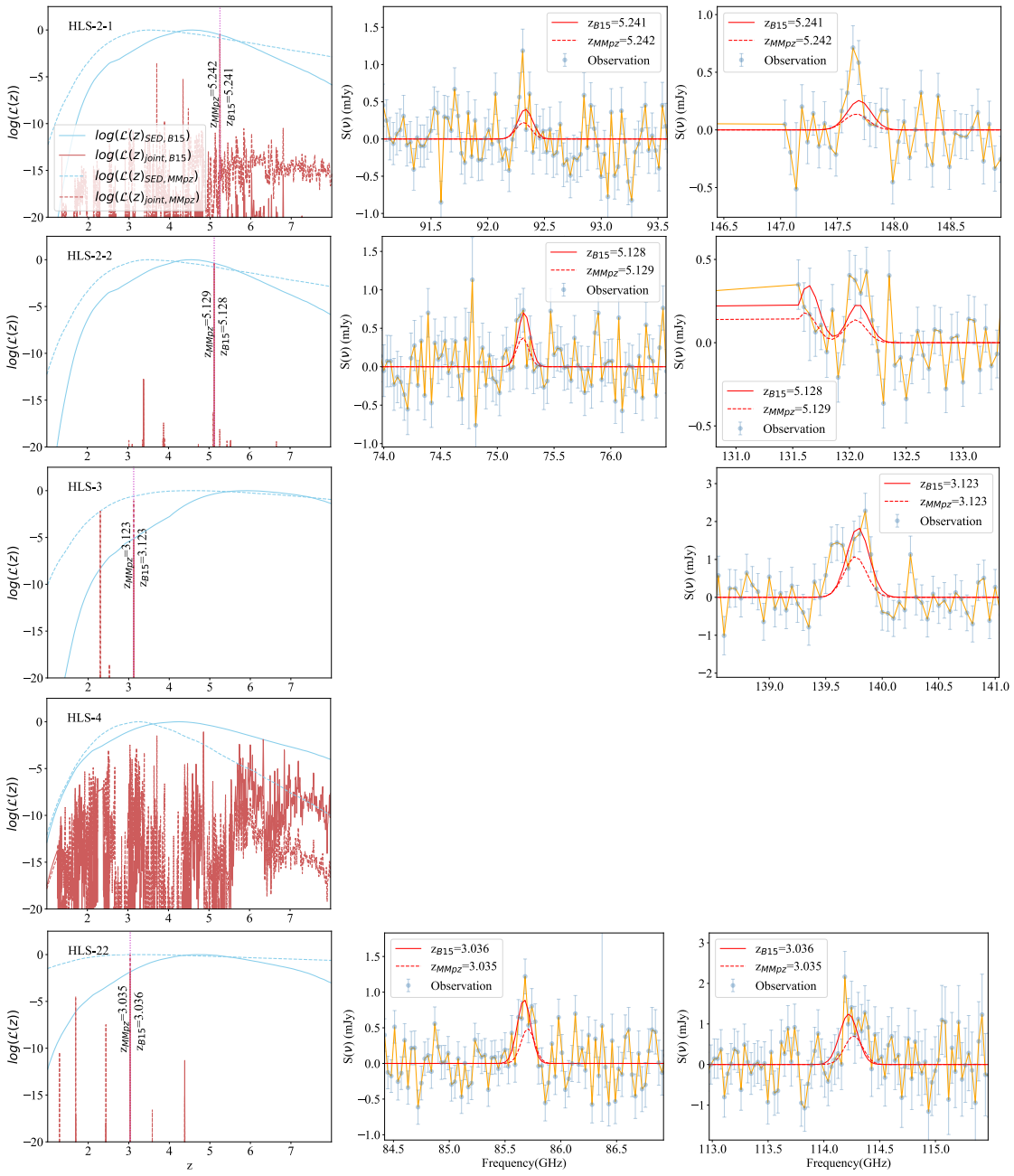

Figure 4.6 – Joint analysis on the redshift of 4 HLS sources with the SED fitting based on (Béthermin et al., 2015) dust templates or MMPZ. The first column shows the normalized log-likelihood and the joint log-likelihood for each source. The second and third column show the cutout of spectra around candidate spectral lines at the best redshift solutions. The lines shown in the second column are detected in the earliest band1 spectral scans (W17EL and W17FA) and those in the third row are detected in the additional follow-up observations (W18FA and S20CL). The spectra models at the most probable redshift based on (Béthermin et al., 2015) or MMPZ IR luminosities are plotted as solid and dashed red lines. We emphasize that these models are not coming from parametric fitting but are generated using the estimate on the total infrared luminosity and the $L_{CO}(L_{[CI]})$-L_{IR} scaling relations.

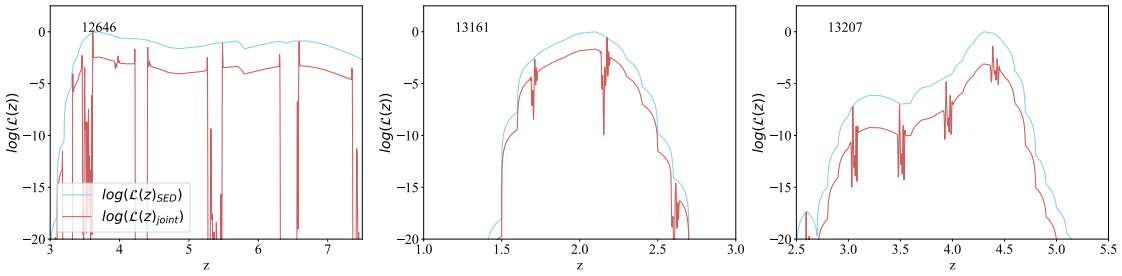

Figure 4.7 – Joint analysis on the redshift of 3 GOODS-N sources with the SED fitting results of CIGALE. The shape of the joint log-likelihood (red solid lines) of GOODS-N sources are significantly different from those of HLS sources in Fig. 4.6, which is due to the noncontinuous redshift coverage of considered spectral lines in the relatively narrow frequency range of the WideX spectra. The smooth parts of the joint log-likelihoods of GOODS-N sources correspond to the redshift ranges with no CO/[CI]/[CII] lines falling into the frequency coverage of the source spectrum.

4.3.4 Robustness of the Joint Analysis Method

The analysis of the source properties of our sample, such as dust mass, temperature, and star-formation rate, largely relies on the estimated redshift from the joint analysis method, which is subject to assumptions on the line widths and line luminosities. To test the robustness of the redshift returned from the joint-analysis method, we make two tests with model spectra of varying line widths and with NOEMA data of more limited spectral coverage.

4.3.4.1 Robustness under Different Line Widths

One of the key assumptions is the width of the emission lines, which is fixed to 500km/s in our practice. Previous studies reveal a correlation between total IR/line luminosity and far-IR to millimeter line width, possibly originating from the regulation of gaseous disk rotation by gravity or (and) feedback from star formation or AGN (Bothwell et al., 2013; Goto and Toft, 2015). The assumed line width generally matches the average of DSFGs with ULIRG-HyLIRG luminosities in infrared, which is similar to the derived IR luminosity of our sample. However, observations also show significant scatters among IR luminous DSFGs. Our sample could be a typical example of the variety of line width of luminous DSFGs, which have line FWHMs ranges from ~250km/s (HLS-2-1) to ~750km/s (HLS-3). Besides, the assumption of Gaussian line profile generally holds for most of our sources, but HLS-3, as described in Sect. 4.4.1, has a significant double-peak feature in the detected emission line in band2.

The impact on the joint analysis results from the mismatch between real and assumed line width and profile are uncertain before our practice. Thus, we make the following test to check if and how the results of this joint analysis could change with the assumption of different line widths. In addition to the default setting of 500 km/s FWHM Gaussian line profile, we further perform the joint analysis with the line pro-

file of model spectra set to Gaussians of 300km/s and 800 km/s in FWHM, using the redshift and infrared luminosity derived from the fit with Béthermin et al. (2015). We identify the redshift solutions of the 4 HLS sources with at least 1 line detected under these 2 different assumptions, using the same method and criteria described in Sect. 4.3.3. The results are listed in Table 4.11.

From the results in Table 4.11, we conclude that the redshift solutions from the joint analysis method introduced by our work are generally not sensitive to the assumptions on emission line widths. For all sources but HLS-22, we find little variation in the redshift solutions under different line width assumptions. The differences of $\Delta z \sim 0.003$, as shown in Fig. 4.8, are mostly originating from the changes in the peak intensity of emission lines, which could lead to slight variations of $\chi^2(z)$. However, such little difference is still within the width of the emission lines, and will neither cause false identification of emission line nor affect the analysis on line fluxes and kinematics in Sect. 4.4.1 with the corresponding central frequency as an initial guess.

Table 4.11 – Redshift of HLS sources from the joint-analysis with models of different line width

Name	$z_{500km/s}$	$z_{300km/s}$	$z_{800km/s}$
HLS-2-1	5.241	5.242	5.243
HLS-2-2	5.129	5.129	5.132
HLS-3	3.123	3.122	3.125
HLS-22	3.036	2.436	3.034

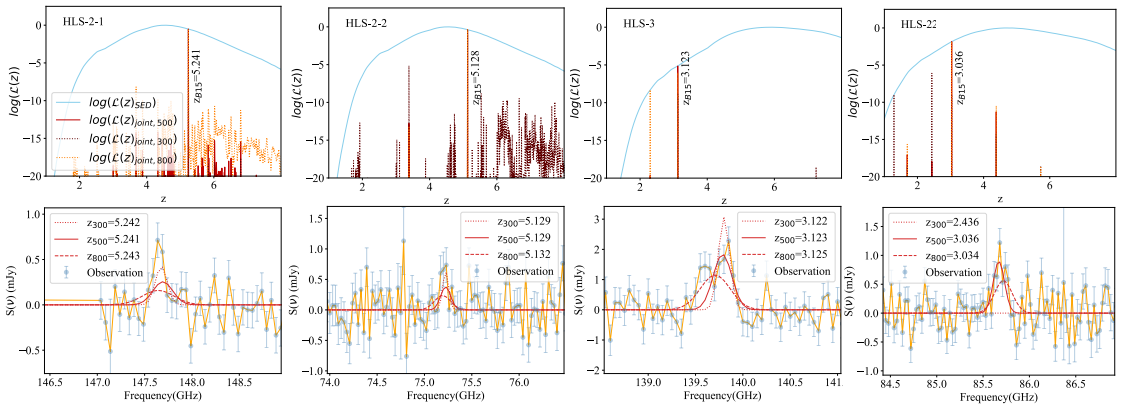

Figure 4.8 – First row: Joint log-likelihood of 4 HLS sources with models spectra with line widths of 300km/s, 500km/s and 800km/s. Second row: Comparison between the models of these 3 line widths at the corresponding redshift solution and the observed source spectra.

The only case of significant inconsistency in redshift from the test is HLS-22, where the procedure using 300km/s line width strongly favors a redshift solution at $z = 2.436$.

Given the frequency of the 2 emission lines detected with high SNR, we are confident about the redshift solutions at $z = 3.036$ from the analysis with the model spectra of 500km/s line width. We check the 300km/s model and the data at z=2.436 and find the mis-identification is caused by a strong noise spike at 100.64 GHz, as shown in Fig. 4.9. The false identification suggests an increased sensitivity to narrow spikes in the spectrum with the decrease of model line width. In our calculation of $\chi^2_{\rm spec}(z)$ and correspondingly, joint log-likelihood, their variation with redshift are dominated by the goodness of match between model and data within the range of model line profiles. With a narrower line width in the model, the number of data points that dominate the variation of $\chi^2_{\rm spec}$(z) will be smaller compared to the cases with wider line width. This will make the analysis with narrow line width more sensitive to single spurious data points, like the noise spike in HLS-22 spectra, and lead to the mis-identification in Fig. 4.9. A less aggressive spectral binning along frequency and a pre-processing with sigma clipping could probably reduce such false identification in practice.

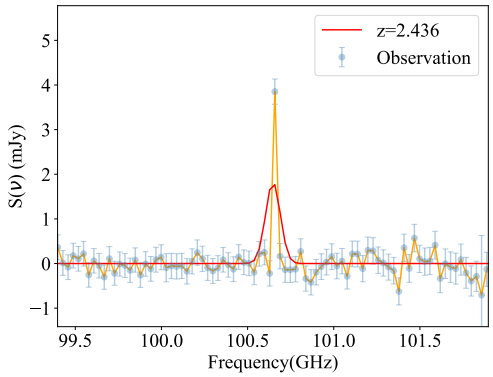

Figure 4.9 – Comparison between the observed spectra of HLS-22 and the model spectra with FHWM of 300 km/s at the best redshift solution z=2.436. The features identified as an emission line is a strong noise spike in the data.

4.3.4.2 Robustness under Narrower Spectral Coverage

Millimeter spectral scans made by interferometers are widely used to blindly search for the emission lines from candidate high redshift DSFGs, determine their spectroscopic redshift, and study the conditions of their cold ISM (Strandet et al., 2016; Fudamoto et al., 2017; Jin et al., 2019; Neri et al., 2020; Reuter et al., 2020). These spectral scan observations are designed to cover a continuous frequency range with several spectral setups. For ALMA and NOEMA, the default setup of the blind spectral scans at their current lowest frequency band covers ~ 31 GHz. The earliest observations in 2018 on HLS sources blindly and continuously cover the spectra of HLS sources between 71 GHz, and 102 GHz in NOEMA band1 with 2 setups, which follows this basic strategy of blind redshift search. To test the joint analysis method under more

Table 4.12 – Redshift of HLS sources from the joint-analysis with the 31 GHz continuous spectra observed in 2018

Name	z_{true}	$z_{B15,2018}$	$z_{MMPZ,2018}$
HLS-2-1	5.241	5.241	5.242
HLS-2-2	5.129	5.131	5.129
HLS-3	3.123	N/A	N/A
HLS-22	3.036	4.380	1.690

realistic conditions in large DSFG redshift survey projects, we apply the method to analyze these band1 spectra and compare their resulting redshifts with the ones in Sect. 4.3.3. The results from this analysis are presented in Table 4.12 and Fig. 4.10, and discussed below.

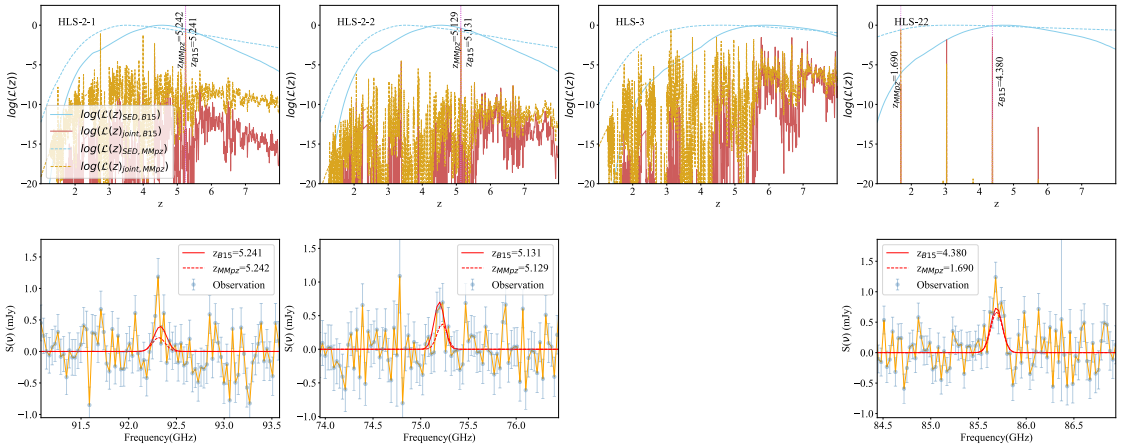

Figure 4.10 – The result of joint analysis on the 4 HLS sources with spectroscopic redshifts derived in Sect. 4.3.3, using only the 31 GHz NOEMA spectral scans observed in 2018. The first row shows the likelihood from SED fittings and joint log-likelihood of photometric and spectroscopic data, using the SED fitting outputs with Béthermin et al. (2015) templates and MMPZ. The comparison between observed spectra and the model spectra predicted by the IR luminosities from the 2 SED fitting results are shown in the second and third rows.

HLS-2-1 and HLS-2-2: the redshift solutions confirmed with the complete data sets are already revealed by the analysis with the output of both the SED fitting technique and the spectra more limited in frequency coverage while being more ambiguous for HLS-2-1 with MMPZ output as prior information. Although the lines are only tentatively detected at most in the spectra, the relatively high redshift of these 2 sources ensures that more than 1 CO line is covered by the spectral scan. If being at the correct redshift, the joint analysis method, in these cases, works equivalently to automatic alignment and stacking of 2 or more lines in the spectra with low SNR. With multiple lines covered, this could numerically boost the stacked SNR of emission lines,

even if none of the single lines are detected with high significance. This could lead to the proper identification of the spectroscopic redshift of these 2 high-z DSFGs, even without the significant detection of CO(8-7) in the new band2 observation.

HLS-22: the analysis based on the SED fitting result of Béthermin et al. (2015) do not significantly improve the rejection of wrong redshift solutions with a single significant emission line. The true redshift is favored almost at the same level as a higher redshift solution at $z = 4.380$. With MMPZ, the analysis returns a mostly favored solution at much lower redshift, while still preserving the true redshift solution as the second solution. Contrary to HLS-2-1 and HLS-2-2, HLS-22 is at a much lower redshift at $z = 3.036$ and falls into the redshift range where only one line could be covered by the spectral scan. With a poorly constrained IR SED and a far-IR photometric redshift only, several ambiguous redshift matching with a single line detection might still be difficult to exclude by the flat SED only log-likelihood. For this kind of sources, similar spectral scans at higher frequencies are possible to cover CO(4-3/7-6) and [CI](1-0/2-1) at the same time, which could help to break the degenerated redshift solutions. The inclusion of deep optical and near-IR data and full SED modeling are also more plausible for these lower redshift sources in extra-galactic deep fields (although unfortunately not available for HLS sources), which could also significantly improve the accuracy of the photometric redshift and break the degeneracy we have here on HLS-22.

HLS-3: No line is detected in the 31 GHz band1 spectral scan, thus no redshift solution is obtained. However, the non-detection helps us to exclude the possibility of several redshift ranges as the solution. It also reveals some "redshift deserts" with no line detection expected under the current frequency coverage and sensitivity. This includes one of the "redshift desert" at $z = 3.0 - 3.3$, covering the most favored redshift solution at $z = 3.123$ in the analysis in Sect. 4.3.3. Under the condition of no line detection, our method could still help to find the most efficient frequency setup of the follow-up observations, which would maximize the number of line detections within these possible redshift ranges.

Given the general robustness of the redshift solutions under different data quality and assumptions, we keep the values found by our default joint analysis with full NOEMA spectral coverage and models of 500km/s line width as the redshift solutions to be applied to HLS-2-1, HLS-2-2, HLS-3 and HLS-22 in the following analysis.

4.4 Physical Properties of Sources

4.4.1 Kinematics and excitation of molecular gas of HLS sources

We find secure redshift solutions to 4 NOEMA sources associated with 3 NIKA2 sources selected in the HLS field, as shown in Table 4.10. Each of these sources has at least one emission line detected with SNR>4 or 2 lines with SNR at 3-4 in NOEMA spectral scans. With these secure line detections, we further measure the flux and line

width of these spectral lines, and derive the corresponding line luminosity at $z_{\rm spec}$. We start the fitting with a single Gaussian model and on the continuum-removed spectra of each source. No matter if they are detected with high significance, all CO/[CI] lines falling into the frequency coverage of NOEMA are considered. To make a more robust analysis on the line width with the relatively noisy spectra, we also force the kinematics of CO and [CI] lines to be the same, during the fitting. As the spectra of HLS-3 shows evidence of a double-peaked line profile, we further quantify the quality of fit under single and double Gaussian models by the Akaike information criterion (AIC) to determine which fit is preferred. AIC is an estimator of prediction error and thereby the relative quality of statistical models for a given set of data. Given a collection of models for the data, AIC estimates the quality of each model, relative to each of the other models and provides a means for model selection. Supposing that we have a statistical model of some data, if k is the number of estimated parameters in the model and $\mathscr{L}$ is the maximized value of the likelihood function for the model, then the AIC value of the model could be described by Eq. 4.10:

$$AIC = 2k - 2ln(\mathscr{L}) \tag{4.10}$$

The preferred model with the best fit to the data is also the one with the minimum AIC value. For HLS-3, the fit with double gaussian model returns an AIC value of -17.1, which suggests a improved fit compared to the single Gaussian model returning a larger value of -11.3. Thus, we take the values from the best-fit of double Gaussian models for the analysis on HLS-3.

The line width, fluxes and 3σ upper limits of CO/[CI] lines for each sources are listed in Table 4.13. We obtain the total flux of each line from the returned Gaussian parameters of the best-fit. The line fluxes with S/N < 3 are given by the 3σ upper limits. For HLS-3 with a double-peaked line profile, the fluxes from the best-fit of two Gaussian components are summed together to obtain the measurement or upper limits of fluxes. The FWHM of the lines from HLS-3 are derived numerically from the best-fit line profile. The corresponding CO/[CI] line luminosities or 3σ upper limits ($L'_{\rm line}$ and $L_{\rm line}$) are also calculated using the Eq. (4.11) and Eq.(4.12) (from Solomon et al. 1997):

$$L'_{\rm line} = 3.25\times10^{7} S_{\rm line}\Delta V \nu_{\rm obs}^{-2} D_L^2 (1+z)^{-3}\,, \tag{4.11}$$

$$L_{\rm line} = 1.04\times10^{-3} S_{\rm line}\Delta V \nu_{\rm rest} D_L^2/(1+z)\,, \tag{4.12}$$

where $S_{\rm line}\Delta V$ is the velocity integrated flux in Jy km s^{-1} , $\nu_{\rm rest} = \nu_{\rm obs}(1+z)$ is the rest frequency in GHz, and D_L is the luminosity distance in Mpc.

The [CI](1-0) lines of HLS-2-1 and HLS-2-2 are covered by the spectral scan but are located at the noisiest edges of the NOEMA sidebands. This makes their upper limits of little scientific value in our following analysis and thus we discard them from the table. The CO(7-6) line of HLS-2-2 is marginally detected but only partly covered by our observations. For this line, we use the output parameters from the spectral line fitting to constrain its flux under a complete Gaussian profile.

Figure 4.11 shows the fit on the emission lines flux and profiles in the NOEMA

Table 4.13 – Emission line fluxes, luminosities and widths of 4 sources in HLS field

Source	Line	F_{obs} (GHz)	S_{line} (mJy km/s)	L'_{line} 10^9 K km/s pc^2	L_{line} 10^7 $L_\odot$	FWHM km/s
HLS-2-1	CO(4-3)	73.852	<240.0	<14.97	<4.70	254
	CO(5-4)	92.309	245.8±65.4	9.81±2.60	6.01±1.59	
	CO(8-7)	147.658	193.2±44.2	3.01±0.69	7.55±1.73	
HLS-2-2	CO(4-3)	75.226	308.5±95.7	18.61±5.77	5.84±1.81	487
	CO(5-4)	94.027	<513.4	<11.19	<6.86	
	CO(7-6)	131.618	<163.9	<3.22	<5.41	
	[CI](2-1)	132.057	196.1±49.6	3.83±0.97	6.50±1.65	
	CO(8-7)	150.406	<151.2	<2.28	<5.72	
HLS-3	CO(3-2)	83.856	<664.9	<32.77	<4.34	752
	CO(5-4)	139.746	1347.3±164.0	23.90±2.91	14.65±1.78	
HLS-22	CO(3-2)	85.691	520.9±81.8	24.47±3.84	3.24±0.50	508
	CO(4-3)	114.250	719.1±170.0	19.00±4.49	5.96±1.41	

spectra on the HLS sources with redshift solutions identified by the joint analysis. The spectra have the same channel width as the ones we used for the joint analysis. From the best fit parameters we find the line widths are generally consistent with the assumption we made during the redshift search in Sect. 4.3.3, with an average FWHM of 500 km/s. Although previous observations reveal that the integrated [CI] and CO lines from the same high-z galaxies may have different line widths and line profiles (Banerji et al., 2018), fixing or relaxing the velocities and widths of different lines during our analysis does not significantly change the quality of the best-fit model.

The observations of 2 sources associated with HLS-2 cover both mid-J (CO(4-3) or CO(5-4)) and high-J CO lines (CO(7-6) or CO(8-7)), allowing us to roughly estimate the conditions of their molecular gas and compare with other DSFGs at similar redshifts using luminosity ratios (expressed in K km/s pc^2). For HLS-2-1, the $L'_{CO(8-7)}/L'_{CO(5-4)}$ is estimated to be 0.31±0.11. This is consistent with the values found in typical high-z SMGs with low excitation (Bothwell et al., 2013) but lower than the reported value of some starburst galaxies and luminous quasars at similar redshift (Rawle et al., 2014; Li et al., 2020). The $L'_{CO(7-6)}/L'_{CO(4-3)}$ and CO(8-7)/CO(4-3) of HLS-2-2 are estimated to be <0.17 and <0.12, respectively. These values are even lower than the typical value of high-z SMGs while still consistent with the low excitation ISM found in the "Cosmic Eyelash" (Danielson et al., 2011).

Apart from CO detections/upper limits, the detection of [CI](2-1) for HLS-2-2 also provides additional insight into the state and condition of its molecular gas reservoir. Andreani et al. (2018) suggested that $L'_{CO(7-6)}/L'_{[CI](2-1)}$ could be used to distinguish secular-evolved (low values) and merger-driven (high values) systems. The [CI] dominated systems with $L'_{CO(7-6)}/L'_{[CI](2-1)}$ around or below 1 are generally found for secular-evolved disk dominated galaxies (Andreani et al., 2018). As neutral carbon could be more easily excited, the low values in secular-evolved systems indicate lower

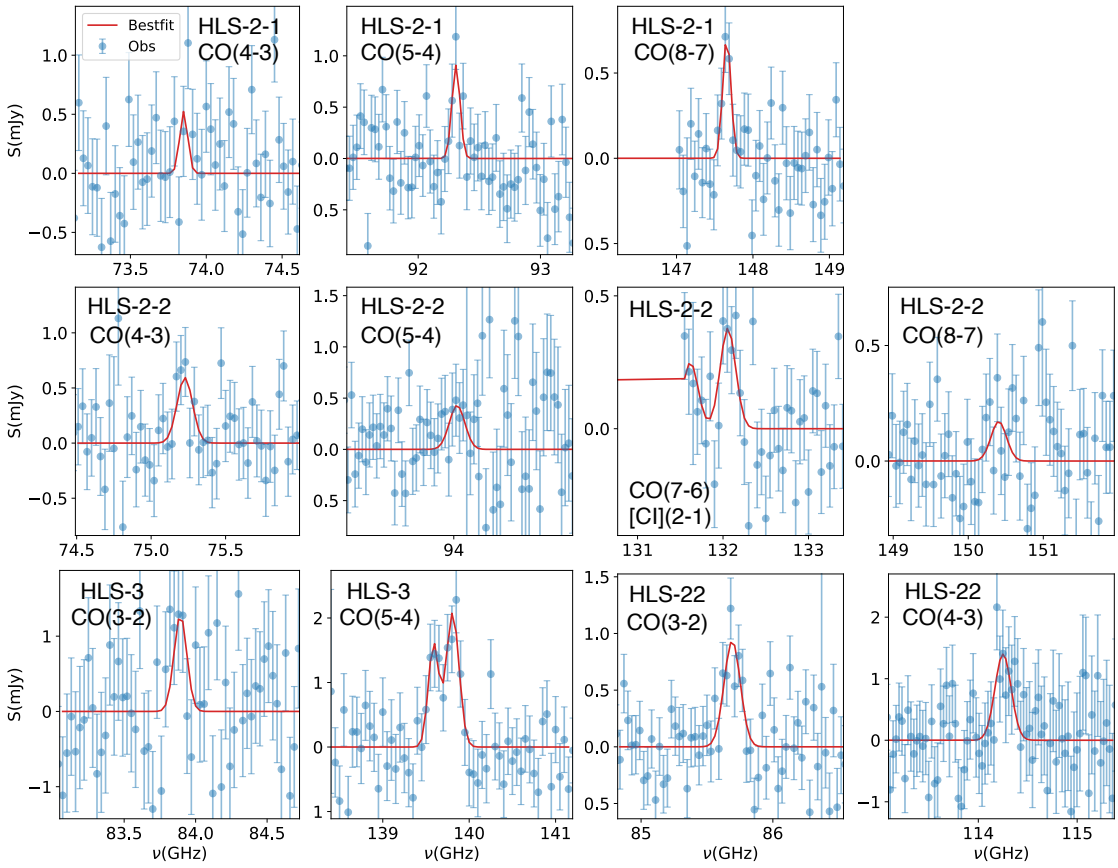

Figure 4.11 – NOEMA data and the best-fit model of all emission lines in the HLS sample listed in Table. 4.13. The name of the source and lines are labeled in each subplot. For the lines coming from the same source, their kinematics are tied to be the same during the fitting. A double-peaked Gaussian model is preferred by the lines from HLS-3 based on AIC, while the rest could be properly fit by single Gaussian models.

gas excitation/more abundant low-density gas. We estimate the $L'_{CO(7-6)}/L'_{[CI](2-1)}$ of HLS-2-1 to be <0.9, which is in agreement with the values found in secularly-evolved galaxies. The low $L'_{CO(7-6)}/L'_{[CI](2-1)}$ also suggests a low excitation molecular gas reservoir in HLS-2-2 and is consistent with the low $L'_{CO(7-6)}/L'_{CO(4-3)}$ and $L'_{CO(8-7)}/L'_{CO(4-3)}$ values in the same galaxy.

For the rest 2 sources with CO detections of less separated quantum numbers J, our observations find $L'_{CO(5-4)}/L'_{CO(3-2)}$ >0.73 in HLS-3 and $L'_{CO(4-3)}/L'_{CO(3-2)}$=0.78±0.22 in HLS-22, respectively. The values of HLS-22 are generally consistent with the average CO SLED of high-z SMGs in Bothwell et al. (2013), being similar to the case of HLS-2-1. HLS-3, on the other hand, has a $L'_{CO(5-4)}/L'_{CO(3-2)}$ ratio higher than typical SMGs in Bothwell et al. (2013) and resembles the average of the SPT sample (Spilker et al., 2014) or the local starburst galaxy M82 (Carilli and Walter, 2013) with higher excitation. However, the observations on these 2 sources do not cover higher-J CO lines like HLS-2, which traces warmer and denser components in the molecular gas reservoir. Thus, with these two line ratio measurements, it is more difficult to conclude if the molecular gas in HLS-3 and HLS-22 has the typical physical condition of that in other high-z galaxies.

4.4.2 Dust mass and dust temperature from modified black body fitting

The Far-IR continuum emission of star-forming galaxies could be well represented by a single-temperature modified black-body model from which the dust temperature (T_{dust}), dust emissivity index (β) and total dust mass (M_{dust}) can be derived. At high redshift, the increasing temperature of the cosmic microwave background (CMB) reduces the contrast of star-forming galaxies with the CMB in Far-IR and millimeter and changes the apparent shape of the spectrum at these frequencies. Considering the impact of the CMB, the observed modified black-body emission of high-z SMG could be expressed as Eq. 4.13 using the optical-thin assumption (da Cunha et al., 2013):

$$S(\nu) = \frac{1+z}{d_L^2} M_{\rm dust} \kappa(\nu) \left[B\left(\nu, \frac{T_{\rm dust}}{(1+z)}\right) - B\left(\nu, \frac{T_{CMB,z}}{(1+z)}\right) \right]. \tag{4.13}$$

As already shown by Eq. 1.4, the dust emissivity $\kappa(\nu)$ in far-IR can be described by a single power law, $k(\nu)=k_0(\nu/\nu_0)^\beta$, where k_0 stands for the absorption cross section per unit dust mass at a given specific frequency ν_0. Here we take $k_{0,850\mu m}$=0.047 m^2/kg from Draine et al. (2014) (also see Berta et al. 2021).

We perform MCMC fitting on the far-IR to millimeter photometric data of HLS and GOODS-N sources in our sample using the optical-thin modified black-body model in Eq. 4.13. The two sources associated with HLS-2 are fitted using their integrated flux, as they have similar redshifts while their individual fluxes at the far-IR could not be obtained with the low resolution SPIRE data. The same fitting is also performed on the bright lensed DSFG HLS J0918+5142in the science verification field, with the new 1.2/2 mm data from NIKA2 observation and the existing flux measurements in

Rawle et al. (2014). For the fit on 12646 and 13161, we adopted the best-fit redshift from both CIGALE and EAZY. For the fit on HLS-4, we adopted the best-fit redshift obtained using the far-IR SED template from Béthermin et al. (2015) and MMPZ.

We developed the MCMC fitting procedures with PyMC3 package. We adopt uniform priors for T_{dust} and M_{dust} and a Gaussian prior centered on 1.8 with σ=0.5 for dust emissivity β [4]. We constrain the temperature to be between T_{CMB} at the given redshifts and 80 K. The redshift values are fixed to z_{fix} given in Table 4.10. We note that although the 2 NOEMA counterparts of HLS-2 are not at the same redshift, the difference between their redshift values is minimal and should not significantly impact the estimation on redshift-dependent parameters, such as the dust temperature.

Figure 4.12 shows as an example the best-fit modified black-body model for HLS-2, as well as the 1σ and 2σ confidence intervals. The original fit with free parameters on HLS-22 and 13161 lead to a non-physically low dust temperature at 16 K and (or) a high β larger than 3, which is due to the limited constraints from SPIRE and low SNR at 3mm continuum (the case of HLS-2), or the lack of data at >1.2mm (the case of 13161). Thus, we perform a new modified black-body fitting on these 2 sources with β fixed to 1.8, being consistent with the average of other HLS and GOODS-N sources, to measure its dust temperature and dust mass. The estimated dust temperature, dust mass, and dust emissivity index of all NIKA2 sources are listed in Table 4.14.

4. The choice of the priors is not affecting the results. For example, using a flat prior with free β changes only the values of β by 10% and the temperatures by ~2-4 K for all sources.

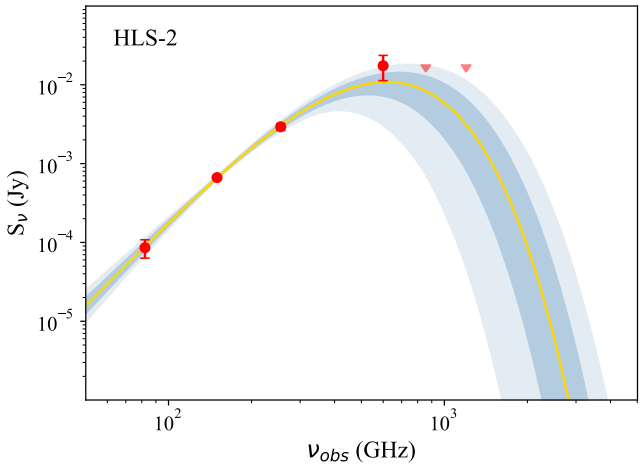

(a) Modified black-body fit on far-IR data

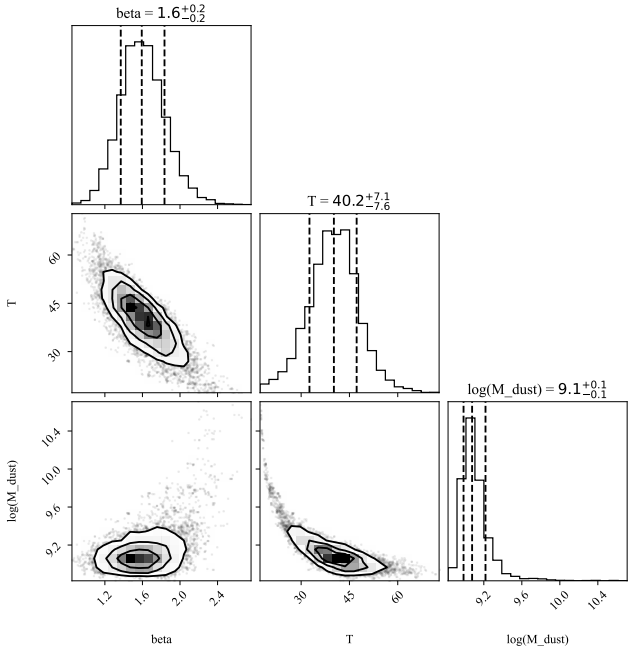

(b) Posterior distribution of parameters

Figure 4.12 – Example of modified black-body fitting on the far-IR to millimeter photometric data of one of our sample galaxies. (a) Photometric data and best-fit model. $\pm1\sigma$ and $\pm2\sigma$ uncertainties of the model are shown with blue shades of different transparency. (b) Corner plot on the posterior distribution of parameters in the fitting. The contours in the corner plots enclose the fraction of mass of the sample corresponding to 1, 1.5, and $2\,\sigma$ in the 2D histogram.

We derive the dust mass of these galaxies of 10^8 to a few times 10^9 $M_\odot$, when apply-

ing the best photo-z from CIGALE or EAZY, respectively, on GOODS-N sources. These values are generally consistent with the dust masses found in blindly selected bright SMGs single-dish surveys (Santini et al., 2010; Miettinen et al., 2017). The abundant dust indicates these high-z dusty star-forming galaxies have already experienced rapid metal enrichment in the first few billion years of the Universe. The dust emissivity β of our GOODS-N and HLS sample (excluding HLS-22) have a median value of 1.75, which is generally consistent with the values found in a variety of galaxies across cosmic time.

We also measure the far-IR luminosities (L_{FIR}) by integrating the model SEDs between 50 and 300 μm at the rest-frame of each source. The L_{FIR} are listed in Table 4.14. Our observations could not properly constrain and model the mid-IR emission of galaxies, which is mainly due to small dust grains, PAH, and possibly AGN torus. Thus, we extrapolate the L_{FIR} (50-300 μm) from our fitting to the total infrared luminosity (L_{IR}, 3-1000 μm) by a factor of 1.3, based on the calibrations given in Graciá-Carpio et al. (2008). We further derive the star formation rates based on the standard scaling relations (Kennicutt and Evans, 2012). The corresponding results are also listed in Table 4.14.

Table 4.14 – Dust properties of NIKA2 sources and HLS J0918+5142 from optical-thin modified black-body fitting. For the fit on all sources, their redshifts are fixed to z_{fix} in Table. 4.10. The dust mass, far-IR luminosity, and SFR of HLS J0918+5142 are corrected by a lensing magnification of 11, as reported by Combes et al. (2012).

Source	z_{fix}	$\log(M_{dust,MBB}/M_\odot)$	$T_{dust,MBB}$ K	β	L_{FIR}(50-300μm) $10^{12}L_\odot$	SFR $M_\odot$/yr
12646	7.3	$8.5^{+0.1}_{-0.1}$	53^{+6}_{-6}	$1.6^{+0.2}_{-0.2}$	$4.46^{+0.47}_{-0.47}$	863^{+91}_{-91}
	3.7	$9.2^{+0.1}_{-0.1}$	30^{+3}_{-3}	$1.6^{+0.2}_{-0.2}$	$1.59^{+0.29}_{-0.30}$	308^{+56}_{-59}
13161	2.8	$8.5^{+0.1}_{-0.1}$	38^{+2}_{-2}	1.8	$1.81^{+0.32}_{-0.32}$	350^{+61}_{-59}
	2.3	$8.7^{+0.1}_{-0.1}$	33^{+2}_{-2}	1.8	$1.24^{+0.24}_{-0.24}$	240^{+43}_{-43}
13207	4.3	$8.0^{+0.2}_{-0.3}$	54^{+11}_{-9}	$1.9^{+0.6}_{-0.5}$	$2.46^{+0.50}_{-0.46}$	476^{+97}_{-89}
HLS-2	5.2	$9.0^{+0.1}_{-0.1}$	43^{+7}_{-8}	$1.5^{+0.2}_{-0.2}$	$5.42^{+1.41}_{-1.50}$	1049^{+273}_{-290}
HLS-3	3.1	$9.6^{+0.2}_{-0.2}$	21^{+5}_{-4}	$1.8^{+0.4}_{-0.3}$	$0.72^{+0.53}_{-0.25}$	139^{+109}_{-48}
HLS-4	4.3	$8.8^{+0.2}_{-0.1}$	39^{+10}_{-9}	$1.7^{+0.4}_{-0.3}$	$3.06^{+1.25}_{-1.32}$	592^{+242}_{-256}
	3.3	$9.1^{+0.2}_{-0.1}$	32^{+8}_{-8}	$1.7^{+0.4}_{-0.3}$	$1.91^{+0.94}_{-0.88}$	370^{+182}_{-170}
HLS-22	3.0	$9.0^{+0.2}_{-0.1}$	26^{+4}_{-4}	1.8	$0.71^{+0.55}_{-0.36}$	137^{+146}_{-70}
HLS J0918+5142	5.2	$9.4^{+0.1}_{-0.1}$	46^{+2}_{-2}	$1.2^{+0.1}_{-0.1}$	$9.73^{+0.36}_{-0.36}$	1883^{+70}_{-70}

The dust temperature of our sample varies significantly from source to source. Fig. 4.13 shows the comparison between the dust temperature of our sample and HLS J0918+5142 with the sources in previous studies (Riechers et al., 2013; Riechers et al., 2014; Riechers et al., 2017; Pavesi et al., 2018a; Béthermin et al., 2020; Faisst et al., 2020; Neri et al., 2020; Bakx et al., 2021; Sugahara et al., 2021) at different redshifts

using the optically-thin assumption, as well as the empirical redshift evolution of dust temperature of normal star-forming and starburst galaxies from (Béthermin et al., 2015) and (Schreiber et al., 2018). The sources show large scatters in dust temperature with respect to these empirical T_{dust}-(z) scaling relations on star-forming/starburst galaxies. Among our sample, the two galaxies from the HLS field with the lowest redshift at $z \sim 3$ (HLS-3 and HLS-22) have the lowest dust temperatures of 20-25 K. These values are significantly lower than those of typical star-forming and starburst galaxies at their redshifts while falling into the regime of SMGs with apparently cold temperatures as reported by some recent studies (Jin et al., 2019; Neri et al., 2020). This population of galaxies could have far-IR SED resembling normal DSFGs at much higher redshift, which explains the significant deviation of the far-IR photometric redshift of HLS-3 from its spectroscopic redshift based on normal star-forming galaxy SEDs in Béthermin et al. (2015). At fixed LIR, we expect galaxies with colder dust temperatures to be brighter at 1.2 mm and thus these galaxies are more favored by our selection, which also explains the higher redshift returned from the template fitting using the stacked SED of the general population of star-forming galaxies. ID 13207 in GOODS-N, on the contrary, has a dust temperature of 54^{+7}_{-7} K, which is ~10 K warmer than typical star-forming galaxies at its redshift. A dust-obscured active galactic nucleus could produce warm dust and alter the shape of far-IR SED. However, we find no counterpart in X-rays at the source position in the Improved Source Catalog of 2Ms Chandra Deep Field North (Xue et al., 2016), making this scenario yet to be tested.

With the 1.2 and 2 mm fluxes from our new observations and the existing fluxes summarized in Rawle et al. (2014), we also re-estimate the dust properties of HLS J0918+5142 using the same modified black-body fitting procedure. We find a best-fit dust temperature of 46±2 K, which is higher than the value in Rawle et al. (2014) at 38±3 K. This difference might be introduced by the significant differences between the GISMO 2 mm flux (9±1 mJy) and our new NIKA2 2mm measurement (14.8±1.5 mJy), which results in a smaller β and, as a result of the β-T degeneracy, a higher dust temperature. Tighter constraints on the continuum fluxes at longer wavelengths (i.e. 3 mm) could solve the tension.

4.4.3 Dust and stellar content of GOODS-N sample from SED modeling

The rich multi-wavelength photometric data of 3 GOODS-N sources (see Sect. 4.2.5) makes it possible to estimate their stellar and dust properties consistently with full SED modeling. With these data, we performed a more detailed full SED modeling with CIGALE. Compared to the photometric redshift analysis derived from CIGALE in Sect. 4.3.1, we here fix the redshift to the single or multiple best-fit solutions from the photometric redshift analysis on the 3 sources. We also use the more versatile dust emission model, "dl2014" (see Draine and Li, 2007; Draine et al., 2014; Boquien et al., 2019), to have independent measurements on their IR luminosities and dust masses to compare with those from the fit of the optically-thin modified black-body. The

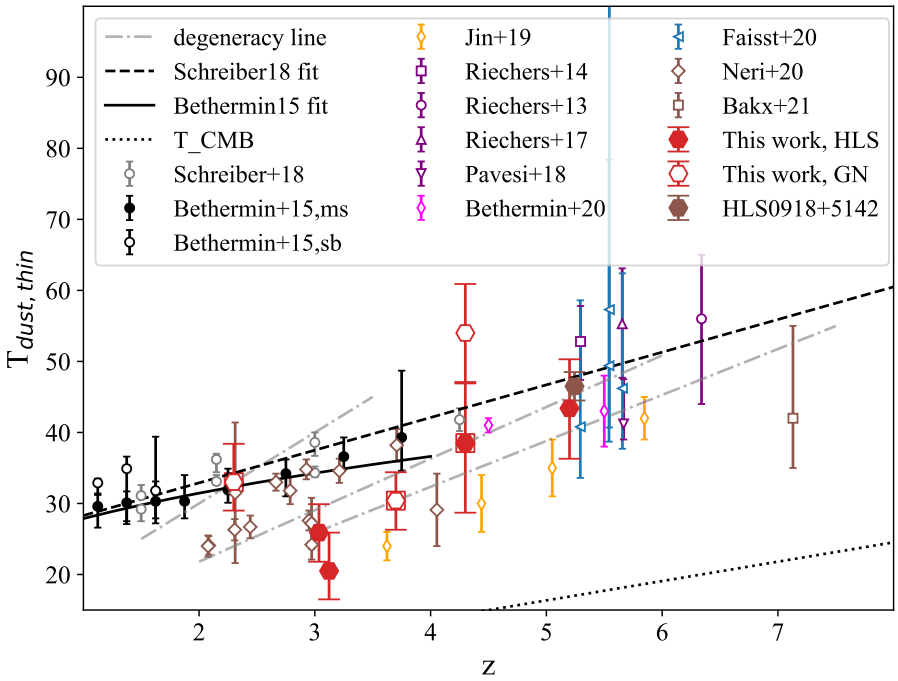

Figure 4.13 – Dust temperature versus the redshift of high-z DSFGs in our sample, and DSFGs/LBGs from literature. The dust temperatures of these sources are all measured under the optically-thin modified black-body model. The corresponding references are listed in the legend. We also overlaid the average T_{dust}-z relation of main sequence galaxies derived by Schreiber et al. (2018) and Béthermin et al. (2015) based on observational data. The 3 sources with uncertain/discrepant photometric redshifts (HLS-4, 12646, and 13161) are further highlighted by red square enveloping the corresponding symbols, and we use dash-dotted grey lines to present the degeneracy between dust temperature and redshift in the plot.

Table 4.15 – Choice of CIGALE parameters for the fitting with "dl2014" model

Parameter	Values
qpah	0.47, 2.50, 4.58, 6.63
umin	0.10, 0.25, 0.60, 1.50, 3.50, 8.00, 20.00, 50.0
alpha	1.0, 1.5, 2.0, 2.5, 3.0
gamma	0, 0.01, 0.03, 0.1, 0.3, 1

Table 4.16 – Dust and Stellar Properties of GOODS-N Sample from Full SED Fitting

Source	z_{fix}	L_{IR} $10^{12}L_\odot$	SFR_{IR} $M_\odot$/yr	M_{dust} $10^8 M_\odot$	$M_{*,CIGALE}$ $10^{11}M_\odot$
12646	7.3	9.85±2.31	1467±344	4.12±0.47	4.89±2.28
	3.7	2.28±0.33	340±49	18.20±2.47	3.31±2.20
13161	2.8	2.88±0.43	429±64	5.17±1.08	2.95±1.70
	2.3	1.89±0.22	281±33	8.11±2.04	5.26±1.91
13207	4.3	5.36±0.78	798±116	2.36±0.68	3.76±0.60

selections of new parameters related to the "dl2014" dust model are listed in Table 4.15.

From the new SED modeling we derive the stellar mass, infrared luminosity and the dust mass of each GOODS-N source. The star formation rates are then estimated based on the derived total infrared luminosity, using the same scaling relation as the one we applied to the results of optically-thin modified black-body fitting. All of these results are listed in Table 4.16.

With these measurements, we compare their stellar mass and star formation rate to typical star-forming galaxies based on their position relative to the star-forming main sequence at their redshifts, as shown in Fig 4.14. The slopes and increments of the star-formation main sequences in the plot for comparison are derived based on the redshift evolution estimated by Speagle et al. (2014). Based on these results from CIGALE fitting, these 3 galaxies have star formation rates generally consistent with the normal star-forming galaxies at similar redshifts. Such consistency suggests that their star formation is more likely to be supported by secular evolution rather than being triggered by more violent processes like galaxy mergers, which is most likely the case of 13161 with an isolated disk-dominated morphology in the HST image. However, for 13207, the HST image reveals two separated components (see Fig. 4.3). It is possible that 13207 is a merger system with a normal star formation rate, but this is hard to test without secure spectroscopic redshifts on the 2 optical components. As for 12646, the non-detection in high-resolution HST data also makes it difficult to conclude the most possible mode of its star formation.

The IR luminosities extrapolated from the modified black-body fitting result in even lower SFR, putting the sources into the regime of even less active star-forming systems compared to the main sequence. However, as mentioned in Sect. 4.4.2, the L_{FIR} and

the corresponding SFR from modified black-body fitting might be underestimated. This could be seen by the comparison between $1.3\times L_{FIR}$ (scaling factor from Graciá-Carpio et al., 2008) in Table 4.14 with the L_{IR} from CIGALE fitting in Table 4.16. The underestimate becomes more significant on sources with higher dust temperatures like 12646 assumed to be at $z = 7.3$ and 13161 at $z = 4.3$, where the scaled IR luminosities based on Table 4.14 and Graciá-Carpio et al. (2008) are 40% lower than the total IR luminosities from the corresponding CIGALE fitting. For sources with low dust temperatures like 13161 and 12646 assumed to be at $z = 3.7$, the results from the two methods are generally consistent with each other. Considering the incompleteness of the IR data coverage in modified black-body fitting and the extrapolation nature of the derived total IR luminosity and SFR from this method, we only keep the SFR derived from CIGALE fitting for the analysis in this section and the following analysis related to SFR/IR luminosities for GOODS-N sources. For HLS sources, we will use the SFR derived with the IR luminosity from modified black-body fitting, which is the only estimation we could have on them.

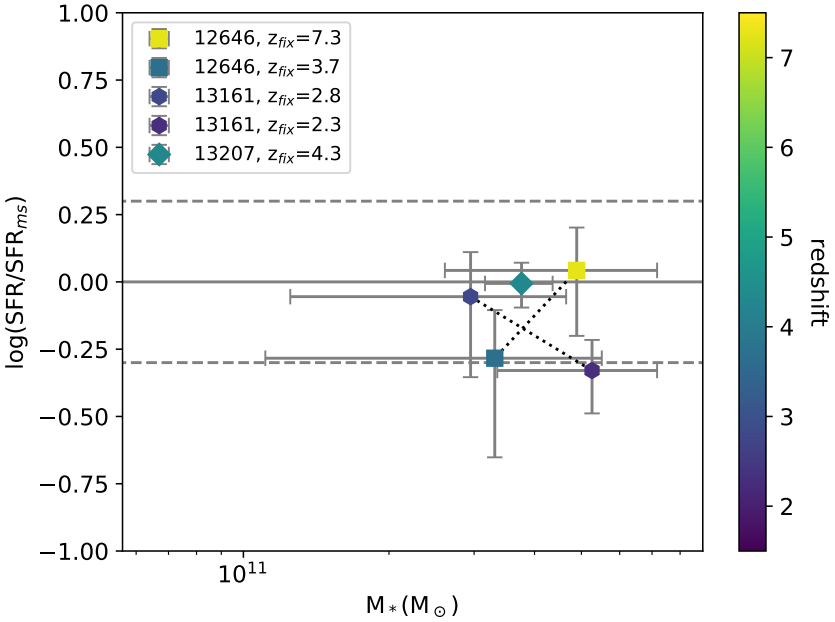

Figure 4.14 – The stellar mass and SFR offset from the star forming main sequence in Speagle et al. (2014) at the indicated redshifts of 3 GOODS-N sources. M_* and SFR derived at different z_{fix} in Table 4.10 are presented and connected by dotted lines. Data points in the plot are color codded based on the corresponding z_{fix}. The dashed line in the plot shows the typical 0.3dex scatter of star formation main sequence.

The new fitting with the "dl2014" model (Draine and Li, 2007; Draine et al., 2014) also provides independent estimates on the dust mass of these 3 GOODS-N galaxies.

For these 3 galaxies, as shown in Fig 4.15, the CIGALE fitting systematically returns a higher dust mass compared to optically-thin modified black-body fitting. Similar systematical difference between dust mass derived from single-temperature modified black-body fitting and those from Draine and Li (2007) model has also been reported by previous studies (e.g. Magdis et al., 2012). However, this will have little impact on the confirmation of the dust-rich nature of these high-z star-forming galaxies.

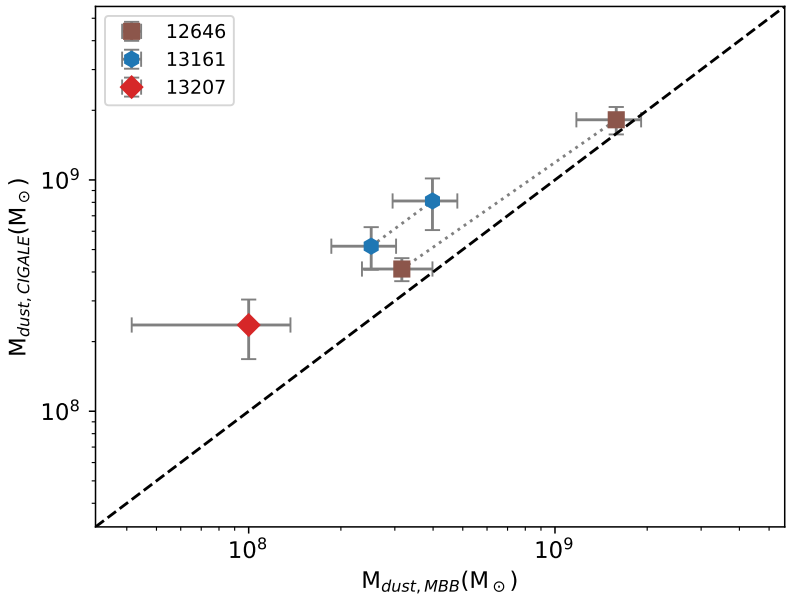

Figure 4.15 – Comparison of the dust masses derived by CIGALE and optically-thin modified black-body fitting. The results of the same source derived with different redshifts are listed in Tables 4.14 and 4.16 and are connected by dashed lines.

4.4.4 Molecular gas properties

Both the CO emission lines and dust continuum in the Rayleigh-Jeans tail of the far-IR SED have been widely applied to estimate the amount of molecular gas in galaxies (Carilli and Walter, 2013; Hodge and da Cunha, 2020). In this section, we present the molecular gas mass measurement on our sample and cross-validate the results with various methods.

The detection/constraints on CO emission lines enable the estimation of the molecular gas mass using the CO luminosity to molecular gas mass conversion factor α_{CO}. However, robust estimations of the conversion factor are mostly made on the lowest J transition, CO(1-0), while CO detections in our sample start from CO(3-2) to CO(5-4). Thus, we need to convert the luminosities of the lowest-J CO line detected in our observations to CO(1-0), in addition to the assumptions on the α_{CO} conversion factor

between CO(1-0) luminosity to molecular gas mass. In our case, we take the advantage of multiple line detections/flux upper limits in the NOEMA spectra of each source to find the matched cases in the literature and roughly estimate the CO(1-0) luminosity and molecular gas mass. As described in Sect. 4.4.1, for each source in our sample, we compare their CO luminosity ratios with literature results and find the cases with CO SLEDs that could reproduce the observed values. For HLS-2-1 and HLS-22, we apply $L'_{CO(5-4)}/L'_{CO(1-0)}$=0.32 and $L'_{CO(3-2)}/L'_{CO(1-0)}$=0.52 from the average SLED of unlensed SMGs in Bothwell et al. (2013) to estimate the CO(1-0) luminosities from CO(5-4) and CO(3-2), respectively. For HLS-2-2 and HLS-3, we find the SLEDs of the "Cosmic Eyelash" (Danielson et al., 2011) and the average of SPT SMGs (Spilker et al., 2014) could well reproduce the observed luminosity ratios. We scaled the luminosities of the lowest J CO lines observed in these sources to their CO(1-0) luminosities by assuming $L'_{CO(4-3)}/L'_{CO(1-0)}$=0.50 and $L'_{CO(5-4)}/L'_{CO(1-0)}$=0.72 to be the same as the 2 SLEDs. With the $L'_{CO(1-0)}$ of these sources (see Table. 4.17), we estimate the total molecular gas mass with a fixed conversion factor α_{CO}. As the derived source star formation rates do not reveal solid evidence of ongoing starburst in our sample, we adopt the typical Milky Way value of α_{CO}=4.36$M_\odot$(K km/s pc^2)$^{-1}$ in our study. The estimated molecular gas masses are also listed in Table. 4.17.

Previous studies also find low α_{CO} values at around 0.8 $M_\odot$(K km/s pc^2)$^{-1}$ in starburst galaxies undergoing major merger. If we adopt this value to the molecular gas mass measurement, it would results in gas masses ($M_{gas,CO}$) five times lower than those listed in Table. 4.17. However, for the HLS sources with CO line detections, these low molecular gas masses are significantly deviating from the measurements using Rayleigh-Jeans dust emission (Scoville et al., 2016, see the description below).

For all sources including those without CO line detections in the spectral scans, we also provide an estimate of their molecular gas mass with their continuum emission in the Rayleigh-Jeans tail. Following the calibration described in Scoville et al. (2016), we derive the luminosity of dust emission at rest-frame 850μm. We use the series of optically-thin modified black-body models generated by the combinations of parameters explored by the MCMC fitting to interpolate/extrapolate the dust luminosity at rest-frame 850μm, $L_{850\mu m}$. Using the conversion factor for SMGs in Scoville et al. (2016) ($L_{850\mu m}/M_{gas}$ = 8.4×10^{19} erg/s/Hz/$M_\odot$), we derive the molecular gas mass from the Rayleigh-Jeans dust emission, noted as $M_{gas,S16}$, as shown in Table 4.17. For the HLS sources with CO-based molecular gas measurement, we find the differences between the molecular gas masses estimated by the two methods are within a factor of 2 and at 1-3×10^{11} $M_\odot$, suggesting a gas-rich nature of these high-z galaxies. For the rest sample without CO detections, we find HLS-4 and 12646 have similarly massive molecular gas reservoirs as the 4 sources with CO detections. However, the molecular gas masses of 13161 and 13207 are estimated to be an order of magnitude lower at around 2×10^{10} $M_\odot$, which corresponds to a molecular gas fraction of around 10% in these 2 galaxies.

With the measurements in Table 4.14 and Table 4.17, we derive the gas-to-dust ratios of the 4 sources (HLS-2-1, HLS-2-2, HLS-3, and HLS-22) with relatively secure spectroscopic redshifts and dust-independent molecular gas mass measurements

Table 4.17 – Molecular gas properties of GOODS-N and HLS sources.

Source	z_{fix}	$L'_{CO(1-0),scaled}$ 10^9 K km/s pc^2	$L_{850\mu m}$ 10^{31} erg/s/Hz	$M_{gas,CO}$ $10^{10}M_\odot$	$M_{gas,S16}$ $10^{10}M_\odot$	τ_{dep} Myr
12646	7.3	—-	$0.67^{+0.14}_{-0.12}$	—-	$8.2^{+1.7}_{1.5}$	54^*
	3.7	—-	$1.65^{+0.20}_{-0.19}$	—-	$19.6^{+2.4}_{-2.2}$	574^*
13161	2.8	—-	$0.15^{+0.08}_{-0.04}$	—-	$1.8^{+1.0}_{-0.5}$	68^*
	2.3	—-	$0.20^{+0.10}_{-0.05}$	—-	$2.4^{+1.2}_{-0.6}$	194^*
13207	4.3	—-	$0.19^{+0.21}_{-0.11}$	—-	$2.3^{+2.6}_{-1.3}$	28^*
HLS-2-1	5.241	30.66±8.13	$0.90^{+0.18}_{-0.14}$	13.4±3.5	$10.6^{+2.1}_{-1.7}$	221^{+104}_{-59}
HLS-2-2	5.128	37.22±11.54	$0.87^{+0.18}_{-0.14}$	16.2±5.0	$10.9^{+2.1}_{-1.7}$	221^{+104}_{-59}
HLS-3	3.123	33.19±4.04	$2.26^{+0.56}_{-0.40}$	14.5±1.8	$26.9^{+6.7}_{-4.8}$	1894^{+1763}_{-945}
HLS-4	4.3	—-	$1.00^{+0.28}_{-0.25}$	—-	$11.9^{+3.3}_{-3.0}$	200^{+193}_{-79}
	3.3	—-	$1.33^{+0.30}_{0.28}$	—-	$15.9^{+3.6}_{-3.3}$	416^{+443}_{-161}
HLS-22	3.036	47.06±7.38	$0.90^{+0.18}_{0.14}$	20.5±3.2	$10.7^{+2.1}_{-1.7}$	756^{+999}_{-366}

Notes. $^{(*)}$ The depletion times of molecular gas are derived from the molecular gas mass estimated based on the rest-frame 850um luminosity from modified black-body fitting and the star formation rate based on the total infrared luminosity from CIGALE. Due to the lack of information on the covariance matrix between the two values from different fitting methods, we only provide the τ_{dep} without uncertainties.

from CO lines. With the assumption on α_{CO} and molecular gas excitation, our analysis yields an average gas-to-dust ratio of 113 on these sources, which is in line with values found in local and high-z massive galaxies (Santini et al., 2010; Rémy-Ruyer et al., 2014; De Vis et al., 2019; Rujopakarn et al., 2019) and consistent with the values expected at solar metallicity (Leroy et al., 2011; Magdis et al., 2012; Shapley et al., 2020). A lower, starburst-like α_{CO} (e.g Downes and Solomon, 1998; Tacconi et al., 2008) will lead to an average gas-to-dust ratio 5 to 6 time lower, which is also consistent with the results of (Rowlands et al., 2014) under similar assumptions but still at the extreme values. Such abundant dust in ISM could be difficult to explain unless the sources are already enriched to super-solar metallicity at $z = 3-5$ (Chen et al., 2013; Santini et al., 2014) or (and) they are undergoing vigorous merger+starburst events (Silverman et al., 2018).

We also derive the depletion time of the molecular gas in each galaxy with the molecular gas mass in Table 4.17, the star formation rate in Table 4.16 for the GOODS-N sample and Table 4.14 for the HLS sample. We use the molecular gas mass derived from the interpolated/extrapolated rest-frame 850μm emission with Scoville et al. (2016) to keep the measurement consistent among all samples with or without CO line detections. The results are also shown in the last column of Table 4.17, as well as in Fig 4.16.

For 12646 and 13161 in the GOODS-N sample, the corresponding gas depletion time is highly redshift dependent in our analysis. Given the uncertainties on the photometric redshift derived from different methods on these 2 sources, it is hard to conclude from our results. However, among the rest of the sources with more accurate

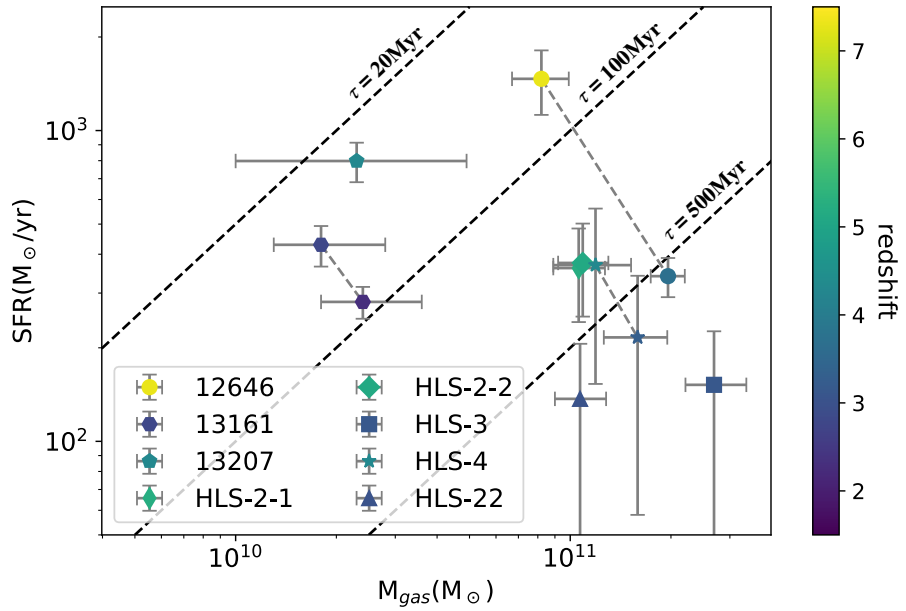

Figure 4.16 – The molecular mass from Rayleigh-Jeans dust emission and the star formation rate of HLS and GOODS-N samples. The dashed lines show the location where molecular gas depletion time correspond to 20 Myr, 100 Myr and 500 Myr. Each source is color coded by the redshift and sources analysed under several ambiguous redshifts are connected with the dotted lines.

redshift estimates or less redshift-dependent gas depletion time, we find 2 populations with distinct properties. Most of the HLS sources show a long gas depletion time of several hundred Myr to a few Gyr, resembling the depletion timescale found in star-forming galaxies with extended morphology and possibly undergoing secular evolution in local and high redshift universe (Genzel et al., 2015; Schinnerer et al., 2016; Aravena et al., 2016). As reported in Table 4.3, HLS-2-1 and HLS-3, are already partially resolved in the dust continuum with compact NOEMA configurations. This further suggests extended distributions of the molecular gas reservoir, and possibly, star formation, in at least part of the HLS samples. On the contrary, 13207 in GOODS-N shows a short gas depletion time of around 30Myr, which is similar to the typical gas depletion times found in merger-driven starburst galaxies or high-z compact star-forming galaxies. However, unlike the starburst mergers, 13027 only has a normal star formation rate compared to the main sequence galaxies at its stellar mass. The normal SFR at its stellar mass, short gas depletion time, and low gas fraction makes 13207 share similar properties of "blue nuggets" (Barro et al., 2016; Barro et al., 2017) or "starburst in main-sequence" (Elbaz et al., 2018), which are thought to be at the final stage before the quenching of star formation. Given the distinct stellar components in the HST image in Fig. 4.3, the low gas depletion time of 13207 probably suggests that the system is at the winging down of star-formation in galaxy merger and will quickly evolve to quiescence.

4.4.5 A possible over-density of DSFGs

The joint analysis on the data of HLS 2-1 and HLS 2-2 reveals that these 2 sources, separated by 12 arcsec on the map, both have a redshift of around 5.2. They are also located within 2 arcmin from HLS J0918+5142 at a similar redshift, which corresponds to a physical transverse distance of ~800 kiloparsec.

Given the identical spectroscopic redshifts of HLS-2-1 and HLS J0918+5142 the physical distance between these two sources is given by their transverse distance (D_t) of 796 kpc, computed following $D_t = D_A \times \theta_{sep}$.

The physical distance between HLS-2-1 (or HLS J0918+5142) to HLS-2-2, which are separated in both redshift and sky coordinates, is approximately estimated using Eq. 4.14 and Eq. 4.15:

$$D_{los} = [D_c(z1) - D_c(z2)]/(1+\bar{z}), \tag{4.14}$$

$$D = \sqrt{{D_t}^2 + {D_{los}}^2}. \tag{4.15}$$

With this method, we derive physical distances (D) of ~9.4 Mpc between HLS-2-1/HLS J0918+5142 to HLS-2-2. [5] The distance between HLS J0918+5142 and HLS-2-1 corresponds to 5.0 comoving Mpc, which is comparable to the scale of a $z = 4.6$ SMG DSFG over-density in COSMOS reported in a recent paper by Mitsuhashi et al., 2021.

5. The bias of peculiar radial velocity estimation might not be a large effect for HLS-2-2 to the other 2 sources. For HLS-2-1 to HLS J0918+5142, if we consider a peculiar radial velocity up to 1000 km/s along the line of sight, it could introduce a bias in the radial distance up to 1.6 Mpc

When assuming the core of the possible structure has the same redshift as HLS-2-1 and HLS J0918+5142, the deviation of the redshift of HLS-2-2 would correspond to a line-of-sight comoving distance of 58 Mpc. This is an order of magnitude larger than the scale of SMG over-density in COSMOS, while still being comparable to the proto-clusters traced by Ly-α emitters at z=5-6 (Jiang et al., 2018; Calvi et al., 2021). Although the stochasticity of star formation makes SMG an unreliable tracer of the most massive halos at intermediate redshift, the high SFR of the 3 sources at such high redshift could only be produced by the most massive galaxies tracing the densest environments in the early Universe (Miller et al., 2015). A more complete redshift survey on the other NIKA2 sources in the HLS field, as well as deep optical-IR observation in the same region, could reveal more members of this possible galaxy over-density to confirm its nature and understand its fate of cosmic evolution.

4.5 Discussion

4.5.1 Cross-validation and tension between different SED modeling

The application of the joint-analysis framework on HLS sources largely relies on the current knowledge of the far-IR SED of high-z galaxies. However, although Herschel provides estimates on the mean far-IR SEDs and the redshift evolution of the main population of star-forming galaxies, these results are also limited by significant source confusion, especially in SPIRE data at longer wavelengths. Moreover, current studies reveal some DSFGs with apparently low-dust temperature (Jin et al., 2019), as well as a significant warm-dust contribution in some starburst galaxies (Eisenhardt et al., 2012; Wu et al., 2012; Fan et al., 2016). These results suggest that a large variation in far-IR SEDs could exist in high-z DSFG populations.

Our choices of the template could not be free from these issues, and this is the reason why we adjust our joint-analysis framework to the results of 2 different far-IR SED templates and modeling framework and make the cross-validation between the results of the two. The analysis with Béthermin et al. (2015) templates and MMPZ mostly shows consistent redshift solutions. This suggests the relative stability of the joint-analysis method with input information from different SED fitting results.

However, some discrepancies on HLS-22 when using typical blind spectral scan conditions in Sect 4.3.4.2 are also found, which leads us to have an additional check on its origin. From the comparison on derived IR luminosity in Fig. 4.5, and the comparison between model and data in Fig. 4.6 and Fig. 4.10, we notice that the estimated infrared luminosity and line fluxes from MMPZ are systematically lower than those from Béthermin et al. (2015). At the correct redshift, the predicted line fluxes of Béthermin et al. (2015) match better with the observed line fluxes compare to MMPZ. On the contrary, MMPZ generally returns more accurate photometric redshifts, especially on HLS-3, where the photometric redshift from Béthermin et al. (2015) significantly deviates from the spectroscopic redshift. However, as indicated

by the low dust temperatures of the HLS sample, it is possible that the properties of far-IR emission of these galaxies are not representative among high redshift star-forming galaxies. Thus, we decide not to make any preference on the choice of dust template and far-IR SED fitting in our framework, and we recommend a cross-validation between the redshift solutions from various method in application.

Besides, the faint emission of HLS sources in SPIRE bands introduce large uncertainties on the constraints on source SEDs around the peak of far-IR emission. This, as a result, could contribute to the difference in IR luminosities derived from methods with different prior constraints (Casey, 2020). These issues also further suggest the importance of matching observation at ALMA band 8-10 frequencies in properly reconstructing the far-IR SED, as well as estimating the IR luminosity and star formation rate of high-z DSFGs selected by millimeter surveys.

4.5.2 Implications for the search and study on high-z DSFGs

In the previous sections, we presented the analysis of the properties of a few NIKA and NIKA2 DSFGs. These studies, especially those on HLS samples, largely rely on the redshift derived from the photometric + spectroscopic joint analysis method. We discuss here the implication and usage of the method in current and future studies on DSFGs and obscured star formation at high redshift.

Our photometric and spectroscopic joint-analysis method provides a promising framework for efficient redshift search on DSFGs. As proved by its application to the DSFG sample in the HLS field, the method could properly find the true redshift of these sources, even if the prior information of optical-IR SEDs is absent. The optical-IR SED analysis could provide photometric redshifts of high accuracy for less obscured, lower redshift DSFGs with better-sampled SEDs like 13161 and 13207 in HST and Spitzer extragalactic deep fields. In our framework, blind spectral scans combined with the full SED modeling could further improve the redshift measurement on these sources with even a single significant millimeter emission line detection, which, on its own, could only lead to several ambiguous redshift solutions and would require further observations to confirm/exclude.

As for the high-z and highly obscured DSFGs, the absence or lack of optical-IR detection and photometry resembles the conditions we have on HLS sources and 12646 in GOODS-N. As the possible progenitors of quiescent galaxies arise at cosmic noon (Straatman et al., 2014; Wang et al., 2019), their number density across the cosmic time, contribution to cosmic star formation rate density, and environment/clustering in space are all key quantities to reveal their nature and roles in the formation and evolution of massive galaxies (Wang et al., 2019; Williams et al., 2019; Fudamoto et al., 2021; An et al., 2019; Lim et al., 2020). These research works require a proper sample selection with accurate and reliable source redshifts as a prerequisite. However, as revealed by our photometric analysis on 12646 and HLS sources and some recent studies (Smail et al., 2021; Manning et al., 2022), it could be difficult to obtain accurate

redshift on candidate high-z DSFGs with only limited IR to millimeter photometric data, even if the source is covered by the most complete deep multi-wavelength observations as in GOODS-N. Our joint-analysis method provides accurate redshift determination on the two $z > 5$ HLS sources with an efficient spectral scan setup and under the condition with only low SNR on single emission lines. This suggests that the method provides a promising framework for efficient redshift surveys on high-z DSFGs in current extragalactic deep fields with current millimeter observing capabilities, such as the NIKA2 Cosmological Legacy Survey reaching detections at mJy to sub-mJy fluxes in COSMOS and GOODS-N.

The issues on poor SED sampling and photometric redshift measurement of current high-z DSFG samples could be further alleviated in the coming JWST era, with the deeper IR data covering these extragalactic deep fields. However, even the largest approved deep JWST surveys, such as COSMOS-Webb, are still not anticipated to cover a larger survey area than existing extragalactic optical-IR deep fields. Some important scientific problems on high-z DSFGs to be addressed by future studies require large survey areas to reduce the cosmic variance, or to cover extreme samples with low space density (e.g. Miller et al., 2018). These research topics, including the accurate clustering measurement of high-z DSFGs, DSFGs in the re-ionization era, high-z star-forming proto-clusters, and most extreme starbursts, could only be made with the forthcoming single-dish surveys of ~100 deg^2 or wider, like CCAT-p (CCAT-Prime collaboration et al., 2021) in far-IR to sub-millimeter and LMT-TolTEC (Wilson et al., 2020) surveys in the millimeter range.

We do not anticipate IR observations at K band or longer wavelength in the near future that covers a similarly large area with the depth match to S-CANDELS. Surveys of such depth would be required to identify candidate high-z DSFGs like 12646 in GOODS-N, as shown in our work. The lack of these wide and deep IR surveys could significantly limit the capability of identifying the multi-wavelength counterparts of high-z DSFGs and estimating their photometric redshift. Our results suggest that the joint-analysis method could be an efficient redshift determination framework/concept to be applied to the study of candidate high-z dust obscured sources in the future far-IR to millimeter blind surveys.

4.6 Summary

We presented our studies on 7 DSFGs selected from the early observations with NIKA and NIKA2 instruments.

We develop a new framework to determine the redshift of sources with the joint analysis of multi-wavelength photometry and millimeter spectral scans. Accounting for the additional constraints on IR luminosity from the SED modeling, we predict the flux of the strongest emission lines from CO, [CI], and [CII], generate the model spectra at given redshifts accordingly, estimate the goodness of match between broad-band

SEDs, models, and the observed millimeter spectra altogether and quantitatively find the most probable redshift solutions based on all this information.

Based on the prior selection of red far-IR to millimeter colors, we identify a sample of 4 millimeter NIKA2 sources of mJy fluxes in the HLS field with possible high redshifts, at $z = 3-7$. We conducted deep NOEMA observations on these sources, and resolve them into 5 individual sources. With the NOEMA spectral scans and the newly developed joint-analysis method, we obtain their redshift and confirm they all have $z > 3$. Our analysis reveals their lower dust temperature compared to the general population of star-forming galaxies. We also derive the molecular gas mass and gas depletion time of the 5 NOEMA sources and find they have long gas depletion times similar to secular evolved galaxies. Furthermore, we find two sources at z=5.2 that are separated by only 5 comoving Mpc, possibly linked to a third source lying at a distance comparable to the proto-cluster size as traced by Ly-α emitters at $z = 5-6$. This could be the hint of an interesting high-z structure in HLS.

The NIKA sample in GOODS-N reveals massive galaxies with a normal star-formation rate compared to the high-z star-formation main sequence. Our analysis supports the high redshift nature of 12646 (AzGN-10), the original target of NIKA observation, while the narrow bandwidth of the spectral scan observation fails to identify any emission line to draw a definitive conclusion. The GOODS-N sample, although limited in number, shows similar average physical properties of IR emission, dust mass, and dust temperature compared to the DSFGs selected from blind surveys. The galaxy 13207, with the least ambiguous photometric redshifts, shows a short gas depletion time of $\sim$ 20-100 Myr on the star-formation main sequence, which might indicate that the galaxy is at the last stage of star-formation quenching.

We demonstrate that our method to constrain the redshift, applied to millimeter-selected DSFGs with far-IR to mm photometry and with NOEMA blind spectral scans, could determine the true redshift accurately. Such accuracy of redshift determination with multiple low S/N emission lines shows promising potential in blind redshift searching on large samples of high-z DSFGs, even in the absence of accurate optical-IR photometric redshifts. The method is especially expected to improve the design and efficiency of blind redshift search on candidate high-z DSFGs detected by the NIKA2 Cosmological Legacy Survey (N2CLS). Indeed, most of the N2CLS sources will be fainter (sub-mJy) than the 7 sources discussed here. The new tool we developed will allow us to mitigate the increase of ALMA and NOEMA time that will be needed for these faint DSFGs.

Conclusions and Perspectives

Dusty star-forming galaxies are critical players in our understanding of cosmic galaxy formation and evolution. They represent the most massive intense star-forming systems in the early Universe, yet many are completely optically obscured. Their easy detection at sub-millimeter wavelengths is due to the luminous emission from dust heated by young stars, as well as the negative k-correction effect due to the significantly peaked emission at rest-frame far-IR. Despite recent progress in the studies on dusty star-forming galaxies, the systematic census on high-z dusty star-forming galaxies is still limited by the lack of wide and relatively deep surveys at long wavelengths of 1-2mm, as well as the difficulties in accurately identifying high-z sources and estimating the source redshifts.

The NIKA2, a recent KIDs-based continuum instrument on IRAM 30m telescope, offers a large field of view, high sensitivity, and relatively high resolutions with simultaneous 1.2/2.0mm observing capability, making it promising for the large area and sensitive millimeter blind surveys targeting on high-z dusty star-forming galaxies. These advantages leads to the emergence of N2CLS, a large 1.2mm and 2.0mm blind survey in GOODS-N and COSMOS field, with a specific focus on the census on high-z dusty star-forming galaxies and obscured star-formation. In my thesis, I was deeply involved in the observations with the N2CLS and NIKA2 pools. The thesis work is also highly associated with the reduction of NIKA2 timeline data and the analysis with a novel end-to-end simulation feature, under the PIIC pipeline. The descriptions and details of the instrument, N2CLS and other NIKA2 blank field surveys, NIKA2 observation procedures, the PIIC data reduction pipeline, and the end-to-end simulation are summarized in the first part of the thesis.

The second part of the thesis research focuses on the analysis of source and galaxy number counts based on N2CLS observations. We developed a new framework to accurately correct the instrumental and statistical effects on source detection and flux measurements, based on the end-to-end simulation feature provided by. In addition to the corrections on the completeness, purity of detection, and flux boosting by noise peaks, the new framework could also account for the impact of pipeline filtering and astrophysical clustering on source flux measurements.

Using the PIIC simulated observation in 117 independent fields in SIDES+Uchuu simulations, we demonstrate the proper recovery of statistical properties of sources and apply it to the real N2CLS GOODS-N and COSMOS observations. We make new measurements of the source number counts at 1.2 and 2 mm in the two fields, which

cover the largest range of flux from a single blank field survey. We find consistent source number counts in GOODS-N and COSMOS in the overlapped flux ranges. We also find consistent source number counts with most of the previous single-dish measurements at similar wavelengths. With the simulation, we are also able to account for the beam effect on the number counts of single-dish observations. This helps us, for the first time for single-dish surveys, derive the galaxy number counts that could be directly comparable with high-resolution interferometric observations. From the analysis and the comparison with ALMA observation, we notice the source-to-galaxy counts correction could be substantial for N2CLS observations and the corrected galaxy counts are also generally consistent with previous results. The comparison with model predictions suggests an underproduction of bright sources compared to our observation.

The third part of the thesis focus on the challenges of redshift measurement of large dusty galaxy samples, which is highly demanding for follow-up studies of N2CLS. These include the difficulties of counterpart identification due to large beams, photometric redshift measurement on optical-IR dark/faint high-z candidates, and inefficiency of blind spectroscopic scans in the millimeter. We explored different methods of redshift determination on 7 candidate high-z sources selected from previous NIKA/NIKA2 observations. One important outcome is the development of a redshift-search framework that jointly accounts for the information from multi-wavelength photometric and spectroscopic observations. In addition to the redshift probability distribution, this framework further uses the photometric SED fitting to quantitatively predict the CO/[CI] spectra of target sources and compare the models at various redshifts with the blind spectral scans. With only far-IR photometric data and NOEMA blind spectral scans, the method successfully identifies 3 secure and 1 possible redshift on 5 sources in NIKA2 science verification data in the HLS field. These redshifts are generally consistent with the expectation in the far-IR selection, and a possible overdensity of dusty galaxies at z~5.2 is revealed. The photometric redshifts of the other 3 sources in GOODS-N are estimated using the multi-wavelength photometry on the counterparts of PdBI continuum sources. These include one galaxy at z=2-3 and another two at z~4.

With the spectral lines and multi-wavelength data, we also studied the properties of molecular gas and star formation in these galaxies. We find that the GOODS-N sample shows normal star formation rate at their high stellar mass, making them located around the star-formation main sequence at their redshifts. Two of the GOODS-N sources have the shortest gas depletion time scale of less than 100 Myr among the whole sample, together with relatively higher dust temperatures. These indicate a transition to quiescence by fast gas depletion by star formation. On the contrary, we find a consistently longer gas depletion timescale and massive gas reservoir in the HLS sample. We also find 2 sources with significantly colder-than-average dust temperatures at their redshifts. This adds a few more samples to the population of cold sources proposed by recent studies and addresses the possible importance of

considering these sources in future models and observations.

Finally and based on the new results presented in this manuscript, we also raise possible directions and topics to be completed in the future. The source/galaxy number counts in the (sub)millimeter brought valuable insights into galaxy formation and evolution. However, recent studies also notice that the number counts from single surveys could significantly be biased to the sources at z=1-3, where most of the sources locate at (Popping et al., 2020; Hodge and da Cunha, 2020). On top of the number counts, obtaining the individual redshift of sources could further constrain model predictions and understand the cosmic evolution of dusty galaxies and obscured star formation. Within the N2CLS project, we plan to use new NOEMA/ALMA continuum observations and ancillary data to first pinpoint the location of DSFGs contribution to the observed N2CLS sources Although continuum alone could not obtain spectroscopic redshift of high accuracy, it could help identify the multi-wavelength counterparts of N2CLS sources. As demonstrated in our work, this could obtain photometric redshift of ~10% accuracy for sources with good photometric coverage. The upcoming deep near and mid-IR JWST data from COSMOS-Webb, PRIMER, FRESCO, and GTO observations in these two fields could further compliment the photometric coverage on high-z, optically-faint sources and improve the redshift estimate. Through the cross-identification with optical-IR data, we will also select the most obscured and optically-dark source, where the accurate but time-consuming blind spectral scans are ultimately mandatory to obtain their redshift.

Following this strategy, a complete continuum follow-up program has already been carried out by NOEMA in early 2022. This program observed 27 N2CLS sources of >95% purity in GOODS-N, which have ambiguous counterpart identification. We observe these sources at 255 and 150 GHz in the continuum, which match with the frequencies of the two NIKA2 bands. The observations reveal at least one counterpart at S/N>4 for all but one source. Some of them are likely to be associated with optically dark/faint sources invisible in HST images, whose accurate optical-IR photometric redshifts could be difficult to obtain with current ancillary data (see Fig. 4.17 for examples). Blind spectral scans on these sources, photometric redshift analysis on the rest of the GOODS-N sample of 95% purity, as well as the JWST FRESCO grism observations in part of the GOODS-N field, could finally help us obtain the accurate redshifts of a complete, secure and unbiased dusty galaxy sample in GOODS-N. This galaxy sample, in addition to the future samples from the complete COSMOS survey, could help construct the cosmic evolution of the dusty star-forming galaxy and the obscured star formation in the first billion years of the Universe. Recent studies find evidence of more than anticipated contribution of obscured star formation up to the end of the reionization era, while the measurements are still based on optically selected samples (Algera et al., 2022). Our N2CLS observations could help perform selection more closely related to source infrared luminosity and obscured star formation, providing a better defined, less biased sample for the measurements of high-z obscured star formation.

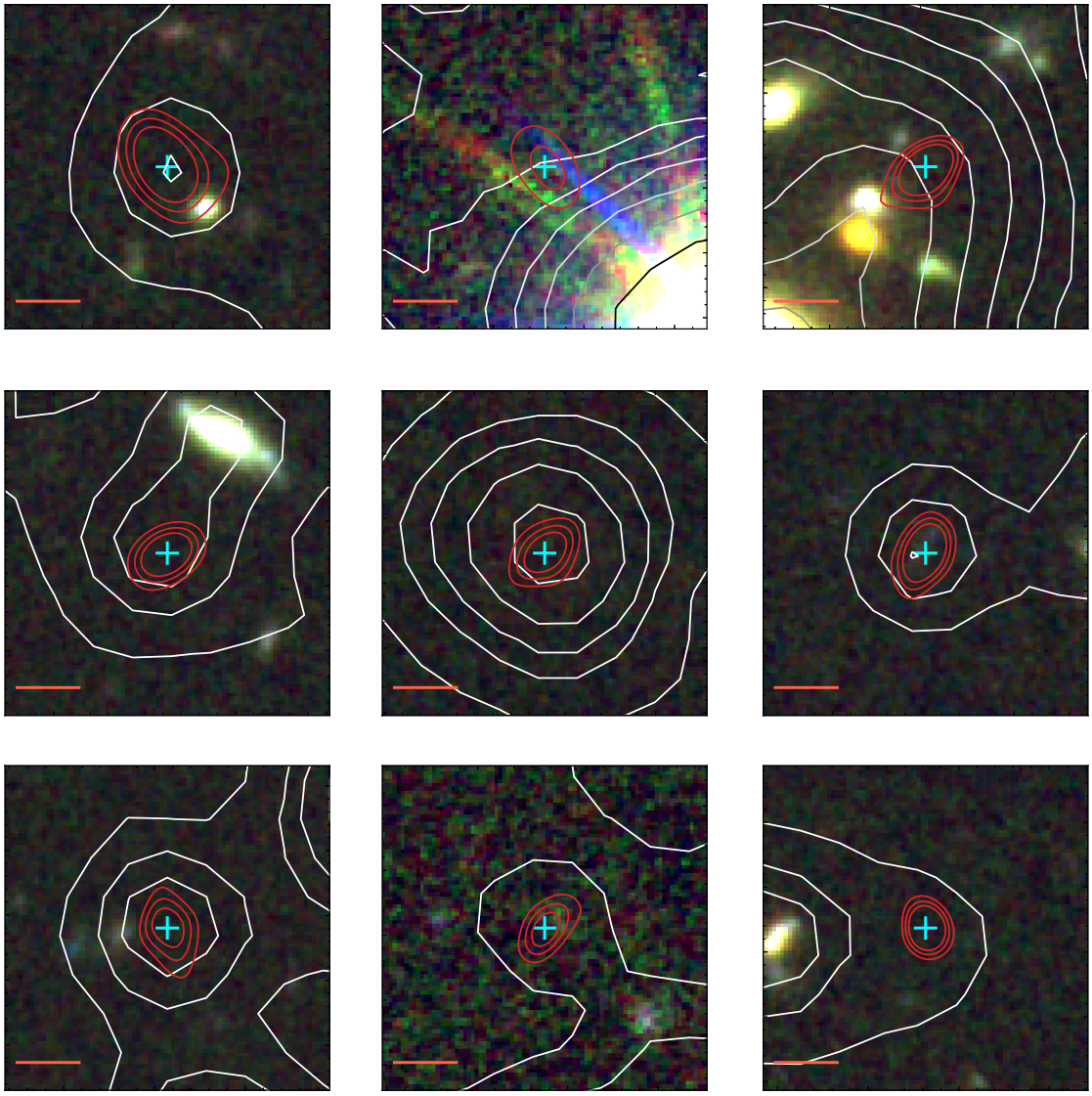

Figure 4.17 – Examples of optically dark/faint sources identified by NOEMA follow-up observations on N2CLS sources in GOODS-N. The cleaned NOEMA data are illustrated by the red contour at levels of 4, 6, and 8 times the RMS of the cleaned images. The peak positions in the cleaned images are highlighted by cyan crosses. The flux distribution at 4.5 μm from Spitzer IRAC observations are shown as white contours between 0 to 0.320 MJy/sr in 9 levels uniformly separated with a logarithmic scale. The background images are generated using HST F814W, F125W, and F160W images in the blue, green, and red channels, respectively. The scale bars in each subplot have lengths of 1".

Beyond the N2CLS survey itself, the results and analysis tools we developed could also have further implications for future research. In our number counts work, we

revealed the impact on source fluxes and number counts due to pipeline filtering and large beams. Although seldom considered in most of the previous observations, these effects could cause substantial biases in our results. We stress the importance of end-to-end simulations and corrections in the planning and data analysis in future deep single-dish surveys, such as CCAT-prime (CCAT-Prime collaboration et al., 2021). These efforts could be especially important when comparing the survey results with model predictions and other statistical studies on dusty galaxies at high redshift.

In our follow-up studies on high-redshift candidates, we introduce a method to constrain the redshift of high-z dusty galaxies, which jointly accounts for the information from photometry and spectral scans. The method could accurately find the redshifts of sources using multiple low S/N emission lines. This shows promising potential in blind redshift searching on large samples of high-z DSFGs, even in the absence of accurate optical-IR photometric redshifts. Several upcoming far-IR to millimeter wide-area surveys, such as CCAT-prime (CCAT-Prime collaboration et al., 2021) and LMT-TolTEC surveys (Wilson et al., 2020), make the census on dusty galaxies in the early Universe as one of their key scientific goals. The more ambitious AtLAST telescope, which is currently in conceptual phases, could further enable large and unbiased surveys on cosmological volumes (Ramasawmy et al., 2022). It is expected to provide continuum measurements and line identification of large samples of high-z galaxies without the need for photometric pre-selection, and unveil the myths of dust formation and obscured star formation well into the reionization era. Our methods could have a promising potential of application in the design and analysis of primary or (and) follow-up observation on their samples, especially when considering the absence of wide-area, optical-IR surveys matched to HST/Spitzer deep fields. Besides, we foresee the potential of the joint analysis principle in the exploration of the extensive and growing ALMA data archive. With the ability of line identification through cross-correlation, the method could bring redshift and line flux constraints on known sources in the ALMA footprint. These resources could have high ancillary value to future research on extragalactic science.

Bibliography

[Ada+14] R. Adam et al. “First observation of the thermal Sunyaev-Zel’dovich effect with kinetic inductance detectors”. In: A&A 569, A66 (Sept. 2014), A66. DOI: 10.1051/0004-6361/201322902. arXiv: 1310.6237 [astro-ph.CO] (cit. on pp. 76, 122).

[Ada+18] R. Adam et al. “The NIKA2 large-field-of-view millimetre continuum camera for the 30 m IRAM telescope”. In: A&A 609, A115 (Jan. 2018), A115. DOI: 10.1051/0004-6361/201731503. arXiv: 1707.00908 [astro-ph.IM] (cit. on pp. 22, 74, 121, 122).

[Air+10] J. Aird et al. “The evolution of the hard X-ray luminosity function of AGN”. In: MNRAS 401.4 (Feb. 2010), pp. 2531–2551. DOI: 10.1111/j.1365-2966.2009.15829.x. arXiv: 0910.1141 [astro-ph.CO] (cit. on p. 38).

[Alg+22] Hiddo Algera et al. “The ALMA REBELS Survey: The Dust-obscured Cosmic Star Formation Rate Density at Redshift 7”. In: *arXiv e-prints*, arXiv:2208.08243 (Aug. 2022), arXiv:2208.08243. arXiv: 2208.08243 [astro-ph.GA] (cit. on p. 172).

[An+18] Fang Xia An et al. “A Machine-learning Method for Identifying Multi-wavelength Counterparts of Submillimeter Galaxies: Training and Testing Using AS2UDS and ALESS”. In: ApJ 862.2, 101 (Aug. 2018), p. 101. DOI: 10.3847/1538-4357/aacdaa. arXiv: 1806.06859 [astro-ph.GA] (cit. on p. 58).

[An+19] Fang Xia An et al. “Multi-wavelength Properties of Radio- and Machine-learning-identified Counterparts to Submillimeter Sources in S2COSMOS”. In: ApJ 886.1, 48 (Nov. 2019), p. 48. DOI: 10.3847/1538-4357/ab4d53. arXiv: 1910.03596 [astro-ph.GA] (cit. on p. 167).

[And+18] Paola Andreani et al. “Extreme conditions in the molecular gas of lensed star-forming galaxies at z 3”. In: A&A 615, A142 (July 2018), A142. DOI: 10.1051/0004-6361/201732560. arXiv: 1802.07430 [astro-ph.GA] (cit. on p. 151).

[Ara+16] M. Aravena et al. “The ALMA Spectroscopic Survey in the Hubble Ultra Deep Field: Continuum Number Counts, Resolved 1.2 mm Extragalactic Background, and Properties of the Faintest Dusty Star-forming Galaxies”. In: ApJ 833.1, 68 (Dec. 2016), p. 68. DOI: 10.3847/1538-4357/833/1/68. arXiv: 1607.06769 [astro-ph.GA] (cit. on pp. 51, 65, 68, 110, 165).

[Are+11] I. Aretxaga et al. “AzTEC millimetre survey of the COSMOS field - III. Source catalogue over 0.72 deg^2 and plausible boosting by large-scale structure”. In: MNRAS 415.4 (Aug. 2011), pp. 3831–3850. DOI: 10.1111/j.1365-2966.2011.18989.x. arXiv: 1105.0890 [astro-ph.CO] (cit. on pp. 62, 64, 95).

[AI11] S. Arnouts and O. Ilbert. *LePHARE: Photometric Analysis for Redshift Estimate*. Astrophysics Source Code Library, record ascl:1108.009. Aug. 2011. ascl: 1108.009 (cit. on p. 139).

[Ash+15] M. L. N. Ashby et al. “S-CANDELS: The Spitzer-Cosmic Assembly Near-Infrared Deep Extragalactic Survey. Survey Design, Photometry, and Deep IRAC Source Counts”. In: ApJS 218.2, 33 (June 2015), p. 33. DOI: 10.1088/0067-0049/218/2/33. arXiv: 1506.01323 [astro-ph.GA] (cit. on pp. 126, 131).

[Aus+10] J. E. Austermann et al. “AzTEC half square degree survey of the SHADES fields - I. Maps, catalogues and source counts”. In: MNRAS 401.1 (Jan. 2010), pp. 160–176. DOI: 10.1111/j.1365-2966.2009.15620.x. arXiv: 0907.1093 [astro-ph.CO] (cit. on pp. 62, 64).

[Bak+20] Tom J. L. C. Bakx et al. “ALMA uncovers the [C II] emission and warm dust continuum in a z = 8.31 Lyman break galaxy”. In: MNRAS 493.3 (Apr. 2020), pp. 4294–4307. DOI: 10.1093/mnras/staa509. arXiv: 2001.02812 [astro-ph.GA] (cit. on p. 40).

[Bak+21] Tom J. L. C. Bakx et al. “Accurate dust temperature determination in a z = 7.13 galaxy”. In: MNRAS 508.1 (Nov. 2021), pp. L58–L63. DOI: 10.1093/mnrasl/slab104. arXiv: 2108.13479 [astro-ph.GA] (cit. on pp. 40, 156).

[Ban+18] Manda Banerji et al. “The interstellar medium properties of heavily reddened quasarsand companions at z∼ 2.5 with ALMA and JVLA”. In: MNRAS 479.1 (Sept. 2018), pp. 1154–1169. DOI: 10.1093/mnras/sty1443. arXiv: 1805.09825 [astro-ph.GA] (cit. on p. 151).

[Bar+98] A. J. Barger et al. “Submillimetre-wavelength detection of dusty star-forming galaxies at high redshift”. In: Nature 394.6690 (July 1998), pp. 248–251. DOI: 10.1038/28338. arXiv: astro-ph/9806317 [astro-ph] (cit. on pp. 61, 90).

[Bar+22] A. J. Barger et al. “A Submillimeter Perspective on the GOODS Fields (SUPER GOODS). V. Deep 450 μm Imaging”. In: ApJ 934.1, 56 (July 2022), p. 56. DOI: 10.3847/1538-4357/ac67e7. arXiv: 2205.01114 [astro-ph.GA] (cit. on pp. 61, 64).

[Bar+16a] I. Baronchelli et al. “The Spitzer-IRAC/MIPS Extragalactic Survey (SIMES) in the South Ecliptic Pole Field”. In: ApJS 223.1, 1 (Mar. 2016), p. 1. DOI: 10.3847/0067-0049/223/1/1. arXiv: 1602.00892 [astro-ph.GA] (cit. on p. 58).

[Bar+18] I. Baronchelli et al. "The Spitzer-IRAC/MIPS Extragalactic Survey (SIMES). II. Enhanced Nuclear Accretion Rate in Galaxy Groups at z ~ 0.2". In: ApJ 857.1, 64 (Apr. 2018), p. 64. DOI: 10.3847/1538-4357/aab78b. arXiv: 1803.06356 [astro-ph.GA] (cit. on p. 58).

[Bar+16b] G. Barro et al. "Sub-kiloparsec ALMA Imaging of Compact Star-forming Galaxies at z ~2.5: Revealing the Formation of Dense Galactic Cores in the Progenitors of Compact Quiescent Galaxies". In: ApJ 827.2, L32 (Aug. 2016), p. L32. DOI: 10.3847/2041-8205/827/2/L32. arXiv: 1607.01011 [astro-ph.GA] (cit. on pp. 40, 53, 165).

[Bar+17] G. Barro et al. "Spatially Resolved Kinematics in the Central 1 kpc of a Compact Star-forming Galaxy at z ~2.3 from ALMA CO Observations". In: ApJ 851.2, L40 (Dec. 2017), p. L40. DOI: 10.3847/2041-8213/aa9f0d. arXiv: 1712.01283 [astro-ph.GA] (cit. on p. 165).

[Bar+13] Guillermo Barro et al. "CANDELS: The Progenitors of Compact Quiescent Galaxies at z ~2". In: ApJ 765.2, 104 (Mar. 2013), p. 104. DOI: 10.1088/0004-637X/765/2/104. arXiv: 1206.5000 [astro-ph.CO] (cit. on pp. 39, 53).

[Bar+19] Guillermo Barro et al. "The CANDELS/SHARDS Multiwavelength Catalog in GOODS-N: Photometry, Photometric Redshifts, Stellar Masses, Emission-line Fluxes, and Star Formation Rates". In: ApJS 243.2, 22 (Aug. 2019), p. 22. DOI: 10.3847/1538-4365/ab23f2. arXiv: 1908.00569 [astro-ph.GA] (cit. on pp. 41, 126, 129, 131, 132, 134, 136).

[Beh+19] Peter Behroozi et al. "UNIVERSEMACHINE: The correlation between galaxy growth and dark matter halo assembly from z = 0-10". In: MNRAS 488.3 (Sept. 2019), pp. 3143–3194. DOI: 10.1093/mnras/stz1182. arXiv: 1806.07893 [astro-ph.GA] (cit. on p. 113).

[BHT15] Kenji Bekki et al. "The Origin of Dust Extinction Curves with or without the 2175 Å Bump in Galaxies: the Case of the Magellanic Clouds". In: ApJ 810.1, 39 (Sept. 2015), p. 39. DOI: 10.1088/0004-637X/810/1/39. arXiv: 1507.03327 [astro-ph.GA] (cit. on p. 44).

[Ben10] Andrew J. Benson. "Galaxy formation theory". In: Phys. Rep. 495.2-3 (Oct. 2010), pp. 33–86. DOI: 10.1016/j.physrep.2010.06.001. arXiv: 1006.5394 [astro-ph.CO] (cit. on p. 33).

[Ber+21] S. Berta et al. "Close-up view of a luminous star-forming galaxy at z = 2.95". In: A&A 646, A122 (Feb. 2021), A122. DOI: 10.1051/0004-6361/202039743. arXiv: 2012.01448 [astro-ph.CO] (cit. on p. 153).

[Ber+07] F. Bertoldi et al. "COSBO: The MAMBO 1.2 Millimeter Imaging Survey of the COSMOS Field". In: ApJS 172.1 (Sept. 2007), pp. 132–149. DOI: 10.1086/520511 (cit. on pp. 62, 64, 95).

[Bét+10] M. Béthermin et al. “Submillimeter number counts at 250 μm, 350 μm and 500 μm in BLAST data”. In: A&A 516, A43 (June 2010), A43. DOI: 10.1051/0004-6361/200913910. arXiv: 1003.0833 [astro-ph.CO] (cit. on p. 124).

[Bét+15] M. Béthermin et al. “Evolution of the dust emission of massive galaxies up to z = 4 and constraints on their dominant mode of star formation”. In: A&A 573, A113 (Jan. 2015), A113. DOI: 10.1051/0004-6361/201425031. arXiv: 1409.5796 [astro-ph.GA] (cit. on pp. 28, 46, 51, 56, 77, 95, 97, 110, 114–116, 118, 120, 124, 136–138, 140, 142–144, 146, 148, 149, 154, 157, 158, 166).

[Bét+20] M. Béthermin et al. “The ALPINE-ALMA [CII] survey: Data processing, catalogs, and statistical source properties”. In: A&A 643, A2 (Nov. 2020), A2. DOI: 10.1051/0004-6361/202037649. arXiv: 2002.00962 [astro-ph.GA] (cit. on pp. 48, 66, 68, 70, 102, 156).

[Bét+17] Matthieu Béthermin et al. “The impact of clustering and angular resolution on far-infrared and millimeter continuum observations”. In: A&A 607, A89 (Nov. 2017), A89. DOI: 10.1051/0004-6361/201730866. arXiv: 1703.08795 [astro-ph.GA] (cit. on pp. 87, 91, 106, 113, 116).

[Bla99] A. W. Blain. “Dust temperature and the submillimetre-radio flux density ratio as a redshift indicator for distant galaxies”. In: MNRAS 309.4 (Nov. 1999), pp. 955–960. DOI: 10.1046/j.1365-8711.1999.02916.x. arXiv: astro-ph/9906438 [astro-ph] (cit. on p. 121).

[Bla+02] Andrew W. Blain et al. “Submillimeter galaxies”. In: Phys. Rep. 369.2 (Oct. 2002), pp. 111–176. DOI: 10.1016/S0370-1573(02)00134-5. arXiv: astro-ph/0202228 [astro-ph] (cit. on p. 77).

[Boq+19] M. Boquien et al. “CIGALE: a python Code Investigating GALaxy Emission”. In: A&A 622, A103 (Feb. 2019), A103. DOI: 10.1051/0004-6361/201834156. arXiv: 1811.03094 [astro-ph.GA] (cit. on pp. 41, 133, 157).

[BFS22] Alessandro Boselli et al. “Ram pressure stripping in high-density environments”. In: A&A Rev. 30.1, 3 (Dec. 2022), p. 3. DOI: 10.1007/s00159-022-00140-3. arXiv: 2109.13614 [astro-ph.GA] (cit. on p. 40).

[Bot+13] M. S. Bothwell et al. “A survey of molecular gas in luminous sub-millimetre galaxies”. In: MNRAS 429.4 (Mar. 2013), pp. 3047–3067. DOI: 10.1093/mnras/sts562. arXiv: 1205.1511 [astro-ph.CO] (cit. on pp. 145, 151, 153, 162).

[Bou+22] R. J. Bouwens et al. “Reionization Era Bright Emission Line Survey: Selection and Characterization of Luminous Interstellar Medium Reservoirs in the z > 6.5 Universe”. In: ApJ 931.2, 160 (June 2022), p. 160. DOI: 10.3847/1538-4357/ac5a4a. arXiv: 2106.13719 [astro-ph.GA] (cit. on pp. 48, 70).

[Bra+05] John Bradley et al. “An Astronomical 2175 Å Feature in Interplanetary Dust Particles”. In: *Science* 307.5707 (Jan. 2005), pp. 244–247. DOI: 10.1126/science.1106717 (cit. on p. 43).

[Bra+22] Larry Bradley et al. *astropy/photutils: 1.5.0*. Version 1.5.0. July 2022. DOI: 10.5281/zenodo.6825092. URL: https://doi.org/10.5281/zenodo.6825092 (cit. on p. 97).

[BvC08] Gabriel B. Brammer et al. “EAZY: A Fast, Public Photometric Redshift Code”. In: ApJ 686.2 (Oct. 2008), pp. 1503–1513. DOI: 10.1086/591786. arXiv: 0807.1533 [astro-ph] (cit. on pp. 134, 139).

[Bri+04] J. Brinchmann et al. “The physical properties of star-forming galaxies in the low-redshift Universe”. In: MNRAS 351.4 (July 2004), pp. 1151–1179. DOI: 10.1111/j.1365-2966.2004.07881.x. arXiv: astro-ph/0311060 [astro-ph] (cit. on p. 38).

[BC03] G. Bruzual and S. Charlot. “Stellar population synthesis at the resolution of 2003”. In: MNRAS 344.4 (Oct. 2003), pp. 1000–1028. DOI: 10.1046/j.1365-8711.2003.06897.x. arXiv: astro-ph/0309134 [astro-ph] (cit. on p. 133).

[Bry18] Sean Bryan. “The TolTEC Camera for the LMT Telescope”. In: *Atacama Large-Aperture Submm/mm Telescope (AtLAST)*. Jan. 2018, 36, p. 36. DOI: 10.5281/zenodo.1159073 (cit. on p. 63).

[BBI05] D. Burgarella et al. “Star formation and dust attenuation properties in galaxies from a statistical ultraviolet-to-far-infrared analysis”. In: MNRAS 360.4 (July 2005), pp. 1413–1425. DOI: 10.1111/j.1365-2966.2005.09131.x. arXiv: astro-ph/0504434 [astro-ph] (cit. on pp. 41, 133).

[Cal+18] A. Calabrò et al. “Near-infrared Emission Lines in Starburst Galaxies at 0.5 < z < 0.9: Discovery of a Merger Sequence of Extreme Obscurations”. In: ApJ 862.2, L22 (Aug. 2018), p. L22. DOI: 10.3847/2041-8213/aad33e. arXiv: 1807.04350 [astro-ph.GA] (cit. on p. 53).

[Cal+21] Rosa Calvi et al. “Probing the existence of a rich galaxy overdensity at z = 5.2”. In: MNRAS 502.3 (Apr. 2021), pp. 4558–4575. DOI: 10.1093/mnras/staa4037. arXiv: 2101.02747 [astro-ph.GA] (cit. on p. 166).

[Cal97] Daniela Calzetti. “Reddening and Star Formation in Starburst Galaxies”. In: AJ 113 (Jan. 1997), pp. 162–184. DOI: 10.1086/118242. arXiv: astro-ph/9610184 [astro-ph] (cit. on p. 35).

[Cañ+15] R. Cañameras et al. “Planck’s dusty GEMS: The brightest gravitationally lensed galaxies discovered with the Planck all-sky survey”. In: A&A 581, A105 (Sept. 2015), A105. DOI: 10.1051/0004-6361/201425128. arXiv: 1506.01962 [astro-ph.GA] (cit. on pp. 40, 51, 71).

[CW13] C. L. Carilli and F. Walter. "Cool Gas in High-Redshift Galaxies". In: ARA&A 51.1 (Aug. 2013), pp. 105–161. DOI: 10.1146/annurev-astro-082812-140953. arXiv: 1301.0371 [astro-ph.CO] (cit. on pp. 153, 161).

[Car+15] S. Carniani et al. "ALMA constraints on the faint millimetre source number counts and their contribution to the cosmic infrared background". In: A&A 584, A78 (Dec. 2015), A78. DOI: 10.1051/0004-6361/201525780. arXiv: 1502.00640 [astro-ph.GA] (cit. on pp. 65, 66).

[Cas+14] C. M. Casey et al. "Are Dusty Galaxies Blue? Insights on UV Attenuation from Dust-selected Galaxies". In: ApJ 796.2, 95 (Dec. 2014), p. 95. DOI: 10.1088/0004-637X/796/2/95. arXiv: 1410.0702 [astro-ph.GA] (cit. on p. 54).

[Cas12] Caitlin M. Casey. "Far-infrared spectral energy distribution fitting for galaxies near and far". In: MNRAS 425.4 (Oct. 2012), pp. 3094–3103. DOI: 10.1111/j.1365-2966.2012.21455.x. arXiv: 1206.1595 [astro-ph.CO] (cit. on pp. 136, 137).

[Cas20] Caitlin M. Casey. "Far-infrared Photometric Redshifts: A New Approach to a Highly Uncertain Enterprise". In: ApJ 900.1, 68 (Sept. 2020), p. 68. DOI: 10.3847/1538-4357/aba528. arXiv: 2007.11012 [astro-ph.GA] (cit. on pp. 136, 137, 167).

[CNC14] Caitlin M. Casey et al. "Dusty star-forming galaxies at high redshift". In: Phys. Rep. 541.2 (Aug. 2014), pp. 45–161. DOI: 10.1016/j.physrep.2014.02.009. arXiv: 1402.1456 [astro-ph.CO] (cit. on pp. 50, 77, 91, 120).

[Cas+17] Caitlin M. Casey et al. "Near-infrared MOSFIRE Spectra of Dusty Star-forming Galaxies at $0.2 < z < 4$". In: ApJ 840.2, 101 (May 2017), p. 101. DOI: 10.3847/1538-4357/aa6cb1. arXiv: 1703.10168 [astro-ph.GA] (cit. on p. 55).

[Cas+18] Caitlin M. Casey et al. "An Analysis of ALMA Deep Fields and the Perceived Dearth of High-z Galaxies". In: ApJ 862.1, 78 (July 2018), p. 78. DOI: 10.3847/1538-4357/aacd11. arXiv: 1806.05603 [astro-ph.GA] (cit. on p. 56).

[Cas+19] Caitlin M. Casey et al. "Physical Characterization of an Unlensed, Dusty Star-forming Galaxy at $z = 5.85$". In: ApJ 887.1, 55 (Dec. 2019), p. 55. DOI: 10.3847/1538-4357/ab52ff. arXiv: 1910.13331 [astro-ph.GA] (cit. on pp. 40, 66).

[Cas+21] Caitlin M. Casey et al. "Mapping Obscuration to Reionization with ALMA (MORA): 2 mm Efficiently Selects the Highest-redshift Obscured Galaxies". In: ApJ 923.2, 215 (Dec. 2021), p. 215. DOI: 10.3847/1538-4357/ac2eb4. arXiv: 2110.06930 [astro-ph.GA] (cit. on pp. 36, 50, 55, 66).

[Cat+14] A. Catalano et al. “Performance and calibration of the NIKA camera at the IRAM 30 m telescope”. In: A&A 569, A9 (Sept. 2014), A9. DOI: 10.1051/0004-6361/201423557. arXiv: 1402.0260 [astro-ph.IM] (cit. on p. 122).

[CT02] S. Cazaux and A. G. G. M. Tielens. “Molecular Hydrogen Formation in the Interstellar Medium”. In: ApJ 575.1 (Aug. 2002), pp. L29–L32. DOI: 10.1086/342607. arXiv: astro-ph/0207035 [astro-ph] (cit. on p. 46).

[CCA+21] CCAT-Prime collaboration et al. “CCAT-prime Collaboration: Science Goals and Forecasts with Prime-Cam on the Fred Young Submillimeter Telescope”. In: *arXiv e-prints*, arXiv:2107.10364 (July 2021), arXiv:2107.10364. arXiv: 2107.10364 [astro-ph.CO] (cit. on pp. 168, 174).

[Ces+96] C. J. Cesarsky et al. “ISOCAM in flight.” In: A&A 315 (Nov. 1996), pp. L32–L37 (cit. on p. 57).

[CDB10] Daniel Ceverino et al. “High-redshift clumpy discs and bulges in cosmological simulations”. In: MNRAS 404.4 (June 2010), pp. 2151–2169. DOI: 10.1111/j.1365-2966.2010.16433.x. arXiv: 0907.3271 [astro-ph.CO] (cit. on p. 39).

[Cha03] Gilles Chabrier. “Galactic Stellar and Substellar Initial Mass Function”. In: PASP 115.809 (July 2003), pp. 763–795. DOI: 10.1086/376392. arXiv: astro-ph/0304382 [astro-ph] (cit. on pp. 46, 133).

[Cha+05] S. C. Chapman et al. “A Redshift Survey of the Submillimeter Galaxy Population”. In: ApJ 622.2 (Apr. 2005), pp. 772–796. DOI: 10.1086/428082. arXiv: astro-ph/0412573 [astro-ph] (cit. on p. 50).

[Cha+22] Scott C. Chapman et al. “CCAT-prime: The 850 GHz camera for Prime-Cam on FYST”. In: *arXiv e-prints*, arXiv:2208.10634 (Aug. 2022), arXiv:2208.10634. arXiv: 2208.10634 [astro-ph.IM] (cit. on p. 63).

[CF00] Stéphane Charlot and S. Michael Fall. “A Simple Model for the Absorption of Starlight by Dust in Galaxies”. In: ApJ 539.2 (Aug. 2000), pp. 718–731. DOI: 10.1086/309250. arXiv: astro-ph/0003128 [astro-ph] (cit. on p. 133).

[Che+13] Bin Chen et al. “Dust, Gas, and Metallicities of Cosmologically Distant Lens Galaxies”. In: *arXiv e-prints*, arXiv:1306.0008 (May 2013), arXiv:1306.0008. arXiv: 1306.0008 [astro-ph.CO] (cit. on p. 163).

[Che+16] Chian-Chou Chen et al. “The SCUBA-2 Cosmology Legacy Survey: Multi-wavelength Counterparts to 10^3 Submillimeter Galaxies in the UKIDSS-UDS Field”. In: ApJ 820.2, 82 (Apr. 2016), p. 82. DOI: 10.3847/0004-637X/820/2/82. arXiv: 1601.02630 [astro-ph.GA] (cit. on p. 55).

[Che+22] Chian-Chou Chen et al. "An ALMA Spectroscopic Survey of the Brightest Submillimeter Galaxies in the SCUBA-2-COSMOS Field (AS2COSPEC): Survey Description and First Results". In: ApJ 929.2, 159 (Apr. 2022), p. 159. DOI: 10.3847/1538-4357/ac61df. arXiv: 2112.07430 [astro-ph.GA] (cit. on pp. 55, 71).

[Com+12] F. Combes et al. "A bright z = 5.2 lensed submillimeter galaxy in the field of Abell 773. HLSJ091828.6+514223". In: A&A 538, L4 (Feb. 2012), p. L4. DOI: 10.1051/0004-6361/201118750. arXiv: 1201.2908 [astro-ph.CO] (cit. on pp. 76, 156).

[Com+15] Julia M. Comerford et al. "Merger-driven Fueling of Active Galactic Nuclei: Six Dual and Offset AGNs Discovered with Chandra and Hubble Space Telescope Observations". In: ApJ 806.2, 219 (June 2015), p. 219. DOI: 10.1088/0004-637X/806/2/219. arXiv: 1504.01391 [astro-ph.GA] (cit. on p. 39).

[Com+11] M. Compiègne et al. "The global dust SED: tracing the nature and evolution of dust with DustEM". In: A&A 525, A103 (Jan. 2011), A103. DOI: 10.1051/0004-6361/201015292. arXiv: 1010.2769 [astro-ph.GA] (cit. on pp. 44, 45).

[Cor+20] Isabella Cortzen et al. "Deceptively cold dust in the massive starburst galaxy GN20 at z ∼ 4". In: A&A 634, L14 (Feb. 2020), p. L14. DOI: 10.1051/0004-6361/201937217. arXiv: 2002.02974 [astro-ph.GA] (cit. on pp. 47, 56, 121).

[Cow+17] L. L. Cowie et al. "A Submillimeter Perspective on the GOODS Fields (SUPER GOODS). I. An Ultradeep SCUBA-2 Survey of the GOODS-N". In: ApJ 837.2, 139 (Mar. 2017), p. 139. DOI: 10.3847/1538-4357/aa60bb. arXiv: 1702.03002 [astro-ph.GA] (cit. on pp. 55, 61, 64, 95).

[da +13] Elisabete da Cunha et al. "On the Effect of the Cosmic Microwave Background in High-redshift (Sub-)millimeter Observations". In: ApJ 766.1, 13 (Mar. 2013), p. 13. DOI: 10.1088/0004-637X/766/1/13. arXiv: 1302.0844 [astro-ph.CO] (cit. on pp. 138, 153).

[Dad+07] E. Daddi et al. "Multiwavelength Study of Massive Galaxies at z~2. I. Star Formation and Galaxy Growth". In: ApJ 670.1 (Nov. 2007), pp. 156–172. DOI: 10.1086/521818. arXiv: 0705.2831 [astro-ph] (cit. on p. 38).

[Dad+09] E. Daddi et al. "Two Bright Submillimeter Galaxies in a z = 4.05 Protocluster in Goods-North, and Accurate Radio-Infrared Photometric Redshifts". In: ApJ 694.2 (Apr. 2009), pp. 1517–1538. DOI: 10.1088/0004-637X/694/2/1517. arXiv: 0810.3108 [astro-ph] (cit. on pp. 40, 41).

[Dad+10a] E. Daddi et al. "Different Star Formation Laws for Disks Versus Starbursts at Low and High Redshifts". In: ApJ 714.1 (May 2010), pp. L118–L122. DOI: 10.1088/2041-8205/714/1/L118. arXiv: 1003.3889 [astro-ph.CO] (cit. on p. 52).

[Dad+10b] E. Daddi et al. "Very High Gas Fractions and Extended Gas Reservoirs in z = 1.5 Disk Galaxies". In: ApJ 713.1 (Apr. 2010), pp. 686–707. DOI: 10.1088/0004-637X/713/1/686. arXiv: 0911.2776 [astro-ph.CO] (cit. on p. 39).

[Dal+17] D. A. Dale et al. "Updated 34-band Photometry for the Sings/KINGFISH Samples of Nearby Galaxies". In: ApJ 837.1, 90 (Mar. 2017), p. 90. DOI: 10.3847/1538-4357/aa6032. arXiv: 1702.05205 [astro-ph.GA] (cit. on p. 41).

[Dal+14] Daniel A. Dale et al. "A Two-parameter Model for the Infrared/Submillimeter/Radio Spectral Energy Distributions of Galaxies and Active Galactic Nuclei". In: ApJ 784.1, 83 (Mar. 2014), p. 83. DOI: 10.1088/0004-637X/784/1/83. arXiv: 1402.1495 [astro-ph.GA] (cit. on p. 133).

[Dal06] A. Dalgarno. "Interstellar Chemistry Special Feature: The galactic cosmic ray ionization rate". In: *Proceedings of the National Academy of Science* 103.33 (Aug. 2006), pp. 12269–12273. DOI: 10.1073/pnas.0602117103 (cit. on p. 47).

[DHT01] T. M. Dame et al. "The Milky Way in Molecular Clouds: A New Complete CO Survey". In: ApJ 547.2 (Feb. 2001), pp. 792–813. DOI: 10.1086/318388. arXiv: astro-ph/0009217 [astro-ph] (cit. on p. 47).

[Dan+11] A. L. R. Danielson et al. "The properties of the interstellar medium within a star-forming galaxy at z= 2.3". In: MNRAS 410.3 (Jan. 2011), pp. 1687–1702. DOI: 10.1111/j.1365-2966.2010.17549.x. arXiv: 1008.3183 [astro-ph.CO] (cit. on pp. 151, 162).

[Day+22] P. Dayal et al. "The ALMA REBELS survey: the dust content of z 7 Lyman break galaxies". In: MNRAS 512.1 (May 2022), pp. 989–1002. DOI: 10.1093/mnras/stac537. arXiv: 2202.11118 [astro-ph.GA] (cit. on p. 40).

[De +14a] Carlos De Breuck et al. "ALMA resolves turbulent, rotating [CII] emission in a young starburst galaxy at z = 4.8". In: A&A 565, A59 (May 2014), A59. DOI: 10.1051/0004-6361/201323331. arXiv: 1404.2295 [astro-ph.GA] (cit. on p. 48).

[De +19a] Carlos De Breuck et al. "A dense, solar metallicity ISM in the z = 4.2 dusty star-forming galaxy SPT 0418-47". In: A&A 631, A167 (Nov. 2019), A167. DOI: 10.1051/0004-6361/201936169. arXiv: 1909.12554 [astro-ph.GA] (cit. on p. 48).

[De +14b] Ilse De Looze et al. "The applicability of far-infrared fine-structure lines as star formation rate tracers over wide ranges of metallicities and galaxy types". In: A&A 568, A62 (Aug. 2014), A62. DOI: 10.1051/0004-6361/201322489. arXiv: 1402.4075 [astro-ph.GA] (cit. on p. 141).

[De +19b] P. De Vis et al. “A systematic metallicity study of DustPedia galaxies reveals evolution in the dust-to-metal ratios”. In: A&A 623, A5 (Mar. 2019), A5. DOI: 10.1051/0004-6361/201834444. arXiv: 1901.09040 [astro-ph.GA] (cit. on p. 163).

[Dec+16a] Roberto Decarli et al. “ALMA Spectroscopic Survey in the Hubble Ultra Deep Field: CO Luminosity Functions and the Evolution of the Cosmic Density of Molecular Gas”. In: ApJ 833.1, 69 (Dec. 2016), p. 69. DOI: 10.3847/1538-4357/833/1/69. arXiv: 1607.06770 [astro-ph.GA] (cit. on p. 69).

[Dec+16b] Roberto Decarli et al. “The ALMA Spectroscopic Survey in the Hubble Ultra Deep Field: Molecular Gas Reservoirs in High-redshift Galaxies”. In: ApJ 833.1, 70 (Dec. 2016), p. 70. DOI: 10.3847/1538-4357/833/1/70. arXiv: 1607.06771 [astro-ph.GA] (cit. on p. 69).

[Dec+19] Roberto Decarli et al. “The ALMA Spectroscopic Survey in the HUDF: CO Luminosity Functions and the Molecular Gas Content of Galaxies through Cosmic History”. In: ApJ 882.2, 138 (Sept. 2019), p. 138. DOI: 10.3847/1538-4357/ab30fe. arXiv: 1903.09164 [astro-ph.GA] (cit. on pp. 36, 38, 69).

[DSC09] Avishai Dekel et al. “Formation of Massive Galaxies at High Redshift: Cold Streams, Clumpy Disks, and Compact Spheroids”. In: ApJ 703.1 (Sept. 2009), pp. 785–801. DOI: 10.1088/0004-637X/703/1/785. arXiv: 0901.2458 [astro-ph.GA] (cit. on pp. 33, 39).

[Dek+20] Avishai Dekel et al. “A mass threshold for galactic gas discs by spin flips”. In: MNRAS 493.3 (Apr. 2020), pp. 4126–4142. DOI: 10.1093/mnras/staa470. arXiv: 1912.08213 [astro-ph.GA] (cit. on pp. 33, 54).

[Del+14] I. Delvecchio et al. “Tracing the cosmic growth of supermassive black holes to z ~ 3 with Herschel”. In: MNRAS 439.3 (Apr. 2014), pp. 2736–2754. DOI: 10.1093/mnras/stu130. arXiv: 1401.4503 [astro-ph.GA] (cit. on p. 38).

[Des+08] Vandana Desai et al. “Redshift Distribution of Extragalactic 24 μm Sources”. In: ApJ 679.2 (June 2008), pp. 1204–1217. DOI: 10.1086/587637. arXiv: 0802.2489 [astro-ph] (cit. on p. 49).

[DBS86] F. X. Desert et al. “Grain temperature fluctuations - A key to infrared spectra”. In: A&A 160.2 (May 1986), pp. 295–300 (cit. on p. 45).

[Dey+08] Arjun Dey et al. “A Significant Population of Very Luminous Dust-Obscured Galaxies at Redshift z ∼2”. In: ApJ 677.2 (Apr. 2008), pp. 943–956. DOI: 10.1086/529516. arXiv: 0801.1860 [astro-ph] (cit. on p. 49).

[Dol+01] H. Dole et al. “FIRBACK: III. Catalog, source counts, and cosmological implications of the 170 mu m ISO”. In: A&A 372 (June 2001), pp. 364–376. DOI: 10.1051/0004-6361:20010449. arXiv: astro-ph/0103434 [astro-ph] (cit. on p. 57).

[DS98] D. Downes and P. M. Solomon. "Rotating Nuclear Rings and Extreme Starbursts in Ultraluminous Galaxies". In: ApJ 507.2 (Nov. 1998), pp. 615–654. DOI: 10.1086/306339. arXiv: astro-ph/9806377 [astro-ph] (cit. on pp. 47, 163).

[DL07] B. T. Draine and Aigen Li. "Infrared Emission from Interstellar Dust. IV. The Silicate-Graphite-PAH Model in the Post-Spitzer Era". In: ApJ 657.2 (Mar. 2007), pp. 810–837. DOI: 10.1086/511055. arXiv: astro-ph/0608003 [astro-ph] (cit. on pp. 45, 157, 160, 161).

[Dra+07] B. T. Draine et al. "Dust Masses, PAH Abundances, and Starlight Intensities in the SINGS Galaxy Sample". In: ApJ 663.2 (July 2007), pp. 866–894. DOI: 10.1086/518306. arXiv: astro-ph/0703213 [astro-ph] (cit. on p. 45).

[Dra+14] B. T. Draine et al. "Andromeda's Dust". In: ApJ 780.2, 172 (Jan. 2014), p. 172. DOI: 10.1088/0004-637X/780/2/172. arXiv: 1306.2304 [astro-ph.CO] (cit. on pp. 153, 157, 160).

[Dre80] A. Dressler. "Galaxy morphology in rich clusters: implications for the formation and evolution of galaxies." In: ApJ 236 (Mar. 1980), pp. 351–365. DOI: 10.1086/157753 (cit. on p. 40).

[Dud+20] U. Dudzevičiūtė et al. "An ALMA survey of the SCUBA-2 CLS UDS field: physical properties of 707 sub-millimetre galaxies". In: MNRAS 494.3 (May 2020), pp. 3828–3860. DOI: 10.1093/mnras/staa769. arXiv: 1910.07524 [astro-ph.GA] (cit. on pp. 54, 90).

[DK10] W. W. Duley and Stanislav Kuzmin. "Vibronic Progressions in Several Diffuse Interstellar Bands". In: ApJ 712.2 (Apr. 2010), pp. L165–L168. DOI: 10.1088/2041-8205/712/2/L165 (cit. on p. 45).

[Dun+17] J. S. Dunlop et al. "A deep ALMA image of the Hubble Ultra Deep Field". In: MNRAS 466.1 (Apr. 2017), pp. 861–883. DOI: 10.1093/mnras/stw3088. arXiv: 1606.00227 [astro-ph.GA] (cit. on pp. 65, 68).

[Eal+10] S. Eales et al. "The Herschel ATLAS". In: PASP 122.891 (May 2010), p. 499. DOI: 10.1086/653086. arXiv: 0910.4279 [astro-ph.CO] (cit. on pp. 58, 59).

[EM86] R. A. Edelson and M. A. Malkan. "Spectral Energy Distributions of Active Galactic Nuclei between 0.1 and 100 Microns". In: ApJ 308 (Sept. 1986), p. 59. DOI: 10.1086/164479 (cit. on p. 42).

[Ega+10] E. Egami et al. "The Herschel Lensing Survey (HLS): Overview". In: A&A 518, L12 (July 2010), p. L12. DOI: 10.1051/0004-6361/201014696. arXiv: 1005.3820 [astro-ph.CO] (cit. on p. 136).

[Eis+12] Peter R. M. Eisenhardt et al. "The First Hyper-luminous Infrared Galaxy Discovered by WISE". In: ApJ 755.2, 173 (Aug. 2012), p. 173. DOI: 10.1088/0004-637X/755/2/173. arXiv: 1208.5517 [astro-ph.CO] (cit. on pp. 49, 59, 166).

[Elb+99] D. Elbaz et al. “Source counts from the 15 mu m ISOCAM Deep Surveys”. In: A&A 351 (Nov. 1999), pp. L37–L40. arXiv: astro-ph/9910406 [astro-ph] (cit. on p. 57).

[Elb+07] D. Elbaz et al. “The reversal of the star formation-density relation in the distant universe”. In: A&A 468.1 (June 2007), pp. 33–48. DOI: 10.1051/0004-6361:20077525. arXiv: astro-ph/0703653 [astro-ph] (cit. on p. 38).

[Elb+11] D. Elbaz et al. “GOODS-Herschel: an infrared main sequence for star-forming galaxies”. In: A&A 533, A119 (Sept. 2011), A119. DOI: 10.1051/0004-6361/201117239. arXiv: 1105.2537 [astro-ph.CO] (cit. on pp. 50, 58, 60).

[Elb+18] D. Elbaz et al. “Starbursts in and out of the star-formation main sequence”. In: A&A 616, A110 (Aug. 2018), A110. DOI: 10.1051/0004-6361/201732370. arXiv: 1711.10047 [astro-ph.GA] (cit. on p. 165).

[Ell+19] Sara L. Ellison et al. “A definitive merger-AGN connection at z ∼ 0 with CFIS: mergers have an excess of AGN and AGN hosts are more frequently disturbed”. In: MNRAS 487.2 (Aug. 2019), pp. 2491–2504. DOI: 10.1093/mnras/stz1431. arXiv: 1905.08830 [astro-ph.GA] (cit. on p. 39).

[Elv+78] M. Elvis et al. “Seyfert galaxies as X-ray sources.” In: MNRAS 183 (Apr. 1978), pp. 129–157. DOI: 10.1093/mnras/183.2.129 (cit. on p. 42).

[Ems+11] Eric Emsellem et al. “The ATLAS^{3D} project - III. A census of the stellar angular momentum within the effective radius of early-type galaxies: unveiling the distribution of fast and slow rotators”. In: MNRAS 414.2 (June 2011), pp. 888–912. DOI: 10.1111/j.1365-2966.2011.18496.x. arXiv: 1102.4444 [astro-ph.CO] (cit. on p. 39).

[Eve+20] W. B. Everett et al. “Millimeter-wave Point Sources from the 2500 Square Degree SPT-SZ Survey: Catalog and Population Statistics”. In: ApJ 900.1, 55 (Sept. 2020), p. 55. DOI: 10.3847/1538-4357/ab9df7. arXiv: 2003.03431 [astro-ph.IM] (cit. on pp. 63, 64).

[Fab+07] S. M. Faber et al. “Galaxy Luminosity Functions to z≃1 from DEEP2 and COMBO-17: Implications for Red Galaxy Formation”. In: ApJ 665.1 (Aug. 2007), pp. 265–294. DOI: 10.1086/519294. arXiv: astro-ph/0506044 [astro-ph] (cit. on p. 39).

[Fab12] A. C. Fabian. “Observational Evidence of Active Galactic Nuclei Feedback”. In: ARA&A 50 (Sept. 2012), pp. 455–489. DOI: 10.1146/annurev-astro-081811-125521. arXiv: 1204.4114 [astro-ph.CO] (cit. on p. 33).

[Fai+20] Andreas L. Faisst et al. “ALMA characterizes the dust temperature of z ∼ 5.5 star-forming galaxies”. In: MNRAS 498.3 (Nov. 2020), pp. 4192–4204. DOI: 10.1093/mnras/staa2545. arXiv: 2005.07716 [astro-ph.GA] (cit. on p. 156).

[Fan+16] Lulu Fan et al. "Infrared Spectral Energy Distribution Decomposition of WISE-selected, Hyperluminous Hot Dust-obscured Galaxies". In: ApJ 823.2, 107 (June 2016), p. 107. DOI: 10.3847/0004-637X/823/2/107. arXiv: 1604.01467 [astro-ph.GA] (cit. on p. 166).

[Faz+04] G. G. Fazio et al. "The Infrared Array Camera (IRAC) for the Spitzer Space Telescope". In: ApJS 154.1 (Sept. 2004), pp. 10–17. DOI: 10.1086/422843. arXiv: astro-ph/0405616 [astro-ph] (cit. on p. 57).

[Fel+17] Robert Feldmann et al. "Colours, star formation rates and environments of star-forming and quiescent galaxies at the cosmic noon". In: MNRAS 470.1 (Sept. 2017), pp. 1050–1072. DOI: 10.1093/mnras/stx1120. arXiv: 1610.02411 [astro-ph.GA] (cit. on p. 33).

[Fer+22] A. Ferrara et al. "The ALMA REBELS Survey. Epoch of Reionization giants: Properties of dusty galaxies at z ≃ 7". In: MNRAS 512.1 (May 2022), pp. 58–72. DOI: 10.1093/mnras/stac460. arXiv: 2202.07666 [astro-ph.GA] (cit. on p. 40).

[Fio+10] N. Fiolet et al. "Mid-infrared spectroscopy of Spitzer-selected ultra-luminous starbursts at z ∼2". In: A&A 524, A33 (Dec. 2010), A33. DOI: 10.1051/0004-6361/201015504. arXiv: 1009.0445 [astro-ph.CO] (cit. on p. 49).

[För+09] N. M. Förster Schreiber et al. "The SINS Survey: SINFONI Integral Field Spectroscopy of z ∼2 Star-forming Galaxies". In: ApJ 706.2 (Dec. 2009), pp. 1364–1428. DOI: 10.1088/0004-637X/706/2/1364. arXiv: 0903.1872 [astro-ph.CO] (cit. on p. 39).

[Fra+18] M. Franco et al. "GOODS-ALMA: 1.1 mm galaxy survey. I. Source catalog and optically dark galaxies". In: A&A 620, A152 (Dec. 2018), A152. DOI: 10.1051/0004-6361/201832928. arXiv: 1803.00157 [astro-ph.GA] (cit. on pp. 66, 68, 110, 121).

[Fra+20] M. Franco et al. "GOODS-ALMA: Using IRAC and VLA to probe fainter millimeter galaxies". In: A&A 643, A53 (Nov. 2020), A53. DOI: 10.1051/0004-6361/202038310. arXiv: 2005.03040 [astro-ph.GA] (cit. on p. 52).

[Fra+21] F. Fraternali et al. "Fast rotating and low-turbulence discs at z ≃ 4.5: Dynamical evidence of their evolution into local early-type galaxies". In: A&A 647, A194 (Mar. 2021), A194. DOI: 10.1051/0004-6361/202039807. arXiv: 2011.05340 [astro-ph.GA] (cit. on p. 53).

[Fud+17] Y. Fudamoto et al. "The most distant, luminous, dusty star-forming galaxies: redshifts from NOEMA and ALMA spectral scans". In: MNRAS 472.2 (Dec. 2017), pp. 2028–2041. DOI: 10.1093/mnras/stx1956. arXiv: 1707.08967 [astro-ph.GA] (cit. on pp. 121, 147).

[Fud+21] Y. Fudamoto et al. “Normal, dust-obscured galaxies in the epoch of reionization”. In: Nature 597.7877 (Sept. 2021), pp. 489–492. DOI: 10.1038/s41586-021-03846-z. arXiv: 2109.10378 [astro-ph.GA] (cit. on pp. 40, 53, 55, 167).

[Fud+22] Y. Fudamoto et al. “The ALMA REBELS Survey: Average [C II] 158 μm Sizes of Star-forming Galaxies from z 7 to z 4”. In: ApJ 934.2, 144 (Aug. 2022), p. 144. DOI: 10.3847/1538-4357/ac7a47. arXiv: 2206.01886 [astro-ph.GA] (cit. on p. 71).

[Fuj+16] Seiji Fujimoto et al. “ALMA Census of Faint 1.2 mm Sources Down to ~0.02 mJy: Extragalactic Background Light and Dust-poor, High-z Galaxies”. In: ApJS 222.1, 1 (Jan. 2016), p. 1. DOI: 10.3847/0067-0049/222/1/1. arXiv: 1505.03523 [astro-ph.GA] (cit. on pp. 65, 66, 91, 110).

[Fuj+20] Seiji Fujimoto et al. “The ALPINE-ALMA [C II] Survey: Size of Individual Star-forming Galaxies at z = 4-6 and Their Extended Halo Structure”. In: ApJ 900.1, 1 (Sept. 2020), p. 1. DOI: 10.3847/1538-4357/ab94b3. arXiv: 2003.00013 [astro-ph.GA] (cit. on p. 70).

[GBB22] Brandt A. L. Gaches et al. “The impact of cosmic-ray attenuation on the carbon cycle emission in molecular clouds”. In: A&A 658, A151 (Feb. 2022), A151. DOI: 10.1051/0004-6361/202142411. arXiv: 2110.06958 [astro-ph.GA] (cit. on p. 47).

[GHA11] C. Gall et al. “Production of dust by massive stars at high redshift”. In: A&A Rev. 19, 43 (Sept. 2011), p. 43. DOI: 10.1007/s00159-011-0043-7. arXiv: 1108.0403 [astro-ph.CO] (cit. on p. 44).

[GS04] Yu Gao and Philip M. Solomon. “The Star Formation Rate and Dense Molecular Gas in Galaxies”. In: ApJ 606.1 (May 2004), pp. 271–290. DOI: 10.1086/382999. arXiv: astro-ph/0310339 [astro-ph] (cit. on p. 48).

[Gar+12] S. García-Burillo et al. “Star-formation laws in luminous infrared galaxies. New observational constraints on models”. In: A&A 539, A8 (Mar. 2012), A8. DOI: 10.1051/0004-6361/201117838. arXiv: 1111.6773 [astro-ph.CO] (cit. on p. 52).

[Gea+17] J. E. Geach et al. “The SCUBA-2 Cosmology Legacy Survey: 850 μm maps, catalogues and number counts”. In: MNRAS 465.2 (Feb. 2017), pp. 1789–1806. DOI: 10.1093/mnras/stw2721. arXiv: 1607.03904 [astro-ph.GA] (cit. on pp. 61, 64, 87, 98, 100, 101).

[GH89] Margaret J. Geller and John P. Huchra. “Mapping the Universe”. In: *Science* 246.4932 (Nov. 1989), pp. 897–903. DOI: 10.1126/science.246.4932.897 (cit. on p. 33).

[Gen+10] R. Genzel et al. “A study of the gas-star formation relation over cosmic time”. In: MNRAS 407.4 (Oct. 2010), pp. 2091–2108. DOI: 10.1111/j.1365-2966.2010.16969.x. arXiv: 1003.5180 [astro-ph.CO] (cit. on pp. 39, 52).

[Gen+15] R. Genzel et al. "Combined CO and Dust Scaling Relations of Depletion Time and Molecular Gas Fractions with Cosmic Time, Specific Star-formation Rate, and Stellar Mass". In: ApJ 800.1, 20 (Feb. 2015), p. 20. DOI: 10.1088/0004-637X/800/1/20. arXiv: 1409.1171 [astro-ph.GA] (cit. on pp. 38, 165).

[GRC11] I. Georgantopoulos et al. "X-ray observations of sub-mm LABOCA galaxies in the eCDFS". In: A&A 526, A46 (Feb. 2011), A46. DOI: 10.1051/0004-6361/201015230. arXiv: 1010.3530 [astro-ph.CO] (cit. on p. 43).

[Gia+04] M. Giavalisco et al. "The Great Observatories Origins Deep Survey: Initial Results from Optical and Near-Infrared Imaging". In: ApJ 600.2 (Jan. 2004), pp. L93–L98. DOI: 10.1086/379232. arXiv: astro-ph/0309105 [astro-ph] (cit. on p. 57).

[Gko+22] A. Gkogkou et al. "CONCERTO: Simulating the CO, [CII], and [CI] line emission of galaxies in a 117 deg^2 field and the impact of field-to-field variance". In: *arXiv e-prints*, arXiv:2212.02235 (Dec. 2022), arXiv:2212.02235. arXiv: 2212.02235 [astro-ph.CO] (cit. on pp. 38, 88, 114).

[Gla+17] Karl Glazebrook et al. "A massive, quiescent galaxy at a redshift of 3.717". In: Nature 544.7648 (Apr. 2017), pp. 71–74. DOI: 10.1038/nature21680. arXiv: 1702.01751 [astro-ph.GA] (cit. on p. 52).

[Góm+18] C. Gómez-Guijarro et al. "Starburst to Quiescent from HST/ALMA: Stars and Dust Unveil Minor Mergers in Submillimeter Galaxies at z ~ 4.5". In: ApJ 856.2, 121 (Apr. 2018), p. 121. DOI: 10.3847/1538-4357/aab206. arXiv: 1802.07751 [astro-ph.GA] (cit. on p. 131).

[Góm+22a] C. Gómez-Guijarro et al. "GOODS-ALMA 2.0: Source catalog, number counts, and prevailing compact sizes in 1.1 mm galaxies". In: A&A 658, A43 (Feb. 2022), A43. DOI: 10.1051/0004-6361/202141615. arXiv: 2106.13246 [astro-ph.GA] (cit. on pp. 50, 53, 66, 68, 91, 110).

[Góm+22b] C. Gómez-Guijarro et al. "GOODS-ALMA 2.0: Starbursts in the main sequence reveal compact star formation regulating galaxy evolution prequenching". In: A&A 659, A196 (Mar. 2022), A196. DOI: 10.1051/0004-6361/202142352. arXiv: 2201.02633 [astro-ph.GA] (cit. on pp. 40, 91).

[Gon+17] E. González-Alfonso et al. "Molecular Outflows in Local ULIRGs: Energetics from Multitransition OH Analysis". In: ApJ 836.1, 11 (Feb. 2017), p. 11. DOI: 10.3847/1538-4357/836/1/11. arXiv: 1612.08181 [astro-ph.GA] (cit. on p. 39).

[Gon+20] Jorge González-López et al. "The ALMA Spectroscopic Survey in the HUDF: Deep 1.2 mm Continuum Number Counts". In: ApJ 897.1, 91 (July 2020), p. 91. DOI: 10.3847/1538-4357/ab765b. arXiv: 2002.07199 [astro-ph.GA] (cit. on pp. 65, 68, 91, 110).

[Gor+03] Karl D. Gordon et al. “A Quantitative Comparison of the Small Magellanic Cloud, Large Magellanic Cloud, and Milky Way Ultraviolet to Near-Infrared Extinction Curves”. In: ApJ 594.1 (Sept. 2003), pp. 279–293. DOI: 10.1086/376774. arXiv: astro-ph/0305257 [astro-ph] (cit. on pp. 43, 44).

[GB76] M. A. Gordon and W. B. Burton. “Carbon monoxide in the Galaxy. I. The radial distribution of CO, H_2, and nucleons.” In: ApJ 208 (Sept. 1976), pp. 346–353. DOI: 10.1086/154613 (cit. on p. 46).

[GT15] Tomotsugu Goto and Sune Toft. “CO luminosity - line-width correlation of submillimeter galaxies and a possible cosmological application”. In: A&A 579, A17 (July 2015), A17. DOI: 10.1051/0004-6361/201526062. arXiv: 1505.00013 [astro-ph.GA] (cit. on p. 145).

[Gra+08] J. Graciá-Carpio et al. “Evidence of enhanced star formation efficiency in luminous and ultraluminous infrared galaxies”. In: A&A 479.3 (Mar. 2008), pp. 703–717. DOI: 10.1051/0004-6361:20078223. arXiv: 0712.0582 [astro-ph] (cit. on pp. 156, 160).

[Gra+18] Mark T. Graham et al. “SDSS-IV MaNGA: stellar angular momentum of about 2300 galaxies: unveiling the bimodality of massive galaxy properties”. In: MNRAS 477.4 (July 2018), pp. 4711–4737. DOI: 10.1093/mnras/sty504. arXiv: 1802.08213 [astro-ph.GA] (cit. on p. 39).

[Gre+04] T. R. Greve et al. “A 1200-μm MAMBO survey of ELAISN2 and the Lockman Hole - I. Maps, sources and number counts”. In: MNRAS 354.3 (Nov. 2004), pp. 779–797. DOI: 10.1111/j.1365-2966.2004.08235.x. arXiv: astro-ph/0405361 [astro-ph] (cit. on p. 62).

[Gre+14] T. R. Greve et al. “Star Formation Relations and CO Spectral Line Energy Distributions across the J-ladder and Redshift”. In: ApJ 794.2, 142 (Oct. 2014), p. 142. DOI: 10.1088/0004-637X/794/2/142. arXiv: 1407.4400 [astro-ph.GA] (cit. on p. 141).

[Gre+08] Thomas R. Greve et al. “A 1200-μm MAMBO survey of the GOODS-N field: a significant population of submillimetre dropout galaxies”. In: MNRAS 389.4 (Oct. 2008), pp. 1489–1506. DOI: 10.1111/j.1365-2966.2008.13631.x. arXiv: 0806.3106 [astro-ph] (cit. on pp. 62, 64, 95).

[Gri+10] M. J. Griffin et al. “The Herschel-SPIRE instrument and its in-flight performance”. In: A&A 518, L3 (July 2010), p. L3. DOI: 10.1051/0004-6361/201014519. arXiv: 1005.5123 [astro-ph.IM] (cit. on p. 58).

[Gri+11] Roger L. Griffith et al. “WISE Discovery of Low-metallicity Blue Compact Dwarf Galaxies”. In: ApJ 736.1, L22 (July 2011), p. L22. DOI: 10.1088/2041-8205/736/1/L22. arXiv: 1106.4844 [astro-ph.CO] (cit. on p. 42).

[Gru+13] C. Gruppioni et al. “The Herschel PEP/HerMES luminosity function - I. Probing the evolution of PACS selected Galaxies to z ≃ 4”. In: MNRAS 432.1 (June 2013), pp. 23–52. DOI: 10.1093/mnras/stt308. arXiv: 1302.5209 [astro-ph.CO] (cit. on p. 50).

[Gru+20] C. Gruppioni et al. “The ALPINE-ALMA [CII] survey. The nature, luminosity function, and star formation history of dusty galaxies up to z ≃ 6”. In: A&A 643, A8 (Nov. 2020), A8. DOI: 10.1051/0004-6361/202038487. arXiv: 2006.04974 [astro-ph.GA] (cit. on pp. 50, 54, 66).

[Har17] C. M. Harrison. “Impact of supermassive black hole growth on star formation”. In: *Nature Astronomy* 1, 0165 (July 2017), p. 0165. DOI: 10.1038/s41550-017-0165. arXiv: 1703.06889 [astro-ph.GA] (cit. on p. 33).

[Hat+11] B. Hatsukade et al. “AzTEC/ASTE 1.1-mm survey of the AKARI Deep Field South: source catalogue and number counts”. In: MNRAS 411.1 (Feb. 2011), pp. 102–116. DOI: 10.1111/j.1365-2966.2010.17658.x. arXiv: 1010.0585 [astro-ph.CO] (cit. on pp. 62, 64).

[Hat+16] Bunyo Hatsukade et al. “SXDF-ALMA 2-arcmin^2 deep survey: 1.1-mm number counts”. In: PASJ 68.3, 36 (June 2016), p. 36. DOI: 10.1093/pasj/psw026. arXiv: 1602.08167 [astro-ph.GA] (cit. on pp. 65, 68, 110).

[Hat+18] Bunyo Hatsukade et al. “ALMA twenty-six arcmin^2 survey of GOODS-S at one millimeter (ASAGAO): Source catalog and number counts”. In: PASJ 70.6, 105 (Dec. 2018), p. 105. DOI: 10.1093/pasj/psy104. arXiv: 1808.04502 [astro-ph.GA] (cit. on pp. 65, 68, 110).

[Hay+13] Christopher C. Hayward et al. “Submillimetre galaxies in a hierarchical universe: number counts, redshift distribution and implications for the IMF”. In: MNRAS 428.3 (Jan. 2013), pp. 2529–2547. DOI: 10.1093/mnras/sts222. arXiv: 1209.2413 [astro-ph.CO] (cit. on p. 91).

[Hay+21] Christopher C. Hayward et al. “Submillimetre galaxies in cosmological hydrodynamical simulations - an opportunity for constraining feedback models”. In: MNRAS 502.2 (Apr. 2021), pp. 2922–2933. DOI: 10.1093/mnras/stab246. arXiv: 2007.01885 [astro-ph.GA] (cit. on p. 91).

[HB14] Timothy M. Heckman and Philip N. Best. “The Coevolution of Galaxies and Supermassive Black Holes: Insights from Surveys of the Contemporary Universe”. In: ARA&A 52 (Aug. 2014), pp. 589–660. DOI: 10.1146/annurev-astro-081913-035722. arXiv: 1403.4620 [astro-ph.GA] (cit. on pp. 33, 39).

[Her+18] R. Herrera-Camus et al. “SHINING, A Survey of Far-infrared Lines in Nearby Galaxies. I. Survey Description, Observational Trends, and Line Diagnostics”. In: ApJ 861.2, 94 (July 2018), p. 94. DOI: 10.3847/1538-4357/aac0f6. arXiv: 1803.04419 [astro-ph.GA] (cit. on p. 48).

[Hil+16] Allison. R. Hill et al. “A Stellar Velocity Dispersion for a Strongly-lensed, Intermediate-mass Quiescent Galaxy at z=2.8”. In: ApJ 819.1, 74 (Mar. 2016), p. 74. DOI: 10.3847/0004-637X/819/1/74. arXiv: 1602.00007 [astro-ph.GA] (cit. on p. 39).

[Hd20] J. A. Hodge and E. da Cunha. “High-redshift star formation in the Atacama large millimetre/submillimetre array era”. In: *Royal Society Open Science* 7.12, 200556 (Dec. 2020), p. 200556. DOI: 10.1098/rsos.200556. arXiv: 2004.00934 [astro-ph.GA] (cit. on pp. 51, 91, 161, 172).

[Hod+12] J. A. Hodge et al. “Evidence for a Clumpy, Rotating Gas Disk in a Submillimeter Galaxy at z = 4”. In: ApJ 760.1, 11 (Nov. 2012), p. 11. DOI: 10.1088/0004-637X/760/1/11. arXiv: 1209.2418 [astro-ph.CO] (cit. on p. 53).

[Hod+13] J. A. Hodge et al. “An ALMA Survey of Submillimeter Galaxies in the Extended Chandra Deep Field South: Source Catalog and Multiplicity”. In: ApJ 768.1, 91 (May 2013), p. 91. DOI: 10.1088/0004-637X/768/1/91. arXiv: 1304.4266 [astro-ph.CO] (cit. on pp. 55, 90).

[Hod+16] J. A. Hodge et al. “Kiloparsec-scale Dust Disks in High-redshift Luminous Submillimeter Galaxies”. In: ApJ 833.1, 103 (Dec. 2016), p. 103. DOI: 10.3847/1538-4357/833/1/103. arXiv: 1609.09649 [astro-ph.GA] (cit. on p. 131).

[Hod+19] J. A. Hodge et al. “ALMA Reveals Potential Evidence for Spiral Arms, Bars, and Rings in High-redshift Submillimeter Galaxies”. In: ApJ 876.2, 130 (May 2019), p. 130. DOI: 10.3847/1538-4357/ab1846. arXiv: 1810.12307 [astro-ph.GA] (cit. on p. 53).

[Hol+13] W. S. Holland et al. “SCUBA-2: the 10 000 pixel bolometer camera on the James Clerk Maxwell Telescope”. In: MNRAS 430.4 (Apr. 2013), pp. 2513–2533. DOI: 10.1093/mnras/sts612. arXiv: 1301.3650 [astro-ph.IM] (cit. on pp. 61, 121).

[Hol+98] Wayne S. Holland et al. “SCUBA: a submillimeter camera operating on the James Clerk Maxwell Telescope”. In: *Advanced Technology MMW, Radio, and Terahertz Telescopes*. Ed. by Thomas G. Phillips. Vol. 3357. Society of Photo-Optical Instrumentation Engineers (SPIE) Conference Series. July 1998, pp. 305–318. DOI: 10.1117/12.317366. arXiv: astro-ph/9809121 [astro-ph] (cit. on p. 61).

[Hop+14] Philip F. Hopkins et al. “Galaxies on FIRE (Feedback In Realistic Environments): stellar feedback explains cosmologically inefficient star formation”. In: MNRAS 445.1 (Nov. 2014), pp. 581–603. DOI: 10.1093/mnras/stu1738. arXiv: 1311.2073 [astro-ph.CO] (cit. on p. 33).

[Hug+98] David H. Hughes et al. “High-redshift star formation in the Hubble Deep Field revealed by a submillimetre-wavelength survey”. In: Nature 394.6690 (July 1998), pp. 241–247. DOI: 10.1038/28328. arXiv: astro-ph/9806297 [astro-ph] (cit. on p. 61).

[Ina+22] Hanae Inami et al. “The ALMA REBELS Survey: dust continuum detections at z > 6.5”. In: MNRAS 515.3 (Sept. 2022), pp. 3126–3143. DOI: 10.1093/mnras/stac1779. arXiv: 2203.15136 [astro-ph.GA] (cit. on p. 40).

[Ino11] A. K. Inoue. “The origin of dust in galaxies revisited: the mechanism determining dust content”. In: *Earth, Planets and Space* 63.10 (Oct. 2011), pp. 1027–1039. DOI: 10.5047/eps.2011.02.013 (cit. on p. 44).

[Isr97] F. P. Israel. “H_2 and its relation to CO in the LMC and other magellanic irregular galaxies”. In: A&A 328 (Dec. 1997), pp. 471–482. arXiv: astro-ph/9709194 [astro-ph] (cit. on p. 47).

[Ivi+07] R. J. Ivison et al. “The SCUBA HAlf Degree Extragalactic Survey - III. Identification of radio and mid-infrared counterparts to submillimetre galaxies”. In: MNRAS 380.1 (Sept. 2007), pp. 199–228. DOI: 10.1111/j.1365-2966.2007.12044.x. arXiv: astro-ph/0702544 [astro-ph] (cit. on p. 90).

[Jia+18] Linhua Jiang et al. “A giant protocluster of galaxies at redshift 5.7”. In: *Nature Astronomy* 2 (Oct. 2018), pp. 962–966. DOI: 10.1038/s41550-018-0587-9. arXiv: 1810.05765 [astro-ph.GA] (cit. on p. 166).

[Jia+21] Linhua Jiang et al. “Evidence for GN-z11 as a luminous galaxy at redshift 10.957”. In: *Nature Astronomy* 5 (Jan. 2021), pp. 256–261. DOI: 10.1038/s41550-020-01275-y. arXiv: 2012.06936 [astro-ph.HE] (cit. on p. 35).

[Jia+19] Qian Jiao et al. “Resolved Neutral Carbon Emission in Nearby Galaxies: [C I] Lines as Total Molecular Gas Tracers”. In: ApJ 880.2, 133 (Aug. 2019), p. 133. DOI: 10.3847/1538-4357/ab29ed. arXiv: 1906.05671 [astro-ph.GA] (cit. on p. 47).

[Jin+19] S. Jin et al. “Discovery of Four Apparently Cold Dusty Galaxies at z = 3.62-5.85 in the COSMOS Field: Direct Evidence of Cosmic Microwave Background Impact on High-redshift Galaxy Observables”. In: ApJ 887.2, 144 (Dec. 2019), p. 144. DOI: 10.3847/1538-4357/ab55d6. arXiv: 1906.00040 [astro-ph.GA] (cit. on pp. 55, 56, 66, 116, 147, 157, 166).

[Jin+22] Shuowen Jin et al. “Diagnosing deceivingly cold dusty galaxies at 3.5 < z < 6: A substantial population of compact starbursts with high infrared optical depths”. In: A&A 665, A3 (Sept. 2022), A3. DOI: 10.1051/0004-6361/202243341. arXiv: 2206.10401 [astro-ph.GA] (cit. on pp. 40, 55, 56).

[JLM92] C. Joblin et al. “Contribution of Polycyclic Aromatic Hydrocarbon Molecules to the Interstellar Extinction Curve”. In: ApJ 393 (July 1992), p. L79. DOI: 10.1086/186456 (cit. on pp. 43, 45).

[Joh+13] S. P. Johnson et al. “X-ray detections of submillimetre galaxies: active galactic nuclei versus starburst contribution”. In: MNRAS 431.1 (May 2013), pp. 662–682. DOI: 10.1093/mnras/stt197. arXiv: 1302.0842 [astro-ph.GA] (cit. on p. 43).

[Jon+21] G. C. Jones et al. “The ALPINE-ALMA [C II] Survey: kinematic diversity and rotation in massive star-forming galaxies at z 4.4-5.9”. In: MNRAS 507.3 (Nov. 2021), pp. 3540–3563. DOI: 10.1093/mnras/stab2226. arXiv: 2104.03099 [astro-ph.GA] (cit. on p. 70).

[Kar+13] A. Karim et al. “An ALMA survey of submillimetre galaxies in the Extended Chandra Deep Field South: high-resolution 870 μm source counts”. In: MNRAS 432.1 (June 2013), pp. 2–9. DOI: 10.1093/mnras/stt196. arXiv: 1210.0249 [astro-ph.CO] (cit. on pp. 65, 66).

[Kau+04] Guinevere Kauffmann et al. “The environmental dependence of the relations between stellar mass, structure, star formation and nuclear activity in galaxies”. In: MNRAS 353.3 (Sept. 2004), pp. 713–731. DOI: 10.1111/j.1365-2966.2004.08117.x. arXiv: astro-ph/0402030 [astro-ph] (cit. on p. 40).

[Ken98] Jr. Kennicutt Robert C. “Star Formation in Galaxies Along the Hubble Sequence”. In: ARA&A 36 (Jan. 1998), pp. 189–232. DOI: 10.1146/annurev.astro.36.1.189. arXiv: astro-ph/9807187 [astro-ph] (cit. on p. 35).

[Ken+11] R. C. Kennicutt et al. “KINGFISH—Key Insights on Nearby Galaxies: A Far-Infrared Survey with Herschel: Survey Description and Image Atlas”. In: PASP 123.910 (Dec. 2011), p. 1347. DOI: 10.1086/663818. arXiv: 1111.4438 [astro-ph.CO] (cit. on p. 40).

[KE12] Robert C. Kennicutt and Neal J. Evans. “Star Formation in the Milky Way and Nearby Galaxies”. In: ARA&A 50 (Sept. 2012), pp. 531–608. DOI: 10.1146/annurev-astro-081811-125610. arXiv: 1204.3552 [astro-ph.GA] (cit. on pp. 46, 156).

[Kew+06] Lisa J. Kewley et al. “The host galaxies and classification of active galactic nuclei”. In: MNRAS 372.3 (Nov. 2006), pp. 961–976. DOI: 10.1111/j.1365-2966.2006.10859.x. arXiv: astro-ph/0605681 [astro-ph] (cit. on p. 42).

[Khu+21] Y. Khusanova et al. “The ALPINE-ALMA [CII] survey. Obscured star formation rate density and main sequence of star-forming galaxies at z > 4”. In: A&A 649, A152 (May 2021), A152. DOI: 10.1051/0004-6361/202038944. arXiv: 2007.08384 [astro-ph.GA] (cit. on pp. 36, 37, 54).

[KO18] Chang-Goo Kim and Eve C. Ostriker. "Numerical Simulations of Multiphase Winds and Fountains from Star-forming Galactic Disks. I. Solar Neighborhood TIGRESS Model". In: ApJ 853.2, 173 (Feb. 2018), p. 173. DOI: 10.3847/1538-4357/aaa5ff. arXiv: 1801.03952 [astro-ph.GA] (cit. on p. 33).

[Kli+20] A. Klitsch et al. "ALMACAL VII: first interferometric number counts at 650 μm". In: MNRAS 495.2 (June 2020), pp. 2332–2341. DOI: 10.1093/mnras/staa1315. arXiv: 2005.01733 [astro-ph.GA] (cit. on p. 66).

[Kli+19] Anne Klitsch et al. "ALMACAL - VI. Molecular gas mass density across cosmic time via a blind search for intervening molecular absorbers". In: MNRAS 490.1 (Nov. 2019), pp. 1220–1230. DOI: 10.1093/mnras/stz2660. arXiv: 1909.08624 [astro-ph.GA] (cit. on p. 71).

[Knu+17] Kirsten K. Knudsen et al. "A merger in the dusty, z = 7.5 galaxy A1689-zD1?" In: MNRAS 466.1 (Apr. 2017), pp. 138–146. DOI: 10.1093/mnras/stw3066. arXiv: 1603.03222 [astro-ph.GA] (cit. on p. 40).

[Koe+11] Anton M. Koekemoer et al. "CANDELS: The Cosmic Assembly Near-infrared Deep Extragalactic Legacy Survey—The Hubble Space Telescope Observations, Imaging Data Products, and Mosaics". In: ApJS 197.2, 36 (Dec. 2011), p. 36. DOI: 10.1088/0067-0049/197/2/36. arXiv: 1105.3754 [astro-ph.CO] (cit. on p. 57).

[Koh19] Kotaro Kohno. "The ALMA lensing cluster survey: initial outcomes". In: *ALMA2019: Science Results and Cross-Facility Synergies*. Dec. 2019, 64, p. 64. DOI: 10.5281/zenodo.3585294 (cit. on p. 68).

[Kre+21] Michael Kretschmer et al. "Evaluating galaxy dynamical masses from kinematics and jeans equilibrium in simulations". In: MNRAS 503.4 (June 2021), pp. 5238–5253. DOI: 10.1093/mnras/stab833. arXiv: 2010.04629 [astro-ph.GA] (cit. on p. 54).

[Lac+04] M. Lacy et al. "Obscured and Unobscured Active Galactic Nuclei in the Spitzer Space Telescope First Look Survey". In: ApJS 154.1 (Sept. 2004), pp. 166–169. DOI: 10.1086/422816. arXiv: astro-ph/0405604 [astro-ph] (cit. on p. 42).

[Lag+04] G. Lagache et al. "Polycyclic Aromatic Hydrocarbon Contribution to the Infrared Output Energy of the Universe at z $\backsim$= 2". In: ApJS 154.1 (Sept. 2004), pp. 112–117. DOI: 10.1086/422392. arXiv: astro-ph/0406016 [astro-ph] (cit. on p. 77).

[Lag+18] Claudia del P. Lagos et al. "Shark: introducing an open source, free, and flexible semi-analytic model of galaxy formation". In: MNRAS 481.3 (Dec. 2018), pp. 3573–3603. DOI: 10.1093/mnras/sty2440. arXiv: 1807.11180 [astro-ph.GA] (cit. on p. 113).

[Lag+19] Claudia del P. Lagos et al. "From the far-ultraviolet to the far-infrared - galaxy emission at $0 \leq z \leq 10$ in the SHARK semi-analytic model". In: MNRAS 489.3 (Nov. 2019), pp. 4196–4216. DOI: 10.1093/mnras/stz2427. arXiv: 1908.03423 [astro-ph.GA] (cit. on p. 113).

[Lag+20] Claudia del P. Lagos et al. "Physical properties and evolution of (sub-)millimetre-selected galaxies in the galaxy formation simulation SHARK". In: MNRAS 499.2 (Dec. 2020), pp. 1948–1971. DOI: 10.1093/mnras/staa2861. arXiv: 2007.09853 [astro-ph.GA] (cit. on pp. 113–115, 118).

[Lap+21] N. Laporte et al. "ALMA Lensing Cluster Survey: a strongly lensed multiply imaged dusty system at $z \geq 6$". In: MNRAS 505.4 (Aug. 2021), pp. 4838–4846. DOI: 10.1093/mnras/stab191. arXiv: 2101.01740 [astro-ph.GA] (cit. on p. 40).

[Le +20] O. Le Fèvre et al. "The ALPINE-ALMA [CII] survey. Survey strategy, observations, and sample properties of 118 star-forming galaxies at $4 < z < 6$". In: A&A 643, A1 (Nov. 2020), A1. DOI: 10.1051/0004-6361/201936965. arXiv: 1910.09517 [astro-ph.CO] (cit. on p. 70).

[Le +05] Emeric Le Floc'h et al. "Infrared Luminosity Functions from the Chandra Deep Field-South: The Spitzer View on the History of Dusty Star Formation at $0 <\sim z <\sim 1$". In: ApJ 632.1 (Oct. 2005), pp. 169–190. DOI: 10.1086/432789. arXiv: astro-ph/0506462 [astro-ph] (cit. on p. 49).

[Le +09] Emeric Le Floc'h et al. "Deep Spitzer 24 μm COSMOS Imaging. I. The Evolution of Luminous Dusty Galaxies—Confronting the Models". In: ApJ 703.1 (Sept. 2009), pp. 222–239. DOI: 10.1088/0004-637X/703/1/222. arXiv: 0909.4303 [astro-ph.CO] (cit. on pp. 58, 60).

[Lel+21] Federico Lelli et al. "A massive stellar bulge in a regularly rotating galaxy 1.2 billion years after the Big Bang". In: *Science* 371.6530 (Feb. 2021), pp. 713–716. DOI: 10.1126/science.abc1893. arXiv: 2102.05957 [astro-ph.GA] (cit. on p. 53).

[Ler+08] Adam K. Leroy et al. "The Star Formation Efficiency in Nearby Galaxies: Measuring Where Gas Forms Stars Effectively". In: AJ 136.6 (Dec. 2008), pp. 2782–2845. DOI: 10.1088/0004-6256/136/6/2782. arXiv: 0810.2556 [astro-ph] (cit. on p. 46).

[Ler+11] Adam K. Leroy et al. "The CO-to-H_2 Conversion Factor from Infrared Dust Emission across the Local Group". In: ApJ 737.1, 12 (Aug. 2011), p. 12. DOI: 10.1088/0004-637X/737/1/12. arXiv: 1102.4618 [astro-ph.CO] (cit. on pp. 47, 163).

[Li20] Aigen Li. "Spitzer's perspective of polycyclic aromatic hydrocarbons in galaxies". In: *Nature Astronomy* 4 (Mar. 2020), pp. 339–351. DOI: 10.1038/s41550-020-1051-1. arXiv: 2003.10489 [astro-ph.GA] (cit. on p. 44).

[LD01] Aigen Li and B. T. Draine. "Infrared Emission from Interstellar Dust. II. The Diffuse Interstellar Medium". In: ApJ 554.2 (June 2001), pp. 778–802. DOI: 10.1086/323147. arXiv: astro-ph/0011319 [astro-ph] (cit. on p. 43).

[Li+20] Jianan Li et al. "Probing the Full CO Spectral Line Energy Distribution (SLED) in the Nuclear Region of a Quasar-starburst System at z = 6.003". In: ApJ 889.2, 162 (Feb. 2020), p. 162. DOI: 10.3847/1538-4357/ab65fa. arXiv: 1912.12813 [astro-ph.GA] (cit. on p. 151).

[Lia+18] Lichen Liang et al. "Submillimetre flux as a probe of molecular ISM mass in high-z galaxies". In: MNRAS 478.1 (July 2018), pp. L83–L88. DOI: 10.1093/mnrasl/sly071. arXiv: 1804.02403 [astro-ph.GA] (cit. on p. 91).

[Lim+20] Chen-Fatt Lim et al. "SCUBA-2 Ultra Deep Imaging EAO Survey (STUDIES). IV. Spatial Clustering and Halo Masses of Submillimeter Galaxies". In: ApJ 895.2, 104 (June 2020), p. 104. DOI: 10.3847/1538-4357/ab8eaf. arXiv: 2004.13616 [astro-ph.GA] (cit. on p. 167).

[Lin+11] R. R. Lindner et al. "A Deep 1.2 mm Map of the Lockman Hole North Field". In: ApJ 737.2, 83 (Aug. 2011), p. 83. DOI: 10.1088/0004-637X/737/2/83. arXiv: 1106.0344 [astro-ph.CO] (cit. on pp. 62, 64, 91, 110).

[Liu+15] Daizhong Liu et al. "High-J CO versus Far-infrared Relations in Normal and Starburst Galaxies". In: ApJ 810.2, L14 (Sept. 2015), p. L14. DOI: 10.1088/2041-8205/810/2/L14. arXiv: 1504.05897 [astro-ph.GA] (cit. on pp. 123, 141).

[Liu+18] Daizhong Liu et al. ""Super-deblended" Dust Emission in Galaxies. I. The GOODS-North Catalog and the Cosmic Star Formation Rate Density out to Redshift 6". In: ApJ 853.2, 172 (Feb. 2018), p. 172. DOI: 10.3847/1538-4357/aaa600. arXiv: 1703.05281 [astro-ph.GA] (cit. on pp. 41, 76, 122, 126, 131, 132, 134, 136).

[Liu+19] Daizhong Liu et al. "Automated Mining of the ALMA Archive in the COSMOS Field (A^3COSMOS). I. Robust ALMA Continuum Photometry Catalogs and Stellar Mass and Star Formation Properties for ~700 Galaxies at z = 0.5-6". In: ApJS 244.2, 40 (Oct. 2019), p. 40. DOI: 10.3847/1538-4365/ab42da. arXiv: 1910.12872 [astro-ph.GA] (cit. on p. 66).

[Liu+22] Weizhe Liu et al. "Galactic Winds across the Gas-rich Merger Sequence. II. Lyα Emission and Highly Ionized O VI and N V Outflows in Ultraluminous Infrared Galaxies". In: ApJ 934.2, 160 (Aug. 2022), p. 160. DOI: 10.3847/1538-4357/ac7a46. arXiv: 2206.09015 [astro-ph.GA] (cit. on p. 39).

[Loi+21] Federica Loiacono et al. “The ALPINE-ALMA [C II] survey. Luminosity function of serendipitous [C II] line emitters at z ∼ 5”. In: A&A 646, A76 (Feb. 2021), A76. DOI: 10.1051/0004-6361/202038607. arXiv: 2006.04837 [astro-ph.GA] (cit. on p. 70).

[Lov+21] Christopher C. Lovell et al. “Reproducing submillimetre galaxy number counts with cosmological hydrodynamic simulations”. In: MNRAS 502.1 (Mar. 2021), pp. 772–793. DOI: 10.1093/mnras/staa4043. arXiv: 2006.15156 [astro-ph.GA] (cit. on p. 91).

[Lut+11] D. Lutz et al. “PACS Evolutionary Probe (PEP) - A Herschel key program”. In: A&A 532, A90 (Aug. 2011), A90. DOI: 10.1051/0004-6361/201117107. arXiv: 1106.3285 [astro-ph.CO] (cit. on pp. 58, 60).

[MD14] Piero Madau and Mark Dickinson. “Cosmic Star-Formation History”. In: ARA&A 52 (Aug. 2014), pp. 415–486. DOI: 10.1146/annurev-astro-081811-125615. arXiv: 1403.0007 [astro-ph.CO] (cit. on pp. 35–38, 54).

[Mad+20] S. C. Madden et al. “Tracing the total molecular gas in galaxies: [CII] and the CO-dark gas”. In: A&A 643, A141 (Nov. 2020), A141. DOI: 10.1051/0004-6361/202038860. arXiv: 2009.00649 [astro-ph.GA] (cit. on pp. 47, 48).

[Mag+12] Georgios E. Magdis et al. “The Evolving Interstellar Medium of Star-forming Galaxies since z = 2 as Probed by Their Infrared Spectral Energy Distributions”. In: ApJ 760.1, 6 (Nov. 2012), p. 6. DOI: 10.1088/0004-637X/760/1/6. arXiv: 1210.1035 [astro-ph.CO] (cit. on pp. 161, 163).

[Mag+19] B. Magnelli et al. “The IRAM/GISMO 2 mm Survey in the COSMOS Field”. In: ApJ 877.1, 45 (May 2019), p. 45. DOI: 10.3847/1538-4357/ab1912. arXiv: 1904.10006 [astro-ph.GA] (cit. on pp. 62, 64, 95, 110, 112).

[MBL18] A. S. Maniyar et al. “Star formation history from the cosmic infrared background anisotropies”. In: A&A 614, A39 (June 2018), A39. DOI: 10.1051/0004-6361/201732499. arXiv: 1801.10146 [astro-ph.CO] (cit. on p. 36).

[Man+22] Sinclaire M. Manning et al. “Characterization of Two 2 mm detected Optically Obscured Dusty Star-forming Galaxies”. In: ApJ 925.1, 23 (Jan. 2022), p. 23. DOI: 10.3847/1538-4357/ac366a. arXiv: 2111.02428 [astro-ph.GA] (cit. on pp. 55, 121, 167).

[Mar+17] A. Maragkoudakis et al. “The sub-galactic and nuclear main sequences for local star-forming galaxies”. In: MNRAS 466.1 (Apr. 2017), pp. 1192–1204. DOI: 10.1093/mnras/stw3180. arXiv: 1611.10085 [astro-ph.GA] (cit. on p. 45).

[Mar+18] D. P. Marrone et al. “Galaxy growth in a massive halo in the first billion years of cosmic history”. In: Nature 553.7686 (Jan. 2018), pp. 51–54. DOI: 10.1038/nature24629. arXiv: 1712.03020 [astro-ph.GA] (cit. on pp. 40, 51, 71).

[Mat+06] Hideo Matsuhara et al. “Deep Extragalactic Surveys around the Ecliptic Poles with AKARI (ASTRO-F)”. In: PASJ 58 (Aug. 2006), pp. 673–694. DOI: 10.1093/pasj/58.4.673. arXiv: astro-ph/0605589 [astro-ph] (cit. on p. 57).

[MS19] Jorryt Matthee and Joop Schaye. “The origin of scatter in the star formation rate-stellar mass relation”. In: MNRAS 484.1 (Mar. 2019), pp. 915–932. DOI: 10.1093/mnras/stz030. arXiv: 1805.05956 [astro-ph.GA] (cit. on p. 38).

[Maz+12] Benjamin A. Mazin et al. “A superconducting focal plane array for ultraviolet, optical, and near-infrared astrophysics”. In: *Optics Express* 20.2 (Jan. 2012), p. 1503. DOI: 10.1364/OE.20.001503. arXiv: 1112.0004 [astro-ph.IM] (cit. on p. 73).

[McA+19] Stuart McAlpine et al. “The nature of submillimetre and highly star-forming galaxies in the EAGLE simulation”. In: MNRAS 488.2 (Sept. 2019), pp. 2440–2454. DOI: 10.1093/mnras/stz1692. arXiv: 1901.05467 [astro-ph.GA] (cit. on p. 91).

[Men+98] V. Mennella et al. “A New Approach to the Puzzle of the Ultraviolet Interstellar Extinction Bump”. In: ApJ 507.2 (Nov. 1998), pp. L177–L180. DOI: 10.1086/311693 (cit. on p. 45).

[MHC99] Gerhardt R. Meurer et al. “Dust Absorption and the Ultraviolet Luminosity Density at z ~3 as Calibrated by Local Starburst Galaxies”. In: ApJ 521.1 (Aug. 1999), pp. 64–80. DOI: 10.1086/307523. arXiv: astro-ph/9903054 [astro-ph] (cit. on p. 35).

[Mie+17] O. Miettinen et al. “An ALMA survey of submillimetre galaxies in the COSMOS field: Physical properties derived from energy balance spectral energy distribution modelling”. In: A&A 606, A17 (Sept. 2017), A17. DOI: 10.1051/0004-6361/201730762. arXiv: 1707.00637 [astro-ph.GA] (cit. on p. 156).

[Mil+18] T. B. Miller et al. “A massive core for a cluster of galaxies at a redshift of 4.3”. In: Nature 556.7702 (Apr. 2018), pp. 469–472. DOI: 10.1038/s41586-018-0025-2. arXiv: 1804.09231 [astro-ph.GA] (cit. on p. 168).

[Mil+15] Tim B. Miller et al. “The bias of the submillimetre galaxy population: SMGs are poor tracers of the most-massive structures in the z ~ 2 Universe”. In: MNRAS 452.1 (Sept. 2015), pp. 878–883. DOI: 10.1093/mnras/stv1267. arXiv: 1501.04105 [astro-ph.GA] (cit. on p. 166).

[Mit+21] I. Mitsuhashi et al. “FIR-luminous [C II] Emitters in the ALMA-SCUBA-2 COSMOS Survey (AS2COSMOS): The Nature of Submillimeter Galaxies in a 10 Comoving Megaparsec-scale Structure at z ∼ 4.6”. In: ApJ 907.2, 122 (Feb. 2021), p. 122. DOI: 10.3847/1538-4357/abcc72. arXiv: 2011.09917 [astro-ph.GA] (cit. on pp. 71, 165).

[Mom+16] Ivelina G. Momcheva et al. “The 3D-HST Survey: Hubble Space Telescope WFC3/G141 Grism Spectra, Redshifts, and Emission Line Measurements for ∼100,000 Galaxies”. In: ApJS 225.2, 27 (Aug. 2016), p. 27. DOI: 10.3847/0067-0049/225/2/27. arXiv: 1510.02106 [astro-ph.GA] (cit. on p. 134).

[Mos+90] M. Moshir et al. “The IRAS Faint Source Catalog, Version 2”. In: *Bulletin of the American Astronomical Society*. Vol. 22. Sept. 1990, p. 1325 (cit. on p. 56).

[Muñ+22] A. M. Muñoz Arancibia et al. “The ALMA Frontier Fields Survey. VI. Lensing-corrected 1.1mm number counts in Abell 2744, MACSJ0416.1-2403, MACSJ1149.5+2223, Abell 370 and Abell S1063”. In: *arXiv e-prints*, arXiv:2203.06195 (Mar. 2022), arXiv:2203.06195. arXiv: 2203.06195 [astro-ph.GA] (cit. on pp. 66, 68).

[Mur+07] Hiroshi Murakami et al. “The Infrared Astronomical Mission AKARI*”. In: PASJ 59 (Oct. 2007), S369–S376. DOI: 10.1093/pasj/59.sp2.S369. arXiv: 0708.1796 [astro-ph] (cit. on pp. 57, 60).

[Mur+14] K. Murata et al. “Polycyclic aromatic hydrocarbon feature deficit of starburst galaxies in the AKARI North Ecliptic Pole Deep field”. In: A&A 566, A136 (June 2014), A136. DOI: 10.1051/0004-6361/201423744. arXiv: 1405.2633 [astro-ph.GA] (cit. on p. 45).

[NO17] Thorsten Naab and Jeremiah P. Ostriker. “Theoretical Challenges in Galaxy Formation”. In: ARA&A 55.1 (Aug. 2017), pp. 59–109. DOI: 10.1146/annurev-astro-081913-040019. arXiv: 1612.06891 [astro-ph.GA] (cit. on p. 33).

[Nan+20] A. Nanni et al. “The gas, metal, and dust evolution in low-metallicity local and high-redshift galaxies”. In: A&A 641, A168 (Sept. 2020), A168. DOI: 10.1051/0004-6361/202037833. arXiv: 2006.15146 [astro-ph.GA] (cit. on p. 40).

[Nel+15] Dylan Nelson et al. “The impact of feedback on cosmological gas accretion”. In: MNRAS 448.1 (Mar. 2015), pp. 59–74. DOI: 10.1093/mnras/stv017. arXiv: 1410.5425 [astro-ph.CO] (cit. on p. 33).

[Nel+19] Dylan Nelson et al. “First results from the TNG50 simulation: galactic outflows driven by supernovae and black hole feedback”. In: MNRAS 490.3 (Dec. 2019), pp. 3234–3261. DOI: 10.1093/mnras/stz2306. arXiv: 1902.05554 [astro-ph.GA] (cit. on p. 33).

[Nel+21] Erica J. Nelson et al. “Spatially resolved star formation and inside-out quenching in the TNG50 simulation and 3D-HST observations”. In: MNRAS 508.1 (Nov. 2021), pp. 219–235. DOI: 10.1093/mnras/stab2131. arXiv: 2101.12212 [astro-ph.GA] (cit. on p. 38).

[Ner+20] R. Neri et al. “NOEMA redshift measurements of bright Herschel galaxies”. In: A&A 635, A7 (Mar. 2020), A7. DOI: 10.1051/0004-6361/201936988. arXiv: 1912.10416 [astro-ph.GA] (cit. on pp. 51, 71, 121, 147, 156, 157).

[Neu+84] G. Neugebauer et al. “The Infrared Astronomical Satellite (IRAS) mission.” In: ApJ 278 (Mar. 1984), pp. L1–L6. DOI: 10.1086/184209 (cit. on p. 56).

[Nol+09] S. Noll et al. “Analysis of galaxy spectral energy distributions from far-UV to far-IR with CIGALE: studying a SINGS test sample”. In: A&A 507.3 (Dec. 2009), pp. 1793–1813. DOI: 10.1051/0004-6361/200912497. arXiv: 0909.5439 [astro-ph.CO] (cit. on pp. 41, 133).

[Oes+16] P. A. Oesch et al. “A Remarkably Luminous Galaxy at z=11.1 Measured with Hubble Space Telescope Grism Spectroscopy”. In: ApJ 819.2, 129 (Mar. 2016), p. 129. DOI: 10.3847/0004-637X/819/2/129. arXiv: 1603.00461 [astro-ph.GA] (cit. on p. 35).

[Oli+12] S. J. Oliver et al. “The Herschel Multi-tiered Extragalactic Survey: HerMES”. In: MNRAS 424.3 (Aug. 2012), pp. 1614–1635. DOI: 10.1111/j.1365-2966.2012.20912.x. arXiv: 1203.2562 [astro-ph.CO] (cit. on pp. 59, 60).

[Oli+00] Seb Oliver et al. “The European Large Area ISO Survey - I. Goals, definition and observations”. In: MNRAS 316.4 (Aug. 2000), pp. 749–767. DOI: 10.1046/j.1365-8711.2000.03550.x. arXiv: astro-ph/0003263 [astro-ph] (cit. on p. 57).

[Ono+14] Yoshiaki Ono et al. “Faint Submillimeter Galaxies Revealed by Multifield Deep ALMA Observations: Number Counts, Spatial Clustering, and a Dark Submillimeter Line Emitter”. In: ApJ 795.1, 5 (Nov. 2014), p. 5. DOI: 10.1088/0004-637X/795/1/5. arXiv: 1403.4360 [astro-ph.GA] (cit. on pp. 65, 66).

[Orm+09] C. W. Ormel et al. “Dust coagulation and fragmentation in molecular clouds. I. How collisions between dust aggregates alter the dust size distribution”. In: A&A 502.3 (Aug. 2009), pp. 845–869. DOI: 10.1051/0004-6361/200811158. arXiv: 0906.1770 [astro-ph.SR] (cit. on p. 44).

[Ote+16] I. Oteo et al. “ALMACAL I: First Dual-band Number Counts from a Deep and Wide ALMA Submillimeter Survey, Free from Cosmic Variance”. In: ApJ 822.1, 36 (May 2016), p. 36. DOI: 10.3847/0004-637X/822/1/36. arXiv: 1508.05099 [astro-ph.GA] (cit. on pp. 68, 110).

[Owe18] Frazer N. Owen. "Deep JVLA Imaging of GOODS-N at 20 cm". In: ApJS 235.2, 34 (Apr. 2018), p. 34. DOI: 10.3847/1538-4365/aab4a1. arXiv: 1803.05455 [astro-ph.GA] (cit. on p. 127).

[Pap+12] Padelis P. Papadopoulos et al. "The Molecular Gas in Luminous Infrared Galaxies. II. Extreme Physical Conditions and Their Effects on the X $_{CO}$ Factor". In: ApJ 751.1, 10 (May 2012), p. 10. DOI: 10.1088/0004-637X/751/1/10. arXiv: 1202.1803 [astro-ph.CO] (cit. on p. 47).

[Pav+18a] Riccardo Pavesi et al. "Hidden in Plain Sight: A Massive, Dusty Starburst in a Galaxy Protocluster at z = 5.7 in the COSMOS Field". In: ApJ 861.1, 43 (July 2018), p. 43. DOI: 10.3847/1538-4357/aac6b6. arXiv: 1803.08048 [astro-ph.GA] (cit. on p. 156).

[Pav+18b] Riccardo Pavesi et al. "The CO Luminosity Density at High-z (COLDz) Survey: A Sensitive, Large-area Blind Search for Low-J CO Emission from Cold Gas in the Early Universe with the Karl G. Jansky Very Large Array". In: ApJ 864.1, 49 (Sept. 2018), p. 49. DOI: 10.3847/1538-4357/aacb79. arXiv: 1808.04372 [astro-ph.GA] (cit. on p. 69).

[Pen+10] Ying-jie Peng et al. "Mass and Environment as Drivers of Galaxy Evolution in SDSS and zCOSMOS and the Origin of the Schechter Function". In: ApJ 721.1 (Sept. 2010), pp. 193–221. DOI: 10.1088/0004-637X/721/1/193. arXiv: 1003.4747 [astro-ph.CO] (cit. on p. 40).

[Pen+11] Kyle Penner et al. "Origins of the extragalactic background at 1 mm from a combined analysis of the AzTEC and MAMBO data in GOODS-N". In: MNRAS 410.4 (Feb. 2011), pp. 2749–2759. DOI: 10.1111/j.1365-2966.2010.17650.x. arXiv: 1009.2503 [astro-ph.CO] (cit. on p. 76).

[Per+08] T. A. Perera et al. "An AzTEC 1.1mm survey of the GOODS-N field - I. Maps, catalogue and source statistics". In: MNRAS 391.3 (Dec. 2008), pp. 1227–1238. DOI: 10.1111/j.1365-2966.2008.13902.x. arXiv: 0806.3791 [astro-ph] (cit. on pp. 62, 64, 95).

[Per+20] L. Perotto et al. "Calibration and performance of the NIKA2 camera at the IRAM 30-m Telescope". In: A&A 637, A71 (May 2020), A71. DOI: 10.1051/0004-6361/201936220. arXiv: 1910.02038 [astro-ph.IM] (cit. on pp. 74, 75, 80, 81, 121, 122).

[Pil+18] Annalisa Pillepich et al. "Simulating galaxy formation with the IllustrisTNG model". In: MNRAS 473.3 (Jan. 2018), pp. 4077–4106. DOI: 10.1093/mnras/stx2656. arXiv: 1703.02970 [astro-ph.GA] (cit. on p. 36).

[Pla+20] Planck Collaboration et al. "Planck 2018 results. VI. Cosmological parameters". In: A&A 641, A6 (Sept. 2020), A6. DOI: 10.1051/0004-6361/201833910. arXiv: 1807.06209 [astro-ph.CO] (cit. on p. 122).

[Pog+10] A. Poglitsch et al. "The Photodetector Array Camera and Spectrometer (PACS) on the Herschel Space Observatory". In: A&A 518, L2 (July 2010), p. L2. DOI: 10.1051/0004-6361/201014535. arXiv: 1005.1487 [astro-ph.IM] (cit. on p. 58).

[Pop+06] Alexandra Pope et al. "The Hubble Deep Field-North SCUBA Super-map - IV. Characterizing submillimetre galaxies using deep Spitzer imaging". In: MNRAS 370.3 (Aug. 2006), pp. 1185–1207. DOI: 10.1111/j.1365-2966.2006.10575.x. arXiv: astro-ph/0605573 [astro-ph] (cit. on p. 40).

[Pop+17] Gergö Popping et al. "ALMA reveals starburst-like interstellar medium conditions in a compact star-forming galaxy at z 2 using [CI] and CO". In: A&A 602, A11 (June 2017), A11. DOI: 10.1051/0004-6361/201730391. arXiv: 1703.05764 [astro-ph.GA] (cit. on p. 53).

[Pop+20] Gergö Popping et al. "The ALMA Spectroscopic Survey in the HUDF: A Model to Explain Observed 1.1 and 0.85 mm Dust Continuum Number Counts". In: ApJ 891.2, 135 (Mar. 2020), p. 135. DOI: 10.3847/1538-4357/ab76c0. arXiv: 2002.07180 [astro-ph.GA] (cit. on pp. 65, 91, 113–116, 118, 172).

[Pug+19] A. Puglisi et al. "The Main Sequence at z ~ 1.3 Contains a Sizable Fraction of Galaxies with Compact Star Formation Sizes: A New Population of Early Post-starbursts?" In: ApJ 877.2, L23 (June 2019), p. L23. DOI: 10.3847/2041-8213/ab1f92. arXiv: 1905.02958 [astro-ph.GA] (cit. on p. 53).

[Ram+22] Joanna Ramasawmy et al. "The Atacama Large Aperture Submillimetre Telescope: key science drivers". In: *Millimeter, Submillimeter, and Far-Infrared Detectors and Instrumentation for Astronomy XI*. Ed. by Jonas Zmuidzinas and Jian-Rong Gao. Vol. 12190. Society of Photo-Optical Instrumentation Engineers (SPIE) Conference Series. Aug. 2022, 1219007, p. 1219007. DOI: 10.1117/12.2627505. arXiv: 2207.03914 [astro-ph.IM] (cit. on p. 174).

[Raw+14] T. D. Rawle et al. "[C II] and ^{12}CO(1-0) Emission Maps in HLSJ091828.6+514223: A Strongly Lensed Interacting System at z = 5.24". In: ApJ 783.1, 59 (Mar. 2014), p. 59. DOI: 10.1088/0004-637X/783/1/59. arXiv: 1310.4090 [astro-ph.CO] (cit. on pp. 151, 154, 157).

[RO77] M. J. Rees and J. P. Ostriker. "Cooling, dynamics and fragmentation of massive gas clouds: clues to the masses and radii of galaxies and clusters." In: MNRAS 179 (June 1977), pp. 541–559. DOI: 10.1093/mnras/179.4.541 (cit. on p. 33).

[Rei+88] M. J. Reid et al. "The Distance to the Center of the Galaxy: H 2O Maser Proper Motions in Sagittarius B2(N)". In: ApJ 330 (July 1988), p. 809. DOI: 10.1086/166514 (cit. on p. 131).

[Rém+14] A. Rémy-Ruyer et al. “Gas-to-dust mass ratios in local galaxies over a 2 dex metallicity range”. In: A&A 563, A31 (Mar. 2014), A31. DOI: 10.1051/0004-6361/201322803. arXiv: 1312.3442 [astro-ph.GA] (cit. on p. 163).

[Reu+20] C. Reuter et al. “The Complete Redshift Distribution of Dusty Star-forming Galaxies from the SPT-SZ Survey”. In: ApJ 902.1, 78 (Oct. 2020), p. 78. DOI: 10.3847/1538-4357/abb599. arXiv: 2006.14060 [astro-ph.GA] (cit. on pp. 40, 51, 54, 63, 71, 147).

[Rie+13] Dominik A. Riechers et al. “A dust-obscured massive maximum-starburst galaxy at a redshift of 6.34”. In: Nature 496.7445 (Apr. 2013), pp. 329–333. DOI: 10.1038/nature12050. arXiv: 1304.4256 [astro-ph.CO] (cit. on pp. 40, 156).

[Rie+14] Dominik A. Riechers et al. “ALMA Imaging of Gas and Dust in a Galaxy Protocluster at Redshift 5.3: [C II] Emission in “Typical” Galaxies and Dusty Starbursts ≈1 Billion Years after the Big Bang”. In: ApJ 796.2, 84 (Dec. 2014), p. 84. DOI: 10.1088/0004-637X/796/2/84. arXiv: 1404.7159 [astro-ph.GA] (cit. on p. 156).

[Rie+17] Dominik A. Riechers et al. “Rise of the Titans: A Dusty, Hyper-luminous “870 μm Riser” Galaxy at z ∼ 6”. In: ApJ 850.1, 1 (Nov. 2017), p. 1. DOI: 10.3847/1538-4357/aa8ccf. arXiv: 1705.09660 [astro-ph.GA] (cit. on p. 156).

[Rie+19] Dominik A. Riechers et al. “COLDz: Shape of the CO Luminosity Function at High Redshift and the Cold Gas History of the Universe”. In: ApJ 872.1, 7 (Feb. 2019), p. 7. DOI: 10.3847/1538-4357/aafc27. arXiv: 1808.04371 [astro-ph.GA] (cit. on p. 70).

[Rie+20] Dominik A. Riechers et al. “COLDz: A High Space Density of Massive Dusty Starburst Galaxies ∼1 Billion Years after the Big Bang”. In: ApJ 895.2, 81 (June 2020), p. 81. DOI: 10.3847/1538-4357/ab8c48. arXiv: 2004.10204 [astro-ph.GA] (cit. on pp. 36, 38, 70).

[Rie+04] G. H. Rieke et al. “The Multiband Imaging Photometer for Spitzer (MIPS)”. In: ApJS 154.1 (Sept. 2004), pp. 25–29. DOI: 10.1086/422717 (cit. on p. 58).

[Riz+20] F. Rizzo et al. “A dynamically cold disk galaxy in the early Universe”. In: Nature 584.7820 (Aug. 2020), pp. 201–204. DOI: 10.1038/s41586-020-2572-6. arXiv: 2009.01251 [astro-ph.GA] (cit. on p. 53).

[RF04] G. Rodighiero and A. Franceschini. “ISOPHOT 95 μm observations in the Lockman Hole. The catalogue and an assessment of the source counts”. In: A&A 419 (May 2004), pp. L55–L58. DOI: 10.1051/0004-6361:20040144. arXiv: astro-ph/0404310 [astro-ph] (cit. on p. 57).

[Row+14] K. Rowlands et al. “The dust budget crisis in high-redshift submillimetre galaxies”. In: MNRAS 441.2 (June 2014), pp. 1040–1058. DOI: 10.1093/mnras/stu605. arXiv: 1403.2995 [astro-ph.GA] (cit. on p. 163).

[Ruj+19] W. Rujopakarn et al. “ALMA 200 pc Resolution Imaging of Smooth Cold Dusty Disks in Typical z ~ 3 Star-forming Galaxies”. In: ApJ 882.2, 107 (Sept. 2019), p. 107. DOI: 10.3847/1538-4357/ab3791. arXiv: 1904.04507 [astro-ph.GA] (cit. on p. 163).

[SM96a] D. B. Sanders and I. F. Mirabel. “Luminous Infrared Galaxies”. In: ARA&A 34 (Jan. 1996), p. 749. DOI: 10.1146/annurev.astro.34.1.749 (cit. on p. 39).

[San+07] D. B. Sanders et al. “S-COSMOS: The Spitzer Legacy Survey of the Hubble Space Telescope ACS 2 deg^2 COSMOS Field I: Survey Strategy and First Analysis”. In: ApJS 172.1 (Sept. 2007), pp. 86–98. DOI: 10.1086/517885. arXiv: astro-ph/0701318 [astro-ph] (cit. on pp. 58, 60).

[San+10] P. Santini et al. “The dust content of high-z submillimeter galaxies revealed by Herschel”. In: A&A 518, L154 (July 2010), p. L154. DOI: 10.1051/0004-6361/201014748. arXiv: 1005.5678 [astro-ph.CO] (cit. on pp. 156, 163).

[San+14] P. Santini et al. “The evolution of the dust and gas content in galaxies”. In: A&A 562, A30 (Feb. 2014), A30. DOI: 10.1051/0004-6361/201322835. arXiv: 1311.3670 [astro-ph.CO] (cit. on p. 163).

[Sau+00] W. Saunders et al. “The PSCz catalogue”. In: MNRAS 317.1 (Sept. 2000), pp. 55–63. DOI: 10.1046/j.1365-8711.2000.03528.x. arXiv: astro-ph/0001117 [astro-ph] (cit. on p. 57).

[Sch+20] D. Schaerer et al. “The ALPINE-ALMA [C II] survey. Little to no evolution in the [C II]-SFR relation over the last 13 Gyr”. In: A&A 643, A3 (Nov. 2020), A3. DOI: 10.1051/0004-6361/202037617. arXiv: 2002.00979 [astro-ph.GA] (cit. on p. 70).

[Sch+16a] E. Schinnerer et al. “Gas Fraction and Depletion Time of Massive Star-forming Galaxies at z ~3.2: No Change in Global Star Formation Process out to z > 3”. In: ApJ 833.1, 112 (Dec. 2016), p. 112. DOI: 10.3847/1538-4357/833/1/112. arXiv: 1610.03656 [astro-ph.GA] (cit. on p. 165).

[Sch+16b] C. Schreiber et al. “Observational evidence of a slow downfall of star formation efficiency in massive galaxies during the past 10 Gyr”. In: A&A 589, A35 (May 2016), A35. DOI: 10.1051/0004-6361/201527200. arXiv: 1601.04226 [astro-ph.GA] (cit. on p. 38).

[Sch+17] C. Schreiber et al. “EGG: hatching a mock Universe from empirical prescriptions⋆”. In: A&A 602, A96 (June 2017), A96. DOI: 10.1051/0004-6361/201629123. arXiv: 1606.05354 [astro-ph.IM] (cit. on pp. 113–116, 118).

[Sch+18] C. Schreiber et al. “Near infrared spectroscopy and star-formation histories of $3 \leq z \leq 4$ quiescent galaxies”. In: A&A 618, A85 (Oct. 2018), A85. DOI: 10.1051/0004-6361/201833070. arXiv: 1807.02523 [astro-ph.GA] (cit. on pp. 39, 46, 52, 56, 157, 158).

[Sco+08] K. S. Scott et al. “AzTEC millimetre survey of the COSMOS field - I. Data reduction and source catalogue”. In: MNRAS 385.4 (Apr. 2008), pp. 2225–2238. DOI: 10.1111/j.1365-2966.2008.12989.x. arXiv: 0801.2779 [astro-ph] (cit. on pp. 51, 62, 64).

[Sco+10] K. S. Scott et al. “Deep 1.1mm-wavelength imaging of the GOODS-S field by AzTEC/ASTE - I. Source catalogue and number counts”. In: MNRAS 405.4 (July 2010), pp. 2260–2278. DOI: 10.1111/j.1365-2966.2010.16644.x. arXiv: 1003.1768 [astro-ph.CO] (cit. on pp. 62, 64).

[Sco+12] K. S. Scott et al. “The source counts of submillimetre galaxies detected at λ= 1.1 mm”. In: MNRAS 423.1 (June 2012), pp. 575–589. DOI: 10.1111/j.1365-2966.2012.20905.x. arXiv: 1203.2609 [astro-ph.CO] (cit. on pp. 91, 110).

[Sco+07] N. Scoville et al. “The Cosmic Evolution Survey (COSMOS): Overview”. In: ApJS 172.1 (Sept. 2007), pp. 1–8. DOI: 10.1086/516585. arXiv: astro-ph/0612305 [astro-ph] (cit. on p. 57).

[Sco+16] N. Scoville et al. “ISM Masses and the Star formation Law at Z = 1 to 6: ALMA Observations of Dust Continuum in 145 Galaxies in the COSMOS Survey Field”. In: ApJ 820.2, 83 (Apr. 2016), p. 83. DOI: 10.3847/0004-637X/820/2/83. arXiv: 1511.05149 [astro-ph.GA] (cit. on pp. 38, 162, 163).

[SWM09] Francesco Shankar et al. “Self-Consistent Models of the AGN and Black Hole Populations: Duty Cycles, Accretion Rates, and the Mean Radiative Efficiency”. In: ApJ 690.1 (Jan. 2009), pp. 20–41. DOI: 10.1088/0004-637X/690/1/20. arXiv: 0710.4488 [astro-ph] (cit. on p. 38).

[Sha+20] Alice E. Shapley et al. “The First Robust Constraints on the Relationship between Dust-to-gas Ratio and Metallicity in Luminous Star-forming Galaxies at High Redshift”. In: ApJ 903.1, L16 (Nov. 2020), p. L16. DOI: 10.3847/2041-8213/abc006. arXiv: 2009.10091 [astro-ph.GA] (cit. on p. 163).

[Shi+20] Hyunjin Shim et al. “NEPSC2, the North Ecliptic Pole SCUBA-2 survey: 850-μm map and catalogue of 850-μm-selected sources over 2 deg^2”. In: MNRAS 498.4 (Nov. 2020), pp. 5065–5079. DOI: 10.1093/mnras/staa2621 (cit. on p. 64).

[Shi+09] M. Shirahata et al. “Far-Infrared Cosmological Survey in AKARI Deep Field South: Galaxy Number Counts”. In: *AKARI, a Light to Illuminate the Misty Universe*. Ed. by T. Onaka et al. Vol. 418. Astronomical Society of the Pacific Conference Series. Dec. 2009, p. 301 (cit. on pp. 57, 60).

[SM12] Joseph Silk and Gary A. Mamon. "The current status of galaxy formation". In: *Research in Astronomy and Astrophysics* 12.8 (Aug. 2012), pp. 917–946. DOI: 10.1088/1674-4527/12/8/004. arXiv: 1207.3080 [astro-ph.CO] (cit. on p. 34).

[Sil+18] J. D. Silverman et al. "Concurrent Starbursts in Molecular Gas Disks within a Pair of Colliding Galaxies at z = 1.52". In: ApJ 868.1, 75 (Nov. 2018), p. 75. DOI: 10.3847/1538-4357/aae64b. arXiv: 1810.01595 [astro-ph.GA] (cit. on p. 163).

[Sim+19] J. M. Simpson et al. "The East Asian Observatory SCUBA-2 Survey of the COSMOS Field: Unveiling 1147 Bright Sub-millimeter Sources across 2.6 Square Degrees". In: ApJ 880.1, 43 (July 2019), p. 43. DOI: 10.3847/1538-4357/ab23ff. arXiv: 1912.02229 [astro-ph.GA] (cit. on pp. 61, 95).

[Sim+20] J. M. Simpson et al. "An ALMA survey of the brightest sub-millimetre sources in the SCUBA-2-COSMOS field". In: MNRAS 495.3 (July 2020), pp. 3409–3430. DOI: 10.1093/mnras/staa1345. arXiv: 2003.05484 [astro-ph.GA] (cit. on pp. 50, 55, 90, 121).

[Sir+09] G. Siringo et al. "The Large APEX BOlometer CAmera LABOCA". In: A&A 497.3 (Apr. 2009), pp. 945–962. DOI: 10.1051/0004-6361/200811454. arXiv: 0903.1354 [astro-ph.IM] (cit. on p. 62).

[Ske+14] Rosalind E. Skelton et al. "3D-HST WFC3-selected Photometric Catalogs in the Five CANDELS/3D-HST Fields: Photometry, Photometric Redshifts, and Stellar Masses". In: ApJS 214.2, 24 (Oct. 2014), p. 24. DOI: 10.1088/0067-0049/214/2/24. arXiv: 1403.3689 [astro-ph.GA] (cit. on p. 134).

[Sma+98] Ian Smail et al. "Faint Submillimeter Galaxies: Hubble Space Telescope Morphologies and Colors". In: ApJ 507.1 (Nov. 1998), pp. L21–L24. DOI: 10.1086/311667. arXiv: astro-ph/9806061 [astro-ph] (cit. on p. 61).

[Sma+21] Ian Smail et al. "An ALMA survey of the S2CLS UDS field: optically invisible submillimetre galaxies". In: MNRAS 502.3 (Apr. 2021), pp. 3426–3435. DOI: 10.1093/mnras/stab283. arXiv: 2010.02250 [astro-ph.GA] (cit. on pp. 51, 53, 167).

[Smo+08] V. Smolčić et al. "A New Method to Separate Star-forming from AGN Galaxies at Intermediate Redshift: The Submillijansky Radio Population in the VLA-COSMOS Survey". In: ApJS 177.1 (July 2008), pp. 14–38. DOI: 10.1086/588028. arXiv: 0803.0997 [astro-ph] (cit. on p. 42).

[Smo+12] V. Smolčić et al. "Millimeter imaging of submillimeter galaxies in the COSMOS field: redshift distribution". In: A&A 548, A4 (Dec. 2012), A4. DOI: 10.1051/0004-6361/201219368. arXiv: 1205.6470 [astro-ph.CO] (cit. on pp. 50, 51).

[Sod+97] T. J. Sodroski et al. “A Three-dimensional Decomposition of the Infrared Emission from Dust in the Milky Way”. In: ApJ 480.1 (May 1997), pp. 173–187. DOI: 10.1086/303961 (cit. on p. 46).

[SDR92] P. M. Solomon et al. “Dense Molecular Gas and Starbursts in Ultraluminous Galaxies”. In: ApJ 387 (Mar. 1992), p. L55. DOI: 10.1086/186304 (cit. on p. 52).

[Sol+97] P. M. Solomon et al. “The Molecular Interstellar Medium in Ultraluminous Infrared Galaxies”. In: ApJ 478.1 (Mar. 1997), pp. 144–161. DOI: 10.1086/303765. arXiv: astro-ph/9610166 [astro-ph] (cit. on p. 150).

[Som+20] L. Sommovigo et al. “Warm dust in high-z galaxies: origin and implications”. In: MNRAS 497.1 (Sept. 2020), pp. 956–968. DOI: 10.1093/mnras/staa1959. arXiv: 2004.09528 [astro-ph.GA] (cit. on p. 46).

[Spe+14] J. S. Speagle et al. “A Highly Consistent Framework for the Evolution of the Star-Forming “Main Sequence” from z ~0-6”. In: ApJS 214.2, 15 (Oct. 2014), p. 15. DOI: 10.1088/0067-0049/214/2/15. arXiv: 1405.2041 [astro-ph.GA] (cit. on pp. 159, 160).

[Spi+14] J. S. Spilker et al. “The Rest-frame Submillimeter Spectrum of High-redshift, Dusty, Star-forming Galaxies”. In: ApJ 785.2, 149 (Apr. 2014), p. 149. DOI: 10.1088/0004-637X/785/2/149. arXiv: 1403.1667 [astro-ph.GA] (cit. on pp. 129, 153, 162).

[Spi+19] Justin S. Spilker et al. “Evidence for Inside-out Galaxy Growth and Quenching of a z ~ 2 Compact Galaxy From High-resolution Molecular Gas Imaging”. In: ApJ 883.1, 81 (Sept. 2019), p. 81. DOI: 10.3847/1538-4357/ab3804. arXiv: 1908.02294 [astro-ph.GA] (cit. on p. 91).

[SFW06] Volker Springel et al. “The large-scale structure of the Universe”. In: Nature 440.7088 (Apr. 2006), pp. 1137–1144. DOI: 10.1038/nature04805. arXiv: astro-ph/0604561 [astro-ph] (cit. on p. 33).

[Sta+19] Stuart M. Stach et al. “An ALMA survey of the SCUBA-2 Cosmology Legacy Survey UKIDSS/UDS field: source catalogue and properties”. In: MNRAS 487.4 (Aug. 2019), pp. 4648–4668. DOI: 10.1093/mnras/stz1536. arXiv: 1903.02602 [astro-ph.GA] (cit. on pp. 50, 55).

[Sta+14] Johannes G. Staguhn et al. “The GISMO Two-millimeter Deep Field in GOODS-N”. In: ApJ 790.1, 77 (July 2014), p. 77. DOI: 10.1088/0004-637X/790/1/77. arXiv: 1311.1485 [astro-ph.CO] (cit. on pp. 62, 64, 95, 110, 112).

[Ste+13] Mauro Stefanon et al. “What are the Progenitors of Compact, Massive, Quiescent Galaxies at z = 2.3? The Population of Massive Galaxies at z > 3 from NMBS and CANDELS”. In: ApJ 768.1, 92 (May 2013), p. 92. DOI: 10.1088/0004-637X/768/1/92. arXiv: 1301.7063 [astro-ph.CO] (cit. on p. 39).

[Ste+10] M. Steglich et al. “Electronic Spectroscopy of Medium-sized Polycyclic Aromatic Hydrocarbons: Implications for the Carriers of the 2175 Å UV Bump”. In: ApJ 712.1 (Mar. 2010), pp. L16–L20. DOI: 10.1088/2041-8205/712/1/L16. arXiv: 1002.3529 [astro-ph.IM] (cit. on pp. 43, 45).

[SPH95] Charles C. Steidel et al. “Lyman Imaging of High-Redshift Galaxies.III.New Observations of Four QSO Fields”. In: AJ 110 (Dec. 1995), p. 2519. DOI: 10.1086/117709. arXiv: astro-ph/9509089 [astro-ph] (cit. on p. 42).

[Str+14] Caroline M. S. Straatman et al. “A Substantial Population of Massive Quiescent Galaxies at z ~4 from ZFOURGE”. In: ApJ 783.1, L14 (Mar. 2014), p. L14. DOI: 10.1088/2041-8205/783/1/L14. arXiv: 1312.4952 [astro-ph.GA] (cit. on p. 167).

[Str+16] M. L. Strandet et al. “The Redshift Distribution of Dusty Star-forming Galaxies from the SPT Survey”. In: ApJ 822.2, 80 (May 2016), p. 80. DOI: 10.3847/0004-637X/822/2/80. arXiv: 1603.05094 [astro-ph.GA] (cit. on pp. 51, 121, 147).

[Str+17] M. L. Strandet et al. “ISM Properties of a Massive Dusty Star-forming Galaxy Discovered at z ~ 7”. In: ApJ 842.2, L15 (June 2017), p. L15. DOI: 10.3847/2041-8213/aa74b0. arXiv: 1705.07912 [astro-ph.GA] (cit. on pp. 40, 121).

[SM96b] A. W. Strong and J. R. Mattox. “Gradient model analysis of EGRET diffuse Galactic γ-ray emission.” In: A&A 308 (Apr. 1996), pp. L21–L24 (cit. on p. 47).

[Sug+21] Yuma Sugahara et al. “Big Three Dragons: A [N II] 122 μm Constraint and New Dust-continuum Detection of a z = 7.15 Bright Lyman-break Galaxy with ALMA”. In: ApJ 923.1, 5 (Dec. 2021), p. 5. DOI: 10.3847/1538-4357/ac2a36. arXiv: 2104.02201 [astro-ph.GA] (cit. on pp. 40, 156).

[Tac+08] L. J. Tacconi et al. “Submillimeter Galaxies at z ~2: Evidence for Major Mergers and Constraints on Lifetimes, IMF, and CO-H_2 Conversion Factor”. In: ApJ 680.1 (June 2008), pp. 246–262. DOI: 10.1086/587168. arXiv: 0801.3650 [astro-ph] (cit. on p. 163).

[Tad+18] K. Tadaki et al. “The gravitationally unstable gas disk of a starburst galaxy 12 billion years ago”. In: Nature 560.7720 (Aug. 2018), pp. 613–616. DOI: 10.1038/s41586-018-0443-1. arXiv: 1808.09592 [astro-ph.GA] (cit. on pp. 39, 53).

[Tad+22] Ken-ichi Tadaki et al. “Detection of nitrogen and oxygen in a galaxy at the end of reionization”. In: PASJ 74.3 (June 2022), pp. L9–L16. DOI: 10.1093/pasj/psac018. arXiv: 2202.09945 [astro-ph.GA] (cit. on p. 48).

[Tak+12] T. Takagi et al. “The AKARI NEP-Deep survey: a mid-infrared source catalogue”. In: A&A 537, A24 (Jan. 2012), A24. DOI: 10.1051/0004-6361/201117759. arXiv: 1201.0797 [astro-ph.CO] (cit. on pp. 57, 60).

[Tan+14] Q. Tan et al. “Dust and gas in luminous proto-cluster galaxies at z = 4.05: the case for different cosmic dust evolution in normal and starburst galaxies”. In: A&A 569, A98 (Sept. 2014), A98. DOI: 10.1051/0004-6361/201423905. arXiv: 1403.7992 [astro-ph.GA] (cit. on pp. 40, 41).

[Tof+14] S. Toft et al. “Submillimeter Galaxies as Progenitors of Compact Quiescent Galaxies”. In: ApJ 782.2, 68 (Feb. 2014), p. 68. DOI: 10.1088/0004-637X/782/2/68. arXiv: 1401.1510 [astro-ph.GA] (cit. on p. 91).

[Tom+16] Adam R. Tomczak et al. “The SFR-M* Relation and Empirical Star-Formation Histories from ZFOURGE* at 0.5 < z < 4”. In: ApJ 817.2, 118 (Feb. 2016), p. 118. DOI: 10.3847/0004-637X/817/2/118. arXiv: 1510.06072 [astro-ph.GA] (cit. on p. 38).

[Tru30] Robert J. Trumpler. “Absorption of Light in the Galactic System”. In: PASP 42.248 (Aug. 1930), p. 214. DOI: 10.1086/124039 (cit. on p. 43).

[TI21] Takafumi Tsukui and Satoru Iguchi. “Spiral morphology in an intensely star-forming disk galaxy more than 12 billion years ago”. In: *Science* 372.6547 (June 2021), pp. 1201–1205. DOI: 10.1126/science.abe9680. arXiv: 2108.02206 [astro-ph.GA] (cit. on p. 53).

[Ume+17] Hideki Umehata et al. “ALMA Deep Field in SSA22: Source Catalog and Number Counts”. In: ApJ 835.1, 98 (Jan. 2017), p. 98. DOI: 10.3847/1538-4357/835/1/98. arXiv: 1611.09857 [astro-ph.GA] (cit. on pp. 65, 68, 110).

[Val+18] Francesco Valentino et al. “A Survey of Atomic Carbon [C I] in High-redshift Main-sequence Galaxies”. In: ApJ 869.1, 27 (Dec. 2018), p. 27. DOI: 10.3847/1538-4357/aaeb88. arXiv: 1810.11029 [astro-ph.GA] (cit. on pp. 47, 141).

[Val+20] Francesco Valentino et al. “The Properties of the Interstellar Medium of Galaxies across Time as Traced by the Neutral Atomic Carbon [C I]”. In: ApJ 890.1, 24 (Feb. 2020), p. 24. DOI: 10.3847/1538-4357/ab6603. arXiv: 2001.01734 [astro-ph.GA] (cit. on pp. 47, 91).

[Val+16] E. Valiante et al. “The Herschel-ATLAS data release 1 - I. Maps, catalogues and number counts”. In: MNRAS 462.3 (Nov. 2016), pp. 3146–3179. DOI: 10.1093/mnras/stw1806. arXiv: 1606.09615 [astro-ph.GA] (cit. on pp. 58–60).

[van+22] D. van der Vlugt et al. “An ultra-deep multi-band VLA survey of the faint radio sky (COSMOS-XS): New constraints on the cosmic star formation history”. In: *arXiv e-prints*, arXiv:2204.04167 (Apr. 2022), arXiv:2204.04167. arXiv: 2204.04167 [astro-ph.GA] (cit. on p. 36).

[Vie+22] Marco P. Viero et al. “The early Universe was dust-rich and extremely hot”. In: MNRAS (July 2022). DOI: 10.1093/mnrasl/slac075. arXiv: 2203.14312 [astro-ph.GA] (cit. on p. 56).

[Vog+20] Mark Vogelsberger et al. "Cosmological simulations of galaxy formation". In: *Nature Reviews Physics* 2.1 (Jan. 2020), pp. 42–66. DOI: 10.1038/s42254-019-0127-2. arXiv: 1909.07976 [astro-ph.GA] (cit. on p. 33).

[Wad+08] Takehiko Wada et al. "AKARI/IRC Deep Survey in the North Ecliptic Pole Region". In: PASJ 60 (Dec. 2008), S517. DOI: 10.1093/pasj/60.sp2.S517 (cit. on pp. 57, 60).

[Wal+12] Fabian Walter et al. "The intense starburst HDF 850.1 in a galaxy overdensity at z ≈ 5.2 in the Hubble Deep Field". In: Nature 486.7402 (June 2012), pp. 233–236. DOI: 10.1038/nature11073. arXiv: 1206.2641 [astro-ph.CO] (cit. on p. 121).

[Wal+16] Fabian Walter et al. "ALMA Spectroscopic Survey in the Hubble Ultra Deep Field: Survey Description". In: ApJ 833.1, 67 (Dec. 2016), p. 67. DOI: 10.3847/1538-4357/833/1/67. arXiv: 1607.06768 [astro-ph.GA] (cit. on p. 69).

[Wan+14] Lingyu Wang et al. "The Revised IRAS-FSC Redshift Catalogue (RIFSCz)". In: MNRAS 442.3 (Aug. 2014), pp. 2739–2750. DOI: 10.1093/mnras/stu915. arXiv: 1402.4991 [astro-ph.GA] (cit. on p. 57).

[Wan+20] Ran Wang et al. "Submillimeter Galaxy studies in the next decade: EAO Submillimetre Futures White Paper Series, 2019". In: *arXiv e-prints*, arXiv:2001.07447 (Jan. 2020), arXiv:2001.07447. arXiv: 2001.07447 [astro-ph.GA] (cit. on p. 63).

[Wan+13] S. X. Wang et al. "An ALMA Survey of Submillimeter Galaxies in the Extended Chandra Deep Field-South: The AGN Fraction and X-Ray Properties of Submillimeter Galaxies". In: ApJ 778.2, 179 (Dec. 2013), p. 179. DOI: 10.1088/0004-637X/778/2/179. arXiv: 1310.6364 [astro-ph.CO] (cit. on p. 43).

[Wan+16] T. Wang et al. "Infrared Color Selection of Massive Galaxies at z > 3". In: ApJ 816.2, 84 (Jan. 2016), p. 84. DOI: 10.3847/0004-637X/816/2/84. arXiv: 1512.02656 [astro-ph.GA] (cit. on p. 51).

[Wan+19] T. Wang et al. "A dominant population of optically invisible massive galaxies in the early Universe". In: Nature 572.7768 (Aug. 2019), pp. 211–214. DOI: 10.1038/s41586-019-1452-4. arXiv: 1908.02372 [astro-ph.GA] (cit. on pp. 40, 51, 53, 136, 167).

[Wan+17] Wei-Hao Wang et al. "SCUBA-2 Ultra Deep Imaging EAO Survey (STUDIES): Faint-end Counts at 450 μm". In: ApJ 850.1, 37 (Nov. 2017), p. 37. DOI: 10.3847/1538-4357/aa911b. arXiv: 1707.00990 [astro-ph.GA] (cit. on pp. 61, 64).

[WD01] Joseph C. Weingartner and B. T. Draine. "Dust Grain-Size Distributions and Extinction in the Milky Way, Large Magellanic Cloud, and Small Magellanic Cloud". In: ApJ 548.1 (Feb. 2001), pp. 296–309. DOI: 10.1086/318651. arXiv: astro-ph/0008146 [astro-ph] (cit. on p. 43).

[Wei+09] A. Weiß et al. "The Large Apex Bolometer Camera Survey of the Extended Chandra Deep Field South". In: ApJ 707.2 (Dec. 2009), pp. 1201–1216. DOI: 10.1088/0004-637X/707/2/1201. arXiv: 0910.2821 [astro-ph.CO] (cit. on pp. 62, 64).

[Wei+13] A. Weiß et al. "ALMA Redshifts of Millimeter-selected Galaxies from the SPT Survey: The Redshift Distribution of Dusty Star-forming Galaxies". In: ApJ 767.1, 88 (Apr. 2013), p. 88. DOI: 10.1088/0004-637X/767/1/88. arXiv: 1303.2726 [astro-ph.CO] (cit. on pp. 71, 121).

[Wet+16] Andrew R. Wetzel et al. "Reconciling Dwarf Galaxies with ΛCDM Cosmology: Simulating a Realistic Population of Satellites around a Milky Way-mass Galaxy". In: ApJ 827.2, L23 (Aug. 2016), p. L23. DOI: 10.3847/2041-8205/827/2/L23. arXiv: 1602.05957 [astro-ph.GA] (cit. on p. 33).

[Whi+17] Katherine E. Whitaker et al. "The Constant Average Relationship between Dust-obscured Star Formation and Stellar Mass from z = 0 to z = 2.5". In: ApJ 850.2, 208 (Dec. 2017), p. 208. DOI: 10.3847/1538-4357/aa94ce. arXiv: 1710.06872 [astro-ph.GA] (cit. on p. 54).

[Whi+00] Richard L. White et al. "The FIRST Bright Quasar Survey. II. 60 Nights and 1200 Spectra Later". In: ApJS 126.2 (Feb. 2000), pp. 133–207. DOI: 10.1086/313300. arXiv: astro-ph/9912215 [astro-ph] (cit. on p. 42).

[WR78] S. D. M. White and M. J. Rees. "Core condensation in heavy halos: a two-stage theory for galaxy formation and clustering." In: MNRAS 183 (May 1978), pp. 341–358. DOI: 10.1093/mnras/183.3.341 (cit. on p. 33).

[Wil+19] Christina C. Williams et al. "Discovery of a Dark, Massive, ALMA-only Galaxy at z ~ 5-6 in a Tiny 3 mm Survey". In: ApJ 884.2, 154 (Oct. 2019), p. 154. DOI: 10.3847/1538-4357/ab44aa. arXiv: 1905.11996 [astro-ph.GA] (cit. on pp. 121, 167).

[Wil+20] Grant W. Wilson et al. "The TolTEC camera: an overview of the instrument and in-lab testing results". In: *Society of Photo-Optical Instrumentation Engineers (SPIE) Conference Series*. Vol. 11453. Society of Photo-Optical Instrumentation Engineers (SPIE) Conference Series. Dec. 2020, 1145302, p. 1145302. DOI: 10.1117/12.2562331 (cit. on pp. 168, 174).

[Wri+10] Edward L. Wright et al. "The Wide-field Infrared Survey Explorer (WISE): Mission Description and Initial On-orbit Performance". In: AJ 140.6 (Dec. 2010), pp. 1868–1881. DOI: 10.1088/0004-6256/140/6/1868. arXiv: 1008.0031 [astro-ph.IM] (cit. on pp. 59, 60).

[Wu+12] Jingwen Wu et al. “Submillimeter Follow-up of WISE-selected Hyperluminous Galaxies”. In: ApJ 756.1, 96 (Sept. 2012), p. 96. DOI: 10.1088/0004-637X/756/1/96. arXiv: 1208.5518 [astro-ph.CO] (cit. on pp. 49, 59, 166).

[Wu+18] Jingwen Wu et al. “Eddington-limited Accretion in z ∼ 2 WISE-selected Hot, Dust-obscured Galaxies”. In: ApJ 852.2, 96 (Jan. 2018), p. 96. DOI: 10.3847/1538-4357/aa9ff3. arXiv: 1703.06888 [astro-ph.GA] (cit. on p. 49).

[Xia+22] M. -Y. Xiao et al. “Starbursts with suppressed velocity dispersion revealed in a forming cluster at z = 2.51”. In: A&A 664, A63 (Aug. 2022), A63. DOI: 10.1051/0004-6361/202142843. arXiv: 2205.07909 [astro-ph.GA] (cit. on p. 53).

[Xue+16] Y. Q. Xue et al. “The 2 Ms Chandra Deep Field-North Survey and the 250 ks Extended Chandra Deep Field-South Survey: Improved Point-source Catalogs”. In: ApJS 224.2, 15 (June 2016), p. 15. DOI: 10.3847/0067-0049/224/2/15. arXiv: 1602.06299 [astro-ph.GA] (cit. on p. 157).

[YLD04] Huirong Yan et al. “Dust Dynamics in Compressible Magnetohydrodynamic Turbulence”. In: ApJ 616.2 (Dec. 2004), pp. 895–911. DOI: 10.1086/425111. arXiv: astro-ph/0408173 [astro-ph] (cit. on p. 44).

[Yan+20a] Lin Yan et al. “The ALPINE-ALMA [C II] Survey: [C II] 158 μm Emission Line Luminosity Functions at z ∼ 4-6”. In: ApJ 905.2, 147 (Dec. 2020), p. 147. DOI: 10.3847/1538-4357/abc41c. arXiv: 2006.04835 [astro-ph.GA] (cit. on p. 70).

[Yan+20b] G. Yang et al. “X-CIGALE: Fitting AGN/galaxy SEDs from X-ray to infrared”. In: MNRAS 491.1 (Jan. 2020), pp. 740–757. DOI: 10.1093/mnras/stz3001. arXiv: 2001.08263 [astro-ph.GA] (cit. on p. 41).

[Yan+22] Guang Yang et al. “Fitting AGN/Galaxy X-Ray-to-radio SEDs with CIGALE and Improvement of the Code”. In: ApJ 927.2, 192 (Mar. 2022), p. 192. DOI: 10.3847/1538-4357/ac4971. arXiv: 2201.03718 [astro-ph.GA] (cit. on p. 41).

[You+11] Lisa M. Young et al. “The ATLAS^{3D} project - IV. The molecular gas content of early-type galaxies”. In: MNRAS 414.2 (June 2011), pp. 940–967. DOI: 10.1111/j.1365-2966.2011.18561.x. arXiv: 1102.4633 [astro-ph.CO] (cit. on p. 39).

[You+09] Joshua D. Younger et al. “The AzTEC/SMA Interferometric Imaging Survey of Submillimeter-selected High-redshift Galaxies”. In: ApJ 704.1 (Oct. 2009), pp. 803–812. DOI: 10.1088/0004-637X/704/1/803. arXiv: 0909.3299 [astro-ph.CO] (cit. on p. 51).

[Zav+17] J. A. Zavala et al. “The SCUBA-2 Cosmology Legacy Survey: the EGS deep field - I. Deep number counts and the redshift distribution of the recovered cosmic infrared background at 450 and 850 μ m”. In: MNRAS 464.3 (Jan. 2017), pp. 3369–3384. DOI: 10.1093/mnras/stw2630. arXiv: 1610.03551 [astro-ph.GA] (cit. on p. 61).

[Zav+18] J. A. Zavala et al. “Constraining the Volume Density of Dusty Star-forming Galaxies through the First 3 mm Number Counts from ALMA”. In: ApJ 869.1, 71 (Dec. 2018), p. 71. DOI: 10.3847/1538-4357/aaecd2. arXiv: 1810.12300 [astro-ph.GA] (cit. on pp. 40, 64, 66, 68, 121).

[Zav+21] J. A. Zavala et al. “The Evolution of the IR Luminosity Function and Dust-obscured Star Formation over the Past 13 Billion Years”. In: ApJ 909.2, 165 (Mar. 2021), p. 165. DOI: 10.3847/1538-4357/abdb27. arXiv: 2101.04734 [astro-ph.GA] (cit. on pp. 36, 54, 56, 66, 68, 110, 112).

[Zyl13] Robert Zylka. *MOPSIC: Extended Version of MOPSI*. Mar. 2013. ascl: 1303.011 (cit. on p. 81).